

# **Synthesis and chemical characterization of photoresists for X-ray imaging**

Zur Erlangung des akademischen Grades eines

**DOKTORS DER NATURWISSENSCHAFTEN**  
(Dr. rer. nat.)

von der KIT-Fakultät für Chemie und Biowissenschaften  
des Karlsruher Instituts für Technologie (KIT)

genehmigte

DISSERTATION

Von

**M. Sc. Vitor Vlnieska**

aus Pres. Venceslau, Sp - Brasilien

Dekan: Prof. Dr. Manfred Wilhelm

Referent: Prof. Dr. Jan-Dierk Grunwaldt

Korreferent: Prof. Dr. Patrick Théato

Tag der mündlichen Prüfung: 23.07.2020



This document is licensed under a Creative Commons Attribution-ShareAlike 4.0 International License (CC BY-SA 4.0):  
<https://creativecommons.org/licenses/by-sa/4.0/deed.en>

*Se as coisas são inatingíveis... ora!  
Não é motivo para não querê-las...  
Que tristes os caminhos, se não fora  
a presença distante das estrelas!*

*Mario Quintana*



---

# Abstract

Several types of imaging technologies and micropatterning production rely on lithography process chain fabrication. Photoresists (or photo-resins) are the main and most important raw material used for lithography techniques. Negative-tone photo-resins are the most suitable raw materials for the production of high aspect ratio (HAR) structures through X-ray lithography. An example of these structures is the optical components known as gratings, used in phase-sensitive imaging systems.

Nowadays, even with the best technologies and radiation sources available, it is still challenging to produce gratings without structural defects or imperfections. For specific applications involving HAR gratings, to find the correct photo-resin with enough quality can be difficult, costly, and time-consuming.

For this reason, photo-resins commercially available for the production of HAR structures (produced mainly through X-ray lithography) were studied, and a characterization methodology was proposed. Through matrix-assisted laser desorption ionization – time of flight – mass spectroscopy (MALDI-TOF-MS) peak masses in the range of 250 to 1300 Da·mol<sup>-1</sup>, which represents a mixture of monomer, dimer, trimer, tetramer, traces of pentamer and hexamer were observed. Three from ten samples presented a high percentage of non-epoxidized oligomer chains. With thermo gravimetric analysis (TGA) significant variations in the volume composition of the solvent (up 5.5 % difference) were found. The same photo-resins (with different lots of fabrication), thus, can present different properties.

A strategy to synthesize and formulate photo-resins was proposed, named as deep and macro levels of properties. Regarding the deep-level, oligomers were synthesized from bisphenol-A. The polymerization synthesis was optimized. Three distinct profiles of polydispersity were obtained. The resins are a mixture of monomers, dimers, trimers, and traces of tetramers. The oligomers presented a wide range of secondary products and their derivative, which were identified mainly by electrospray ionization (micro) time of flight mass spectroscopy (ESI- $\mu$ -TOF-MS) and nuclear magnetic resonance (NMR) techniques.

Still working at the deep-level of properties, the alkylation of the hydroxyl groups presented a wide range of structures, which were characterized and quantified using spectroscopy techniques such as ESI- $\mu$ -TOF-MS and NMR, as well as differential scanning calorimetry (DSC) and elemental analysis through scanning electron microscopy (SEM) and energy-dispersive X-ray (EDX) spectroscopy methods. The epoxidized resins presented an epoxidation ratio of 96 % in the phenolic positions. The alkylation reaction also presented derivative products, which were characterized with NMR and SEM-EDX. An epoxidation ratio between 1:2 and 1:3 (bisphenol-A:epichlorohydrin) was found. Regarding DSC experiments, it is interesting to note that epoxy resins with epoxidation degrees from 50 to 96 % mol·mol<sub>polymer</sub><sup>-1</sup>, presented glass transition temperature (*T<sub>g</sub>*) lower than room temperature. This characteristic restricts its usage for photoresist

formulations. Since the physical state always remains viscous, the epoxidation degree plays a role in two properties: sensitivity of the photoresist and its physical state. This result is new, and no publications related to this characteristic were found in the literature.

Afterwards the macro-level of properties was applied to prepare the formulations. Epoxy resins were used to formulate photo-resins in the simplest way possible. Three photo-resins were formulated using the synthesized resins, hexafluoroantimonate triaryl sulfonium salts as photoinitiator and cyclopentanone was applied as a solvent.

The formulations were evaluated initially using a squared pattern of  $1.3 \text{ mm}^2$ . The best formulations were then studied in a pattern structure varying from 50 down to  $1 \text{ }\mu\text{m}$  period. The patterned structures were compared with the chemical composition of the photo-resins.

Without the usage of any other additives in the formulations, it was possible to achieve good quality structures with UV lithography. In the first trial of experiments with large structures (squared pattern of  $1.3 \text{ mm}^2$ ) good quality structures were produced with several formulations. In this case, the properties of the epoxy resins seem to be not significant enough to observe improvements in the structures. It is suggested that the deep-level of properties can be relaxed when structures above  $50 \text{ }\mu\text{m}$  are produced.

In the second trial of experiments, structures from 50 to  $10 \text{ }\mu\text{m}$  period were successfully produced. The best results were achieved using  $40 \text{ \% mol}\cdot\text{mol}_{\text{polymer}}^{-1}$  for the epoxidation degree and  $30 \text{ \% mol}\cdot\text{mol}_{\text{polymer}}^{-1}$  for the photoinitiator. The polydispersity of the epoxy resins starts to play a significant role with structures smaller than  $50 \text{ }\mu\text{m}$  period. In this case, formulations with epoxy resin R1 presented structures with better resolution and quality in comparison with the other two formulations.

The quality of microstructures below  $50 \text{ }\mu\text{m}$  seems to be highly dependent on the resin material and its properties. For better reproducibility and efficiency in the lithography techniques, the deep and macro levels of properties shall be applied to synthesize and formulate photoresists.

---

# Kurzfassung

Verschiedenste Arten von Bildgebungstechnologien und die Herstellung von Mikromustern beruhen auf der Herstellung von Lithografie-basierten Prozessketten. Fotolacke (oder Fotoharze) sind die hauptsächlichsten und wichtigsten Basisstoffe, die für Lithografiertechniken nötig sind. Negativlacke sind die am besten geeigneten Fotolacke für die Herstellung von Strukturen mit hohem Aspektverhältnis („high aspect ratio, HAR“) durch Röntgenlithografie. Ein Beispiel für diese Strukturen sind die als Gitter bezeichneten optischen Komponenten, die in phasenempfindlichen Abbildungssystemen verwendet werden.

Heutzutage ist es selbst mit den besten verfügbaren Technologien und Strahlungsquellen immer noch eine Herausforderung, Gitter ohne strukturelle Defekte oder Mängel herzustellen. Bei speziellen Anwendungen mit HAR-Gittern kann es schwierig, kostspielig und zeitaufwendig sein, den richtigen Fotolack mit ausreichender Qualität zu finden.

Aus diesem Grund wurden kommerziell erhältliche Fotolacke für die Herstellung von HAR-Strukturen (hauptsächlich durch Röntgenlithographie hergestellt) untersucht und Charakterisierungsmethodiken entwickelt. Bei der MALDI-TOF-MS („matrix-assisted laser desorption ionization – time of flight – mass spectroscopy“) wurden ein Massenbereiche von 250 bis 1300 Da·mol<sup>-1</sup> beobachtet, welches ein Gemisch aus Monomer, Dimer, Trimer, Tetramer und geringe Beträge von Pentamer und Hexamer aufzeigt. Mit der TGA („thermogravimetric analysis“) wurden signifikante Abweichungen in der Volumenzusammensetzung des Lösungsmittels festgestellt (bis zu 5,5 % Abweichung). Drei von zehn Proben wiesen einen hohen Prozentsatz an nicht-epoxidierten Oligomerketten auf. Dieselben Fotoharze (mit unterschiedlichen Herstellungschargen) können daher unterschiedliche Eigenschaften aufweisen.

Es wurde eine Strategie zur Synthese und Formulierung von Fotoharzen vorgeschlagen, die als „deep“ (tiefgehend, molekular) und „macro-level“ (Makroebene) zum Einstellen der Eigenschaften bezeichnet wurde. In bezug auf den „deep-level“ wurden Oligomere aus Bisphenol-A synthetisiert. Die Polymerisationssynthese wurde optimiert. Es wurden drei verschiedene Profile der Polydispersität erhalten. Die Harze sind eine Mischung aus Monomeren, Dimeren, Trimeren und geringe Beträge von Tetrameren. Die Oligomere stellten eine breite Palette von Sekundärprodukten und deren Derivate dar, die hauptsächlich durch ESI- $\mu$ -TOF-MS („electrospray ionization (micro) time of flight mass spectroscopy“) und NMR („nuclear magnetic resonance“)-Techniken identifiziert wurden.

Die Alkylierung der Hydroxylgruppen, die zum molekularen Teil der Einstellung der Eigenschaften gehört, bot eine breite Palette von Strukturen, die mit spektroskopischen Techniken wie ESI- $\mu$ -TOF-MS und NMR sowie mit DSC („differential scanning calorimetry“) und Elementaranalyse-Charakterisierungsmethoden wie SEM-EDX („scanning electron microscopy (SEM) and energy-dispersive X-ray (EDX) Spectroscopy“)

charakterisiert und quantifiziert wurden. Die Epoxid-Harze wiesen in den phenolischen Positionen ein Epoxidverhältnis von 96 % auf. Die Alkylierungsreaktion resultiert auch in Derivatprodukten, die mit NMR und SEM-EDX charakterisiert wurden. Es wurde ein Epoxidationsverhältnis zwischen 1:2 und 1:3 (Bisphenol-A:Epichlorhydrin) gefunden. In Bezug auf DSC-Experimente ist es wichtig festzuhalten, dass Epoxidharze mit Epoxidationsgraden von 50 bis 96 % mol $\cdot$ mol<sub>polymer</sub><sup>-1</sup> eine „glass transition temperature“ ( $T_g$ ) unter Raumtemperatur aufwiesen, eine Eigenschaft, die ihre Verwendung für Zusammensetzungen des Fotolacks einschränkt. Da der physikalische Zustand immer viskos bleibt, spielt der Epoxidationsgrad bei zwei Eigenschaften eine Rolle: der Empfindlichkeit des Fotolacks und seinem physikalischen Zustand. Dieses Ergebnis ist neu, und in der Literatur wurden keine Veröffentlichungen zu diesem Merkmal gefunden.

Danach wurde die Anpassung auf Makroebene zur Einstellung der optimalen Formulierung vorgenommen. Epoxidharze wurden verwendet, um Fotoharze auf einfachste Weise zu formulieren. Drei Photoharze wurden unter Verwendung der synthetisierten Harze genutzt, wobei Hexafluoroantimonat-Triarylsulfoniumsalze als Photokatalysator und Cyclopentanon als Lösungsmittel verwendet wurden. Die Formulierungen wurden zunächst unter Verwendung eines quadratischen Musters von 1,3 mm<sup>2</sup> ausgewertet. Die besten Zusammensetzungen wurden dann in einer Musterstruktur untersucht, die von 50 bis zu 1  $\mu$ m Periode variiert. Die gemusterten Strukturen wurden mit der chemischen Zusammensetzung der Fotoharze verglichen.

Ohne die Verwendung anderer Additive in den Formulierungen konnten mit der UV-Lithographie Strukturen von guter Qualität erzielt werden. Im ersten Versuch von Experimenten mit großen Strukturen (quadratisches Muster von 1,3 mm<sup>2</sup>) wurden mit mehreren Formulierungen Strukturen guter Qualität erzeugt. In diesem Fall scheinen die Eigenschaften der Epoxidharze nicht signifikant genug unterschiedlich zu sein, um Verbesserungen in den Strukturen zu beobachten. Es wird vorgeschlagen, dass Einstellung der Eigenschaften auf molekularer Ebene (deep-level) aufgelockert werden kann, wenn Strukturen über 50  $\mu$ m erzeugt werden.

Im zweiten Reihe an Versuchen wurden erfolgreich Strukturen von eins 50 bis eins 10  $\mu$ m Perioden hergestellt. Die besten Ergebnisse wurden unter Verwendung von 40 % mol $\cdot$ mol<sub>polymer</sub><sup>-1</sup> für den Epoxidationsgrad und 30 % mol $\cdot$ mol<sub>polymer</sub><sup>-1</sup> für den Photokatalysator erzielt. Die Polydispersität der Epoxidharze beginnt bei Strukturen, die kleiner als eine 50  $\mu$ m Periode sind, eine bedeutende Rolle zu spielen. In diesem Fall zeigten Formulierungen mit Epoxidharz R1 Strukturen mit besserer Auflösung und Qualität im Vergleich zu den beiden anderen Formulierungen.

Die Qualität von Mikrostrukturen unter 50  $\mu$ m scheint stark vom Harzmaterial und dessen Eigenschaften abhängig zu sein. Für eine bessere Reproduzierbarkeit und Effizienz der Lithografiertechniken sollten die Tiefen- und Makroebenen der Eigenschaften für die Synthese und Formulierung von Fotolacken genutzt werden.

---

# Summary

<b>Abstract</b> .....	<b>I</b>
<b>Kurzfassung</b> .....	<b>III</b>
<b>Acknowledgment</b> .....	<b>VII</b>
<b>1 INTRODUCTION</b> .....	<b>1</b>
1.1 Grating-based interferometry imaging and its applications.....	2
1.2 Gratings and the lithography process.....	7
1.3 The photoresists.....	16
1.5 State of the art for grating-based interferometry techniques, lithography and photoresists.....	30
<b>2 OBJECTIVE</b> .....	<b>31</b>
<b>3 REACTION PROCEDURES, MATERIALS AND METHODS</b> .....	<b>32</b>
3.1 Polymerization of bisphenol-A.....	32
3.2 Epoxidation of the oligomers.....	33
3.3 Materials.....	33
3.4 Methods.....	33
3.5 Fourier-transform Infrared Spectroscopy (FTIR).....	33
3.6 Thermogravimetric Analysis (TGA).....	34
3.7 Matrix-Assisted Laser Desorption Ionization Mass Spectroscopy (MALDI-TOF-MS).....	34
3.8 Electrospray Ionization - Time of Flight – Mass Spectroscopy (ESI- $\mu$ -TOF-MS).....	35
3.9 Nuclear Magnetic Resonance Spectroscopy (NMR).....	35
3.10 Differential Scanning Calorimetry (DSC).....	36
3.11 Formulation of the photo-resins.....	37
3.12 Quality evaluation through UV lithography.....	38
3.13 Test pattern structures through Deep-UV and UV lithography.....	40
3.14 Deep-UV and UV lithography exposures.....	40
3.15 Plasma Etching.....	41
3.16 Spin-coating.....	41
3.17 Scanning Electron Microscopy.....	41
3.18 Scanning Electron Microscopy – Energy Dispersive Spectroscopy of X-rays (SEM-EDX).....	42
3.19 Optical microscope measurements.....	42
<b>4 CHARACTERIZATION OF COMMERCIAL PHOTORESISTS</b> <sup>1</sup> .....	<b>44</b>
4.1 Characterization Methodology.....	44
4.2 FTIR spectroscopy.....	45
4.3 Thermogravimetric Analysis (TGA).....	46
4.4 Matrix-Assisted Laser Desorption Ionization Mass Spectroscopy (MALDI-TOF-MS).....	48
4.5 Conclusion.....	56
<b>5 SYNTHESIS AND CHARACTERIZATION OF EPOXY RESINS</b> <sup>1</sup> .....	<b>57</b>
5.1 Polymerization reaction.....	57
5.2 Alkylation of the phenolic groups and characterization.....	68
5.3 Conclusions.....	78
<b>6 LITHOGRAPHIC PERFORMANCE OF THE SYNTHESIZED EPOXY RESINS</b> <sup>1</sup> .....	<b>80</b>
6.1 Photo-resins formulation.....	80
6.2 UV Lithography (qualitative evaluation).....	81
6.3 UV and Deep-UV lithography (50 down to 1 $\mu$ m).....	87

6.4	Conclusions .....	90
<b>7</b>	<b>CONCLUSIONS AND FUTURE PERSPECTIVES .....</b>	<b>92</b>
<b>8</b>	<b>REFERENCES .....</b>	<b>94</b>
<b>9</b>	<b>Appendix A .....</b>	<b>100</b>
9.1	Scientific supporting information .....	100
9.2	List of publications during Ph.D. period .....	126

---

# Acknowledgment

I would like to thank the persons who have given insights, hands-on, and discussions to the development of this project. Prof. Dr. Jan-Dierk Grunwaldt, who was always motivated to discuss and to share his experience. Dr. Danays Kunka who is the core person of this project, and the idealizer of the initial insights. They have guided me a lot during the last years. I will be always very grateful for their lessons. Dr. Klaus Bade, who supported me from the beginning in the laboratory. Our research group, mainly Andrey Mikhaylov and Margarita Zakharova, who helped me with knowledge (physics) and hands-on in several experiments. Also, I would like to say thank you to the employees of IMT who have supported this project, especially Alexandra Moritz, who helped me all the time regarding the workshop and Heike Fornasier, who taught me several techniques in the cleanroom.

Regarding institutions, first I would like to thank DAAD for the funding during this period, a special thank you to my mentor Maria José Salgado-Martinez, who was always ready to help me regarding my immigration to Germany and funding. Also, I want to thank KHYS (especially Jutta Klein-Hitpaß) and INTL (especially Oliver Kaas) for all support given, mainly related to international affairs and opportunities for conferences and exchanges. Still to INTL, to thank the promoted events with students since I was accepted as a Ph.D. student at KIT. I thank also KSOP for the opportunities given to improve my knowledge with seminars and MBA modules offered to the Ph.D. students. I would like to thank the institutes IMT, ITCP, INT, KARA, and IKFT to provide structure and resources for this project.

I have learned a lot during the last years.

A would like to say thank you to my family (Raquel, Rafael e Vanessa) and close friends, Michael Oldenburg, Andrey Mikhaylov, Natalia Kiseleva, Margarita Zakharova, Roman Lyubimenko and Emil Marmleyev for all the support and friendship. Last but not least, a very special thank you to my better half, Radana Bogdan, who was always at my side during this journey, she changed my life for better.



# 1 INTRODUCTION

In the last twenty years, conventional X-ray imaging techniques (e.g., radiography) have been incredibly improved with several approaches. Among them, notably high interest receives the development of grating-based interferometric techniques, which results in imaging analysis with higher resolution and more information. When it is compared with radiography, grating-based interferometric techniques have as a main advantage of the possibility to differentiate regions with low densities in the sample [1, 2].

One of these techniques, the Talbot interferometry, is capable of analyzing three different properties when X-ray interacts with matter, extracting simultaneously information regarding transmittance, diffraction, and phase shift of the X-ray wavelength [3].

To achieve such capability of imaging, radiography systems have to be modified, where the main change is the addition of optical components, known as gratings. These optical components have to fulfill minimum requirements to be used in the experimental setup, which can only be achieved using lithography fabrication techniques. The features of the gratings usually lead to high aspect ratio (HAR) structures, a characteristic that imposes several challenges for the lithography technology [2, 4, 5].

Lithography fabrication is a technology of transferring patterns, having several intermediate steps to produce micro and nano components such as micro-electrical mechanical systems (MEMS), processors, micro-optical components, etc. It relies primarily on its main raw material, known as photoresist or photo-resin. The quality of the components fabricated by the lithography process is highly dependent in the chemical characteristics of the photoresists [6-14].

Grating-based interferometric techniques have been pushed lithography fabrication to the limits of the technology, where gratings with lower periods, defect-free structures, and large areas have to be fabricated. These features impose challenges to the quality control of the raw materials used in lithography (photoresists), as well as to pursue a strict control of the lithography fabrication parameters [15].

In this direction, three main topics will be presented for a comprehensive understanding of this thesis' motivation. In section 1.1, grating-based interferometric imaging and its applications are presented, explaining their physical principle, the modifications in the X-ray imaging experimental setup applying gratings, and an example of one of the several grating-based interferometric techniques, the Talbot interferometry. At the end of this topic, its actual challenges and limitations are presented. In the next section (1.2), the most common design and features of the gratings, as well as the lithography process, are discussed. The main limitations related to gratings fabrication are presented. In the last topic, and not less relevant (1.3), a historical perspective of the development of the photoresist is presented with its main advances and formulations in the course of almost two hundred years of its history. It will be presented the best suitable formulations to fabricate HAR structures and, the actual challenges regarding photoresists for HAR structures.

## 1.1 Grating-based interferometry imaging and its applications

Grating-based interferometry imaging techniques have been developed to achieve images with better resolution and to provide more information about the sample. One of its main advantages is the possibility to characterize samples with low densities, which it is not possible to realize with conventional X-ray imaging (radiography) [1-3, 5, 16]. In radiography, an X-ray source generates a beam that is projected towards an object, and the image is recorded by a detector, as Figure 1 shows.

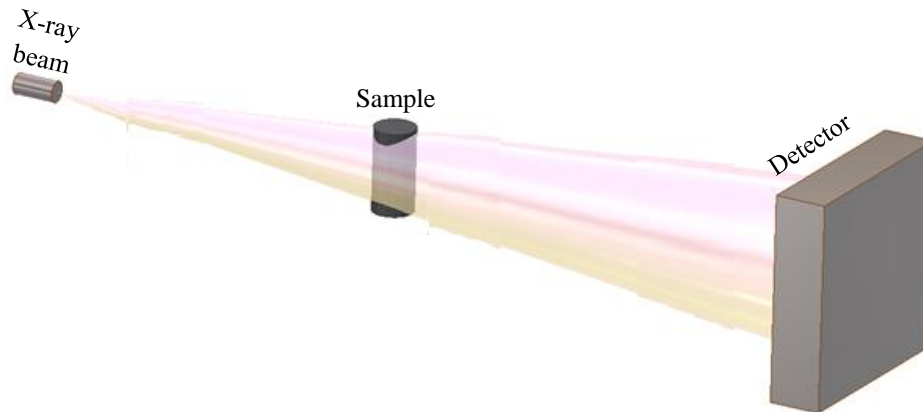


**Figure 1:** Conventional X-ray imaging setup

Conventional radiography is based on the absorption of X-rays. Since the beam intensity decreases depending mainly on the atomic number, density differences, and concentration inside the sample, the variations can be measured directly with the help of an X-ray detector, giving bright and dark regions. It provides useful information for strong absorbing materials.

Nevertheless, conventional radiography has limited applicability for distinguishing materials with similar absorption coefficients such as soft tissues, light materials, and specimens whose internal structure differs slightly regarding density.

X-ray grating-based imaging techniques are one of the alternatives to overcome the limitations of conventional X-ray radiography. One of these types of imaging, the grating-based interferometry, is based in the Talbot effect, described in 1836 by H. F. Talbot. [17].

In his publication, Talbot describes a non-common light effect:

“...common solar light appears to play the part of homogeneous light, and to achromatize itself; if I may use such an expression, in a very high degree of perfection.”

Talbot discovered the self-imaging of periodic structures. The physical effect occurs when plane-parallel light falls onto an absorption mask with periodic openings. The light will generate images of this grating in multiples of a well-defined distance, called the Talbot length.

Although the physical effect was documented more than 150 years ago, only 17 years ago, Momose et al. (2003) reported their initial grating-based experimental setup [1, 2].

To understand this effect and to distinguish similar absorption coefficients, it is necessary to comprehend the interaction of X-ray with the matter. When X-ray penetrates matter, the amplitude and the direction of propagation of the electromagnetic wavefront beam are affected. The amplitude is attenuated due to the absorption coefficient of the sample. The phase is shifted due to the distinct refraction index of the corresponding mediums (sample and air), and small refraction of the X-rays occurs depending on the features of the sample.

The use of those effects improves the quality of the image considerably, providing simultaneously three types of information [1, 2]. Figure 2 presents these effects when X-ray interacts with matter.

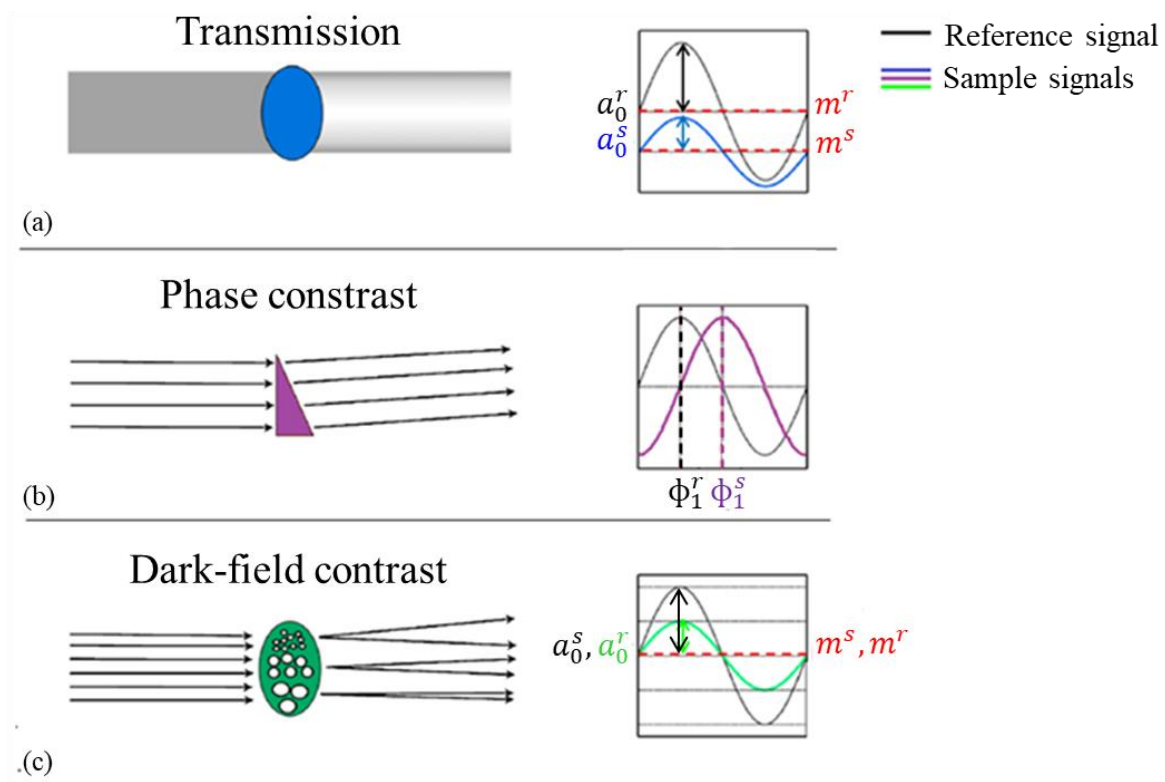


**Figure 2:** Three contrast modalities in a grating-based interferometer: (a) attenuation (transmission) of the X-ray beam, (b) phase shift, and (c) scattering produced by the sample. Additionally, the reference and sample signals are shown on the right side, adapted from Pfeiffer et al., 2013 [3] (Elsevier and Copyright Clearance Center, license number 5060261297355)

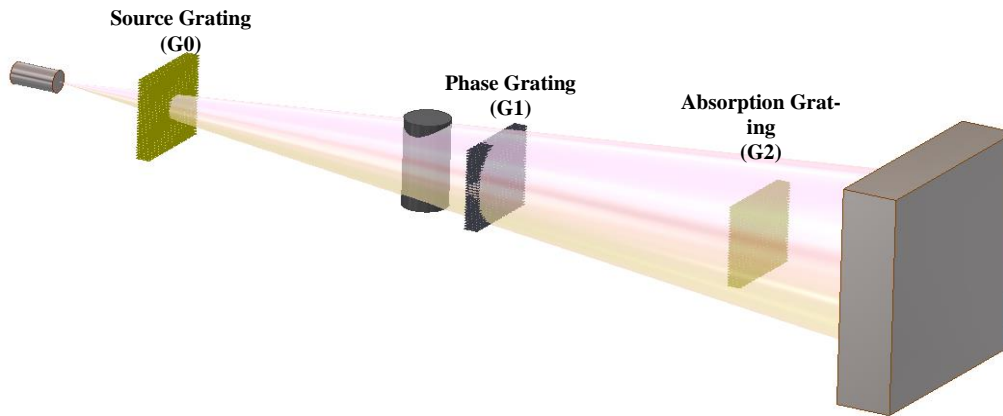
In practice, with X-ray grating-based imaging it is possible to obtain the typical X-ray radiography image (Figure 2 (a) - transmission) and two complementary images, one related to the refractive index (Figure 2 (b) - phase-contrast) and the other one related to the small-angle scattering (Figure 2 (c) – dark-field contrast). These two additional images provide new relevant information about the sample. In Table 1, equation 1 is related to the attenuation effect, which is the loss of transmission signal effect, equation 2 calculates the phase shift, and equation 3 is associated with the dark-field contrast.

**Table 1:** Equations associated with the transmission, phase contrast, and dark-field contrast [1, 5].

$T = \frac{a_0^s}{a_0^r} \quad (1)$	$\Delta\varphi = \varphi_1^s - \varphi_1^r \quad (2)$	$V^r = \frac{a_0^r}{m^r}; V^s = \frac{a_0^s}{m^s}; V^n = \frac{V^s}{V^r} \quad (3)$
-------------------------------------	---	---

In equation 1,  $T$  is the normalized average transmission of the sample,  $a_0^r$  is related to the reference signal,  $a_0^s$  is associated with the sample signal. In equation 2,  $\Delta\varphi$  is the difference between the sample and reference phases, where  $\varphi_1^s$  is the sample phase, and  $\varphi_1^r$  is the reference phase. In equation 3, the dark-field is given by the relative decrease of the visibility in the system due to the sample, defined by the normalized visibility ( $V^n$ ). Visibility is defined, taking into account the maximum and minimum intensities, as shown in equation 4 (section 1.2) [1, 5].

In order to detect the effects above mentioned, it is necessary to implement modifications in the experimental setup, where the main parts to be added are optical components known as *gratings*. Depending on the grating-based imaging technique, one-, two- or three gratings may be necessary between the X-ray tube and the detector on the standard setup. One of the most challenging configurations, for optical alignments and grating production, is the grating-based interferometric setup used with a laboratory source (cone-beam). Figure 3 demonstrates the grating-based interferometric setup.

**Figure 3:** General X-ray interferometric imaging system with a laboratory source

In Figure 3, the source grating (G0) is positioned close to the X-ray source. It is an aperture mask with transmitting slits to generate a periodicity and partial coherence in the case of the cone-beam source. Phase grating (G1), has the function to act as a phase mask, and creates periodic phase modulation in the wavefront, obtaining in this way a periodic pattern as a signal. The G2 grating has the same periodicity and orientation of G1, and it is positioned in the detection plane, close to the detector. When a sample is placed close to G1, the pattern intensity is altered, and this alteration can be quantitatively calculated [16].

Various research groups have been working and developing grating-based imaging techniques, and since the beginning of 2000 decade, these methods have been used for several purposes. One of these applications is presented below [2, 5].

Imaging by differential phase contrast (DCPI) is one novel developed phase-sensitive X-ray imaging techniques. It is ideal for non-destructive tests, with materials of low absorption [15]. This technique can be applied in almost all fields of research to achieve characterization by X-ray imaging. Figure 4 presents an example of its application in material sciences.

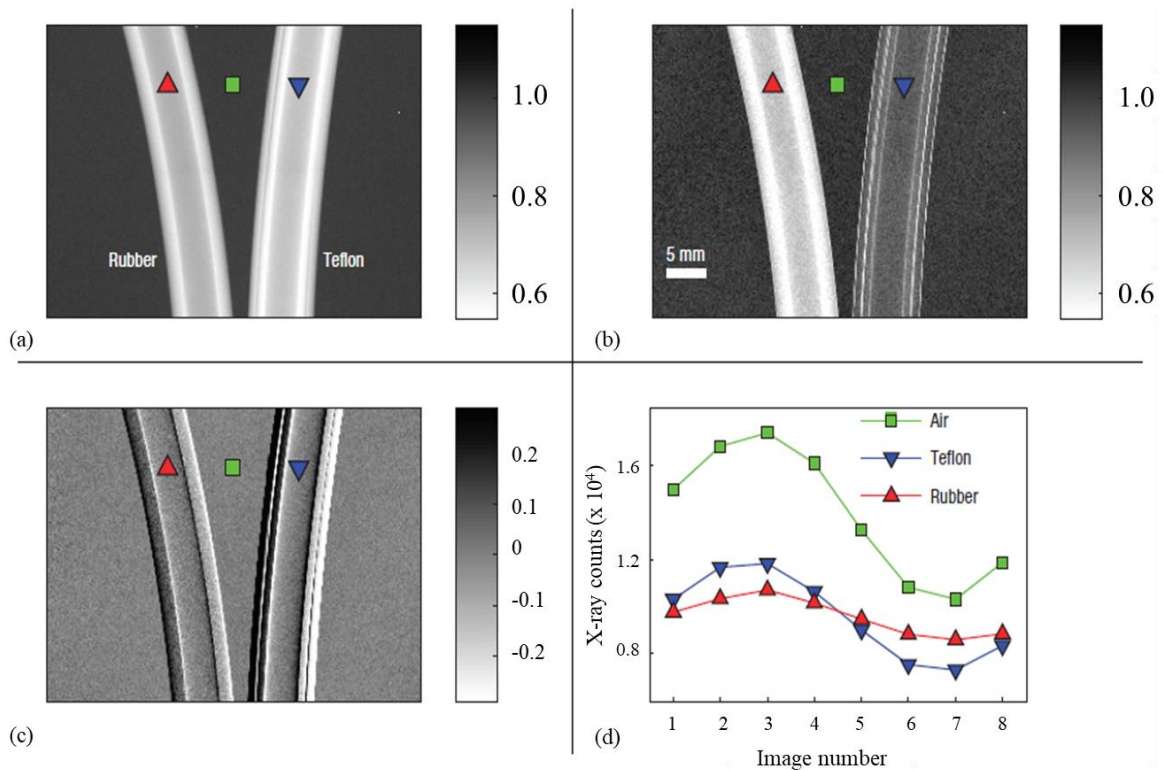


**Figure 4:** Comparison of a Teflon (PTFE) and natural rubber plastic tubes: (a) conventional X-ray transmission image, (b) dark-field contrast image, (c) differential-phase contrast image, (d) intensity oscillations extracted from a series of eight measurements in an interferometric setup. Images from Pfeiffer et al. (2008) [16] (Springer Nature and Copyright Clearance Center, license number 5060290933842)

In Figure 4, it is interesting to note in (b) and (d) the loss of visibility in the detector pixel behind the natural rubber tube. The decrease in visibility is due to the strong small-angle scattering produced by rubber pore structures. The phase contrast (Figure 4 (c)) provides better information on the border of the tubes. The total exposure time for the whole data set was 40 seconds. Figure 5 presents an example in the biomedical field.

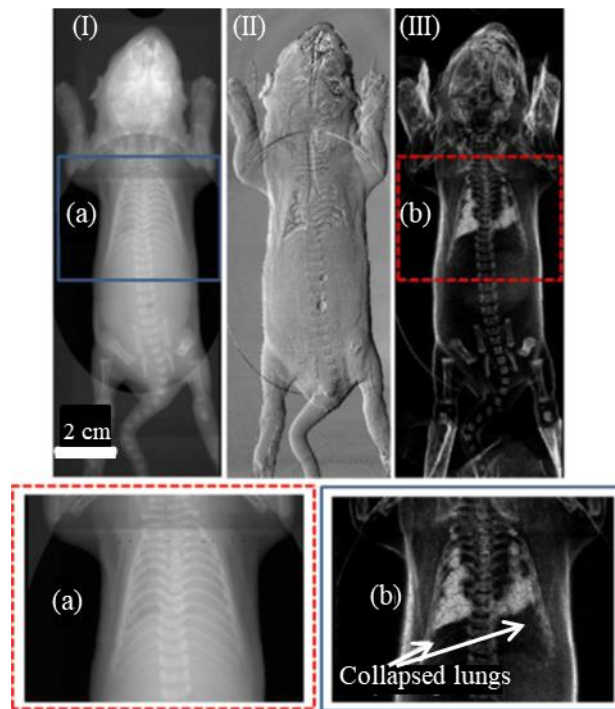


**Figure 5:** Comparison between conventional X-ray image and images generated based on the Talbot effect. (a) Conventional X-ray radiography. (b) Dark-field contrast. In the upper part, between (a) and (b), Phase contrast imaging. Reproduced from Gkoumas et al. (2016) [18] (Elsevier and Copyright Clearance Center, license number 5060300022673)

In Figure 5 upper part, (a) one can see the absorption image, the middle one is the differential phase contrast, showing the refraction of the trachea, and borders of organs of the mice; and (b) is the dark field image. In this example, comparing the conventional absorption method (a) and dark field (b), the enlarged images in the lower part show the visualization of the collapsed lungs of the mice in (b) meanwhile in the image (a) is only possible to see the high absorbing imaging from the bones [18].

Although grating-based interferometric imaging techniques can better characterize samples, challenges regarding the fabrication technology of the gratings have to be overcome. For example, it is a necessity to increase the field of view (FoV) of the imaging system for the medicine field. Due to the limitation of lithography technology, gratings are produced usually in areas varying from 3 to 5 cm<sup>2</sup>. Schröter et al. (2017) proposed the tiling of several gratings into a carrier substrate, increasing the field of view to 20 cm<sup>2</sup>. However, restrictions regarding the visibility of the gratings, such as the inter-grating gap (approximately 50 μm of the distance between the gratings), can be a limitation for specific applications [19].

The resolution of the interferometric imaging is inversely proportional to the periodicity of the gratings and detectors, which results in the comparison of the smaller periods in the gratings, the higher resolution in the imaging. Nowadays, it is possible to fabricate gratings with periods of approximately 1.2 μm and heights up to 120 μm (see Figure 7), reaching values of 100 for HAR structures. Nevertheless, it is still not possible to produce gratings with these features reaching constant homogeneity (regarding the quality of the structures) in the whole area of the grating. Several parameters in the lithography fabrication process and the chemical composition of the photoresists are directly related to the final quality of gratings [4, 15].

## 1.2 Gratings and the lithography process

Gratings are the main optical components in an X-ray grating-based imaging setup. Gratings typically have the shape of several walls (lamellas) in parallel with one each other. Initially, there are two essential characteristics to consider when the gratings are designed, the period, and the aspect ratio. Figure 6 presents the most straightforward design of the gratings used in interferometric techniques.

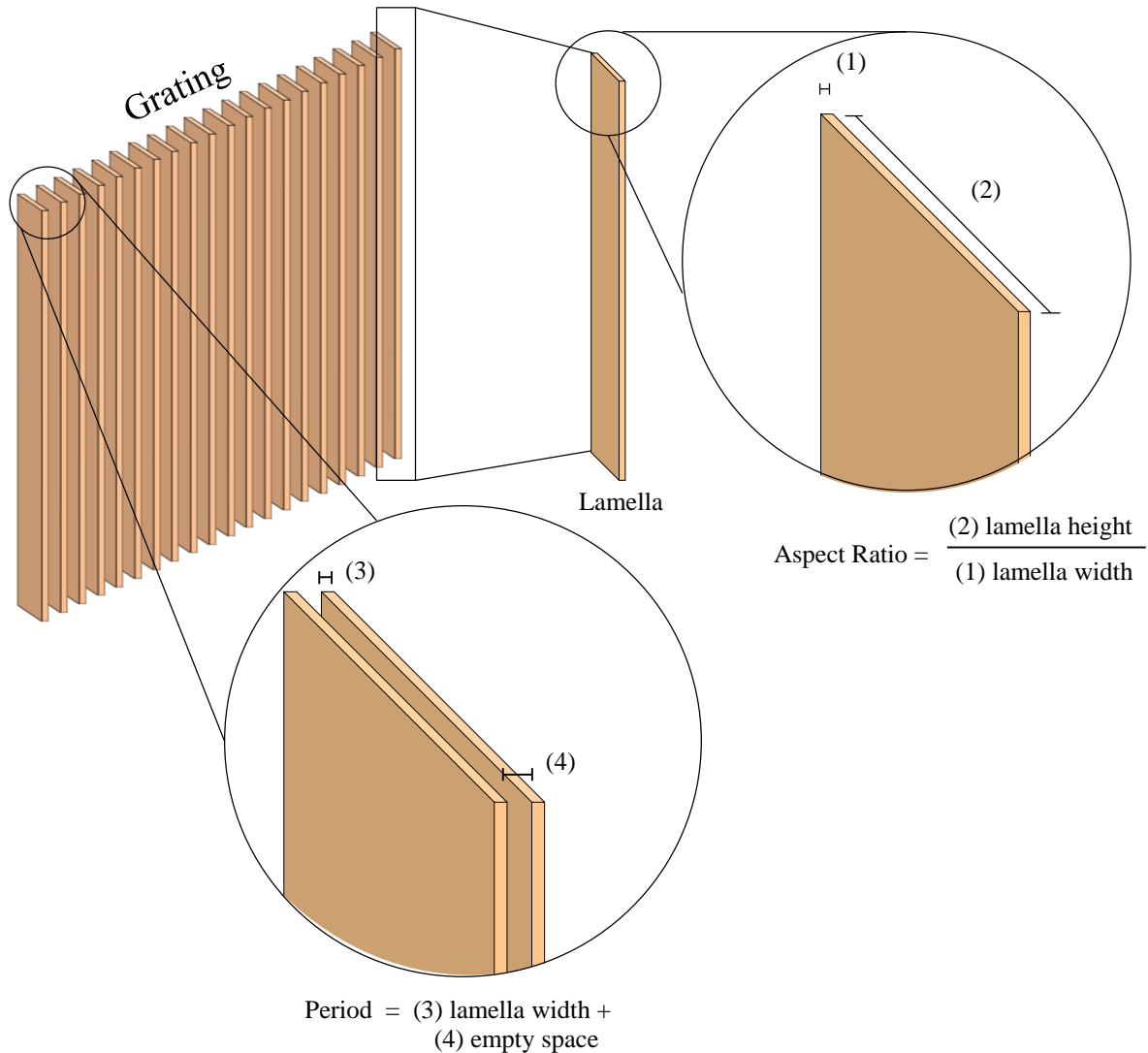


**Figure 6:** Grating design and concepts of aspect ratio and period

Depending on the experiment, the energy and experimental configuration varies. Different imaging setups, such as synchrotron sources or X-ray tubes, demand different types of gratings. The aspect ratio and pattern quality have a direct influence on the performance of the interferometric technique.

An important parameter to evaluate is the interaction of the X-ray source with the gratings, which is given by the visibility ( $V$ ) value. Lamellas of the gratings need to be high enough to attenuate the X-ray radiation in the places

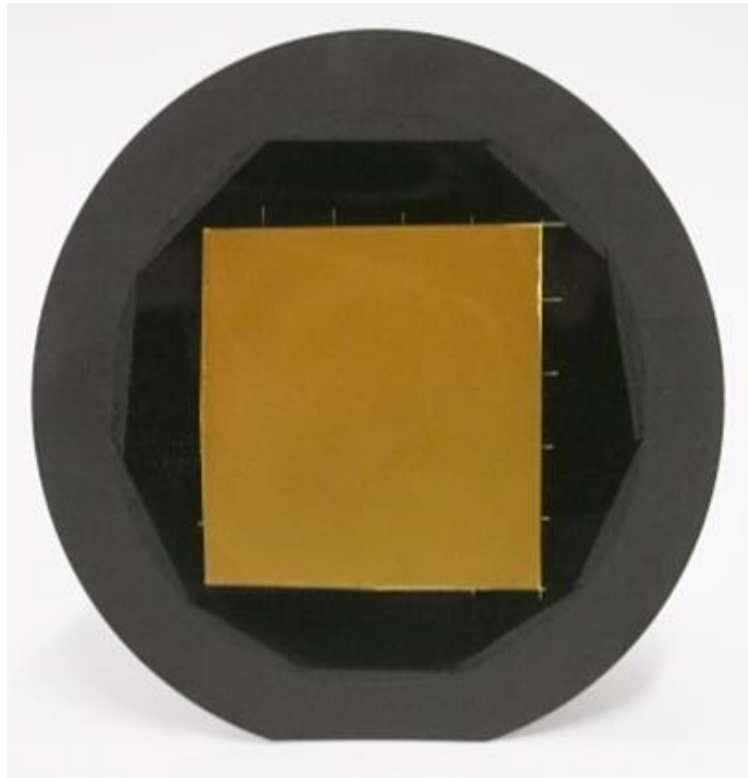
where it has to be stopped. Furthermore, the pattern has to be homogeneous to provide sufficient image quality in phase contrast. The concept of visibility is defined by equation 4 [19-22].

$$V = \frac{I_{max} - I_{min}}{I_{max} + I_{min}} \quad (4)$$

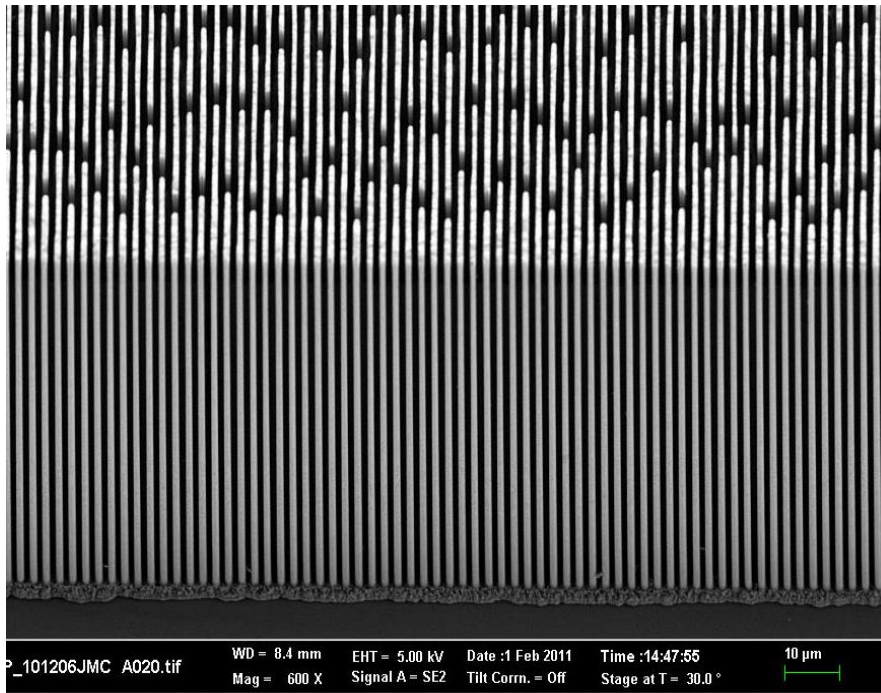
In equation 4,  $V$  is the calculated visibility, whereas  $I$  represent the intensities (maximum and minimum) measured in the detector [21].

The energy of the X-rays defines the thickness of the absorber (lamella height). Typical examples of design energies for different applications range between 20 to 100 keV. For example, using approximately 100 keV, the lamellas of the gratings should have around 200  $\mu\text{m}$  height to absorb this energy efficiently. In most of the cases, the gratings are produced using gold as electroplating material.

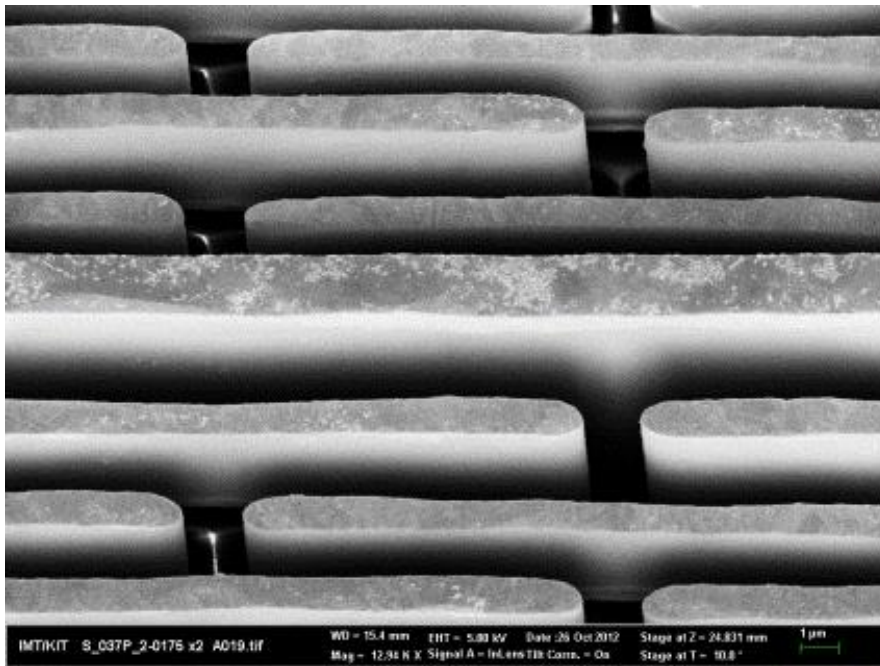
In X-ray grating-based interferometry, for example, in DCPI, the higher the resolution, the smaller should be the detector pixel size combined with the smallest gratings period. With smaller periods, the smaller are the distances between the optical components in the experimental setup. Figure 7 (a) presents a grating produced at IMT/KIT, in the image (b), the magnification shows features of a height of 120  $\mu\text{m}$ , whereas in (c) a 2.4  $\mu\text{m}$  period grating, which leads to an aspect ratio of 100. The amplification was made through scanning electron microscopy (SEM).



(a) Wafer with approximately 10 cm diameter (4 inches) and grating (gold region) with dimensions of 5 x 5 cm<sup>2</sup>



(b) SEM overview picture of a typical grating, showing an approximate height of 120 μm



(c) Amplified SEM grating image, showing a period of approximately 2.4 μm

**Figure 7:** Images of a gold HAR grating. (a) 5 x 5 cm<sup>2</sup> grating. (b) SEM picture showing the lamella height of the grating. (c) SEM picture showing the periodicity of the grating. The grating was produced trough X-ray lithography technology (IMT and Kara – KIT, Karlsruhe - Germany)

The necessity to achieve high aspect ratio (HAR) structures and the smallest possible period in the gratings' design generates several challenges in the fabrication process, affecting the reproducibility and the final quality of the gratings. Figure 8 presents the most common defects that lead to the low quality of the gratings during their production.

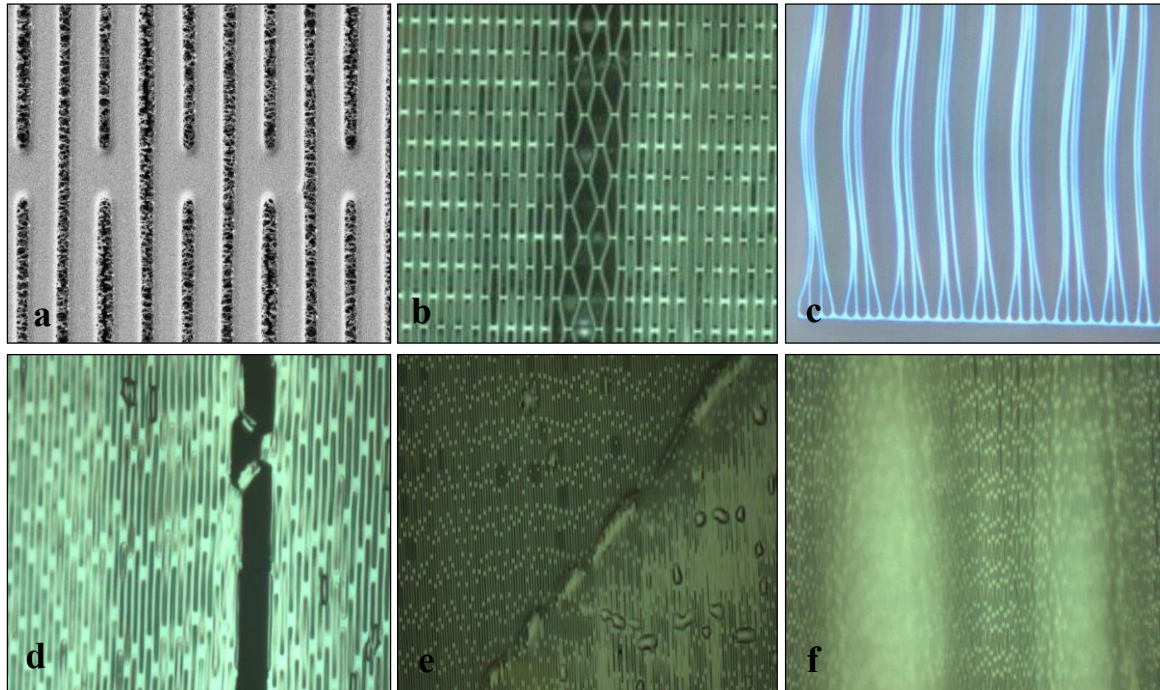
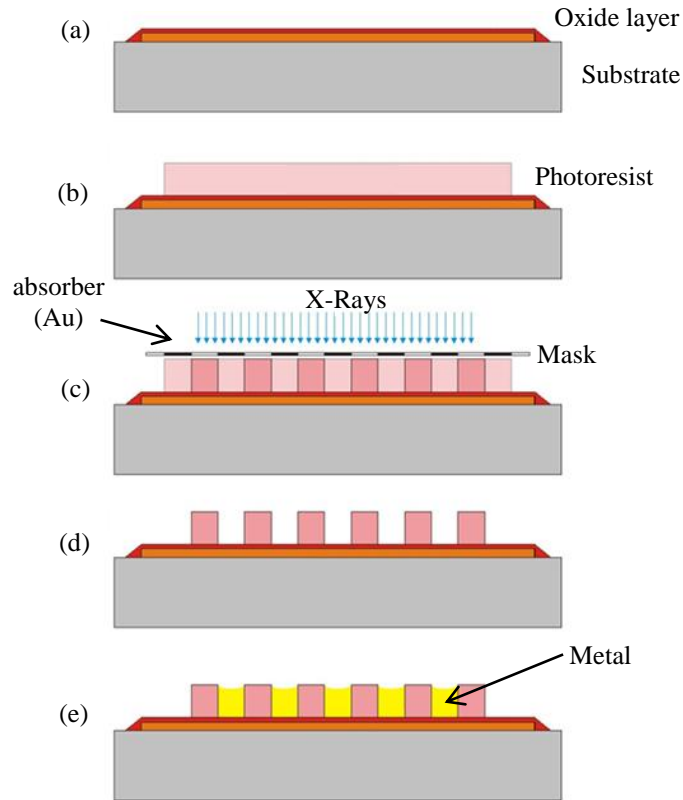


**Figure 8:** Defects during the microfabrication process using lithography technology: (a) unwanted cross-links, (b) lamellae deformation, (c) HAR structure collapse, (d) cracks (e) bubbles, (f) poor adhesion (non-homogeneity in the focusing imaging at microscope). Reproduced from Vlnieska et al (2018) [4] (CC BY)

To understand and identify how to overcome these challenges (Figure 8), it is necessary first to comprehend the production of the gratings. To obtain gratings with small periods and HAR structures is mandatory to use techniques capable of transferring patterns with high precision and accuracy. These features are only possible to be achieved using sources of deep X-ray (synchrotron) combined with microlithography techniques [23].

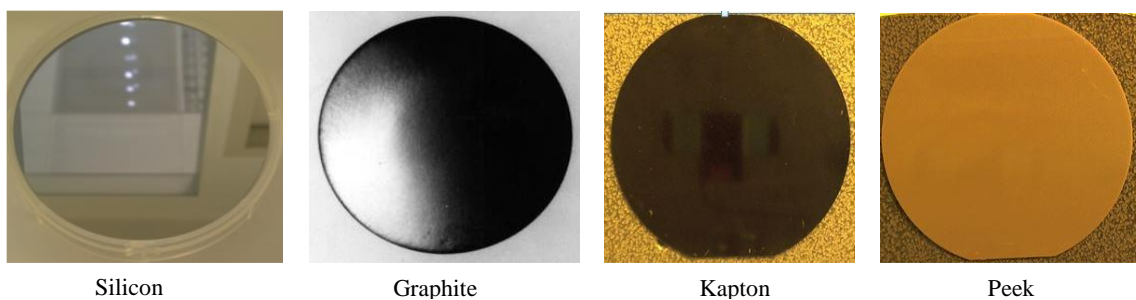
The lithography technique is a patterning transfer thorough radiation. One of the ways to classify lithography techniques is regarding the type of light source, such as ultraviolet (UVL) (400 to 365 nm), deep-ultraviolet (DUVL) (248 or 193 nm), extreme-ultraviolet lithography (EUVL) (approximately 14 nm), X-ray lithography (XRL, and deep-X-ray lithography, DXRL, 0.4 to 4nm), electron beam lithography (e-beam) and ion beam lithography (IBL) (it varies regarding focal length, wavelength, lens diameter), are the most used ones [24].

In most of the cases to transfer a pattern, it is necessary to have a mask, a photosensitive material, and a source of radiation, such as X-ray, UV, electron-beam (e-Beam) [20, 21]. Figure 9 presents the main steps of the lithography technique, followed by electroplating in the last step.



**Figure 9:** Main processing steps used in the lithography process (details see text)

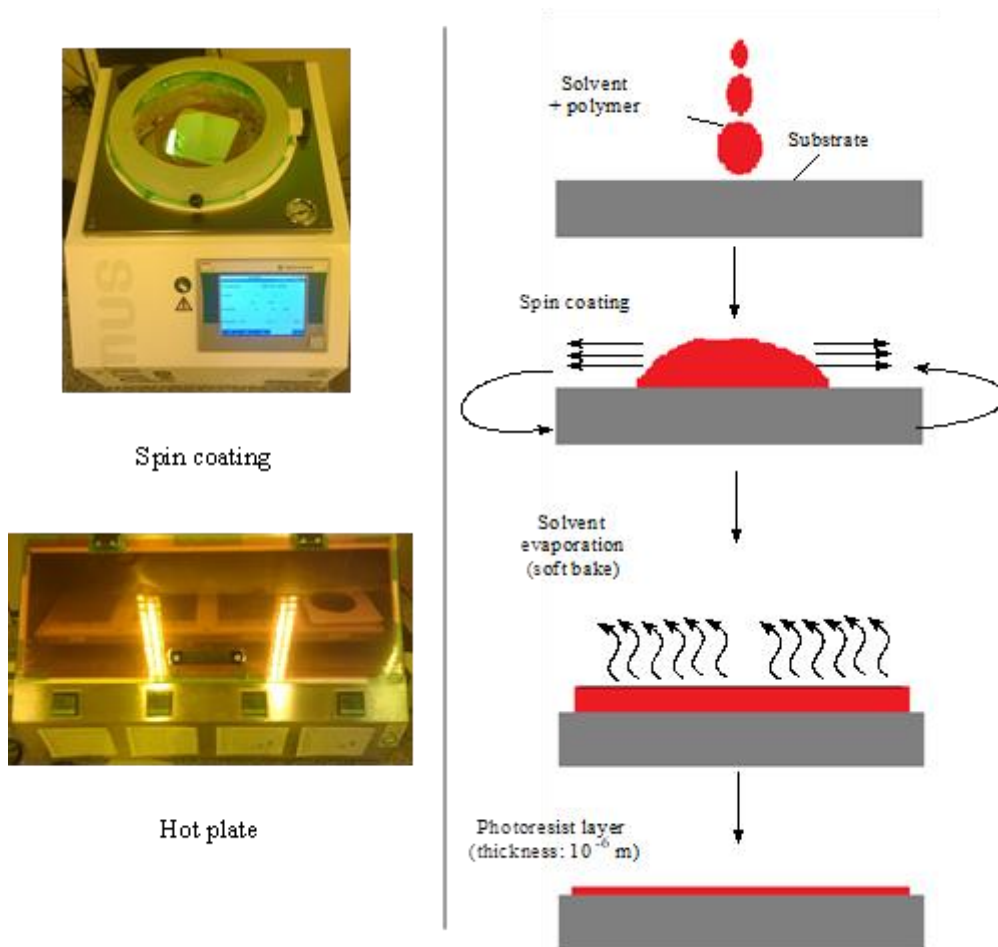
In Figure 9, the five main steps to produce gratings are depicted. In (a), the substrate is chosen according to the final application. Commercially available several types of substrates (or also known as wafers). They consist of a thin plate with a thickness usually varying from 200  $\mu\text{m}$  to 1000  $\mu\text{m}$ , in several diameters. In some substrates, there is also a possibility to have an additional thin layer on the surface, normally an oxidized layer in the range of 2.5  $\mu\text{m}$  thickness. [16, 17]. Figure 10 presents examples of wafers used in lithographic techniques.



**Figure 10:** Example of commercially available substrates

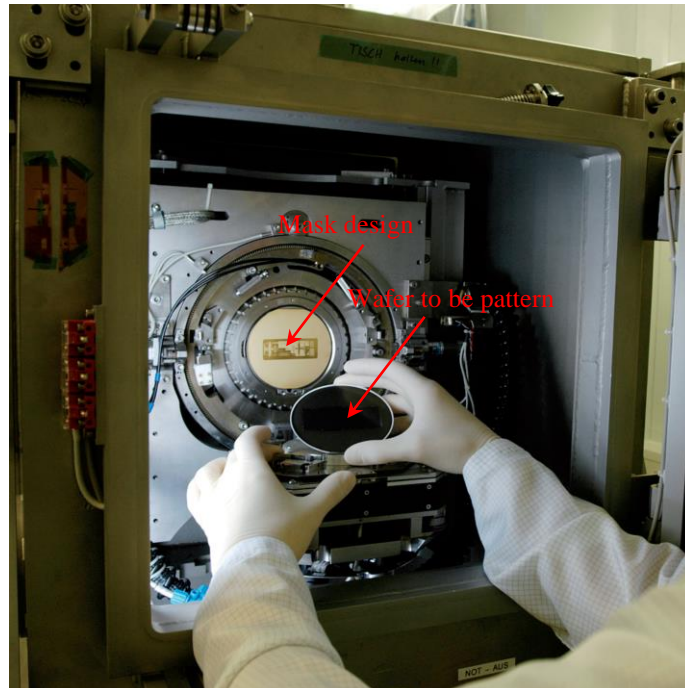
The second step, Figure 9 (b), is the deposition of a photoresist layer on the substrate. It can vary between 5 to 3500  $\mu\text{m}$  given by the application. The spin-coating technique is the most applied method to deposit the photoresist and is generally followed by soft heating to evaporate the solvent (called soft bake). The parameters used in the spin coating and heating ramp depend mainly on the thickness desired in the layer and the viscosity of the photoresist.

Figure 11 exemplifies these steps.



**Figure 11:** Schematic drawing representing the spin coating and soft bake steps

In the next step of the gratings production, in the exposure step (Figure 9 (c)), the photoresist is exposed through a designed pattern (called a *mask*), with light. For high aspect ratio (HAR) structures, X-ray from synchrotrons sources is the best alternative as a light source, achieving deep penetration and avoid diffraction effects during the irradiation [25]. The exposure step has several parameters depending on the wavelength of the light, like the intensity doses of the beam source, time of the exposure, the distance between the mask design and photoresist [26]. Figure 12 shows the exposure step in the case of X-ray irradiation using the synchrotron radiation source at Karlsruhe Research Accelerator (KARA) - KIT (Karlsruhe - Germany).



**Figure 12:** Exposure step at LITHO 2 beamline at KARA - KIT (Karlsruhe - Germany)

In the case of X-ray light source from synchrotrons, typically, the masks have heights varying from 3 to 35  $\mu\text{m}$  approximately and are made by gold. In the next step (Figure 9 (d)), where the material is irradiated, the chemical composition of the photoresist is changed, creating or cleaving chemical bonds [27]. Figure 13 presents a diagram to elucidate the processing of positive and negative tone photoresists.

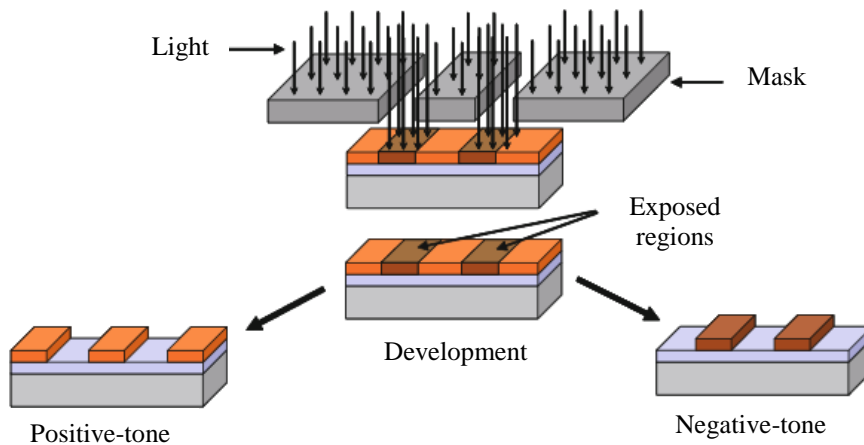


**Figure 13:** Positive and negative-tone photoresists adapted from Henderson (1978) [28] (Springer Nature and Copyright Clearance Center, license number 5060300885010)

In Figure 13, the tone of the photoresist depends on the chemical composition of the photoresist. For photoresists where the bonds are cleaved in the exposed region, they are defined as positive-tone photoresist. In contrast, photoresists where the bonds are created in the irradiated area (crosslinking reaction), they are defined as negative-tone photoresists

When the lithography process involves X-ray irradiation, the most applied photo-resin is the negative type due to the better characteristics of patterning HAR structures [10, 29-31]. In the case of the negative photoresists, in the development step, the non-irradiated region is removed using an appropriate solvent, leading to a negative design if compared with the mask. These properties are detailed discussed in chapter 1.3.

The last step in the lithography process (Figure 9 (e)) is the electroplating of the metal into the designed pattern. For X-ray grating-based interferometry, the most common metals applied are gold and nickel. In electrodepositing, there are crucial parameters to be controlled and measured, such as the temperature of the bath, concentration of the electrolyte solution, the current applied, the voltage applied, time and, stirring speed. [32, 33]. At IMT-KIT (Karlsruhe – Germany), the gold salt used for the electroplating is  $\text{NaAuSO}_3$  (Sodium gold sulfite). Figure 14 presents the experimental procedure to perform the electroplating.

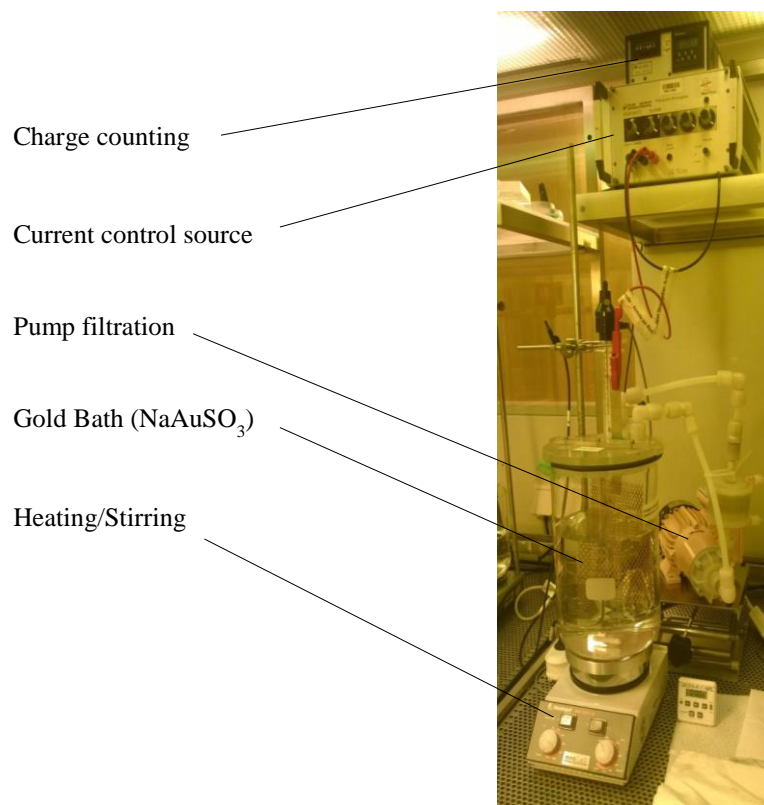


**Figure 14:** Electrodepositing bath located in the cleanroom facilities at IMT- KIT (Karlsruhe-Germany)

The electrochemical reactions are presented in Figure 15 when sodium gold sulfite salt ( $\text{NaAuSO}_3$ ) is used as the electrolyte.

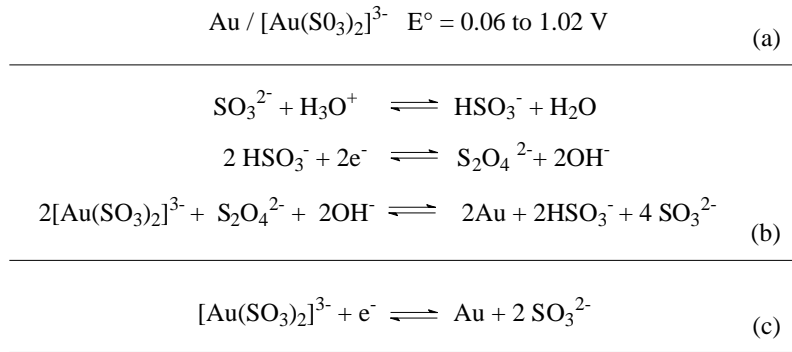


**Figure 15:** electrochemical reactions for Gold sulfite salt. (a) Standard reduction potential. (b) Chemical reduction of Gold in neutral pH. (c) Chemical reduction with a pH above 8.0. Adapted from Hydes et al.(1979) [34] (Copyright under open access license)

To electroplate HAR structures, for the point of view of the photoresists, its chemical composition has to be stable enough to resist to pH variations, temperatures ranging from 25 to 65 °C, electroplating times up to hundreds of hours of processing and it has to be neutral (insulator) regarding the current flow at the electroplating bath [32, 33].

Figure 16 presents a general overview of the variables related to each step in the microlithography.

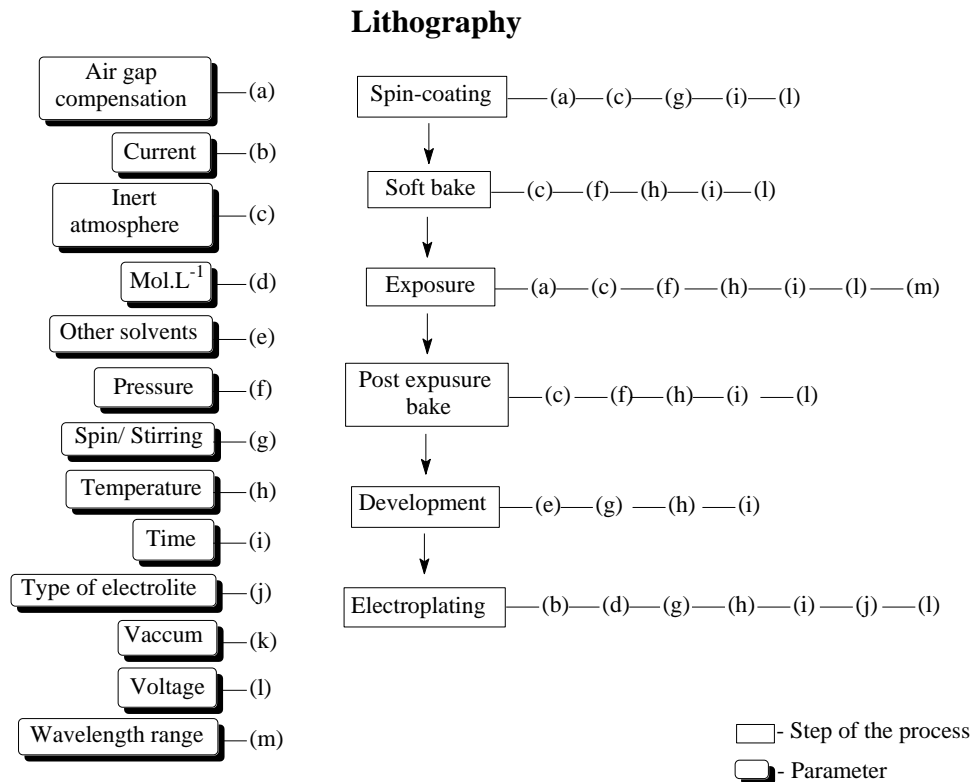


**Figure 16:** Parameters to control correlated with the lithographic steps

As a summary, during the fabrication process of the gratings, several parameters must be controlled. Most of the parameters have direct influence and cause changes in the mechanical and physical-chemical properties of the photoresists, leading to a preliminary conclusion: to enhance the quality of the gratings, it is necessary to improve the process parameters simultaneously with the properties of the photoresists [8, 11, 13, 25, 35-43].

Photoresists play a decisive role in the whole lithography process, from the spin coating until the electroplating. Processing parameters, chemical composition, and physical-chemical properties of this material are directly related to the reproducibility and the quality of gratings production. Consequently, it is crucial to discuss with more details the chemical composition and successful formulations along with the history of the photoresists.

Photoresists are the main raw material used in several lithography techniques. They have a broad range of applications in the semiconductor and electronics industry, such as MEMS, optical sensors, micro pieces of watches, radiation sensors, optical fiber components, conductive microstructures, photonic crystals [29, 44, 45].

When the fabrication of HAR structures is necessary, depending on the structural requirements and other boundary conditions, either a negative or a positive tone photoresist is used. PMMA (polymethylmethacrylate) is one of the examples for positive-tone photoresists. It delivers high structural quality but suffers from low sensitivity, resulting in long exposure times, especially for HAR structures [36, 39]. Chemically amplified negative-tone photoresists are much more sensitive and present better performance for HAR fabrication [6-14].

For negative-tone photoresists, an example widely used is the photoresist based on epoxy resin, commercially known as SU8 or EPON. Its mechanical properties and processing parameters are very well described in the literature [29, 46-48]; however, there are few sources of information regarding the chemical properties of this photoresist.

Less attention has been given to the chemical structure and the effects caused by the photoinitiator, additives, and solvent in the photo resin mixtures. In order to understand the chemistry of photoresists, definitions such as positive-tone, negative-tone, chemically amplified photoresist, and other aspects, an outline of the photoresists is presented.

### 1.3 The photoresists

Resist materials initially were developed to be used in the printing industry and, although the photoresists, as we know nowadays, were developed nearly 40 years ago, the history of photoresist is strongly connected with the beginnings of photography, discovered almost two centuries ago [4, 49].

In 1826, Joseph Nicéphore Niépce developed a lithographic method that resulted in the first photograph, which he named *heliograph*. In his experiment, he coated a polished pewter plate with a tar known as bitumen of Judea. Interestingly, Niépce discovered that bitumen of Judea was soluble in lavender oil, leading to high-quality coatings in the pewter plate. After the coating, he exposed the plate to a view of his courtyard, which was focused on the plate using a simple camera (known as *Obscura*). After the exposure, the plate was developed with a mixture of lavender oil and white petroleum. The remaining coating was a relief structure in the organic coating, generating the image.

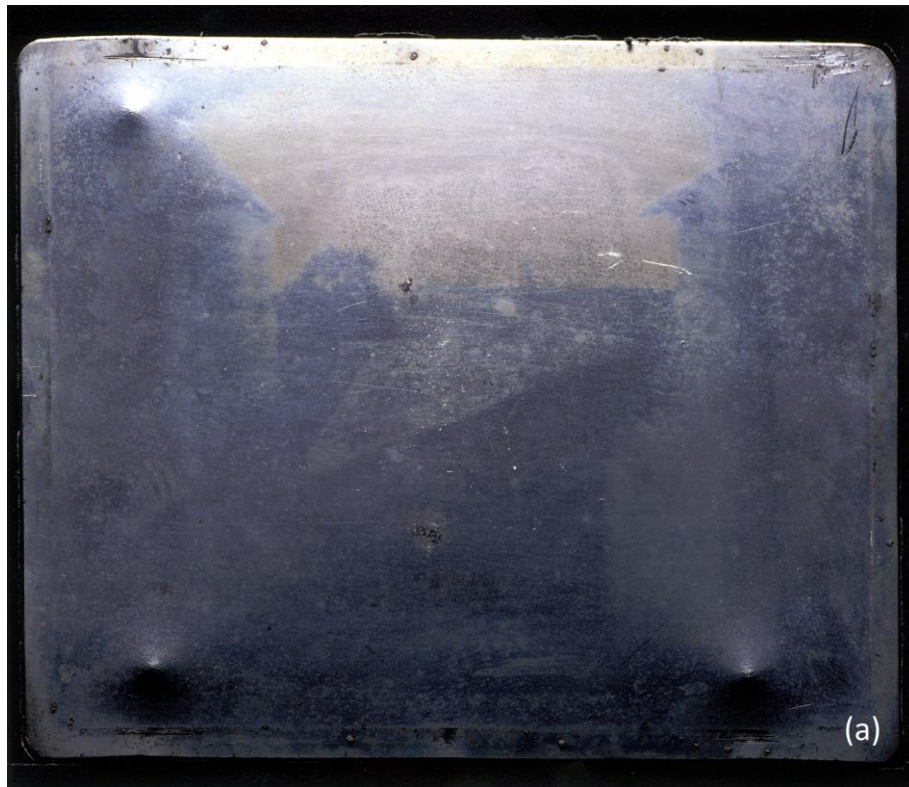


**Figure 17:** The famous “*Point de vue du Gras*”, first Niépce’s permanent photograph: a) pewter plate after development, b) reproduction of the pewter plate. Both images are under public domain, via Wikimedia Commons [51, 52]

Although Niépce’s photography proved to be a successful experiment, the picture is considered one of the grey-scale, an effect due to the lack of bitumen of Judea sensitivity [50].

Niépce worked not only with projection printing but as well as with photo engraving or photogravure, an ancient process from the production of the semiconductors as it is known nowadays. Niépce is considered both the inventor of photography and photolithography. Figure 18 presents one of the firsts Niépce’s photoengraving, made from a drawing of the *Cardinal d’Amboise* [50].

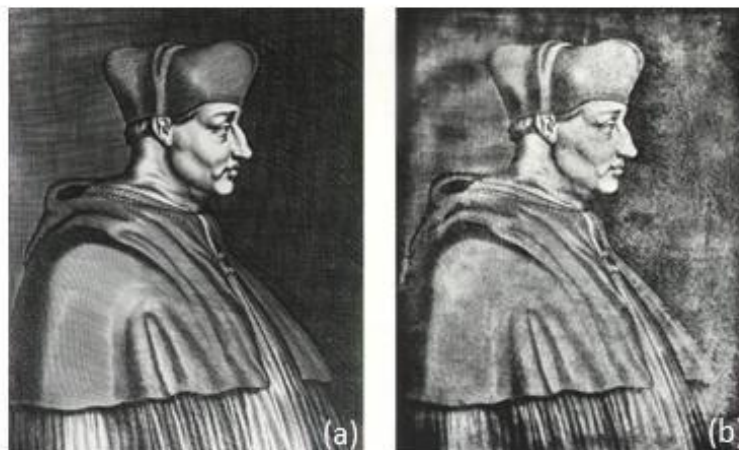


**Figure 18:** Comparison between the original engraving and the heliography of Joseph Nicéphore Niépce: a) engraving of "Portrait of Georges d'Amboise" (1650), b) heliography of the engraving (1826). Both images are under public domain, via Wikimedia Commons [53]

The lack of sensitivity pushed the development of new materials to fulfill more efficiently the photolithography. In 1840 Becquerel mixed starch and dichromate, where he was the first one to use the term "resist" to describe the formulation. William Henry Fox Talbot also prepared a formulation using ammonium dichromate in gelatin (DCG), which improved the sensitivity to the light, made it possible to do the development with water and, reduced the time of exposure in orders of magnitude compared with other formulations. The dichromate gelatin resist is historically one of the most important ones. It has enlarged the photolithography industry, being used for the whole next century in recording and transferring images to printing plates made of metal and stone [27, 50].

Although dichromate gelatin was a successful formulation, it has a disadvantage, known as a *dark reaction*. It can be explained by a slow crosslinking reaction between gelatin and dichromate salt, even in the dark. Figure 19 illustrates the structure of gelatin, ammonium dichromate, and the *dark-reaction* [27, 50, 54].

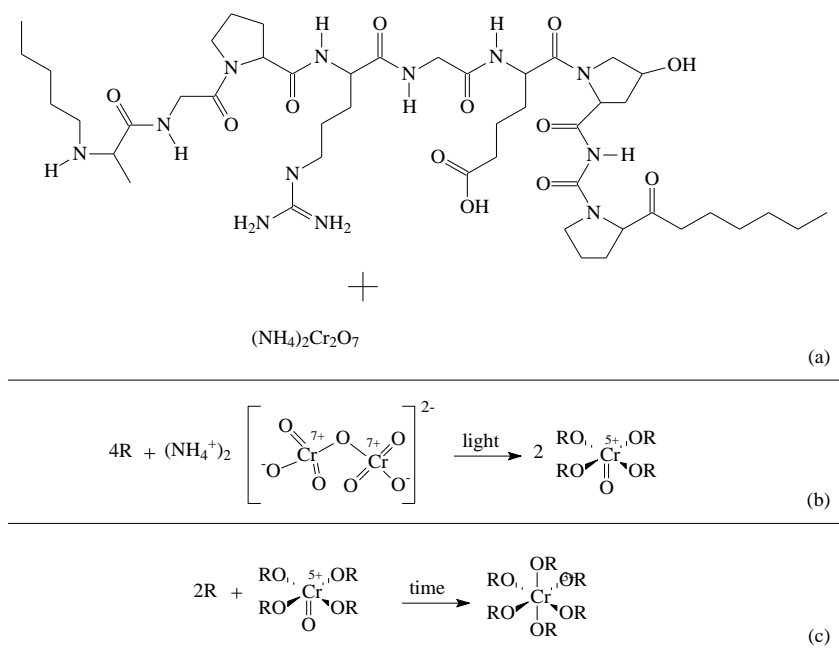


**Figure 19:** Dichromate gelatin formulation. (a) Gelatin and ammonium dichromate. (b) reduction of chromium 7+ to chromium 5+ . (c) reduction of chromium 5+ to chromium 3+, schematics adapted from Wang et al. (2017) (CC BY) and Blyth et al. (2006) (CC BY) [55, 56]

The absorption spectrum of dried and unexposed DCG film is approximately in the range of 330 to 400 nm. Exposing DCG causes the reduction of chromium atoms, from  $\text{Cr}^{7+}$  to  $\text{Cr}^{3+}$ . The reduction to  $\text{Cr}^{3+}$  creates the cross-linking reaction between the gelatin molecules and causes the insolubilization in the water of this matrix. The exact mechanism of the chromium reduction with gelatin is not completely described. Literature suggests that during DCG exposure, gelatin- $\text{Cr}^{5+}$  is instantly formed, which is represented in Figure 19 (b), being able to stay many hours in this oxidation state. After a long period,  $\text{Cr}^{5+}$  atoms are reduced to  $\text{Cr}^{3+}$  (Figure 19 (c)). In Figure 19 (b) and (c) "R" represents the amino and acid groups from gelatin structure. One can observe that the reactions are not in stoichiometric equilibrium. It is assumed, for this case, that added oxygen atoms to the chromium ions are from gelatin structure [56, 57].

When the first attempts to produce integrated circuits emerged, around 1925, the imaging material used was dichromate gelatin. The initial studies were made by William Shockley and his co-workers at Bell Laboratories. The dichromate gelatin presented limitations regarding its performance, mainly during the etching step, where it was necessary to use strong acids to do the etching process [50, 55]. The available resists at that time were designed for the printing process, where its application was to produce printing master plates. The resist imaging and etching steps, in this case, do not need to be rapidly processed. Thus the photosensitivity of the material was not a significant feature [49, 54].

An effort to improve the formulation generated collaboration between Bell and Kodak research Laboratories. The director of Kodak Research Laboratories delivered the challenge to Louis Minsk.

Minsk knew that gelatin was a protein and a polymeric material; thus, his main idea was to substitute this material. In the literature, he found the only solid-state photodimerization reaction knew at that time, the cinnamic acid dimerization. He proposed a solution using this reaction combined with poly(vinylalcohol), which generated poly(vinylcinnamate), hoping that the cinnamate groups would be reactive enough for cross-linking when exposed to light. Figure 20 presents the reaction and the mechanism [50, 54].



Poly(vinylcinnamate), the resist from Louis Minsk, was instantly a success. It resulted in images with sharp edges, excellent resistance to strong etchants like hydrofluoric acid and, an essential property, no dark reaction, resulting in a long shelf lifetime, giving the possibility to sell pre-coated plates. With the success of Minsk resist, Bell laboratories started to produce semiconductor devices on a small scale, but unfortunately, the adhesion of the resist to the surface of the substrate was not satisfactory [49, 50, 54].

The Kodak Research laboratory in Harrow, England, was contacted, and they suggested a new type of resist, a light-sensitive material based on rubber adhesive. The development of this idea started when Martin Hopher (head of the Graphic Arts) discussed the problem with his lunch partner, the organic chemist Hans Wagner. He suggested using the photochemistry of azido-compounds. Azido compounds generate intermediates under the photolysis reaction that improve the adhesion in a variety of substrates. This information came from the research from Professor Leopold Horner from Mainz University, Germany [50].

Wagner's idea was to synthesize bis-azides and mix them with rubber of low molecular weight. This new formulation provided high-quality images and strong adhesion to glass and silicon wafers. Figure 21 presents the bis-azide proposed by Hans Wagner [27, 50, 54].

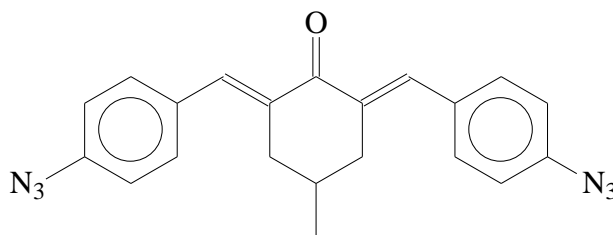


**Figure 21:** 2,6-bis(4-azidobenzal)-4-methylcyclohexanone, bis-azide proposed by Hans Wagner

Kodak named the formulation as “Kodak Thin Film Resist”, KTFR. The KTFR resist became the primary raw material used for the semiconductor industry, from 1957 until 1972 [27, 50, 54].

In the year of 1972, the dimensions (regarding period, see Figure 6) of semiconductor devices were in the range of 2.0 micrometers, reaching the limit of the resolution of the KTFR resist.

In a search for a resist with lower resolution limit, it was found that the Kalle company in Wiesbaden (Germany) had a material since 1950, used to produce positive printing plates, known as the *blueprint*. Its chemistry is based in diazonaphthoquinones (DNQ's). Later on, based in this chemistry, a new formulation was the first DNQ's resist, which was a mix of DNQ and novolac resin. Figure 22 presents the blueprint resist and its photo-reaction with light and post-processing reactions [49, 50, 54, 58].

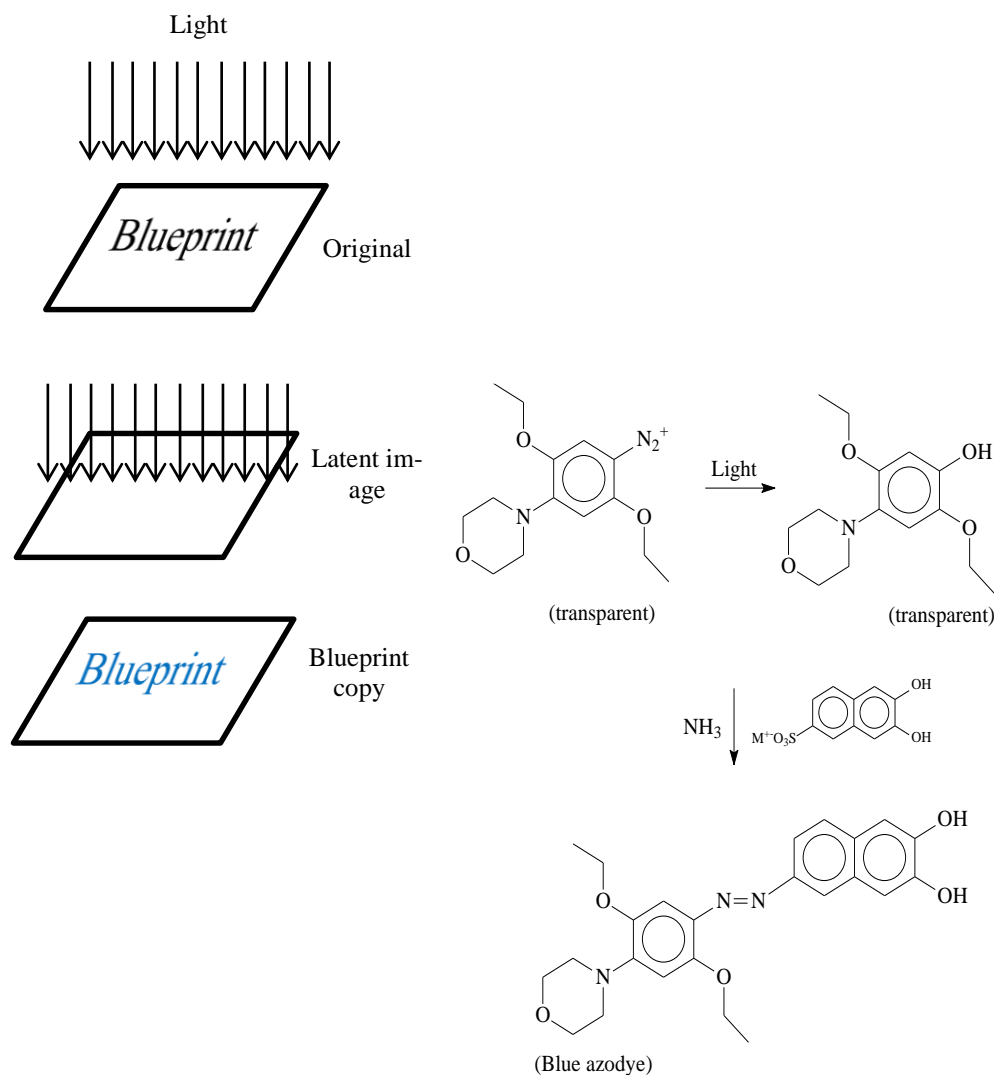


**Figure 22:** Chemical reactions of the Blueprint resist from Kalle Company

In Figure 22, during exposure to light, DNQ is hydrolyzed; in this step both reagent and products are transparent. Afterwards ammonia and dinol salt coupler (2,3-dihydroxy-6-naphthalenesulfonic salt) are added, which reacts only with the non-exposed DNQ, resulting in a blue azodye.

Most of the DNQ's photoresist technology is assigned to Oskar Süß, head of the chemistry laboratories at Kalle. Blueprint plates were sold in pre-coated plates and were introduced in the fifties decade under the name Ozatec ®. In the United States of America (USA), the printing plates were supplied by Azoplate, an affiliate of Hoechst AG (among which Kalle company was a subsidiary as well). In the USA, the used tradename was "AZ photoresists". In 1972, photoresists based in DNQ photoreactions dominated the market of the semiconductor industry, including high-end applications [49, 50, 54, 58].

DNQ's photoresist present high resolution, and the main advantages were a higher resist contrast and no swelling during the development step. Although a fragility and inferior resistance to wear when compared to the negative-tone photoresists, DQN resists were the choice for the production of 16KB to 16MB device generations, reaching 90 % of the photoresist world market for approximately 25 years. During this trajectory, several improvements and technological advances were achieved, allowing reaching structures with resolution in the range of 0.25  $\mu\text{m}$  [49, 50, 54, 58].

At the beginning of the eighties decade, most of the UV lithography machines have used pressure mercury lamps as an irradiation source. These equipment were capable of working in two regimes of irradiation in the near-UV (350 - 400 nm of wavelength) and deep-UV (240-260 nm of wavelength). For deep-UV, the irradiation intensity was only in the range of 10% compared with near-UV. The low intensity of deep-UV forced a redesign of the AZ photoresists. One of the strategies was to change the formulation of the photoresists to compensate the low sensitivity in DUVL, making them more photoreactive, which resulted in formulations of a new age of research, afterwards named chemically amplified photoresists [59].

Chemical amplification means that the first reaction in the photoresist system is a chemical reaction generating a catalyst. The catalyst acts in the matrix, accelerating cascade reactions or a chain reaction.

In a perfect case scenario, using the conventional formulations, when one photon during the exposure is absorbed, there will be a conversion of the sensitizer molecule to a photoproduct, leading to a quantum yield of 1.0 (one photon generates one photoproduct). Chemically amplified photoresists are able to achieve quantum yields higher than 1.0, which means one photon can produce one or several photoproducts [49].

The firsts formulations for such a system were earlier described by Goerge H. Smith and James A. Bonham, from 3M Company in 1973, but never exploited by the company. Figure 23 presents one of the several examples in the reaction system proposed by Smith and Bohnam [58] .

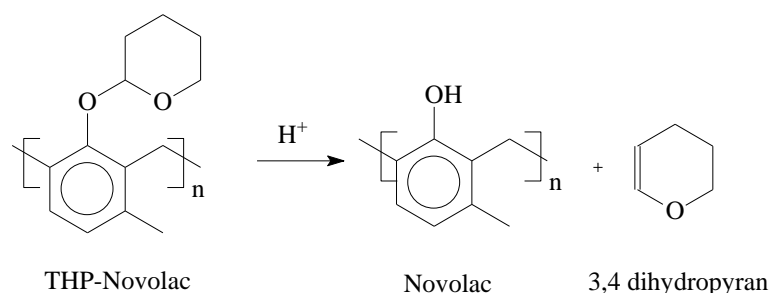


**Figure 23:** THP-Novolac system. Positive-tone photoresist developed by Smith and Bonham

In Figure 23, THP is tetrahydropyran, the molecule attached in the phenolic position of the Novolac resin. The initial polymeric matrix is insoluble in water, whereas Novolac resin is soluble. During the exposure step, a Lewis acid is generated (photoacid), catalyzing the cleavage between THP and Novolac. The result is a photoresist significantly more sensitive to the light. It is important to note that the Lewis acid acts only as an enhancer for the sensitivity property. It does not create a cascade or scission chain reaction in this formulation attempt.

In 1978, at IBM San Jose Research Center in San Jose, California - USA – Grant William in cooperation with Prof. Jean Fréchet from University of Ottawa - Canada - and Hiroshi Ito, (at the time Postdoc fellow at IBM) started to test other polymers for amplified photoresists. Ito proposed a basic matrix from the ionic polymerization of phthalaldehyde, which results in poly(phthalaldehyde). Using photoacids previously studied by James Crivello of General Electric, they achieved the first chemically amplified positive-tone photoresist. One can see that the idea suggested by them is basically the same one proposed by Smith and Bonham in their patent [59].

The firsts formulations achieved values of photosensitivity two orders of magnitude higher than the DNQ photoresist system, allowing the usage of deep-UV radiation with good yields. However, the formulation could not be

considered as a *resist* system. During the development step, the photoresist presented no resistance and was washed away. Figure 24 presents the amplified resist formulated based on Ito's idea [50, 60].

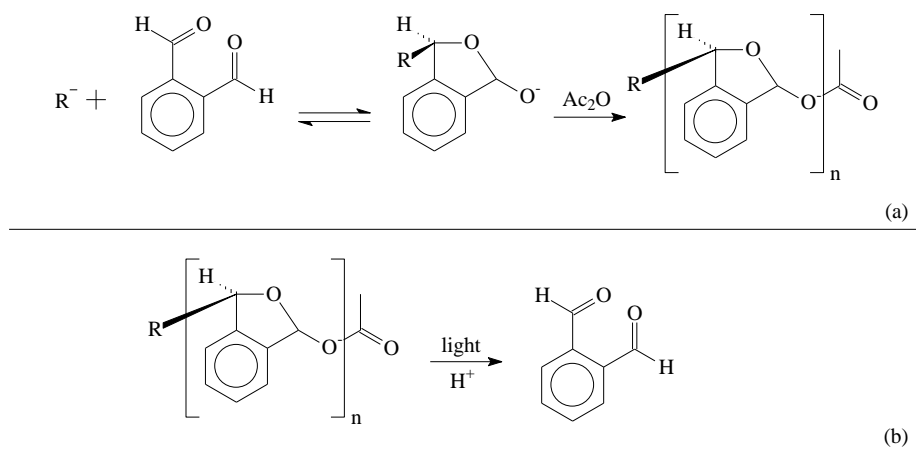


**Figure 24:** First amplified photoresist produced at IBM. (a) Anionic polymerization of phthalaldehyde. (b) cleavage of poly(phthalaldehyde), catalyzed by iodonium salts, a photoacid generator

In Figure 24 (a) poly(phthalaldehyde) is synthesized through ionic polymerization. In Figure 24 (b), the photoinitiator reacts with light, releasing a proton the reaction medium, which opens the poly(phthalaldehyde) polymeric chain. It is interesting to note that in this reaction, only one proton is responsible for creating a cascade scission chain reaction.

With iodonium salts as a photoinitiator, Wilson and Fréchet proposed a substitute for the polymer matrix of poly(phthalaldehyde), the poly(*t*-bocstyrene), as Figure 25 pictures [61-63].

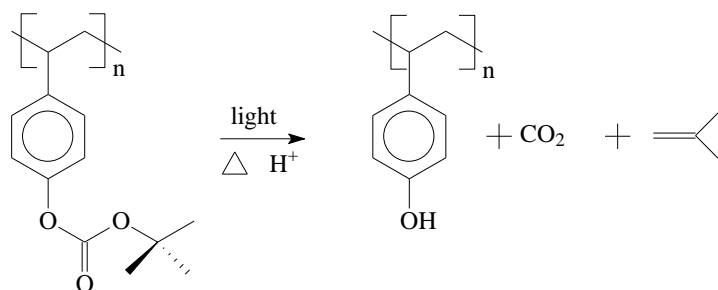


**Figure 25:** Poly(*t*-bocstyrene) and its deprotection reaction. Poly(vinylphenol) is the main product

The poly(*t*-bocstyrene) presented the great advantage to be developed either in positive or negative tones, where the changing of the developer decides the image tone and has the same high sensitivity observed with poly(phthalaldehyde). Named as PBOCST resist, it was produced on a large scale by Kodak and used by IBM for the production of DRAM memories. PBOCST photoresist allowed the first fully commercial application of deep-UV lithography, producing 100 substrates per hour (12,7 cm diameter), reaching 0.9 microns resolution [61].

Chemically amplified photoresists caused a considerable technological advance in the lithography process. At the end of 1980, most of the production in the semiconductor industry was working with features in the range of submicrometer. Although its advances, chemically amplified photoresists have one disadvantage, or in a better expression, it still has a challenge to be solved, known as *fluctuating sensitivity*. This issue became clearer when

these photoresists started to be fully used in a high volume manufacturing (HVM) scale process. There was a substantial variation in the exposure parameters during the irradiation step, which means for the same photoresist, the exposure values were not constant.

One of the first approaches to measure and identify different sensitivity values for photoresists was proposed by Taylor et al. (1984). Interestingly, the experiment was aimed to identify the sensitivity of different photoresist formulations processed through electron beam lithography (e-beam lithography) [64]. Later on, Turner et al. (1989) proposed a general definition for lithographic techniques based on the work of Taylor et al. (1984). It defines the characterization of the photoresists measuring how fast and how sensitive are the photoresists to the doses irradiation, which he named as *contrast*, represented it by equation 5 a and 5 b [27]:

$$\gamma = \log \left( \frac{D_p^0}{D_p^i} \right) \quad (5 a)$$

*Positive photoresist*

$$\gamma = \log \left( \frac{D_n^{1.0}}{D_n^i} \right) \quad (5 b)$$

*Negative photoresist*

Equations 5 a and b correlates the sensitivity of the photoresists measuring the amount of irradiation delivered to the photoresist with the remaining developed thickness (after it is developed with a certain solvent). In equation 5 a,  $D_p^i$  is the exposure that results in the initial loss thickness of the photoresist in a particular developer.  $D_p^0$  is the exposure that leads to the complete dissolution of the photoresist thickness. For negative-tone photoresists,  $D_n^i$  is the exposure that leads to the initial gelation (crosslinking),  $D_n^{1.0}$  is the exposure that results in a completely cross-linking reaction of the region, and no thickness of the photoresists is lost in the development step [27]. Figure 26 exemplifies the typical graphs for positive and negative photoresists.

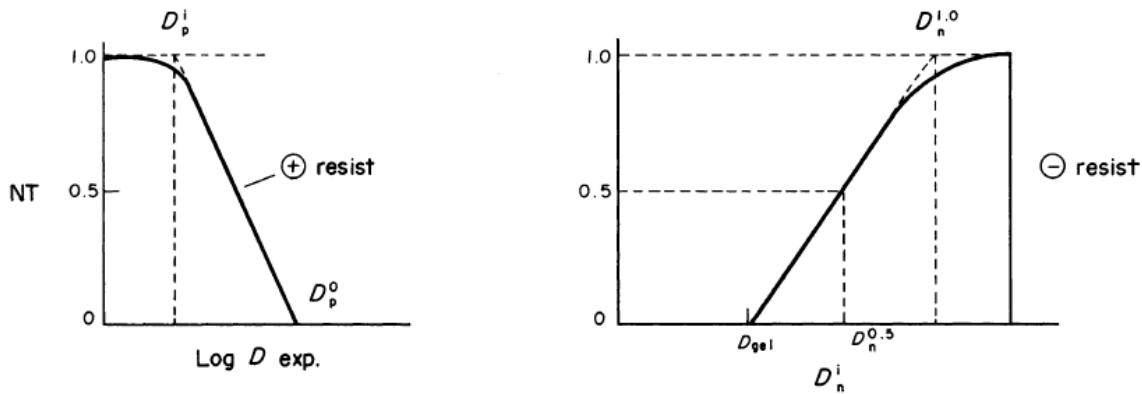


**Figure 26:** Typical contrast curves for positive and negative photoresists. Reproduced from Turner et al (1989) [27] (Elsevier and Copyright Clearance Center, license number 5060361388160)

For X-ray lithography, Kunka et al. (2014) presented a method to measure the contrast for negative-tone photoresists, which is a slightly modified version from Turner et al. (1989). Equation 6 presents the approach proposed:

$$\gamma = \left( \log_{10} \left( \frac{D_2}{D_1} \right) \right)^{-1} \quad (6)$$

In equation 6,  $D_1$  is the dose exposure that results in 10% remaining of the original thickness (100% of crosslinking reaction),  $D_2$  is the dose exposure to obtain 90% of the original thickness (100% of crosslinking reaction). As an example, Figure 27 presents the ideal behavior for positive and negative photoresists, following equation 6.

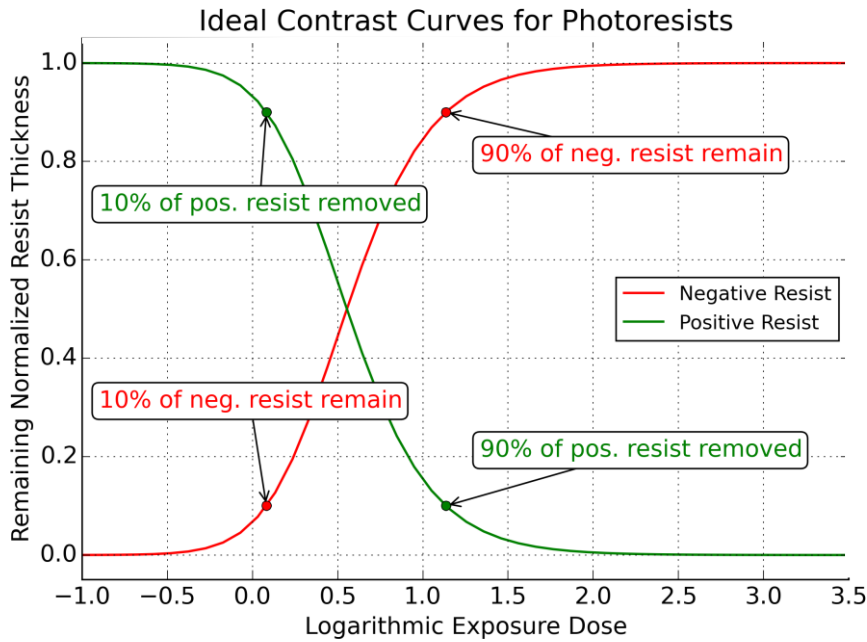


**Figure 27:** Ideal Contrast curves for positive and negative photoresists. The contrast curve is a logarithmic sensitivity plot showing the normalized resist thickness vs. exposure dose

A real example is presented in Figure 28, with the sensitivity evaluation for the same negative-tone photoresist, with different fabrication lots.

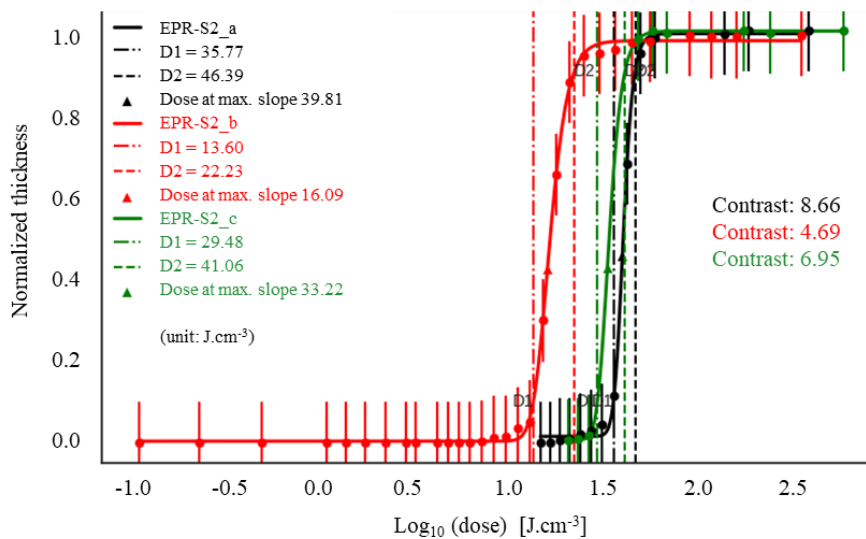


**Figure 28:** Contrast curves from the same photoresist (same brand and different fabrication lots)

For applications such as HAR structures, produced by X-ray lithography, the contrast ideally should be higher than five (this threshold is determined empirically for each type of photoresist and lithographic technique). For example, in Figure 27, the photoresist EPR-S2\_b is not sensitive enough to be used in X-ray lithography. It is interesting to

note, that although the photoresists are the same, the photoresist EPR-S2\_c presents circa 48 % less contrast than EPR-S2\_a.

For high-end applications such as the production of optical components for interferometry techniques, the constraints and features regarding design are very challenging. In the history of the photoresists, a large number of formulations and approaches were proposed; however, just a few of them are able to fulfill the requirements for the production of the interferometric optical components.

A photoresist based on bisphenol-A, known commercially as SU-8, was developed and patented by IBM in 1989. Afterwards it was continued to be produced by Shell Chemical under the trade name of EPON SU-8 epoxy resin [65, 66]. The SU-8 photoresist has been used for more than 30 years in the field of microlithography. Since the early seventies, negative tone photoresists (photo-resins) have been the best suitable photo-resins to achieve HAR structures by lithography techniques such as Deep X-ray lithography (DXRL) and deep UV lithography (DUVL) [67-73]. The SU-8 photoresist is applied in most of the processes that involve high precision in the pattern, high exposure intensity, and HAR structures. It presents better characteristics when compared to other photoresists [29].

SU-8 is a mixture of several compounds. In a simplified formulation, it consists mainly of a polymer and a photoacid generator, both solubilized in a solvent. Depending on the final application more additives can be mixed to enhance specific properties such as resinous modifiers (influencing properties like flexibility, toughness, peel strength, adhesion, etc.), fillers, colorants and dyes, and other additives (e.g., rheological additives) [74, 75]. The molecular structure of the primary compounds for this photoresist is shown in Figure 29.

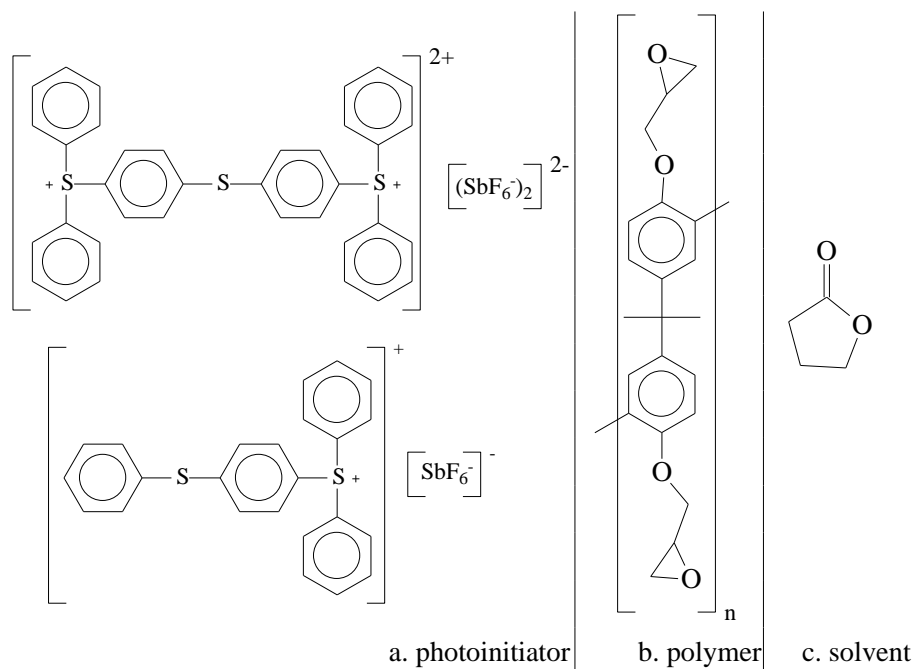


**Figure 29:** Main chemical compounds in the SU-8 photoresist. a. Triarylsulfonium hexafluoroantimonate salts; b. Aryl-epoxy polymer; c. Butyrolactone

In this formulation system, which is considered a chemically amplified system, the crosslinking reaction starts with the photoinitiator, which reacts with light (in this case, X-ray or UV light), releasing a proton to the reaction

medium. Consecutively, the proton reacts with the epoxy group, generating a cascade reaction between the polymeric chains. Figure 30 shows the mechanism.

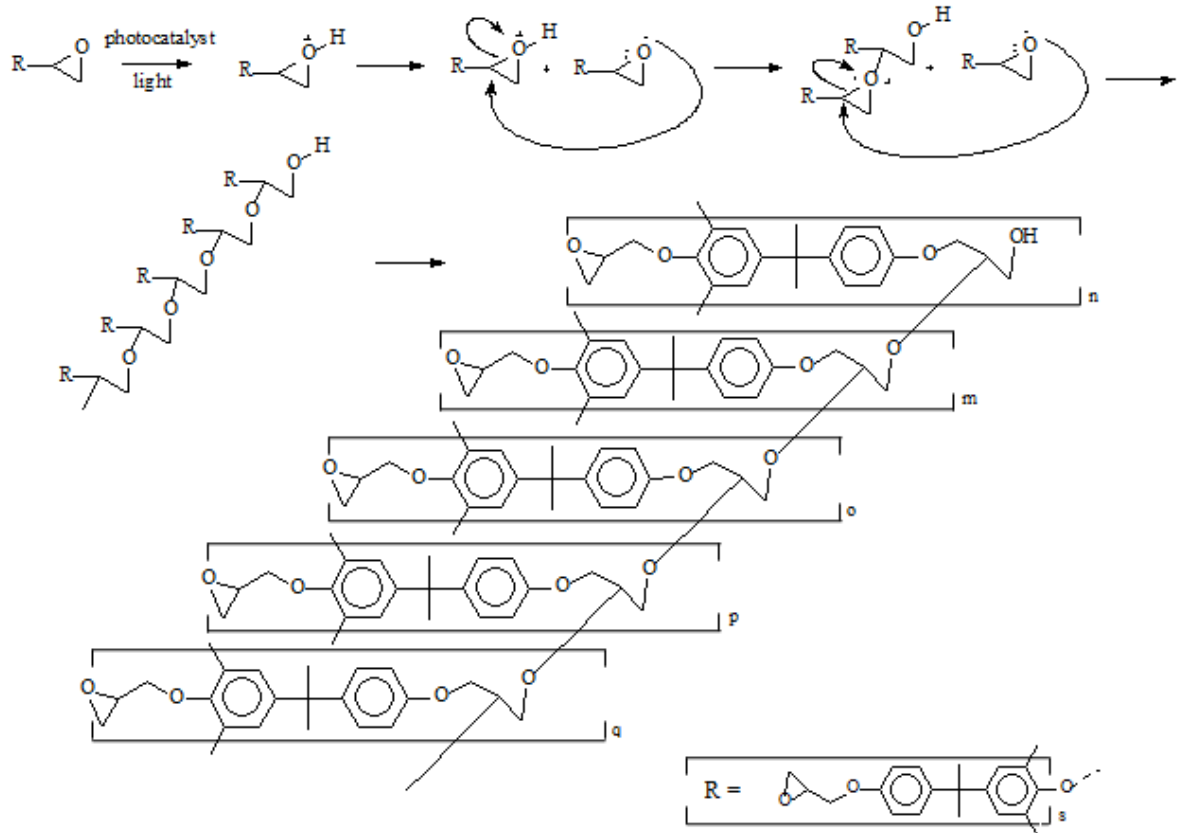


**Figure 30:** Crosslinking reaction for SU-8 photoresist. Reproduced from Vlnieska et al (2020) [76] (CC BY)

The sensitivity is evidently correlated with the chemical composition of the photoresists. For chemically amplified photoresists, this correlation seems to be more strongly connected, primarily due to the photoinitiator reaction path (amplification phenomenon). For SU-8, the reaction path is dependent on the epoxy content, together with the amount of triarylsulfonium hexafluoroantimonate salts (photoinitiator) [75]. Once the photoinitiator is activated with a light beam (X-ray in this case), the proton released in the medium initiates a cascade reaction in the epoxy groups. Assuming that the epoxy groups are close enough to one each other, the cascade reaction progress through the polymer chains (“n”, “m”, “o”, “p”, “q”), connecting the oligomer chains, which leads to a rigid and permanent solid-state structure. Nevertheless, this reaction path is not presented in the literature. In the case of epoxy-based photoresists such as SU-8, it seems to be crucial to study the epoxidation content, the amount of photoinitiator, the polydispersity of the polymeric chains and the amount of solvent in the formulations. These chemical properties shall be correlated with the lithographic performance of the photoresists.

In this direction, it is necessary to integrate three fields of research, the photoresists production (polymer science), the X-ray lithography technology and the X-ray grating-based imaging techniques. In this case, the dimensions characteristics of the gratings would have a parameter to be associated to the photoresists formulation. An alternative is to use the evaluation of the contrast, firstly proposed by Taylor et al. (1984) and afterwards adapted for

X-ray lithography by Kunka et al. (2014) [15]; however, until now, no correspondence with contrast of the photoresists is well combined with their formulations. A methodology named deep and macro levels of properties can be used to perform the synthesis, characterization and control of the photoresists. Using SU-8 formulation as an example scenario, Figure 31 presents this methodology.

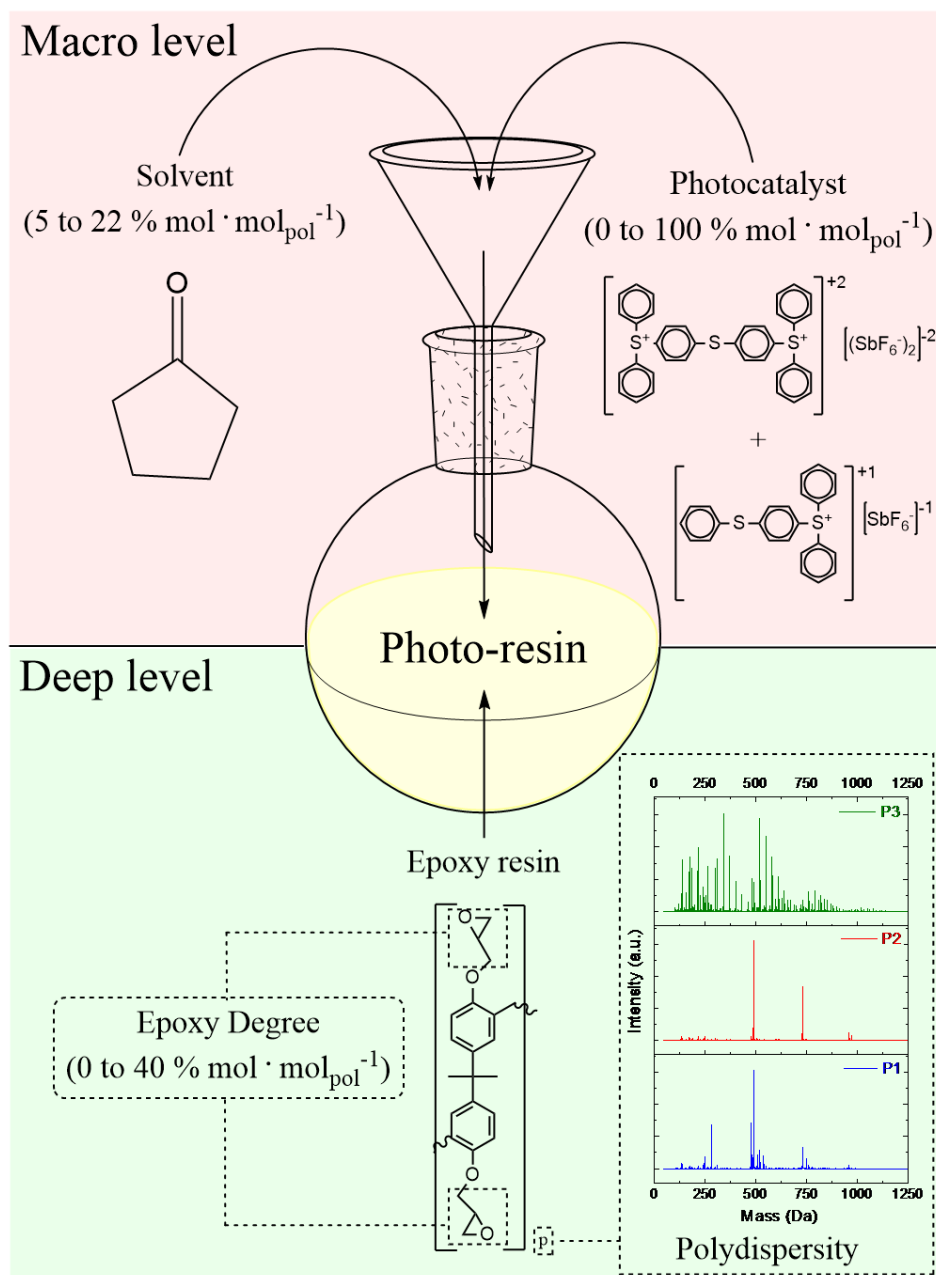


**Figure 31:** Deep and macro levels of formulation for epoxy based photo-resins. Reproduced from Vlnieska et al (2020) [76] (CC BY)

For instance, it will be interesting to divide this process into two main parts, as mentioned by “Deep” and “Macro” levels. The deep-level is crucial to standardize the synthesis of the polymer as close as possible to the desired properties. For epoxy negative photoresists based on bisphenol-A, it is essential to elucidate at least two reactions: the standardization of the polymerization step, as well as a standardization of the alkylation in the phenolic positions of bisphenol-A (epoxidation step). These are the main challenges to define the final properties of the resin

that will compose the photoresist. The deep-level is commonly performed on a laboratory scale. For example, in Figure 32 (down, right side) in the deep-level, there are three polymers that can be used in the formulations with different polydispersities. P1, P2 and P3 are the same polymer, however the mass spectra show distinct molecular weight distributions due to the distinct lengths of the oligomer chains [77]. Afterwards, in this specific case, the epoxy content can also be tuned.

The macro-level would be the formulation of the photoresists, mixing the resin previously synthesized with at least two more necessary compounds: a photoinitiator and a solvent. Other chemical compounds in this step are also commonly added to tune the overall properties of the mixture. These components are widely known in the industry field as resinous modifiers (influencing properties like flexibility, toughness, peel strength, adhesion, etc.), fillers, colorants, and dyes, other additives (e.g., rheological additives, flame retardants) [74]. The macro-level is commonly performed in a scaled-up production (industry).

### **1.4 State of the art for grating-based interferometry techniques, lithography and photoresists**

The state-of-the art for photoresists, together with the gratings production using X-ray lithography were discussed, which are directly correlated with grating-based imaging systems. Regarding the grating-based interferometric techniques, they can provide a significant advance in conventional imaging systems using X-ray sources. With the usage of special optical components, known as gratings, it is possible to produce images with more information and better resolution. Techniques such as Talbot interferometry are one of the promising approaches for the next generation of X-ray imaging. However, technical limitations still have to be solved, for example, the increase of the field of view and the production of gratings with high homogeneity and defect-free structures.

Lithography process fabrication using X-ray light from synchrotron sources is the only alternative to fabricate gratings for Talbot-interferometry. Features of the gratings like periodicity, area size, and height of the lamellas impose enormous challenges for the lithography fabrication and for the quality control of the raw materials.

The primary raw material applied in lithography is the photoresist, a photoreactive material used to perform pattern transferring. Since the applications such as gratings demand features in the range of sub micrometers for periodicity and heights in the range of hundreds of microns, the lithography techniques and the quality of the raw materials are always pushed to its technological limits.

Along with the history of lithography, several photoresist formulations were proposed; nevertheless, just a few of them are able to fulfill the requirements to fabricate gratings. Chemically amplified photoresists, for example, SU-8 photoresist, are one of the main materials used in gratings fabrication with HAR structures. Although SU-8 presents good performance for HAR fabrication, major issues still have to be solved, like the sensitivity fluctuation and the elaboration of a standardized protocol relating to the chemical properties and lithographic properties of the photoresists. A strategy to first understand and then control and produce photoresists, using deep and macro levels of the formulation can be an alternative to produce photoresist with customized quality for X-ray lithography.

## 2 OBJECTIVE

The production of the gratings through X-ray lithography suffers from low yields of reproducibility and a small percentage of the final components classified as defect-free structures. In order to overcome these two problems, an alternative is to optimize the synthesis and the formulations of the photoresists. As presented in the introduction, in the literature, there is a lack of information regarding the chemical composition for the photoresists and its lithographic properties. For instance, it would be important to acquire a deeper understanding and especially find a concise relationship between the chemical composition and the lithographic properties of the photoresists.

Publications about the best suitable photoresist used for HAR structures suggest the SU-8 formulation, patented by IBM in 1989. Since this time, only few reports have been published with respect to the chemical composition of this photoresist. What is known in its composition is little: mainly the need of a polymer based on bisphenol-A, a photoinitiator, and a suitable solvent. Information about extra additives and the properties of the polymer are not available in the open literature. For high end-applications (e.g., gratings), however, where the dimension features are in the technological limits of the lithography techniques, the properties of the photoresists might be a decisive factor to achieve better success in the fabrication of these components.

In this direction, the aim of this work is to investigate the relationship between the chemical composition of the photoresists and their lithographic properties. For this purpose existing formulations will be investigated (chapter 4). A procedure to synthesize, characterize, and formulate photo-resins will be developed and studied both on a molecular and product design level, previously named as deep and macro levels of properties (see section 1). In the deep-level of properties, the polymerization of bisphenol-A will be studied and optimized, followed by the optimization of the alkylation reaction in the phenolic positions of the polymeric chains (epoxidation reaction). The results are mainly reported in chapter 5. In the macro-level of properties, photoresists will be formulated in the simplest possible version, using the synthesized resins, a photoinitiator, and a solvent. The aim is to use them for lithographic technologies in-house (chapter 6).

Besides characterization of commercially available photoresists, the experimental work is thus divided into two main fields:

Deep-level: Synthesize, characterize and formulate photo-resins to be used on the lithography process. The photo-resins will be characterized using mainly physical-chemical techniques such as Fourier-transform Infrared Spectroscopy (FTIR), Hydrogen and Carbon Nuclear Magnetic Resonance Spectroscopy ( $^1\text{H-NMR}$  and  $^{13}\text{C-NMR}$ ), Matrix-Assisted Laser Desorption Ionization – Time of Flight - Mass Spectroscopy (MALDI-TOF-MS), micro Electrospray Ionization – Time of Flight – Mass Spectroscopy (ESI- $\mu$ -TOF-MS), Thermogravimetric Analysis (TGA) and Differential Scan Calorimetry (DSC).

Macro-level: Different formulations of photo-resins will be prepared regarding the polymeric profile of the resins, amount of photoinitiator, and amount of solvent. Photosensitivity to UV beam sources and efficiency regarding the patterning reproducibility will be evaluated. Several formulations of the photo-resins will be compared.

# 3 REACTION PROCEDURES, MATERIALS AND METHODS

## 3.1 Polymerization of bisphenol-A

The polymerization of bisphenol-A was studied in different conditions. Several values of molar ratios between the reagents were evaluated to standardize the polydispersion of the oligomer chains. The resins were synthesized in the Institute of Microstructure Technology, Karlsruhe Institute of Technology (IMT-KIT), Karlsruhe – Germany.

In a 50 mL one-necked flask, Bisphenol-A and a solution of NaOH/formaldehyde were added. The system was connected to a reflux condenser. Different parameters as the concentration of the NaOH/formaldehyde solution, molar ratio Bisphenol-A: formaldehyde, temperature, time, pressure, as well as the presence of solvent were studied (see Table 2). After the reaction completion, the residual water was removed by distillation, at 140 ° (heating plate), until distilled products were no more observed. The products were then characterized by NMR and mass spectroscopy techniques.

**Table 2:** Parameters and its values for the polymerization reaction

Experiment	Temperature (°C)	Molar ratio (bisphenol-A: H <sub>2</sub> O)	Molar ratio (bisphenol-A:formaldehyde)	Time <sup>a</sup> (hours)
01	130	1:31.68	1:0.5	0.5
02	130	1:31.68	1:0.6	0.5
03	130	1:31.68	1:0.7	0.5
04	130	1:31.68	1:0.8	0.5
05	130	1:31.68	1:0.9	0.5
06	130	1:31.68	1:1	0.5
07	60	1:31.68	1:1.5	0.01 to 8
08	75	1:31.68	1:3.0	0.01 to 8
09	90	1:31.68	1:5.0	0.01 to 8
10	100	1:31.68	1:1.5	0.01 to 8
11	115	1:31.68	1:3.0	0.01 to 8
12	130	1:31.68	1:5.0	0.01 to 8
13	120	1:31.68	1:1.5	0.01 to 8
14	135	1:31.68	1:3.0	0.01 to 8
15	150	1:31.68	1:5.0	0.01 to 8
16	150	1:31.68	1:1.5	0.01 to 8
17	165	1:31.68	1:3.0	0.01 to 8
18	180	1:31.68	1:5.0	0.01 to 8
19	60	-	1:1.5	0.01 to 8
20	75	-	1:3.0	0.01 to 8
21	90	-	1:5.0	0.01 to 8
22	100	-	1:1.5	0.01 to 8
23	115	-	1:3.0	0.01 to 8
24	130	-	1:5.0	0.01 to 8
25	120	-	1:1.5	0.01 to 8
26	135	-	1:3.0	0.01 to 8
27	150	-	1:5.0	0.01 to 8
28	150	-	1:1.5	0.01 to 8
29	165	-	1:3.0	0.01 to 8
30	180	-	1:5.0	0.01 to 8

<sup>a</sup>each reaction (7 to 30) was evaluated in intervals of 10 min approximately, collecting aliquots of the reaction.

## 3.2 Epoxidation of the oligomers

The alkylation reaction was studied in an attempt to optimize the yield of epoxy groups inserted in the phenolic positions of the polymeric chains. The epoxidized resins (poly(2,2-bis-(4-oxy(methyloxirane)phenyl)-propan) were synthesized in the Institute of Microstructure Technology, Karlsruhe Institute of Technology (IMT-KIT), Karlsruhe – Germany.

In a 100 mL one-necked flask, oligomers were added in a molar ratio of 1:25 (oligomers: tetrahydrofuran (THF)) with the solvent. After the complete solution, a molar ratio of  $1:6 \times 10^{-2}$  (oligomers:  $\text{BF}_3\text{Et}_2\text{O}$ ) was added to the mixture. After one hour under constant heating at 45 °C, a molar ratio of 1:20 (oligomers: epichlorohydrin) was slowly and carefully added to the reaction, during circa 4 hours, where after 3 hours adding epichlorohydrin, the reaction system had the temperature increased to 70 °C. The reaction system was cooled to room temperature and, an alkali solution was added, with molar ratio 1:2.1 (oligomers: alkali), the reaction system was heated to 60 °C for 3 hours. After cooling down to room temperature, the reaction mixture was neutralized with an acid solution until pH near to 7. A molar ratio of 1:175 (oligomers:  $\text{H}_2\text{O}$ ) of water was used to wash the solution (four times 1:175). The organic layer was separated, and the solvent was evaporated. The products obtained were characterized by reported methods.

## 3.3 Materials

The chemicals and consumables were purchased from Sigma-Aldrich (Darmstadt, Germany). Bisphenol-A ( $\geq 99\%$ ), p-formaldehyde ( $\geq 94.0\%$ ), epichlorohydrin ( $\geq 99\%$ ) and, Boron trifluoride etherate ( $\text{BF}_3$  content: 46-51%) ( $\text{BF}_3\text{Et}_2\text{O}$ ) were the main chemicals used for the synthesis procedures. Triarylsulfonium hexafluoroantimonate salts or also known as triarylsulfonium salts (TAS) (50 wt. % in propylene carbonate) and polar solvents as acetone (99.6%), cyclopentanone (98.0 %), isopropanol (anhydrous, 99,5%), were the main chemicals used to perform synthesis and formulation of the photoresists. All chemicals were used as received.

## 3.4 Methods

The characterization methods and lithographic procedures bellow described are organized in chronological order of application, following the necessity of the chapters four five and six.

## 3.5 Fourier-transform Infrared Spectroscopy (FTIR)

Commercially available photoresists (negative-tone ones, based in bisphenol-A), were evaluated through FTIR in order to identify the main organic functions present in the composition of these materials. Samples were named epoxy resins series 1 (EPR-S1a and EPR-S1b), and epoxy resins series 2 (EPR-S2 a, EPR-S2 b, EPR-S2 c, EPR-S2 d, EPR-S2 e, EPR-S2 f, EPR-S2 g, EPR-S2 h). FTIR measurements were performed in the chemistry department of the Federal University of Paraná, Curitiba, Brazil.

Sample preparation:

A KBr crystal (dimensions: 1.0 x 1.0 x 0.5 cm) was previously cleaned with acetone, removing any residual contamination from the surfaces of the crystal.

The KBr crystal was attached to the holder, and a background signal was acquired.

The KBr crystal was placed on a scale. Circa  $5 \pm 2$  mg of the photoresist (liquid phase) was applied on top of the crystal. The crystal was carefully attached to the holder of the equipment.

After waiting circa 10 min to slightly spread the drop of photoresist, the measurement was taken.

The analyses by FTIR were performed using a spectrometer model B-100 (Bomem of Hartmann & Braun – Germany). Spectra were obtained in a range of 4000 to 500  $\text{cm}^{-1}$  with a resolution of 4  $\text{cm}^{-1}$  and 32 scans in transmittance mode.

### 3.6 Thermogravimetric Analysis (TGA)

Commercially available photoresists (negative-tone ones, based in bisphenol-A), were evaluated through TGA to identify the solvent content, crosslinking, and degradation temperature peaks. Samples were named epoxy resins series 1 (EPR-S1a and EPR-S1b), and epoxy resins series 2 (EPR-S2 a, EPR-S2 b, EPR-S2 c, EPR-S2 d, EPR-S2 e, EPR-S2 f, EPR-S2 g, EPR-S2 h). FTIR measurements were performed in the chemistry department of the Federal University of Paraná, Curitiba, Brazil. For this purpose, the samples were prepared as follows:

- 1) In an Alumina ( $\text{AlO}_3$ ) crucible for TGA measurements, placed on a scale, circa  $40 \pm 10$  mg of the sample was weighted.
- 3) The crucible was inserted in the TGA chamber equipment.
- 4) The sample weight value was recorded in the TGA software. Afterwards the measurement was initiated.

The measurements were performed in a NETZSC TG-209 (Erich NETZSCH GmbH & Co. Holding KG, Selb, Germany), in an oxidative atmosphere (synthetic air). The temperature range of the operation was 25 - 800  $^{\circ}\text{C}$ , with a heating ramp of 10  $^{\circ}\text{C}\cdot\text{min}^{-1}$

### 3.7 Matrix-Assisted Laser Desorption Ionization Mass Spectroscopy (MALDI-TOF-MS)

To characterize the distribution of the polymer chains, commercially available photoresists were evaluated through MALDI-TOF-MS. Samples were named epoxy resins series 1 (EPR-S1a and EPR-S1b), and epoxy resins series 2 (EPR-S2 a, EPR-S2 b, EPR-S2 c, EPR-S2 d, EPR-S2 e, EPR-S2 f, EPR-S2 g, EPR-S2 h). MALDI-TOF-MS experiments were performed in the chemistry department of the Federal University of Paraná, Curitiba, Brazil. For this purpose, the samples were prepared as follows:

- 1) Samples were prepared weighing  $4 \pm 2$  mg of photoresist in a vial, placed in the scale.
- 2) Samples were diluted in 1 mL of acetone.

3) The matrix was prepared in a separate vial weighing approximately  $10 \pm 2$  mg of 2,4-Dihydroxybenzoic acid (DHB) and approximately  $4 \pm 2$  mg of sodium chloride (NaCl). Afterwards the mixture was solubilized in 1 mL of acetone.

4) The sample and matrix were mixed in a 1:1 volume ratio (100  $\mu$ L of each), and this mixture was added on the MALDI target plate, carefully using a micropipette setup in a volume of 1  $\mu$ L.

5) The target plate was laid to evaporate the solvent. After circa 30 min, the target plate was inserted in the equipment, and the spectra were acquired.

The spectra were recorded on a KRATOS AXIMA Performance MALDI instrument (Shimadzu – Japan). Nitrogen laser was applied as an irradiation source with 337 nm of wavelength. The analyses were carried out with the following characteristics: negative polarity, flight path-linear, mass-high - 20 kV voltage, 100-150 pulses per spectrum.

### 3.8 Electrospray Ionization - Time of Flight – Mass Spectroscopy (ESI- $\mu$ -TOF-MS)

The polymeric distribution of the synthesized resins was characterized through ESI- $\mu$ -TOF-MS. The samples were named R1, R2, and R3. ESI- $\mu$ -TOF-MS experiments were performed in the Institute of Nanotechnology, Karlsruhe Institute of Technology (INT-KIT), Karlsruhe – Germany. For this purpose, the samples were prepared as follows:

1) Samples were prepared weighing circa  $10 \pm 2$  mg of photoresist in a vial, placed in the scale.

2) Samples were diluted in 1 mL of acetone.

3) Samples were consecutively diluted until the concentration of  $10^{-6}$  mol·mL<sup>-1</sup>

3) With a micropipette, circa 20  $\mu$ L of the solutions were inserted in a special needle designed for this equipment.

4) The needle was assembled in the holder. Afterwards the holder was placed in the chamber of ESI- $\mu$ -TOF-MS, and the measurements were acquired.

The spectra were recorded on a microOTOF-QII spectrometer (Bruker-Germany). The acquisition was settled to negative mode,  $5,5 \times 10^3$  volts, no pressure at the nebulizer, dry gas flow at 3.0 mL·mL<sup>-1</sup>, the dry temperature of 90 °C, transfer system with RF 1 and RF 2 at 200 VPP, Hexapole at 100 VPP, ion energy of 3.0 eV, collision energy at 12.0, collision RF of 250 VPP, the transfer time of 70  $\mu$ s, pre-storage of 5.0  $\mu$ s. The mass range was initially recorded from  $1 \times 10^2$  to  $1 \times 10^4$  m·z<sup>-1</sup>; after not observing any peaks in the high mass region, the spectra were recorded in a range  $1 \times 10^2$  to  $2.5 \times 10^3$  m·z<sup>-1</sup>.

### 3.9 Nuclear Magnetic Resonance Spectroscopy (NMR)

The products of the polymerization and alkylation reactions were characterized by proton NMR (<sup>1</sup>HNMR) and carbon NMR (<sup>13</sup>CNMR). For the polymerization products, the samples were named R1, R2, and R3. For alkylation

products (epoxidation reaction), the samples were named R1-ep, R2-ep, R3-ep. ESI- $\mu$ -TOF-MS experiments were performed in the Institute of Nanotechnology, Karlsruhe Institute of Technology (INT-KIT), Karlsruhe – Germany. For this purpose, the samples were prepared as follows:

- 1) In a vial, placed on a scale, circa  $40 \pm 3$  mg of the resin was weighted.
- 2) 0.5 milliliter of hexadeuteroacetone (acetone- $d_6$ , containing 0.03% (v/v) tetramethylsilane) was added to the vials.
- 3) After complete solubilization, the solution was transferred to the NMR tube.
- 4) The samples were placed in the automatic carrier, and the spectra were acquired.

The spectra were obtained in a Bruker 500 MHz NMR (Bruker – Germany). The experiments, such as protons ( $^1\text{H}$ -NMR) and carbon ( $^{13}\text{C}$ -NMR), were performed using the standard parameters predetermined by Bruker's software. The proton experiments were acquired with 124 scans and carbon experiments with 1024 scans.

### 3.10 Differential Scanning Calorimetry (DSC)

The products of the polymerization and alkylation reactions were characterized through DSC. For the polymerization products, the samples were named R1, R2, and R3. For alkylation products (epoxidation reaction) the samples were named R1-ep, R2-ep, R3-ep. DSC experiments were performed in the Institute for Chemical Technology and Polymer Chemistry, Karlsruhe Institute of Technology (ITCP-KIT), Karlsruhe – Germany. For this purpose, the samples were prepared as follows:

- 1) In an Aluminum crucible (for DSC measurements), placed on a scale, circa  $10 \pm 3$  mg of the sample was weighted.
- 2) The crucible was sealed with a cap in an appropriate machine sealer.
- 3) The crucible was inserted into DSC chamber equipment.
- 4) The sample weight value was recorded in the DSC software. Afterwards the measurement was initiated.

Heating ramp sequence for samples R1, R2, and R3:

The analyses were performed in a DSC 30 (Mettler-Toledo Instruments – Giessen - Germany). The heating ramp was programed as it follows:

- 1) Heating until  $180\text{ }^\circ\text{C}$ ; with the heating flow of  $10\text{ }^\circ\text{C}\cdot\text{min}^{-1}$
- 2) 3 minutes isotherm
- 3) Cooling until  $-50\text{ }^\circ\text{C}$ ; with the cooling flow of  $10\text{ }^\circ\text{C}\cdot\text{min}^{-1}$
- 4) Heating until  $180\text{ }^\circ\text{C}$ ; with the heating flow of  $10\text{ }^\circ\text{C}\cdot\text{min}^{-1}$
- 5) Cooling until  $25\text{ }^\circ\text{C}$ ; with the cooling flow of  $10\text{ }^\circ\text{C}\cdot\text{min}^{-1}$

Heating ramp sequence for samples R1-ep, R2-ep, and R3-ep:

The measurements were performed in a DSC 30 (Mettler-Toledo Instruments – Germany). The samples were evaluated following the heating procedure:

- 1) Cooling until  $-150^{\circ}\text{C}$ ; with the cooling flow of  $10^{\circ}\text{C}\cdot\text{min}^{-1}$
- 2) 3 minutes isotherm
- 3) Heating until  $35^{\circ}\text{C}$ ; with the heating flow of  $10^{\circ}\text{C}\cdot\text{min}^{-1}$
- 4) Cooling until  $25^{\circ}\text{C}$ ; with the cooling flow of  $10^{\circ}\text{C}\cdot\text{min}^{-1}$

### 3.11 Formulation of the photo-resins

Epoxy resins (with different polydispersities and different epoxidation degrees), a photoinitiator and a solvent were used to prepare the formulas for the epoxy-based photo-resins. The formulations of the photo-resins were performed in the Institute of Microstructure Technology, Karlsruhe Institute of Technology (IMT-KIT), Karlsruhe – Germany. Table 3 presents the properties and the quantities to prepare the photo-resins.

**Table 3:** Oligomer characteristics, quantities for the photo-resin formulations and, chemical compounds

Level of formulation	Compound	Range (% $\text{mol}\cdot\text{mol}_{\text{polymer}}^{-1}$ )
Deep-level (oligomer composition)	Profile of Resin (polydispersity)	P1, P2, P3
	Epoxidation degree	0; 10; 20; 30; 40
Macro-level (added chemicals to the formulation)	Photoinitiator	0; 3; 5; 10; 30; 50; 100
	Solvent	0 - 22*

\* the solvent concentration varies to reach the right viscosity

In Table 3, regarding the epoxy resins, two characteristics were considered to be evaluated in the formulations, the polydispersity, and the epoxidation degree. The photoinitiator applied in this formulation is a mix of triaryl-sulfonium hexafluoroantimonate salts (50 wt. % in propylene carbonate). The solvent applied for the formulations was cyclopentanone, where its primary function is to obtain a specific viscosity for the formulation ( $850\pm 20 \text{ mPa}\cdot\text{s}^{-1}$ ;  $25^{\circ}\text{C}$ ;  $1\cdot 10^3 \text{ s}$ ).

To easily understand the formulations, a label code was used:



P: profile of the resin

ED: epoxidation degree

C: photoinitiator

x: type of resin

y: the amount of epoxy groups

z: the amount of catalyst

As an example, P<sub>3</sub>ED<sub>20</sub>C<sub>30</sub> means a formulation with the resin R3, epoxidation degree of 20 % mol·mol<sub>polymer</sub><sup>-1</sup>, and 30 % mol·mol<sub>polymer</sub><sup>-1</sup> of the photoinitiator. Mol<sub>polymer</sub> is defined as the molar mass of the monomer (228.29 g·mol<sup>-1</sup>)

### 3.12 Quality evaluation through UV lithography

Photo-resins with a variety of formulations (see Table 3) were evaluated in a qualitative manner through UV lithography to correlate the chemical composition of the photo-resins and its lithographic performance. The photo-resins were processed in the cleanroom facilities, located at the Institute of Microstructure Technology, Karlsruhe Institute of Technology (IMT-KIT), Karlsruhe – Germany. In the cleanroom environment, temperature and humidity were controlled (23 °C, 45 - 50 % H<sub>2</sub>O). Figure 32 presents the preparation for UV lithography.

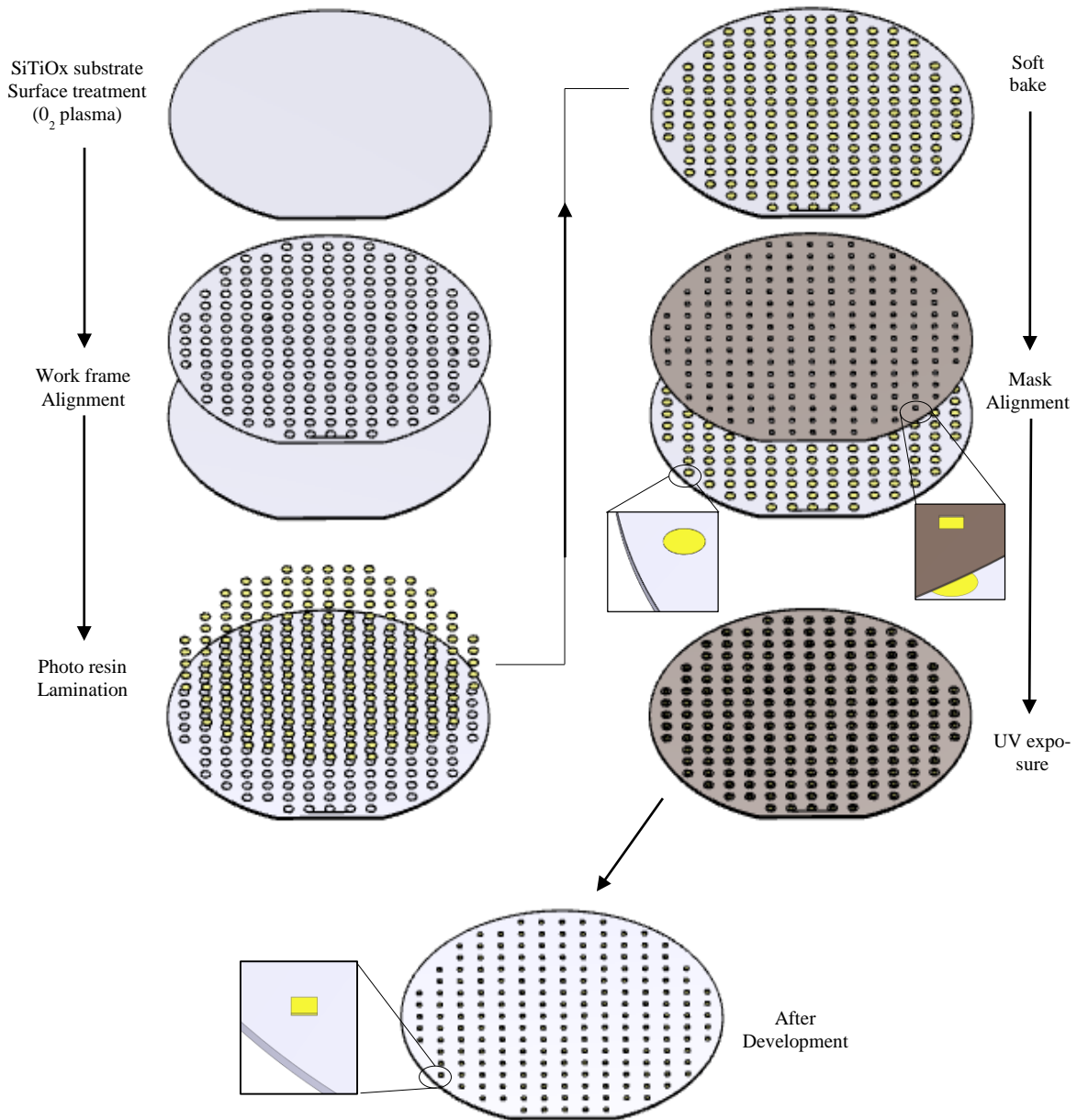


**Figure 32:** Qualitative evaluation of the photo-resins. Reproduced from Vlnieska et al (2020) [76] (CC BY)

In Figure 32 (a), the substrate used was silicon titanium oxide (SiTiOx) (550  $\mu\text{m}$  of thickness, the diameter of 4 inches (10.16 cm), and circa 2.5  $\mu\text{m}$  of TiOx layer in the surface). SiTiOx substrates were pre-cleaned with plasma etching (PE) (see section method 3.15). After PE the substrate was laid on a heating plate at 95  $^{\circ}\text{C}$ , for 10 min.

Afterwards a work frame lamination was glued to the substrate (Figure 32 (b)). The working frame is an adhesive itself. The features of the work frame are a circle shape with three millimeters diameter and approximately 120  $\mu\text{m}$  height.

The photo-resins were laminated in the work frame (Figure 32 (c)). Using a tiny needle, small drops of photo-resins were placed in the circular shapes of the work-frame. After that, the photo-resins were leveled with the surface of the work frame, through lamination with a small spatula. After lamination, the substrate was laid in a heating plate at 65  $^{\circ}\text{C}$  during 6 hours, (Figure 32 (d))

In Figure 32 (e), a mask made of Kapton® (120 µm thickness, with squared shapes of 2.3 mm<sup>2</sup>) was aligned with the work-frame. After alignment, the photo-resins were exposed at flood exposure mode (see 3.2.8 Deep-UV and UV lithography exposures) (Figure 32 (f)). After exposure, the samples were laid in the oven for 12 hours at 65 °C.

The development was made using 2-methoxy-1-methyl ethyl acetate (PGMA) and isopropanol (ISO) as developers, following the order and time: 7 min in PGMA and 5 min in ISO. The wafers were laid at room temperature overnight to dry out the excess of the solvent

### 3.13 Test pattern structures through Deep-UV and UV lithography

Photo-resins P<sub>1</sub>ED<sub>40</sub>C<sub>30</sub>, P<sub>2</sub>ED<sub>40</sub>C<sub>30</sub>, and P<sub>2</sub>ED<sub>40</sub>C<sub>30</sub>, were evaluated through deep-UV and UV lithography, in order to correlate the chemical composition of the photo-resins and its lithographic performance.

The photo-resins were processed at the cleanroom facilities, located in the Institute of Microstructure Technology, Karlsruhe Institute of Technology (IMT-KIT), Karlsruhe – Germany. In the cleanroom environment, temperature and humidity were controlled (23 °C, 45 - 50 % H<sub>2</sub>O). The samples were prepared as follows:

SiTiOx substrates (550 µm of thickness, the diameter of 1 cm and circa 2.5 µm of TiOx layer in the surface) were pre-cleaned with reactive ion etching (RIE) (see 3.3.10 Reactive Ion Etching procedure). After PL the substrate was laid in a heating plate at 95 °C, for 10 min.

Substrates were coated with the samples P<sub>1</sub>ED<sub>40</sub>C<sub>30</sub>, P<sub>2</sub>ED<sub>40</sub>C<sub>30</sub>, and P<sub>2</sub>ED<sub>40</sub>C<sub>30</sub> using the spin-coating technique (see section method 3.16). After spin-coating, the substrates were laid in an oven at 65 °C, for 6 hours.

The coated substrates (1cm diameter) were glued in a 4 inches (10.16 cm) diameter silicon substrate, using double-sided adhesive tape. The samples were placed in a holder from the EVG mask aligner equipment. The samples were exposed using deep-UV and UV light. (see section method 3.14). After exposure, the samples were laid in an oven for 12 hours at 65 °C.

The development was made using 2-methoxy-1-methyl ethyl acetate (PGMA) and isopropanol (ISO) as developers, following the order and time: 7 min in PGMA and 5 min in ISO. The wafers were laid at room temperature overnight to dry out the excess of the solvent

### 3.14 Deep-UV and UV lithography exposures

Substrates containing the photo-resins were exposed through deep-UV and UV light to evaluate the lithographic properties of the photo-resins and compare them with its formulations. The photo-resins were processed at the cleanroom facilities, located in the Institute of Microstructure Technology, Karlsruhe Institute of Technology (IMT-KIT), Karlsruhe – Germany. In the cleanroom environment, temperature and humidity were controlled (23 °C, 45 - 50 % H<sub>2</sub>O).

The photo-resins layers were exposed using an EVG mask aligner (EV Group, Sankt Florian am Inn, Austria) with  $2.8 \text{ mW}\cdot\text{cm}^{-2}$  radiation intensity ( $0.15 \text{ mW}\cdot\text{cm}^{-2}$  deviation) using the filter for wavelengths shorter than 365 nm. For the first trial of experiments, a mask made of Kapton® (125  $\mu\text{m}$  of thickness) was used, with squares of 2.3  $\text{mm}^2$ . For the second trial, a chromium mask was used as a test pattern, with dimensions of the structures varying from 50 down to 1  $\mu\text{m}$ . The exposure was carried out in a flood exposure mode. The dose delivered to the surface of the photoresist was  $1,0 \times 10^4 \text{ mJ}\cdot\text{cm}^{-2}$ .

### 3.15 Plasma Etching

Silicon Titanium Oxide substrates were pre-cleaned with plasma etching. Plasma etching was processed at the cleanroom facilities, located in the Institute of Microstructure Technology, Karlsruhe Institute of Technology (IMT-KIT), Karlsruhe – Germany. In the cleanroom environment, temperature and humidity were controlled (23 °C, 45 - 50 %  $\text{H}_2\text{O}$ ).

Substrates were laid directly in the chamber of the equipment. The cleaning procedure was carried out in an equipment model, Etchlab 200, from Sentech (Berlin, Germany). The parameters for the plasmas etching were: 100W; 400 mTorr and 170 V in the reaction chamber; running time of 600 seconds.

### 3.16 Spin-coating

Samples  $\text{P}_1\text{ED}_{40}\text{C}_{30}$ ,  $\text{P}_2\text{ED}_{40}\text{C}_{30}$ , and  $\text{P}_3\text{ED}_{40}\text{C}_{30}$  were spin-coated using the available spin-coating techniques at the cleanroom facilities, located in the Institute of Microstructure Technology, Karlsruhe Institute of Technology (IMT-KIT), Karlsruhe – Germany. In the cleanroom environment, temperature and humidity were controlled (23 °C, 45 - 50 %  $\text{H}_2\text{O}$ ). The sample were prepared as follows: At first, the substrates (SiTiOx, 550  $\mu\text{m}$ , 1 cm diameter) were placed in the holder for the spin-coating equipment. Next, the vacuum-line was activated. A small amount of the samples were poured in the substrates. The spin-coating was performed to achieve 20-30  $\mu\text{m}$  thickness, with the following ramp parameters: 1500 rpm, speed rate of  $100 \text{ rpm}\cdot\text{s}^{-1}$ , for 60 seconds; 60 seconds rest; 2750 rpm, speed rate of  $100 \text{ rpm}\cdot\text{s}^{-1}$ , during 75 seconds

### 3.17 Scanning Electron Microscopy

The structures obtained after deep-UV and UV lithography were evaluated using scanning electron microscopy SEM. The instrument is located at the cleanroom facilities in the Institute of Microstructure Technology, Karlsruhe Institute of Technology (IMT-KIT), Karlsruhe – Germany. In the cleanroom environment, temperature and humidity were controlled (23 °C, 45 - 50 %  $\text{H}_2\text{O}$ ).

Sample preparation:

Samples were glued with a special adhesive tape (for SEM measurement) in a silicon substrate (500  $\mu\text{m}$  thick, with a 4-inch diameter (10.16 cm)), used for as a base plate. The substrate was fixed in a holder for 4 inches substrate. The holder was inserted into the SEM chamber, and the measurements were obtained.

The measurements were conducted in an equipment model Zeiss Supra 60 VP, from Bruker Nano GmbH (Berlin, Germany). The parameters were: from 0.7 to 10 KeV for the beam, Density: 6125, Primary energy: 10 m, Takeoff angle: 35 degrees, Tilt angle: 0, Azimut angle: 0, Detector type: Bruker X-flash 6 series, Detector thickness: 0.45, Si dead layer: 0.08, Calibration, abs.: - 477.65, Mn FWHM: 146.563, Fano factor: 0.145, Channels: 2057, Aperture: 120  $\mu\text{m}$ , Current: 2.28  $\mu\text{mA}$ .

### **3.18 Scanning Electron Microscopy – Energy Dispersive Spectroscopy of X-rays (SEM-EDX)**

The synthesized oligomers R1, R2, and R3, epoxidized oligomers R1-ep, R2-ep, and R3-ep, were evaluated through scanning electron microscopy – energy dispersive spectroscopy of X-rays (SEM-EDX) to determine the atom composition. SEM-EDX is located at the cleanroom facilities, in the Institute of Microstructure Technology, Karlsruhe Institute of Technology (IMT-KIT), Karlsruhe – Germany. In the cleanroom environment, temperature and humidity were controlled (23  $^{\circ}\text{C}$ , 45 - 50 %  $\text{H}_2\text{O}$ ).

Sample preparation:

A silicon substrate (500  $\mu\text{m}$  thick, with a 4-inch diameter (10.16 cm)), was used for the measurements.

A frame with several circular (3 mm diameter) shapes was glued in the substrate, forming a pillar volume of  $3.0 \times 10^3 \mu\text{m} \times 120 \mu\text{m}$  (diameter  $\times$  height). A similar procedure can be observed in Figure 30 (b).

After gluing the frame, the substrate was laid in an oven overnight at 75  $^{\circ}\text{C}$ .

The samples (resins R1, R2, and R3, epoxidized resins R1-ep, R2-ep, R3-ep, and bisphenol-A) were diluted in cyclopentanone and applied in the pillar volume shape.

The substrate was laid in an oven overnight at 95  $^{\circ}\text{C}$  to evaporate the solvent.

The measurements were conducted in an equipment model Zeiss Supra 60 VP, from Bruker Nano GmbH (Berlin, Germany). The chamber parameters were the same as section 3.3.10 - Scanning Electron Microscopy. For the EDX measurements, the following specifications were applied: aperture 200  $\mu\text{m}$  wide, working distance 25 mm, and the number of counts: from 4.5 to  $7.2 \times 10^3$ .

### **3.19 Optical microscope measurements**

Photo-resins with a variety of formulations (see Table 3) were evaluated through an optical microscope, after the lithographic processing.

The evaluation was made at the cleanroom facilities, located in the Institute of Microstructure Technology, Karlsruhe Institute of Technology (IMT-KIT), Karlsruhe – Germany. In the cleanroom environment, temperature and humidity were controlled (23 °C, 45 - 50 % H<sub>2</sub>O).

Sample preparation:

A silicon substrate (500 μm thick, with a 4-inch diameter (10.16 cm)), with the developed formulations, was placed in the table holder of the optical microscope.

After focusing the cavities with the photo-resins formulations, the pictures were recorded.

The measurements were conducted in a digital microscope VHX, using the lenses model VH-Z 20R – RZ x20 – x200, from Keyence (Itasca, USA). The images were taken with magnifications varying from 175 to 200 times, with white light and no filters in the optical path.

# 4 CHARACTERIZATION OF COMMERCIAL PHOTORESISTS <sup>1</sup>

Negative-tone photoresists are the best suitable photoresists for HAR structures fabrication through X-ray lithography (XRL). Within the negative-tone photoresists` category, one of them is the best alternative for HAR structure fabrication through XRL, known as SU-8. Nevertheless, in section 1.3, it was shown that SU-8 presents fluctuations regarding its photosensitivity properties, affecting the exposure step in the lithography process. The sensitivity can be directly related to the chemical composition of this photoresist.

Since there is a lack of information in the literature regarding the chemical properties of SU-8, it is crucial first to understand and characterize the SU-8 type photoresists. Characterization methods such as FTIR, TGA, and MALDI-TOF-MS were performed to determine the main chemical characteristics of SU-8 photoresists. A methodology for characterizing the epoxy-based material photoresists was proposed. Photoresists commercially available and known in the lithography market as SU-8 were studied.

In this chapter, the main organic functions, amount of epoxy groups, polydispersion of the oligomeric chains, degradation temperatures, and amount of solvent were determined for ten different fabrication lots of the same photoresist.

## 4.1 Characterization Methodology

Commercially available negative-tone photoresists applied for HAR structures fabrication through X-ray lithography samples were evaluated and characterized. Two brands, named as epoxy resin series 1 (EPR-S1), with two production batches and epoxy resin series 2 (EPR-S2) with eight production batches, are shown in Table 4.

**Table 4:** Evaluated negative-tone photoresists.

Photoresist	
Brand 1	EPR-S1-a
	EPR-S1-b
Brand 2	EPR-S2-a
	EPR-S2-b
	EPR-S2-c
	EPR-S2-d
	EPR-S2-e
	EPR-S2-f
	EPR-S2-g
	EPR-S2-h

1. This chapter is based on the publication: Vlnieska, V., Zakharova, M., Börner, M., Bade, K., Mohr, J., Kunka, D., *Chemical and Molecular Variations in Commercial Epoxide Photoresists for X-ray Lithography*. Applied Sciences, 2018. **8**(4)

## 4.2 FTIR spectroscopy

The photoresists were characterized through FTIR (see section method 3.5) to determine the main organic groups in the molecular structure. Figure 33 presents FTIR spectra for the photoresist EPR-S1-b, while Figure 34 presents the main organic groups characterized. All samples were individually characterized, and afterwards, their spectra are presented in Figure 34 (condensed).

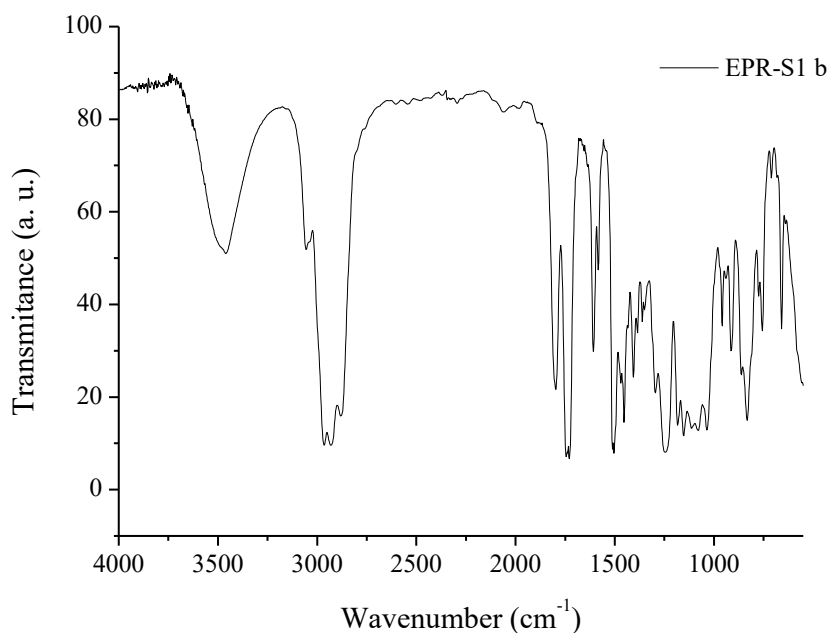


**Figure 33:** FTIR of the sample EPR-S1-b. Reproduced from Vlnieska et al (2018) [4] (CC BY)

Regarding the composition of the photoresists, were identified eight main specific regions in the FTIR spectra (Figure 33). The region is  $3475\text{ cm}^{-1}$  is a vibration typically assigned to hydroxyl groups ( $\text{OH}^-$ ), and the region at  $2930\text{ cm}^{-1}$  confirms the presence of methyl, methylene, and aromatic hydrogens in the structure of the sample. The regions in  $1798$  and  $1735\text{ cm}^{-1}$  are assigned for carbonyl of ketones, acids, esters, and lactones groups. The regions of  $1600$  and  $829\text{ cm}^{-1}$  are assigned to alkenes, and the region in  $1247\text{ cm}^{-1}$  is assigned to the organic group ether. Figure 34 resumes the organic groups present in the evaluated photoresists. One can compare it with Figure 29 (b), where the structure from SU-8 polymer is depicted [78, 79].

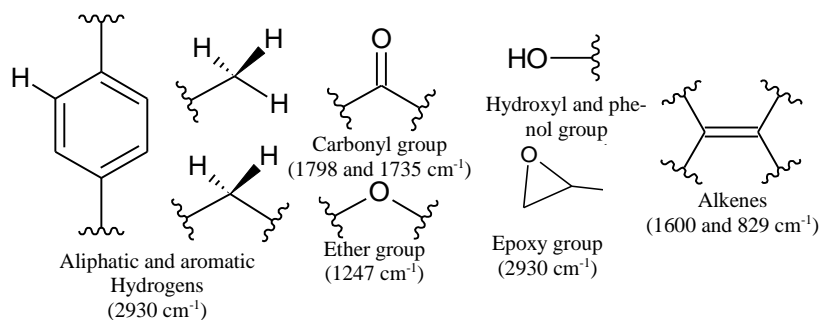


**Figure 34:** Organic groups identified in FTIR analysis. Reproduced from Vlnieska et al (2018) [4] (CC BY)

In Figure 35 is presented the spectra for all EPR-S1 and EPR-S2 series. Regarding the organic functional groups, were found distinct assignments in the region of carbonyl groups (range of  $1700\text{--}1800\text{ cm}^{-1}$ ). Series EPR-S1 contain a less intense band and it is divided in two bands.

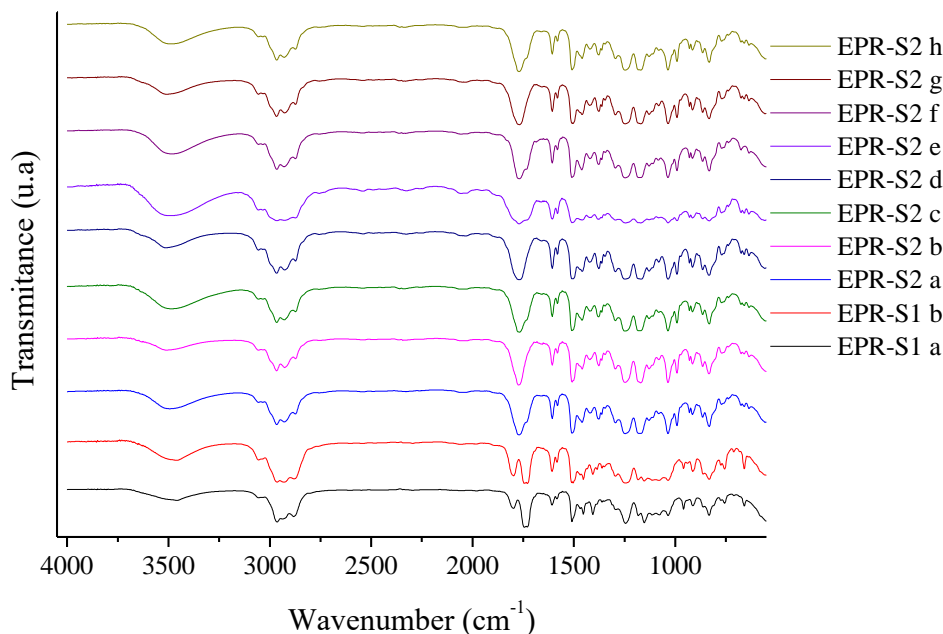


**Figure 35:** FTIR spectra for EPR-S1 and EPR-S2 photoresists. Reproduced from Vnieska et al (2018) [4] (CC BY)

All expected organic functional groups that characterize the oligomers were present in the EPR-S1 and EPR-S2 samples. Nevertheless, other organic functional groups were characterized, indicating the presence of other chemical compounds (e.g., solvents, photoinitiators, etc.) [80].

However, an intriguing result can be observed in the region of  $3475\text{ cm}^{-1}$  (assigned to the phenolic groups), which presented relatively high intensity, especially for samples EPR-S2-b, EPR-S2-d, and EPR-S2-e. The high amount of phenolic groups clearly indicates the non-total reaction during the alkylation of the phenolic positions (epoxidation of the polymer matrix).

### 4.3 Thermogravimetric Analysis (TGA)

TGA was applied in this characterization methodology mainly to identify the solvent content in the photoresists composition. Figure 36 presents the degradation curve for resin EPR-S1-a as an example to explain the main degradation events during the heating of the material (see section method 3.5)

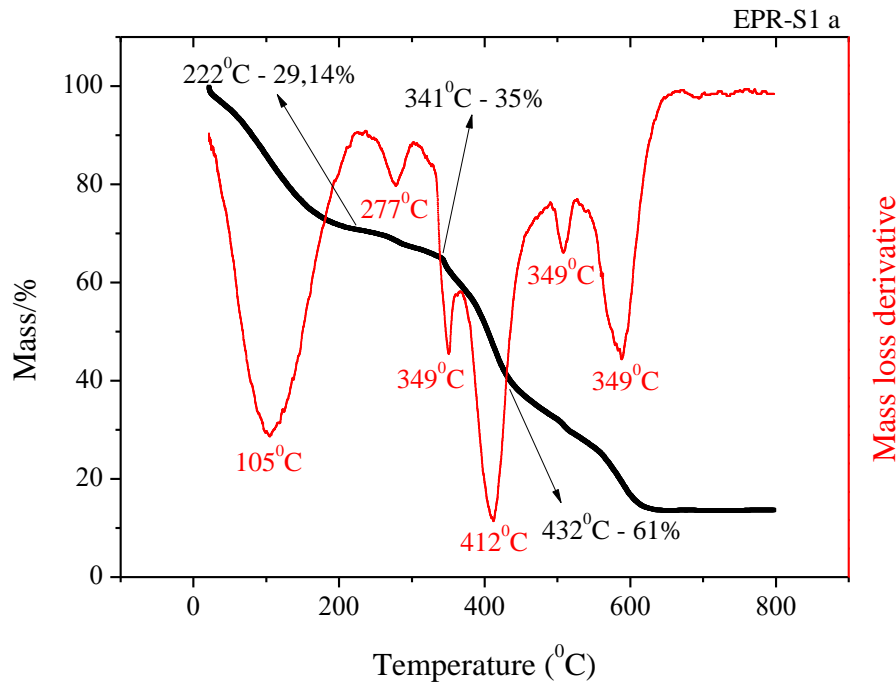


**Figure 36:** TGA and derivative curve from sample EPR-S1-a. Reproduced from Vlnieska et al (2018) [4] (CC BY)

In Figure 36, the heating curve can be divided into three main parts: the region of solvent evaporation (room temperature until 220 °C), the region of the crosslinking process (220–320 °C), and the region of degradation (320–650 °C) [80, 81]. The derivative curve (red line) indicates each event of mass loss in the heating curve. Figure 37 shows the TGA curves for all of the characterized photoresists. There are differences in the solvent content of up to 5.5 % approximately. Usually, the solvent is applied in the photoresist formulation to obtain the same viscosity value. Since the viscosity is a physical-chemical parameter directly related to the molecular composition [82], if the solvent content varies, noticeably the molecular composition of the photoresists shall be distinct. Figure 37 shows the TGA analysis for the all EPR photoresists.

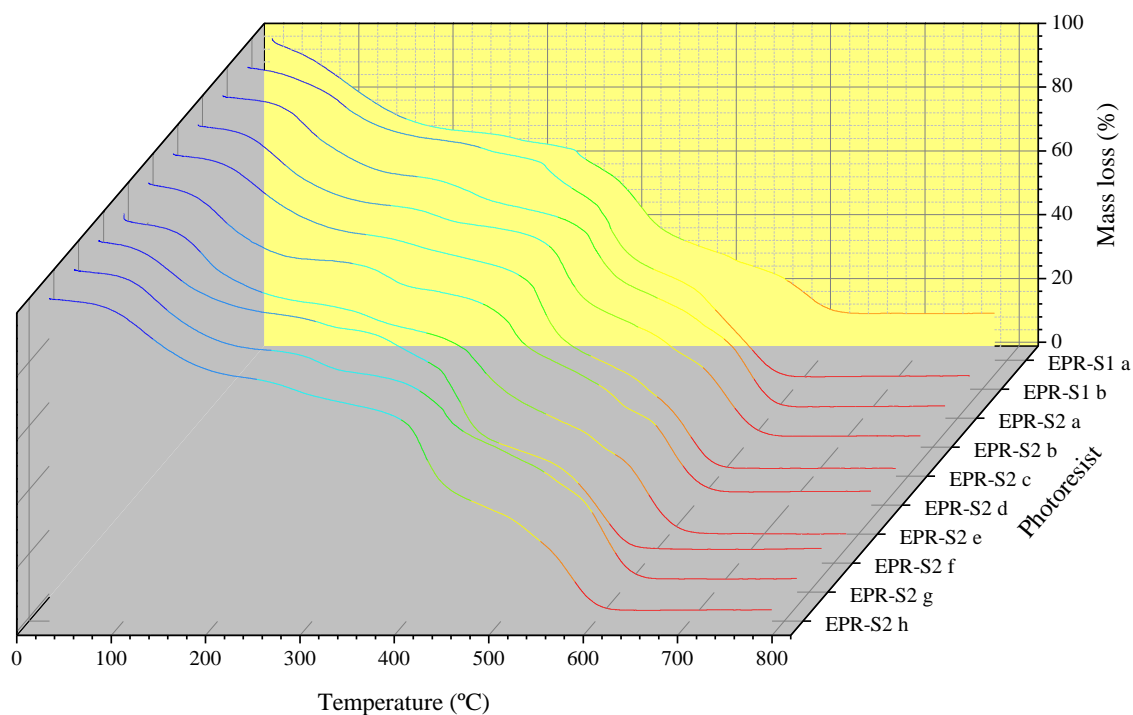


**Figure 37:** TGA of the photoresists. Adapted from Vnieska et al (2018) [4] (CC BY)

Regarding series EPR-S2, the measurements showed solvent content between 22.66 % and 28.15 %. The two samples of the EPR-S1 series also demonstrated considerable differences in the solvent content. These variations were not significant for most of the final applications from lithography. Nevertheless, for DXRL, it could be a significant difference, resulting in distinct lithographic performances for the photoresists. This evidence provides motivation to investigate the polymeric properties of the photoresists. In this direction, in order to observe the composition of the resins in molecular size and polydispersity, the resins were evaluated by MALDI-TOF-MS.

## 4.4 Matrix-Assisted Laser Desorption Ionization Mass Spectroscopy (MALDI-TOF-MS)

In the MALDI-TOF-MS (see section method 3.7), the photoresists were evaluated, focusing only on the oligomers chain sizes. There is no influence in the solvent content and photoinitiator for these measurements. The structure of the polymer chains for EPR photoresists is represented in Figure 38.

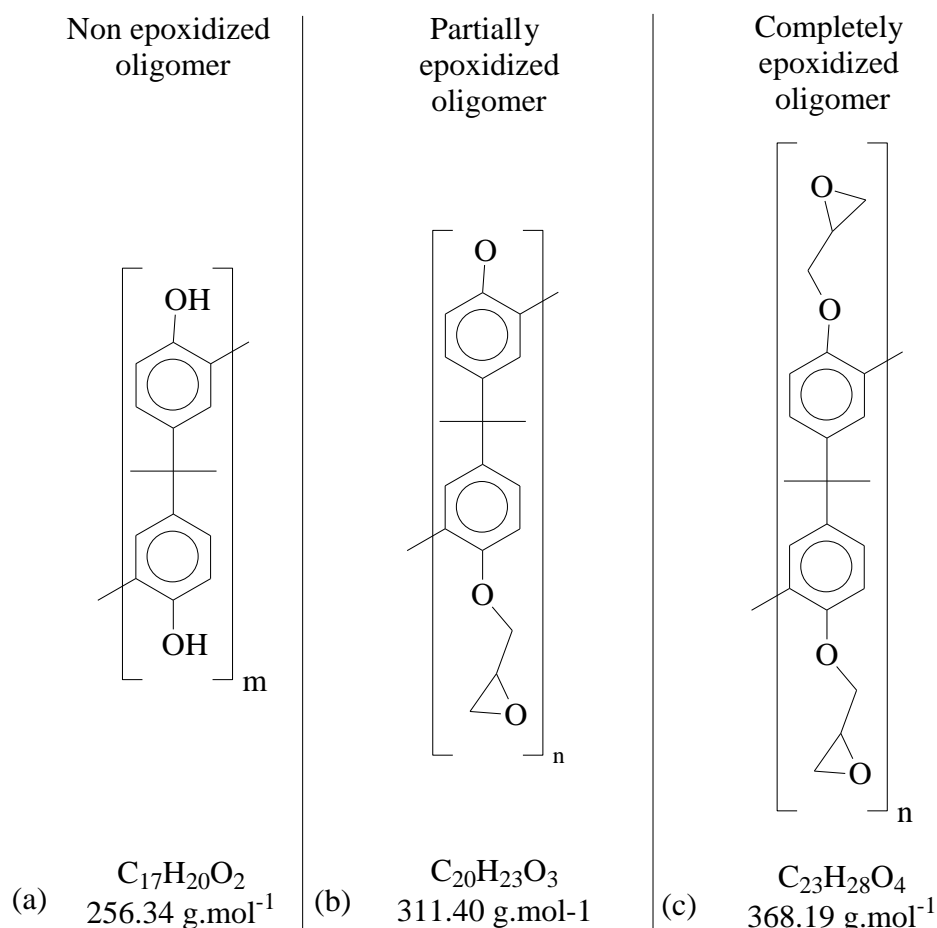


**Figure 38:** Oligomer structures, their molecular masses and chemical formulas. In (a) non epoxidized oligomer; in (b) partially epoxidized oligomer, and in (c) completely epoxidized oligomer

As evidenced by FTIR, the photoresists present structures with high amount of phenolic groups. Therefore, for the oligomer chains characterization, it has to be considered at least three structures in this analysis, as depicted by Figure 38.

MALDI-TOF-MS spectroscopy is a technique that allows characterizing samples in a semi-quantitative manner, mainly due to the fact that the mechanism of ionization is not completely known in the literature. However it presents the advantage of analyzing intact polymer/oligomer molecules, avoiding fragmentation reactions. The ionization reaction is considered a soft reaction process, and the polymer/oligomer sample/MATRIX are normally not affected by the solution and preparation methods. It has advantages such as considerably high sensitivity, and is also an ideal technique to evaluate properties like polydispersion, data of the repeat units, impurities, and additives in synthetic polymers, still, MALDI-TOF-MS spectroscopy can be applied to a broad range of polar and non-polar polymers with larger extensions of molecular masses [83-87].

In the past, before the development of the ionization sources for mass spectroscopy, not many characterization techniques were available to study mass distribution in polymer samples. At that time, mainly secondary ion mass spectrometry (SIMS) and field desorption (FD) could provide information regarding mass distribution properties, nevertheless, with considerable limitations. The samples had to be soluble and should had the maximum molecular masses near to  $1 \times 10^4$  Da.mol<sup>-1</sup> [88]. In other hand, NMR spectroscopy and chromatography techniques can

provide information regarding molecular structures and molecular sizes, but the chain sizes distribution cannot be fully understood with these methods, predominantly for polymer samples with a large range of mass distribution [89].

The distribution of the polymer chains that compose the photoresists was studied. Figure 39 shows the MALDI-TOF-MS spectra for the EPR photoresists.

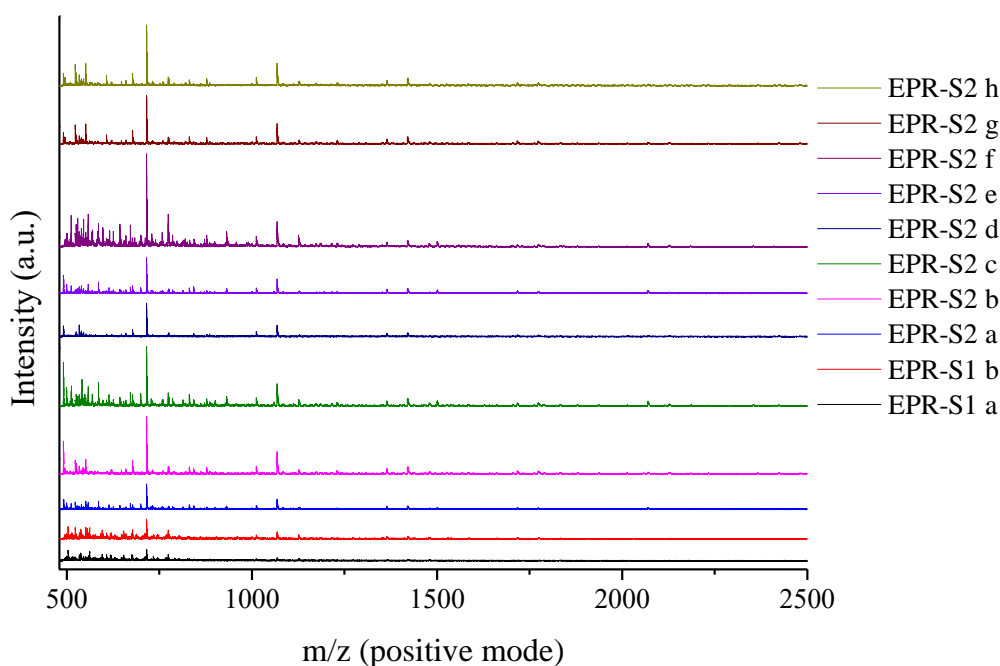


**Figure 39:** MALDI-TOF of EPR-S1 and EPR-S2 photoresists. Reproduced from Vnieska et al (2018) [4] (CC BY)

The majority of the polymer chains in the EPR photoresists are composed by distributions of dimers (region of 715 Da) and trimers (region of 1067 Da). Consequently the polymers are in fact named as oligomers. Although the major compounds in the photoresist samples are the same, distinct profiles of distribution sizes were observed. For example, sample EPR-S2-f presented a variety of mass peaks that were not present in other samples of this evaluation. Such variances can be correlated with the polymerization synthesis parameters. Observing the region spectra of low-mass (Figure 40, between 500 and 800 Da), samples can be classified into groups: the samples EPR-S2-c and EPR-s2-f; samples EPR-S2-a, EPR-S2-b and EPR-S2-e; samples EPR-S2-g, and EPR-S2-h; the sample EPR-S2-d; and finally, the EPR-S1 series (not presented in Figure 40). Samples EPR-S2-c and EPR-S2-f presented a variance of mass peaks in the low-mass region spectra, which indicates a high polydispersity or/and high amount of secondary products from the polymerization synthesis.

Samples EPR-S2-a, EPR-S2-b and EPR-S2-e were composed mostly of dimers and trimers of approximately same size, and with secondary products from the monomer. A similar distribution profile was found for the samples EPR-S2-g, and EPR-S2-h, however, with less amount of secondary products from the monomer. The compositions of sample EPR-S2-d and the EPR-S1 series consist mostly of dimer molecules, presenting secondary products in the spectra region related to the monomer. These differences in molecular size distribution might result directly in different physical-chemical properties.

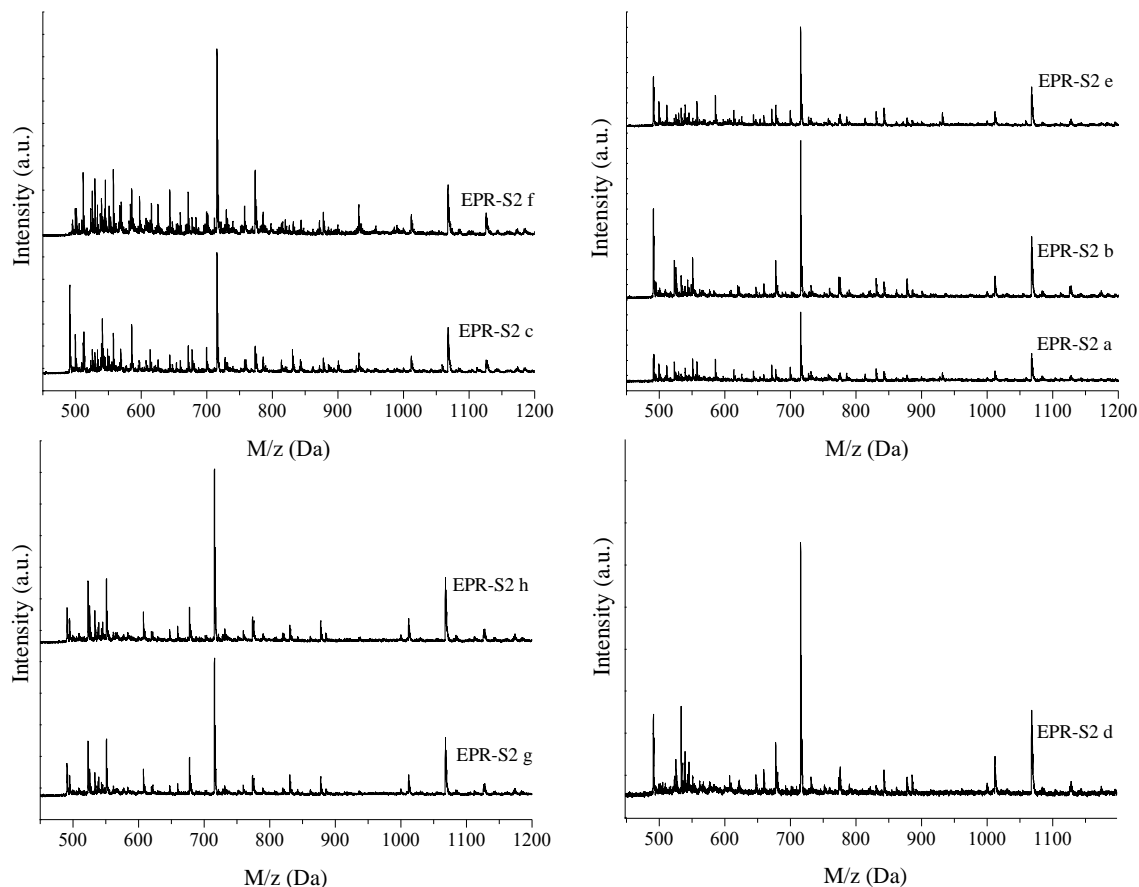


**Figure 40:** Region of 450–1200 Da in the MALDI-TOF of EPR-S1 and EPR-S2 photoresists. Reproduced from Vlnieska et al (2018) [4] (CC BY)

In Figures 40 and 41 it is possible to notice a range of peaks in the spectra that indicates different structures for the oligomers, most probably related to the variations in the epoxy groups of the molecules. Considering the non-totally epoxidized molecules, the theoretical possible structures for each oligomer are as follows: monomer two possible peaks; dimer four possible peaks (Figure 41 using the dimer as an example); trimer six possible peaks; tetramer eight possible peaks; pentamer ten possible peaks; and hexamer twelve possible peaks.

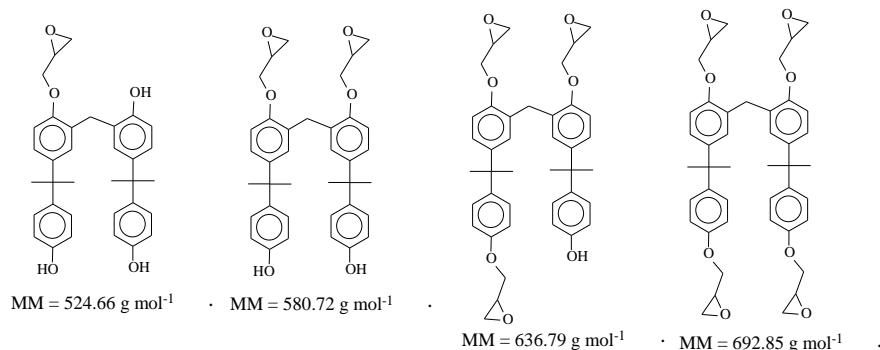


**Figure 41:** Mass variation in function of the substitution epoxidation rate for the dimer molecular structure. Reproduced from Vlnieska et al (2018) [4] (CC BY)

The examples in Figure 41 do not consider secondary products possibly generated during polymerization and epoxidation reaction steps. Taking in account the substitution epoxidation rate, the molar mass can vary roughly in 30%. Table 5 presents the theoretical possible masses of the oligomer's size.

**Table 5:** Oligomer size mass peaks compared with the substitution epoxidation rate.

Oligomer	ED0	ED1	ED2	ED3	ED4	ED5	ED6	ED7	ED8	ED9	ED10	ED11	ED12
Monomer	228.29	284.36	340.32	-	-	-	-	-	-	-	-	-	-
Dimer	468.59	524.66	580.72	636.79	692.85	-	-	-	-	-	-	-	-
Trimer	708.89	764.96	821.02	877.09	933.15	989.22	1045.28	-	-	-	-	-	-
Tetramer	949.20	1005.26	1061.32	1117.39	1173.45	1229.52	1285.58	1341.65	1397.71	-	-	-	-
Pentamer	1213.49	1343.62	1269.55	1399.68	1325.62	1455.75	1381.68	1511.81	1437.74	1567.87	1493.81	-	-
Hexamer	1429.80	1485.86	1541.93	1597.99	1654.06	1710.12	1766.19	1822.25	1878.31	1937.38	1988.43	2046.51	2102.57

ED = Substitution epoxidation rate, named here as epoxidation degree (see Figure 40 as example); Mass peaks unit = Daltons.

Reproduced from Vnieska et al (2018) [4] (CC BY)

MALDI-TOF has the advantage of avoiding analyte fragmentation if a light-absorbing compound is used as matrix. Consequently, only intact molecules are observed in the mass spectra. However, in order to achieve a better understanding of the mass spectra, it is necessary to take into account the matrix compound and its influence during the ionization process. Usually the matrix compound interacts with sample, leading to the generation of adducts and changing the expected Dalton values for each peak in the spectra [83, 88-92]. In this study, DHB and sodium chloride were used as matrices. The possible adduct masses for the monomer are presented in Figure 42 as example of the matrix interaction with the studied samples. Adduct formation can occur through all oligomers present in the samples. In consequence, one can expect in the mass spectra three distinct mass peaks for the same molecular structure (pure oligomer, sodium adduct, and DHB adduct). Due to the random ionization process, eventually not all mass values will be observed. Table 6 presents the mass peaks correlated with the oligomer sizes, epoxidation rate and adduct interaction. Although DHB adducts do not typically occur [87-91], the masses for these adducts were also calculated.

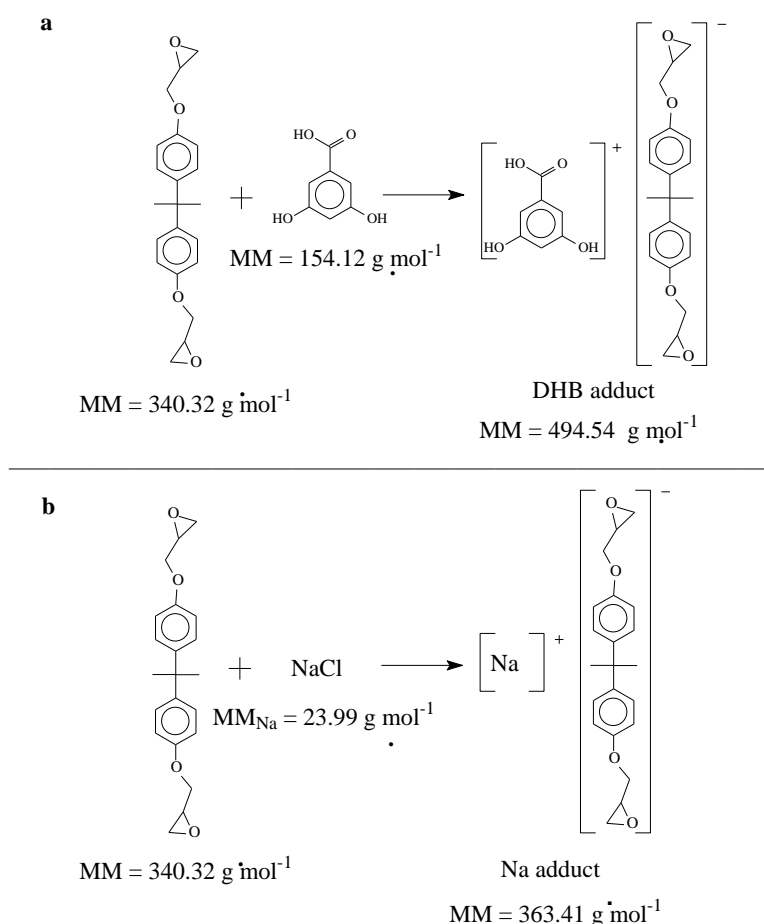


**Figure 42:** Aryl-epoxy resin monomer and its adducts. (a) Dihydroxybenzoic acid (DHB) adduct, (b) Sodium adduct. Reproduced from Vnieska et al (2018) [4] (CC BY)

**Table 6:** Mass peaks related to oligomer sizes, epoxidation rate and type of adduct.

Epoxidation degree	ED0		ED1		ED2		ED3		ED4		ED5		ED6	
	aNa	aDHB												
Oligomer														
Monomer	251.28	382.41	307.35	438.48	363.31	494.44	-	-	-	-	-	-	-	-
Dimer	491.58	622.71	547.65	678.78	603.71	734.84	659.78	790.91	715.84	846.97	-	-	-	-
Trimer	731.88	863.01	787.95	919.08	844.01	975.14	900.08	1031.21	956.14	1087.27	1012.21	1143.34	1068.27	1199.4
Tetramer	972.19	1103.32	1028.25	1159.38	1084.31	1215.44	1140.38	1271.51	1196.44	1327.57	1252.51	1383.64	1308.57	1439.7
Pentamer	1212.49	1343.62	1268.55	1399.68	1324.62	1455.75	1380.68	1511.81	1436.74	1567.87	1492.81	1623.94	1548.87	1680
Hexamer	1452.79	1583.92	1508.85	1639.98	1564.92	1696.05	1620.98	1752.11	1677.05	1808.18	1733.11	1864.24	1789.18	1920.31
Epoxidation degree	ED7		ED8		ED9		ED10		ED11		ED12			
	aNa	aDHB												
Oligomer														
Tetramer	1364.64	1495.77	1420.7	1551.83	-	-	-	-	-	-	-	-		
Pentamer	1604.94	1736.07	1661	1792.13	1717.07	1848.2	1773.13	1904.26	-	-	-	-		
Hexamer	1845.24	1976.37	1901.3	2032.43	1960.37	2091.5	2011.42	2142.55	2069.5	2200.63	2125.56	2256.69		

Mass peaks unit = Daltons; aNa = Mass peaks values of sodium adducts; aDHB = Mass peaks values of dihydroxybenzoic acid adducts. Reproduced from Vnieska et al (2018) [4] (CC BY)

With the correlation of tables Table 5 and Table 6 it was possible to characterize the main oligomer fractions within the photoresists composition. The peaks with higher intensity in the regions for each oligomer are 491 (sodium adduct, dimer ED0), 533 (dimer derivate, not present in tables 5 and 6), 715 (sodium adduct, dimer ED4), 1067 (sodium derivate, trimer ED6), 1364 (sodium adduct, tetramer ED7), and 1419 (sodium adduct, tetramer ED8) Da. As reported in the literature, mostly of the spectra peaks were correlated with sodium adducts. Oligomer

derivate were studied and discussed in chapter 5. In Figure 43, the mentioned mass peaks and its oligomer structures are depicted.

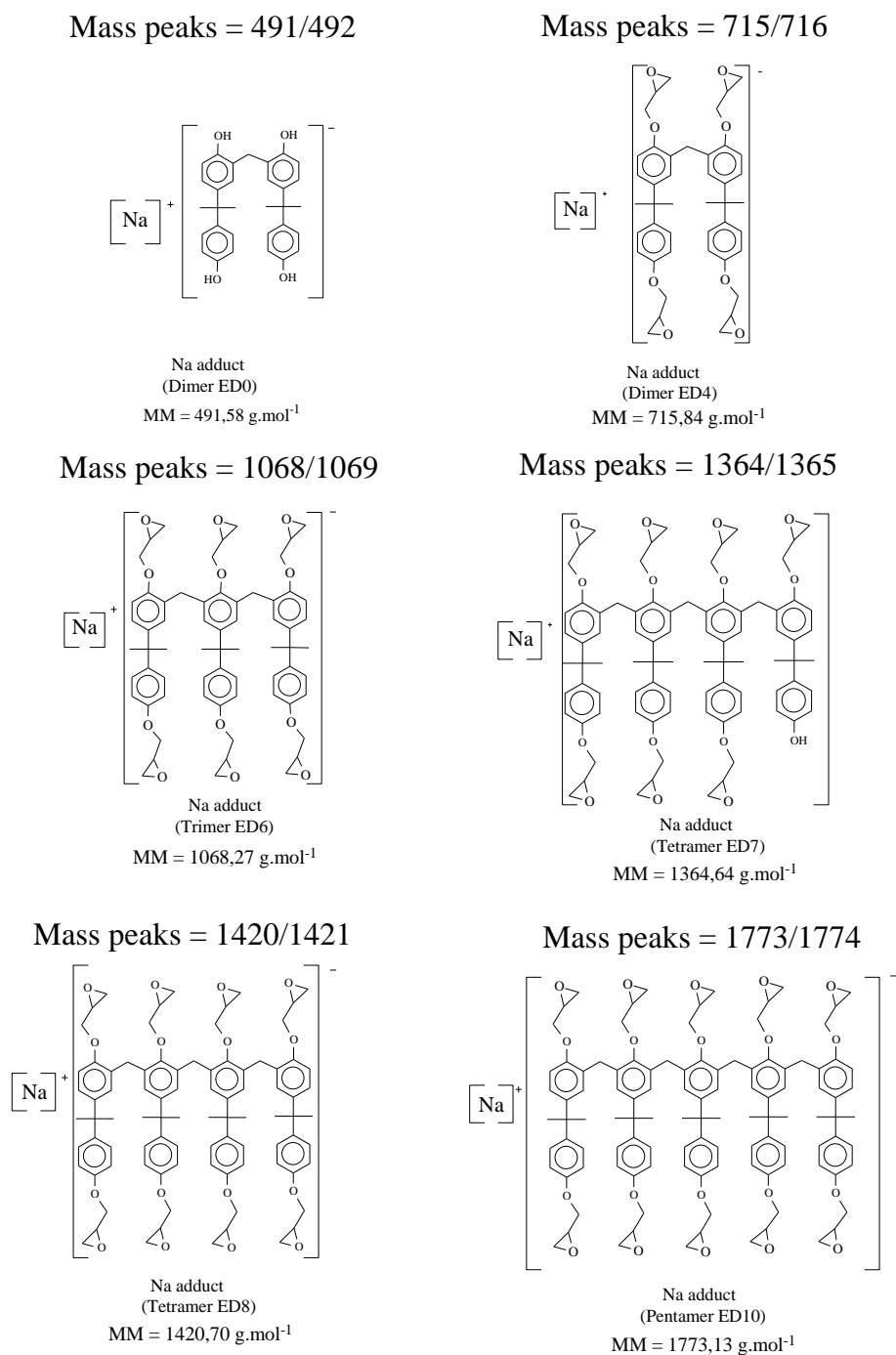


**Figure 43:** Oligomer structures related to the mass peaks in the MALDI-TOF spectra. Reproduced from Vlnieska et al (2018) [4] (CC BY)

One can notice in the spectra (Figures Figure 39 and Figure 40) high concentration of the dimer ED4 (715/716 Da) in the whole set of evaluated samples. Part of the samples presented dimer ED0 (491/492 Da). Since this oligomer does not present epoxy groups in its composition, it can be interpreted as a contaminant in the aryl epoxy resins. Relative high concentrations of trimer ED6 were found in all studied samples, traces of tetramers ED7 and ED8 were also present in all samples. Interestingly, samples EPR-S2-c and EPR-S2-f presented a broad range of secondary product traces (oligomers not entirely epoxidized) from 500 to 1000 Da, which is a significant characteristic

to be observed in the samples composition. The spectra depict in Figures Figure 44 and Figure 45 were studied and the assigned peaks to epoxidized and non epoxidized oligomers were compared. This comparison was made individually for each repeat unit mass range.

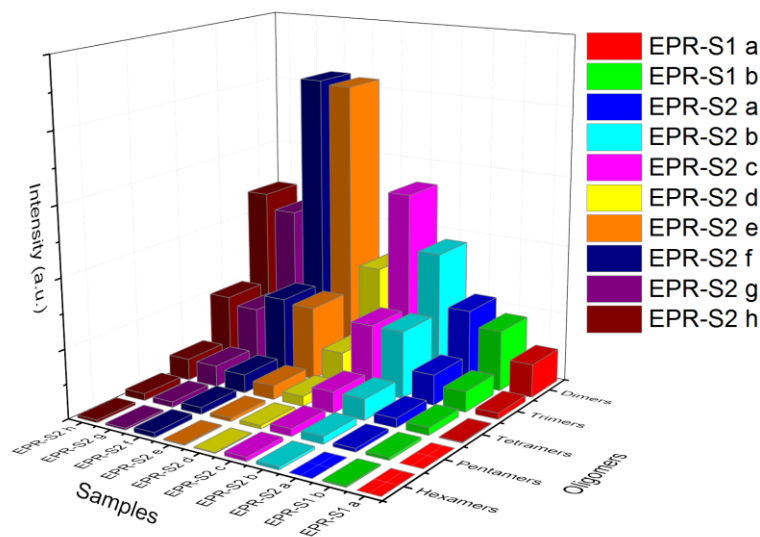


**Figure 44:** EPR-S1 and EPR-S2 series and its epoxidized oligomer compositions. Reproduced from Vnieska et al (2018) [4] (CC BY)

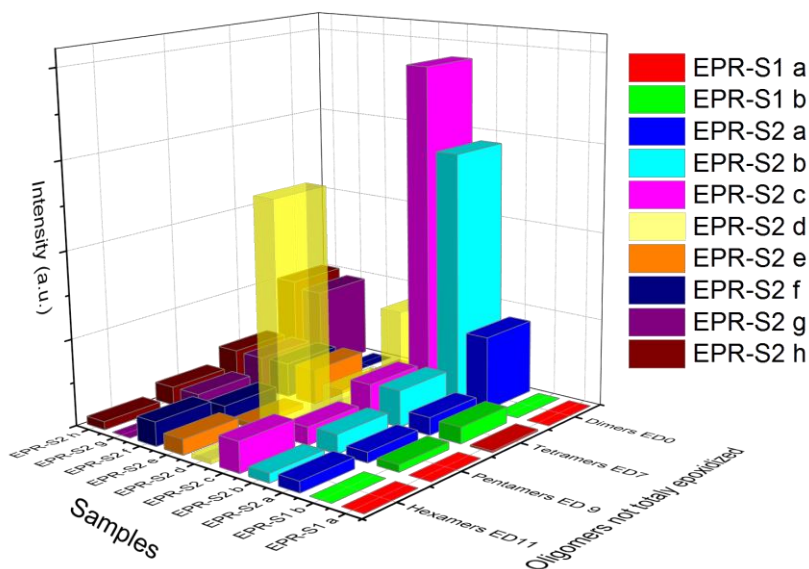


**Figure 45:** EPR-S1 and EPR-S2 series and their non-totally epoxidized oligomer compositions. Reproduced from Vnieska et al (2018) [4] (CC BY)

The samples presented distinct oligomer composition profiles mainly in the assigned range of spectra for dimers and trimers (Figure 44) and in the assigned range of spectra for the non-totally epoxidized dimers (dimers ED0, Figure 45) (e.g., EPR-S2-b and EPR-S2-c were the most relatively concentrated regarding dimers ED0; sample

EPR-S2-c presented almost four times higher concentration when compared with other samples). Samples of EPR-S1 series presented small amounts of dimer ED0. It is interesting to notice the relative high concentration of the dimers ED0 in the samples, which is comparable with the epoxidized oligomers.

## 4.5 Conclusion

In this chapter, negative photoresists based on epoxy resins and applied in deep X-ray lithography were studied. FTIR spectra confirmed the organic groups and molecular structures of the compounds in the photoresists, which seems to be in accordance with the literature (section 1.3). However, between the series EPR-S1 and EPR-S2, a slight difference in the region of the carbonyl groups was observed, which could indicate the presence of esters, or carboxylic acids in the structures. Regarding the structure of the oligomers, it was found a distinct characteristic; the phenolic positions are not totally epoxidized. The samples EPR-S2-b, EPR-S2-d, and EPR-S2-e presented relatively high content of phenolic groups, which strongly indicates the non-completely alkylation of the oligomers.

The solvent content was evaluated through TGA. The maximum difference between the samples was 5.5 % of mass loss. The photoresists evaluated seem to have a distinct polymeric profile, leading to the investigation of the polymer composition of the photoresists through mass spectroscopy.

The polymers that compose the photoresists were characterized using MALDI-TOF-MS. They are, in reality, oligomers with a low molar mass range, from 250 to 1750 Da. Were found significant differences regarding epoxidation degree (as it was indicated by FTIR) and the polydispersion of the oligomers. There is no information in the literature about the epoxidation variation content for photoresists used in DRXL. Since the epoxidation degree is a crucial property to determine the photosensitivity of the photoresist. These chemical characterization findings indicate the importance of the epoxydation degree to efficiently tune photoresists formulation. The same photoresists (with different lots of fabrication) presented different properties.

# 5 SYNTHESIS AND CHARACTERIZATION OF EPOXY RESINS <sup>1</sup>

As observed in chapter four, photoresists (from the same brand, developed for the same application and diverging only in fabrication batches) can present significant variations in the chemical composition. The most important chemical in the photoresist composition is the polymer structure. Regarding the evaluated photoresists, it became clear that the distribution of the oligomeric chains and the epoxidation degree are essential parameters to be controlled.

In this chapter, the polymerization and alkylation reactions of the resins that compose the photoresist were studied and optimized. The resins are polymerization products from bisphenol-A, and the epoxy groups were alkylated using epichlorohydrin. Deep-level of properties (see section 1.3) was applied to optimize the polymerization reaction from bisphenol-A. The forward reaction, known as the epoxidation (alkylation of the phenolic groups in the oligomer chains), is mainly responsible for providing the curing effect (together with a photoinitiator), which is a crosslinking reaction during the exposure step in lithographic techniques. The combination of all these factors, the polymerization, epoxidation, formulation with at least a photoinitiator and a solvent, generates a photoresist with unique physico-chemical characteristics.

## 5.1 Polymerization reaction

Figure 46 depicts the mass polymerization reaction performed using bisphenol-A as monomer. The achieved polymerization products were, in most of the cases, oligomeric mixtures with chain sizes varying from 1 to 5 repeat units. (see section method 3.1). The mass polymerization reaction was optimized applying factorial planning technique. By varying the polymerization reaction parameters (such as temperature, pressure, molar ratio between reagents and reaction time) was possible to control and to tune the chain sizes, as well as its distribution, and to make a prediction regarding the amount of the secondary and tertiary products generated from it [93, 94]. Depending on the monomer and reagents of the polymerization reaction, it can be difficult to control, resulting in a wide range of possible products.

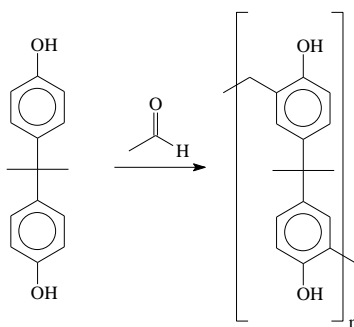


**Figure 46:** Mass polymerization of bisphenol-A and formaldehyde

1. This chapter is based on the publication: Vlnieska, V., Mikhaylov, A., Zakharova, M., Blasco, E., Kunka, D., *Epoxy Resins for Negative Tone Photoresists*. *Polymers*, 2019. **11**(9)

This mass polymerization can be carried out in a basic or acidic medium, the basic medium was the selected one to perform the reaction. The proposed bisphenol-A polymerization mechanism is presented in Figure 47.

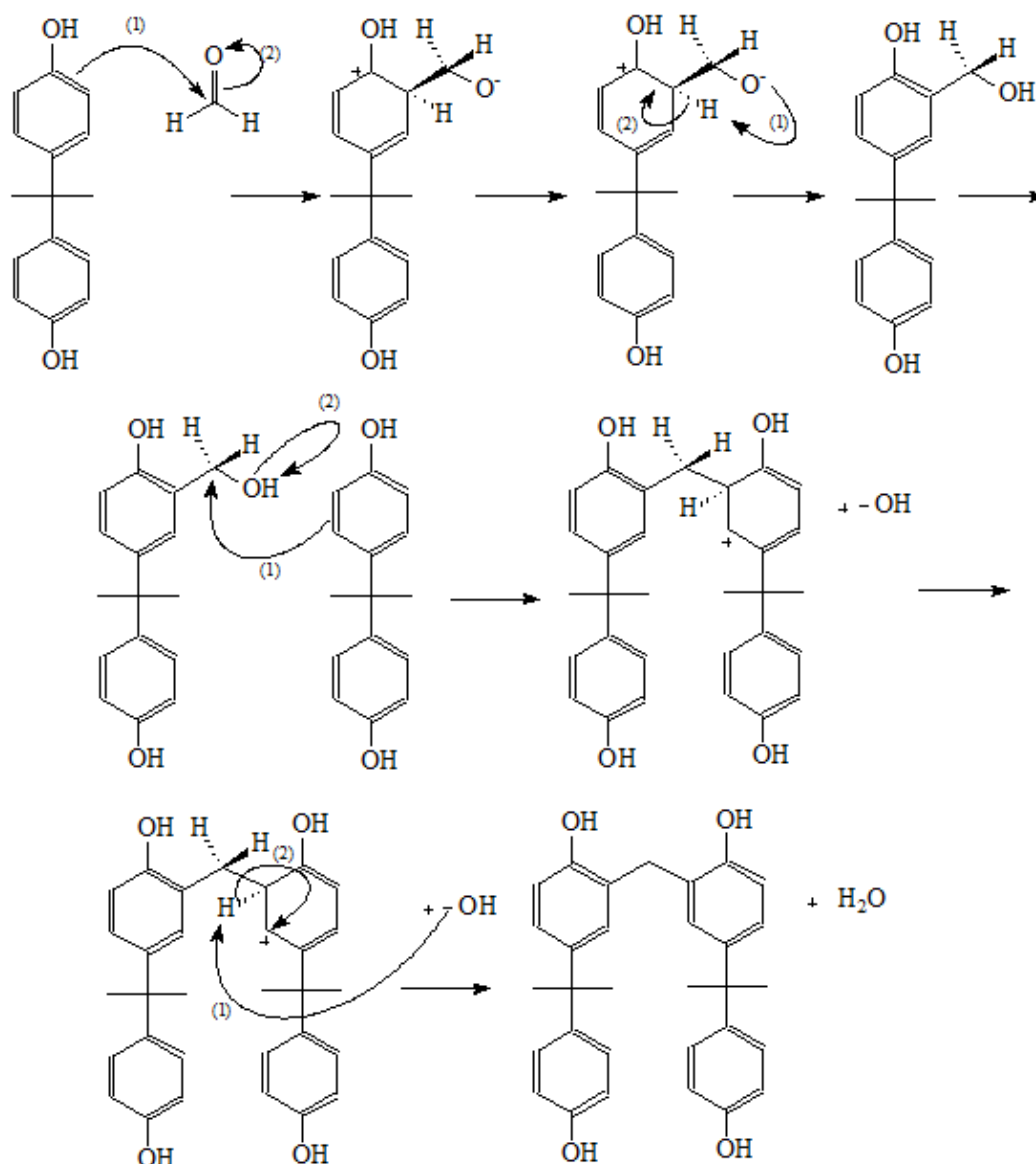


**Figure 47:** Proposed mechanism for the bisphenol-A polymerization in basic medium

In Figure 47, the bisphenol-A methylation occurs through electrophilic aromatic substitution mechanism. The temperature increment in the reaction medium increases the reactivity of the aromatic electrons in the bisphenol-A molecule. Acting as nucleophiles, the aromatic electrons react with formaldehyde (methylation reaction). Afterwards a second bisphenol-A molecule reacts in the methylated carbon, creating a carbon bridge between two bisphenol-A molecules. In the section method 3.1 one can see the studied correlation between the reaction parameters for the methylation reaction.

Afterwards, the products of each reaction batch (with distinct reaction parameters) were characterized using ESI- $\mu$ -TOF-MS spectroscopy. The samples were initially evaluated in terms of the oligomer size, primary, and derivate of the primary products, following the similar methodology previously described in chapter 4. At the end of the

characterization (all reaction batches in Table 2, made in triplicates), three products were carefully studied, named as R1, R2, and R3, which the ESI- $\mu$ -TOF-MS spectra is presented in Figure 48 (see also section method 3.8).

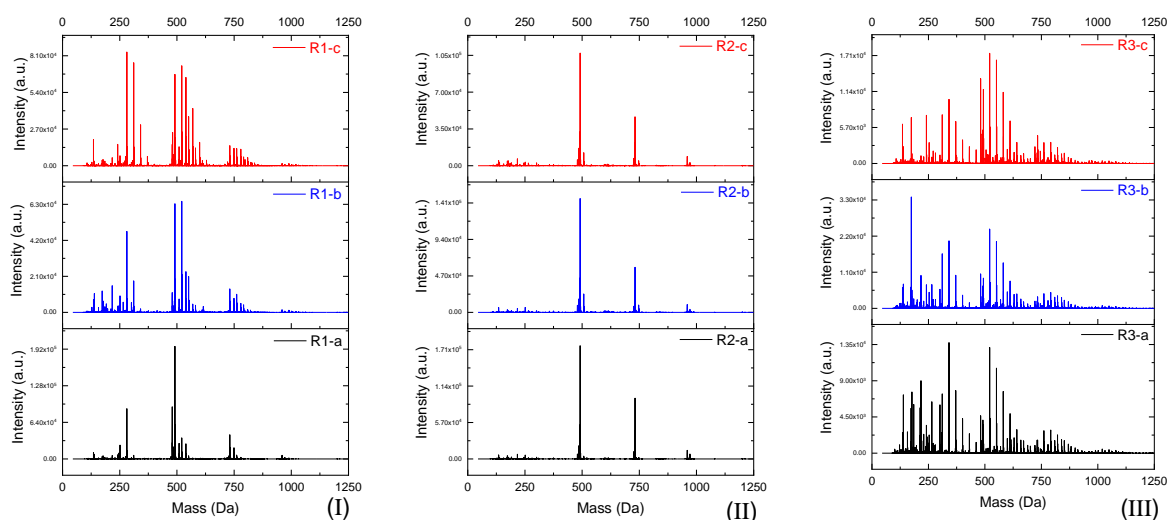


**Figure 48:** ESI- $\mu$ -TOF-MS spectra of the polymerization reactions R1, R2 and R3. Reproduced from Vnieska et al (2019) [75] (CC BY)

Spectra in Figure 48 present a distinct oligomeric distribution profile for each reaction batch (R1, R2 and R3). Reaction R1 presented a mixture of monomers, dimers, and traces of trimers, with significant amount of derivate products (methoxyl radicals). Reaction R2 presented a clean oligomeric distribution profile, mainly composed of dimers and low concentration of trimers. Reaction R3 presented the highest oligomeric distribution profile (polydispersity), with presence of secondary products in all oligomers, which were previously identified as monomers, dimers, trimers, and traces of tetramers.

By the control of the mass polymerization reaction parameters it was possible to obtain oligomeric mixtures containing low amounts of derivate products (R2) and oligomeric mixtures with high amounts and broad mass distribution profile of derivate products (R2 and R3). Since the mass polymerization reaction seems to regularly generates derivate products, the possibility to achieve a “pure” oligomeric distribution profile appears to be out of reality. In regarding this subject, it is useful to define what it should be considered as a “pure” oligomeric distribution profile, and what a derivate product is. For instance, the mer that has no other ramification besides the methylene bound connecting the monomers can be considered the “pure” oligomer; any other structures are then derivate products, which are variations in the end and in the reactive positions of the oligomer chains. Figure 49 depicts a simplified approach for the molecular structures of the derivate products, using the monomer structure as an oligomeric chain. This assumption does not consider methylation reactions in all positions of the aryl ring and in the phenolic position, as well as it presents the relative reactivity of each derivate product.

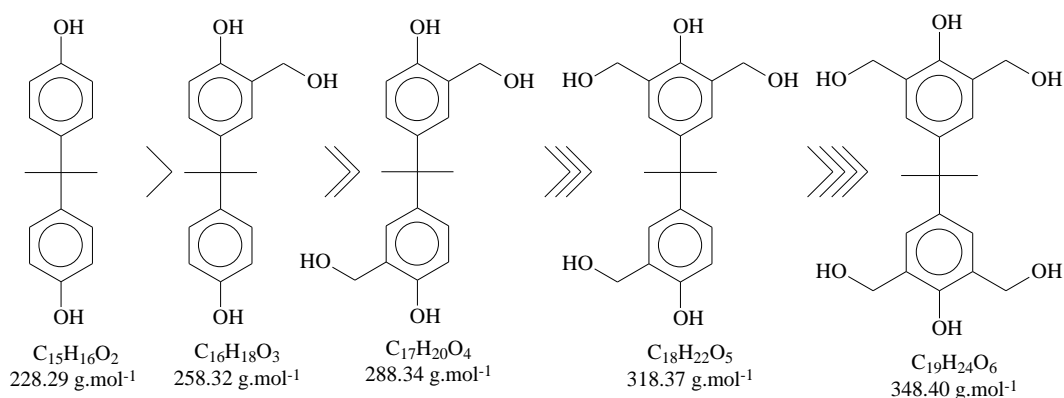


**Figure 49:** Mass polymerization derivate products, considering the monomer as chain size example. Reproduced from Vlnieska et al (2019) [75] (CC BY)

In Figure 49, one can notice in the monomer structure (bisphenol-A) that only the ortho positions of the aromatic ring (the most reactive ones) were considered as substitution positions for the methylation. Consequently, for each monomer unit, it is possible to achieve until four methylation substitutions. When one of the methylation substitution is performed, the reactivity of the aromatic ring tends to decrease once the substitution group is a moderate deactivator for the ring [93]. This approach can be applicable to all chains of the oligomeric products, generating a wide range of derivate possibilities. The longer the oligomeric chain size, the higher the probabilities to obtain derivate products. The likelihood to have slight changes in the substitution group structures might be also significant to appraise. Figure 50 presents termination groups.

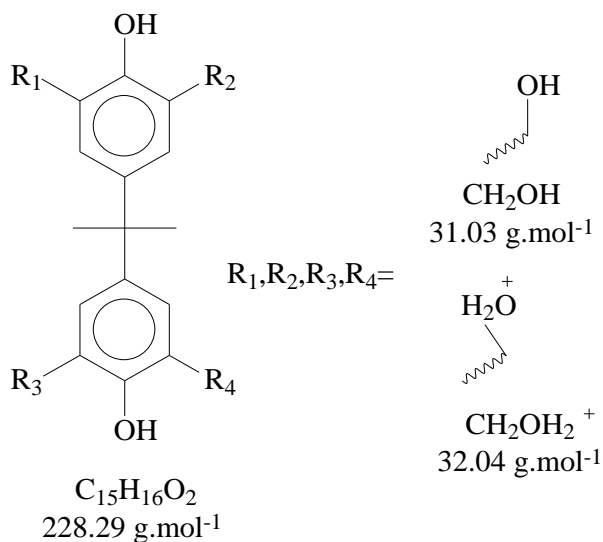


**Figure 50:** Proposed chemical structure for the termination groups. Reproduced from Vlnieska et al (2019) [75] (CC BY)

As an example, in the spectra from reaction R3-c (Figure 48 (III)), the masses of each neutral *mer* were selected (Figure 51 (a)). Afterwards, at the dimer region mass, most of the peaks for the derivate products were selected. (Figure 51, b). Sodium adducts that can be formed during the ionization step might be also considered [83, 84, 86, 88, 91].

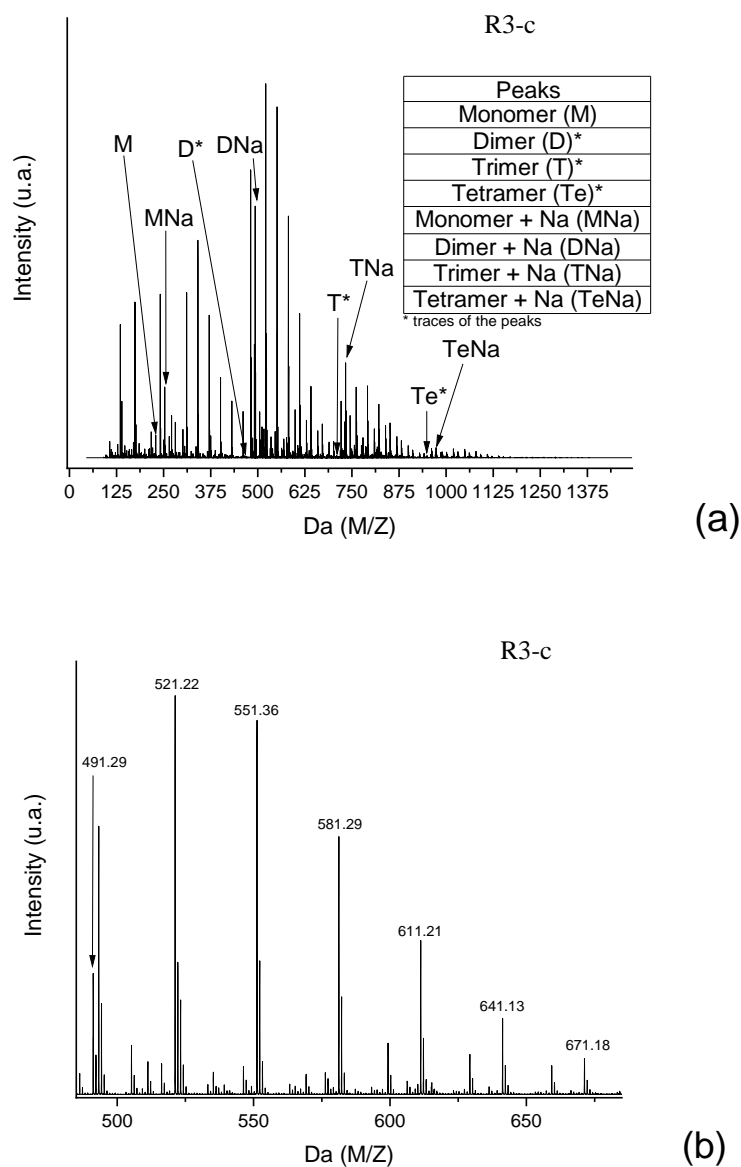


**Figure 51:** ESI- $\mu$ -TOF-MS spectra of the mass polymerization reaction R3-c. In (a), full spectra, where the neutral *mers* and sodium adducts were identified. In (b), derivate products in the dimer region. Reproduced from Vlnieska et al (2019) [75] (CC BY)

In Figure 51 (a), one can see the high intensity of the sodium adduct peaks in all spectra regions of the *mers*. During mass polymerization reaction, the addition of formaldehyde molecules is randomly distributed in the ortho positions of the aryl ring, generating derivate products with intervals of 30 Da approximately. Figure 52 depicts the derivate product structures in the dimer region and with sodium adduct formation.

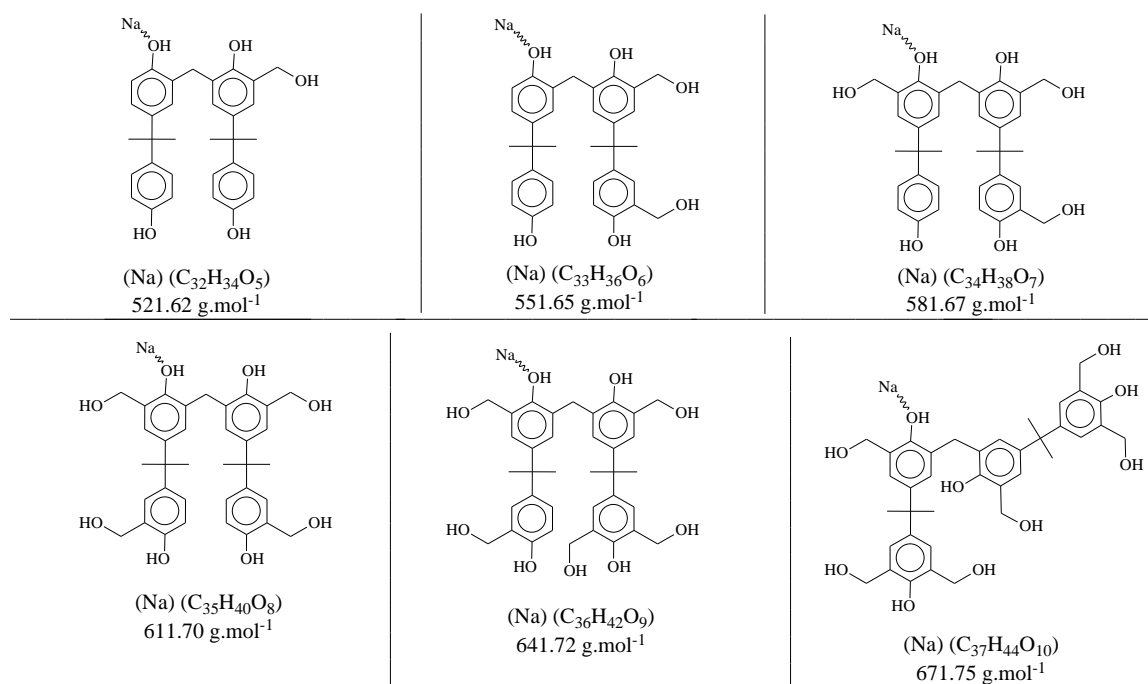


**Figure 52:** Sodium adducts from derivate products in the dimer region spectra (mass peak measures from sample R3-c). Reproduced from Vlnieska et al (2019) [75] (CC BY)

The reactivity of the derivate products seem to be reasonable with the proposal made in Figure 49, in the mass spectra, all derivate products for all *mers* and all samples followed the same pattern regarding relative intensity. The most intense peaks were assign for the derivate product with one methoxyl group as ramification. Other mass peaks also follow this reactivity (Figure 51 (b) as an example).

The investigation of the derivate product reactivity was realized for the other *mer* spectra regions as well. Table 7 presents derivate products for each *mer* of the oligomeric resins. From table 7, one can see that the derivate products are mainly present in samples R1 and R3. Sodium adducts were considered to be generated with 1 until 6 sodium atoms.

**Table 7:** Characterization of the *mers* and derivate products for R1, R2, and R3, based on the spectra presented in Figure 42 I (b), II (b), and III (b).

Polymer	<i>Mer</i>	Adduct/radical <sup>a</sup>	Mass (Da) <sup>b</sup>	Relative Intensity <sup>c,e</sup> (monomer level)	Relative intensity <sup>d,e</sup> (dispersion level)	
R1	Monomer	Adduct	-	-	-	
		1Na	250.99	*	**	
		Sec. Product	-	-		-
		1Na/rad	280.88	***		
		1Na/2rad	311.02	***		
		1Na/3rad	341.14	**		
	1Na/4rad	375.17	Trace			
	Dimer	Adduct	-	-	-	***
		1Na	491.22	***		
		3Na	537.48	***		
		Sec. Products	-	-	-	
		1Na/1rad	521.40	***		
		1Na/2rad	551.44	**		
		3Na/1rad	568.97	***		
		1Na/3rad	581.26	*		
	3Na/2rad	598.99	**			
	Trimer	Adduct	-	-	-	*
		1Na	731.31	***		
2Na		749.67	***			
4Na		797.49	**			
6Na		839.41	*			

		Sec. Product	-	-		
		1Na/1rad.	761.02	***		
		2Na/1rad.	779.24	***		
		1Na/2rad.	791.37	**		
		2Na/2rad.	809.72	**		
		1Na/3rad. or 5Na	820.94	*		
		4Na/1rad.	827.06	*		
		1Na/4rad. or 5Na/1rad.	851.54	*		
		2Na/7rad. or 3Na/6rad	959.07	*		
		1Na/8rad.	971.19	*		
		4Na/6rad.	989.89	*		
		5Na/6rad.	1001.11	*		
		6Na/6rad.	1019.80	*		
R2	Monomer	Adduct	-	-	*	
		1Na	251.13	*	*	
	Dimer	Adduct	-	-	***	
		1Na	491.21	***	***	
	Trimer	Sec. Product	-	-	*	
		Adduct	-	-	*	
		1Na	731.39	***	**	
		2Na	747.36	*	**	
		Sec. Product	-	-	*	
		2Na/7rad. or 3Na/6rad.	959.44	*	*	
	R3	Monomer	5Na/5rad.	972.45	*	*
			Adduct	-	-	*
1Na			253.62	*	**	
Sec. Product			-	-	**	
Dimer		1Na/2rad.	312.15	***	**	
		1Na/3rad.	341.41	***	**	
		1Na/4rad.	370.68	***	**	
		Adduct	-	-	***	
		Sec. Product	-	-	***	
		1Na/1rad.	521.22	***	***	
		1Na/2rad.	551.36	***	***	
		1Na/3rad.	581.29	***	***	
Trimer	1Na/4rad.	611.21	**	***		
	1Na/5rad.	641.13	**	***		
	1Na/6rad.	671.18	*	***		
	3Na/6rad.	721.49	**	***		
	4Na/6rad.	733.02	***	***		
	Adduct	-	-	***		
	1Na	733.02	***	**		
	5Na	821.68	**	**		
	Sec. Product	-	-	*		
	1Na/1rad.	761.42	***	**		
	1Na/1rad.	791.55	***	**		
	2Na/2rad. or 3Na/1rad.	809.23	**	*		
Tetramer	1Na/3rad.	821.68	**	*		
	2Na/3rad.	839.46	**	*		
	1Na/4rad.	851.39	**	*		
	2Na/4rad. or 3Na/3rad.	869.40	*	*		
	6Na/2rad.	899.44	*	*		
	1Na/6rad.	911.43	Trace	*		
	6Na/3rad.	929.47	Trace	*		
	1Na/7rad. or 5Na/4rad.	941.36	Trace	*		
	2Na/7rad. or 6Na/4rad.	961.49	Trace	*		
	1Na/8rad.	973.30	Trace	*		
	6Na/5rad.	989.54	Trace	*		
	5Na/6rad.	1001.57	Trace	*		
6Na/6rad.	1019.57	Trace	*			
5Na/7rad.	1031.59	Trace	*			
6Na/7rad.	1049.62	Trace	*			
5Na/8rad.	1061.61	Trace	*			
6Na/8rad.	1079.61	Trace	*			
R3	Tetramer	Adduct	-	-	*	
		1Na	973.30	Trace	*	
		2Na	989.54	Trace	*	
		5Na	1061.61	Trace	*	
		Sec. Product	-	-	*	
		1Na/1rad.	1001.57	Trace	*	
		2Na/1rad.	1019.57	Trace	*	
		1Na/2rad.	1031.59	Trace	*	
		2Na/2rad. or 3 Na/1rad.	1049.62	Trace	*	
		1Na/3rad.	1061.61	Trace	*	
		6Na	1079.61	Trace	*	
		1Na/4rad.	1091.63	Trace	*	
6Na/1rad.	1109.67	Trace	*			
1Na/5rad.	1121.65	Trace	*			
6Na/2rad.	1139.37	Trace	*			

<sup>a</sup> Number of sodium atoms and radicals composing the adduct/ramified *mer*

<sup>b</sup> Dalton mass for adducts with one or more sodium atoms or derivate products with one or more sodium and/or radicals in the *mer* chain

<sup>c</sup> Relative intensity - Monomer level: Qualitative Intensity comparison within the *mer* spectra region

<sup>d</sup> Relative intensity: *mers* intensity comparison in the overall spectra

<sup>e</sup> Qualitative rating: \* - minor concentration; \*\* - approximately middle concentration; \*\*\* - predominant concentration

Reproduced from Vlnieska et al (2019) [75] (CC BY)

Although most of the mass peaks were identified with the theoretical values of the adducts and derivate products, as presented in Figure 52, some mass peak values were in between two possible structures or, in some cases, one single mass peak value can represent two distinct structures. The multiple possibilities of an assigned structure for one mass peak value can be explained with few implications that should be considered on this characterization

method. During ionization step, the masses of the molecular structures slightly change their values, in this oligomeric matrix the oligomers have several susceptible positions to be ionized (predominantly the hydroxyl groups attached to the aromatic ring). To illustrate this approach, Figure 53 depicts two situations: in (a) is an example of two structures in the same range of theoretical mass and, in (b) it represents the mass variations in the ionization step of the ESI- $\mu$ TOF-MS spectroscopy in one of the tetramers identified. This assumption is based only in the hydroxyl group ionization.

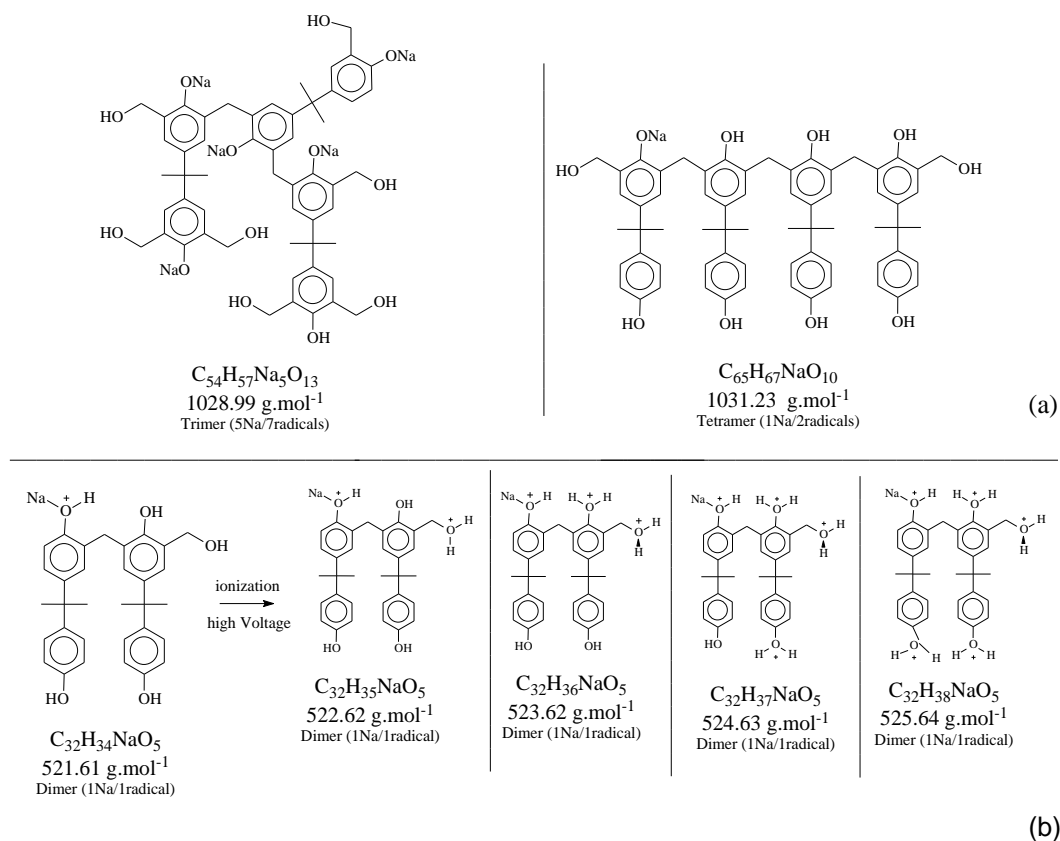


**Figure 53:** Multiple structure assignment in the ESI- $\mu$ TOF-MS characterization technique. (a) two different structures for the same range of mass. (b) ionization of the phenol groups in one of the tetramers structure. Reproduced from Vlnieska et al (2019) [75] (CC BY)

Despite the fact that sodium adducts, ionized structures, and derivate products are randomly generated (leading to a broad range of mass assignment to a single molecular structure), this characteristic helps to identify the oligomers, creating a fingerprint of the mass polymerization system. As an example, Figure 54 presents an mass peak assigned to the dimer oligomer derivate, with one sodium atom and one methoxyl radical. The mass peak variations are assigned to the ionization of the phenolic and methoxyl groups, and it was observed in all mass peaks with relative high intensity. The assignments of these mass peaks are in accordance with the number of phenolic and methoxyl groups present in the oligomer molecular structure.

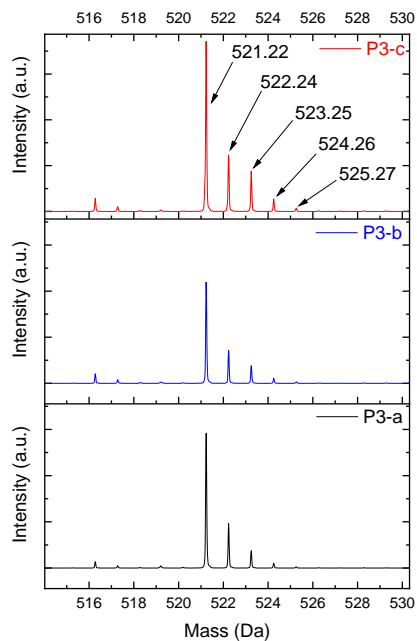


**Figure 54:** Amplification of the dimer derivate spectra (1Na/1rad.) in the region of 515 to 530 Da. Reproduced from Vlnieska et al (2019) [75] (CC BY)

Additionally, the oligomers were characterized by NMR spectroscopy. In order to better understand the derivate products Figure 55 presents the chemical structure with marked hydrogens (based on the monomer structure), and Table 8 shows the amplified NMR spectra regions and its integral values. Full NMR spectra are available in the appendix, pictures A1 to A4 (see section method 3.9).

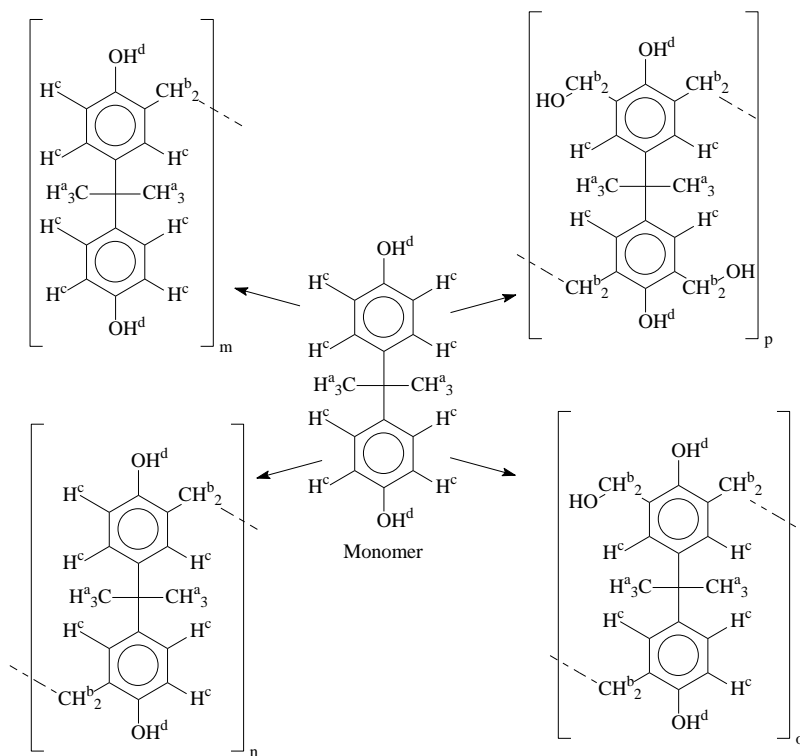
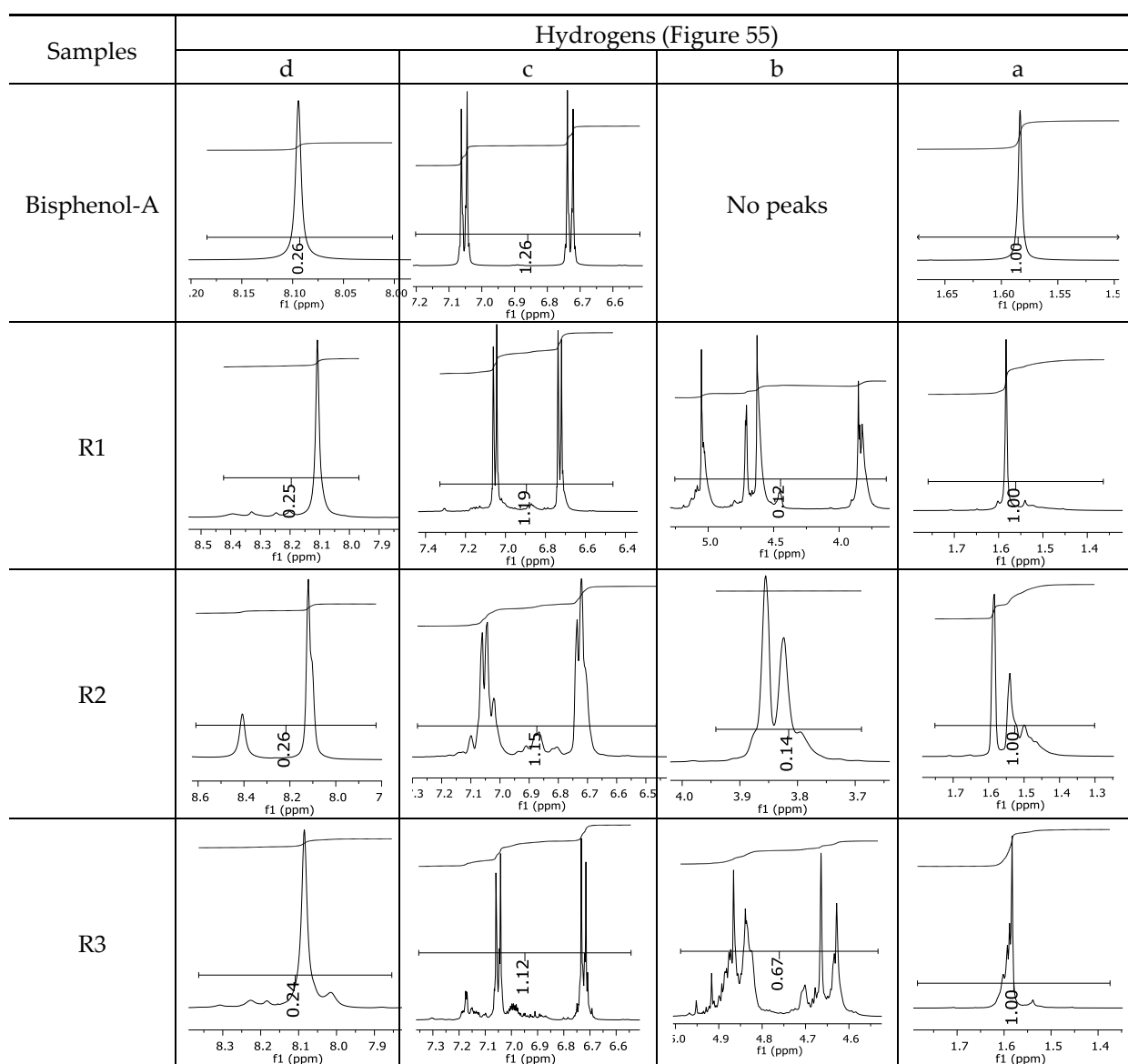


**Figure 55:** Monomer chemical structure and its derivate with labeled hydrogens. Reproduced from Vlnieska et al (2019) [75] (CC BY)

As previously discussed, the derivative are expected to be mainly at the orto positions of the aromatic ring. Derivate from meta positions as well as the ones generated in the phenolic fractions are not considered in this assumption. In NMR full spectra, one can see the singlet at 2.83 ppm and the multiplet at 2.05 ppm, which are assigned to solvent and moisture (see full spectra in appendix, Figures A1 to A4). The multiplets in the region of 6.55 – 7.05 ppm are assigned for the aromatic hydrogens (Table 8 - c). The deployment in the regions of phenolic aromatic groups (Table 8 - d) methyl groups (Table 8 - a) and phenolic groups (Table 8 - d) are due to the mass polymerization reaction and its derivate, generating asymmetry in the structure. The comparison between region “a” and “d” shows that the phenolic groups are unreacted during the mass polymerization. The methylation of the resins can be calculated as presented in equation 6, which considers the comparison between aromatic hydrogens area (8 hydrogens) and methyl hydrogens area (6 hydrogens). The bisphenol-A spectra was used as reference value.

**Table 8 :** Amplified  $^1\text{H}$ NMR spectra of the samples bisphenol-A, R1, R2, and R3.



Reproduced from Vlnieska et al (2019) [75] (CC BY)

$$s. r. = 1 - \left( \frac{c_{\text{sample}} * 2}{c_{\text{bisphenol-A}}} - 1 \right) \quad [6]$$

In equation 6 *s.r.* is the substitution ratio, and *c* is the integral value from the aromatic region (Table 8 - c). The integral of the aromatic region provides information only about the reacted amount of hydrogens, not being possible to distinguish if the product is a methylene bridge or a methyl-hydroxyl group. Table 9 presents the substitution ratio for each synthesized polymer.

**Table 9:** R1, R2 and R3 substitution ratios.

Sample	s.r. (%)
R1	11.2
R2	17.5
R3	22.3

Reproduced from Vlnieska et al (2019) [75] (CC BY)

Since the spectra region in Table 8 - b was assigned to the methylene bridges, methyl-hydroxyl groups and possible residues of unreacted p-formaldehyde (one can see it in R3 spectra, where the signal in the range of 9.5 ppm confirms traces of the p-formaldehyde), a precise assignment for each group is not achievable [95].

The substitution ratio calculation seems to be in accordance with the applied ESI- $\mu$ -TOF-MS characterization method. A substitution ratio of 25 % would be a methylene bridge/methyl-hydroxyl group for every monomer structure within the polymer chains. Considering that the oligomeric chains have “n” mostly in the range of 2 to 4, these values turn out to be a high substitution ratio, expressing a high content of derivate products for the oligomer R3, for example.

Afterwards the oligomers were evaluated by differential scanning calorimetry. Figure 56 presents the DSC curves for the samples R1, R2, and R3.

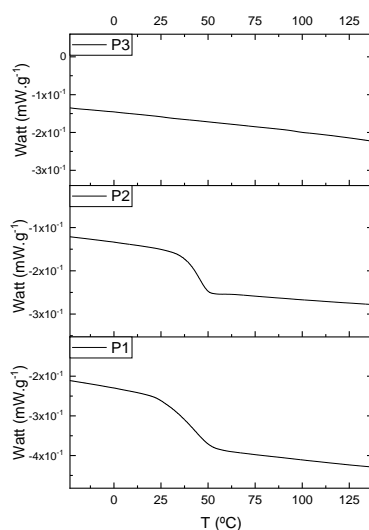


**Figure 56:** R1, R2, and R3 DSC curves. Reproduced from Vlnieska et al (2019) [75] (CC BY)

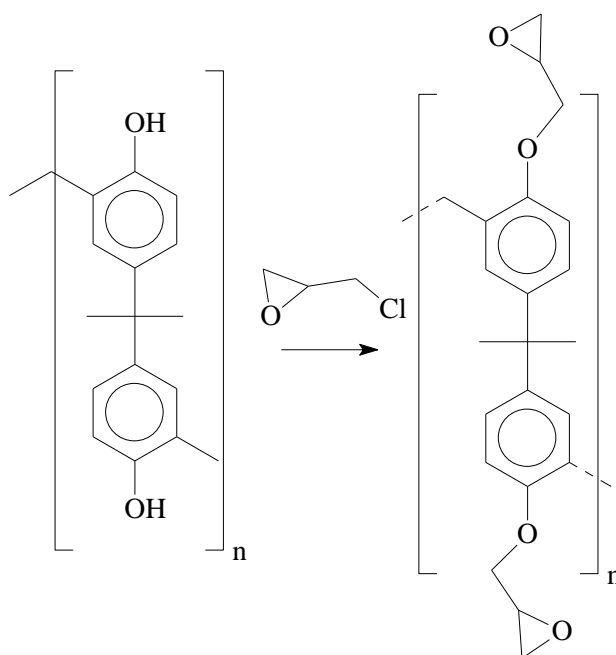
The

The comparison of the sample DSC curves indicates three distinct profiles of heating behavior. Sample R1 presented  $T_g$  (glass transition temperature) starting at  $30.7^\circ\text{C}$ , with  $0.67 \text{ J}\cdot(\text{g}\cdot^\circ\text{C})^{-1}$ . Sample R2 exhibited  $T_g$  starting at  $49.1^\circ\text{C}$ , with  $0.71 \text{ J}\cdot(\text{g}\cdot^\circ\text{C})^{-1}$ . Sample R3 presented no  $T_g$ , indicating that there is no presence of crystalline phase in this material. Regarding samples R1 and R2, the crystalline phase is more pronounced in sample R2 [96]. These results seem to indicate the following behavior: once the concentrations of derivate products increase, crystalline phases decrease. DSC supports the results of the previously performed characterization techniques. Although samples are all based in the same monomer, each oligomer matrix presented distinct profile of mass distribution, molecular sizes, and properties [97, 98].

## 5.2 Alkylation of the phenolic groups and characterization

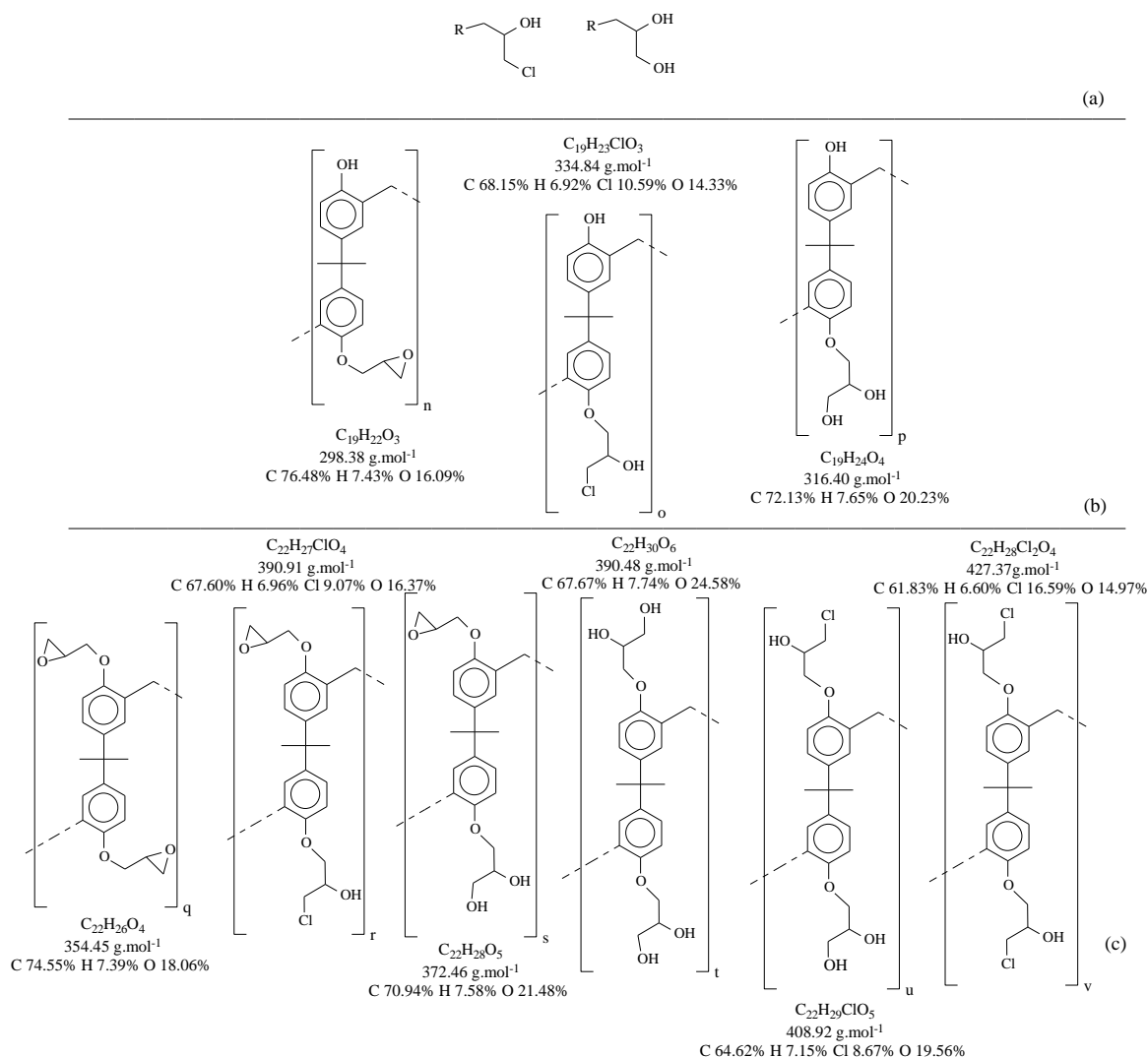
The substitution reaction of the polymer chains was carried out through the phenolic groups. The alkylation was studied in order to generate an optimized substitution yield. Figure 57 presents the reaction for this step, using epichlorohydrin as substitution agent. The alkylation reaction is the second step to obtain aryl epoxy resins, which are the main component to formulate photoresists. Epoxy groups, together with the photoinitiator from the photoresist formulation, are responsible to generate the crosslinking reaction during the irradiation step in lithographic techniques.

Alkylation using epoxy groups as the substitution agent are applied for several chemical products [93, 94], for aryl epoxy resins, the control and characterization of the this reaction is necessary because the epoxy content in conjunction with the amount of photoinitiator will result in the photoresist photosensitivity properties. All reaction and formulation steps such as mass polymerization, alkylation with epoxy groups, formulation using aryl epoxy resins, a photoinitiator and a solvent generate a photoresist with unique characteristics, resulting in a fingerprint for each batch of synthesis.



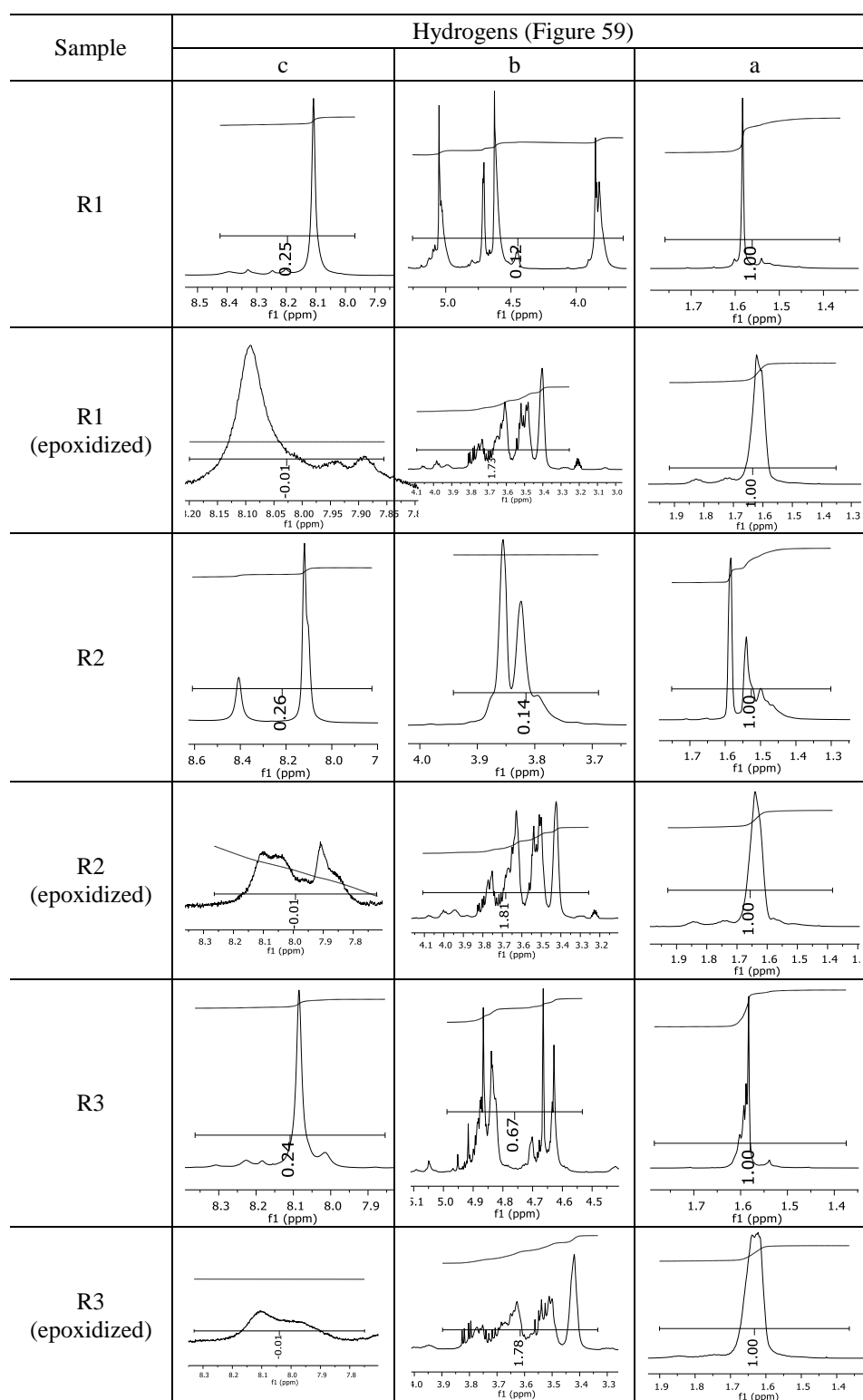
**Figure 57:** Epoxidation reaction (alkylation of the phenolic groups). Reproduced from Vlnieska et al (2019) [75] (CC BY)

Figure 58 depicts the possibilities of epoxy radicals and secondary products generated during epoxidation reaction [99], using the monomer as an example for the polymer chain. If all obtained oligomers in mass polymerization reaction and its derivate are considered, the possibilities of distinct molecular structures and masses become increasingly wide. During phenolic groups alkylation, for each structure (as an example, the ones identified in Table 7), there is a likelihood to generate at least three other derivate for each phenolic group.



**Figure 58:** Derivate from epoxidation reaction. In (a): epoxidation derivate; in (b): bisphenol-A mono-epoxy derivate; in (c): bisphenol-A di-epoxy derivate. Reproduced from Vlnieska et al (2019) [75] (CC BY)

Since epoxy groups are directly related to the photoresists photosensitivity, it is crucial to quantify the amount of epoxy and derivate groups inserted in the oligomer chains. The characterization method applied for the quantification was NMR spectroscopy. The main peaks in the spectra were evaluated before and after the reaction. The methodology to quantify the epoxy content was based in the work of Dorsey et al. (1977), Fleming (1985), and Garcia and Soares (2002) [100-102], with modifications to suit to this characterization. Table 10 presents amplified spectra regions and their integral values, comparing samples before and after the epoxidation reaction. Full spectra can be found in the appendix. Figure 59 presents the chemical structure marked with the hydrogens of interest to be studied (based on the monomer structure).

**Table 10:**  $^1\text{H}$  NMR spectra (zoom in) for the samples P1, P1-ep; P2, P2-ep, and P3; P3-ep

Reproduced from Vnieska et al (2019) [75] (CC BY)

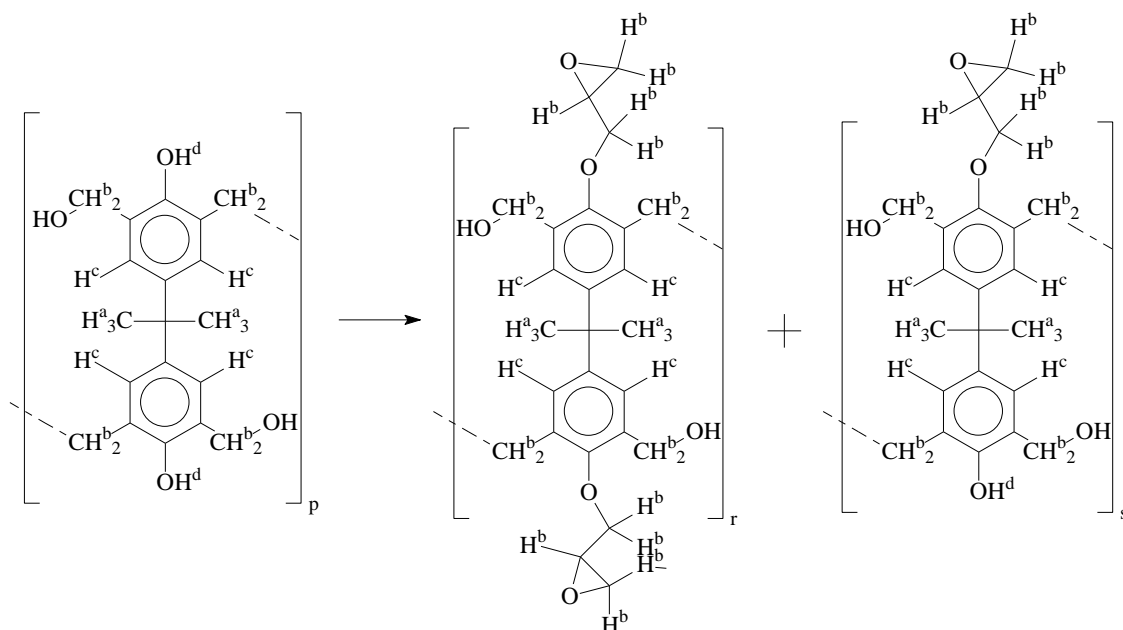


**Figure 59:** Oligomer “p”, epoxidized oligomers “r” and “s” and its chemical structures with labeled hydrogens. Reproduced from Vlnieska et al (2019) [75] (CC BY)

In Figure 59, it was considered as example the oligomer chain with two hydroxyl groups into the monomer structure and, as one of the products, a partial substitution reaction (oligomer “s”). The epoxy content could be determined by the integration between the assigned peaks to the methyl groups from the polymeric chain and the region in 3.25 to 4.25 ppm, assigned to the hydrogens from the epoxy group [79, 100-102]. However, for this kind of resin, the determination is not realistic; since the methyl hydroxyl groups from derivate products also are assigned to this ppm region, it is not possible to distinguish the signals among them. An alternative would be to use the phenolic signal before and after epoxidation reaction, taking into account that this value estimates only the reacted phenolic groups, representing the overall substitution with epoxy groups, with all derivate possibilities (see Figure 58). Table 11 presents the epoxidation ratio (e.r.) achieved for the samples R1-ep, R2-ep, and R3-ep.

**Table 11:** Epoxidation ratio for the samples R1-ep, R2-ep, and R3-ep.”

Sample	e.r. (%)
R1-ep	96.00
R2-ep	96.15
R3-ep	95.83

Reproduced from Vlnieska et al (2019) [75], (CC BY)

The amount of epoxy groups was also evaluated by carbon experiment, based on the work of Fleming (1985) [101]. The carbon spectra can help to distinguish between the epoxy and methylene groups. In this case, the presence of the derivate epoxy products (Figure 58) does not affect significantly the shifting of the signal. Figure 60 presents the chemical structures with numbered carbons for bisphenol-A, non-epoxidized and epoxidized oligomers. Table 12 presents ppm values assigned for each carbon from bisphenol-A, the oligomers, and its epoxidized products. Full spectra can be found in appendix.

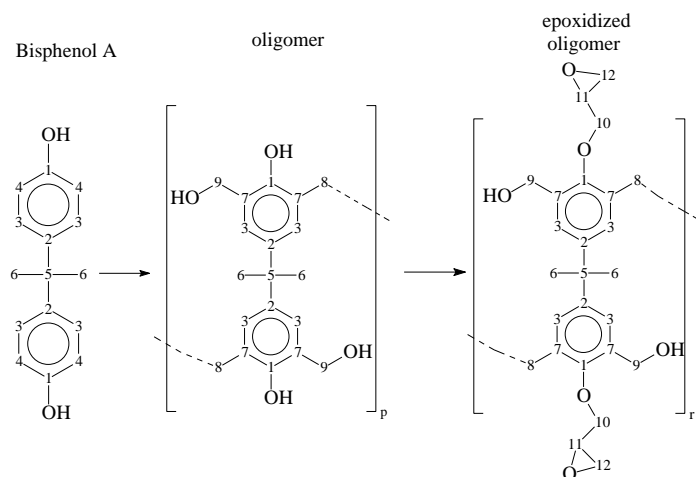


**Figure 60:** Chemical structures with numbered carbons of the bisphenol-A, oligomer, and epoxidized oligomer. Reproduced from Vlnieska et al (2019) [75] (CC BY)

**Table 12:**  $^{13}\text{C}$  NMR shift values (ppm) for the samples bisphenol-A, R1, R2, R3, R1-ep, R2-ep and R3-ep

Samples	Carbons (Figure 60)											
	1	2	3	4	5	6	7	8	9	10	11	12
Bisphenol-A	155 (1)	142 (1)	115 (1)	128 (1)	42 (1)	31 (1)	-	-	-	-	-	-
R1	156 (6)	142 (2)	115 (2)	-	42 (2)	31 (1)	128 (5)	-	-	-	-	-
R1-ep	157 (1)	143 (1)	114 (4)	-	45 (2)	27 (10)	128 (1)	27 (10)	68 (1)	71 (9)	51 (2)	46 (4)
R2	152 (3)	143 (6)	115 (2)	-	42 (1)	31 (3)	128 (10)	-	-	-	-	-
R2-ep	157 (1)	143 (1)	114 (1)	-	43 (6)	27 (9)	128 (1)	27 (9)	68 (2)	71 (12)	51 (2)	46 (4)
R3	154 (3)	142 (2)	115 (5)	-	42 (3)	31 (3)	126 (8)	-	-	-	-	-
R3-ep	-	-	114 (1)	-	44 (3)	27 (8)	128 (1)	27 (8)	68 (2)	71 (10)	51 (2)	46 (4)

Legend: AAA (B) – AAA = mean ppm value; (B) = number of deployed peaks in the ppm mean region.  
Reproduced from Vlnieska et al (2019) [75] (CC BY)

The multiplet in approximately 30 ppm is associated with the solvent, as well as the peak at 206 ppm. The peaks in 27-31 ppm represent the methyl groups and the methylene bridges (6 and 8 – Figure 60). The peaks in 41 to 51 ppm are associated with the quaternary carbon (5 – Figure 60). The region between 45 to 75 ppm – is assigned to the epoxy group carbons (10, 11, and 12 – Figure 60), except for the peak in 63, assigned for the carbon's methylene bridge (8 – Figure 60). The peaks related to the aromatic carbons are in the region near to 115 ppm (meta) and 130 ppm (ortho) (3 and 4 – Figure 60). The peak near 140 ppm is associated with the carbons from para position (2 – Figure 60). The peak near 160 ppm is related to the carbon bonded in the hydroxyl group (1 – Figure 60). Comparing the bisphenol-A and the resins R1, R2, and R3, one can see a significant asymmetry, as evidenced by the deployment of the peaks in the spectra (see Table 12 and number of deployed peaks). This is due to the polymerization reaction. The presence of epoxy carbons on the region 50 to 75 ppm, which is evident from the comparison of resins and its epoxidized products, confirms the reaction quantified by proton NMR.

The amount of epoxy groups was also compared using SEM-EDX. Table 13 presents the relative ratio of the atoms for bisphenol-A, samples R1, R2, R3 and, R1-ep, R2-ep, R3-ep. Full spectra of the samples can be found in the appendix.

**Table 13:** Relative percentage ratio of the atoms for non-epoxidized and epoxidized resins

-	Relative % of atoms			
Sample	Carbon	Oxygen	Chlorine	Silicon
R1	84.27 ( $\pm 8.0$ )	15.72 ( $\pm 2.6$ )	-	-
R1-ep	75.77 ( $\pm 8.7$ )	19.09 ( $\pm 2.9$ )	5.12 ( $\pm 0.97$ )	-
R2	84.90 ( $\pm 8.2$ )	14.83 ( $\pm 2.5$ )	0.39 ( $\pm 0.09$ )	-
R2-ep	75.01 ( $\pm 8.7$ )	19.17 ( $\pm 2.9$ )	5.63 ( $\pm 1.1$ )	0.26 ( $\pm 0.04$ )
R3	84.64 ( $\pm 8.2$ )	15.02 ( $\pm 2.5$ )	0.34 ( $\pm 0.07$ )	-
R3-ep	73.77 ( $\pm 8.5$ )	21.12 ( $\pm 3.0$ )	5.46 ( $\pm 1.0$ )	0.64 ( $\pm 0.10$ )

Reproduced from Vlnieska et al (2019) [75] (CC BY)

Table 13 presents the average of triplicates. Considering the structure of the resin as a pure oligomer, without ending groups and derivate, the theoretical value of the relative percentage for oxygen would be 13.2 %. The resins presented average of 15.2 % of oxygen atoms, suggesting circa 2.0 % of the oxygen atoms coming from termination and/or derivate groups, as presented in Figure 58. Since the samples were evaluated together at the SEM, one can see small amounts of chlorine in the non-epoxidized resins, which is a slight contamination from the epoxidized resins, coming along with the time during the high voltage exposure. Regarding epoxidized samples, an average of 4.6 % of increased oxygen atoms was observed, as well as 5.4 % chlorine atoms. In order to interpret with better accuracy this reaction system, some boundary conditions were applied:

1°: Once the alkylation was performed in excess of epichlorohydrin, it would be possible to expect an alkylation via epoxy groups, increasing the epoxy weight [101, 103, 104].”

2°: To evaluate the derivate products from the alkylation reaction, it was considered for elucidation only the possibilities from one to five epoxy groups by each bisphenol-A molecule (Figure 58).

The increase of oxygen atoms in the samples was expected and it confirms the alkylation reaction; meanwhile, the chlorine amount indicated an interesting result: epoxy groups could be composed in reality by most of its chlorine derivate (Figure 58 (a)).

The compositions of the elemental analysis indicate that the epoxy resins have structures varying from 1:3 and 1:4 (bisphenol-A:epichlorohydrin). Epoxy weight higher than these proportions were disregarded since the percentage of oxygen atoms start to be in the range of 30% (the higher oxygen atom composition measured was 21.12 %). Chlorine atoms composition of 5,4 % indicates the chloride derivate of the epoxy groups, containing only one Chlorine atom per epoxidized mer, as presented in Figure 61, structures number 3, 5, 9 and 11.

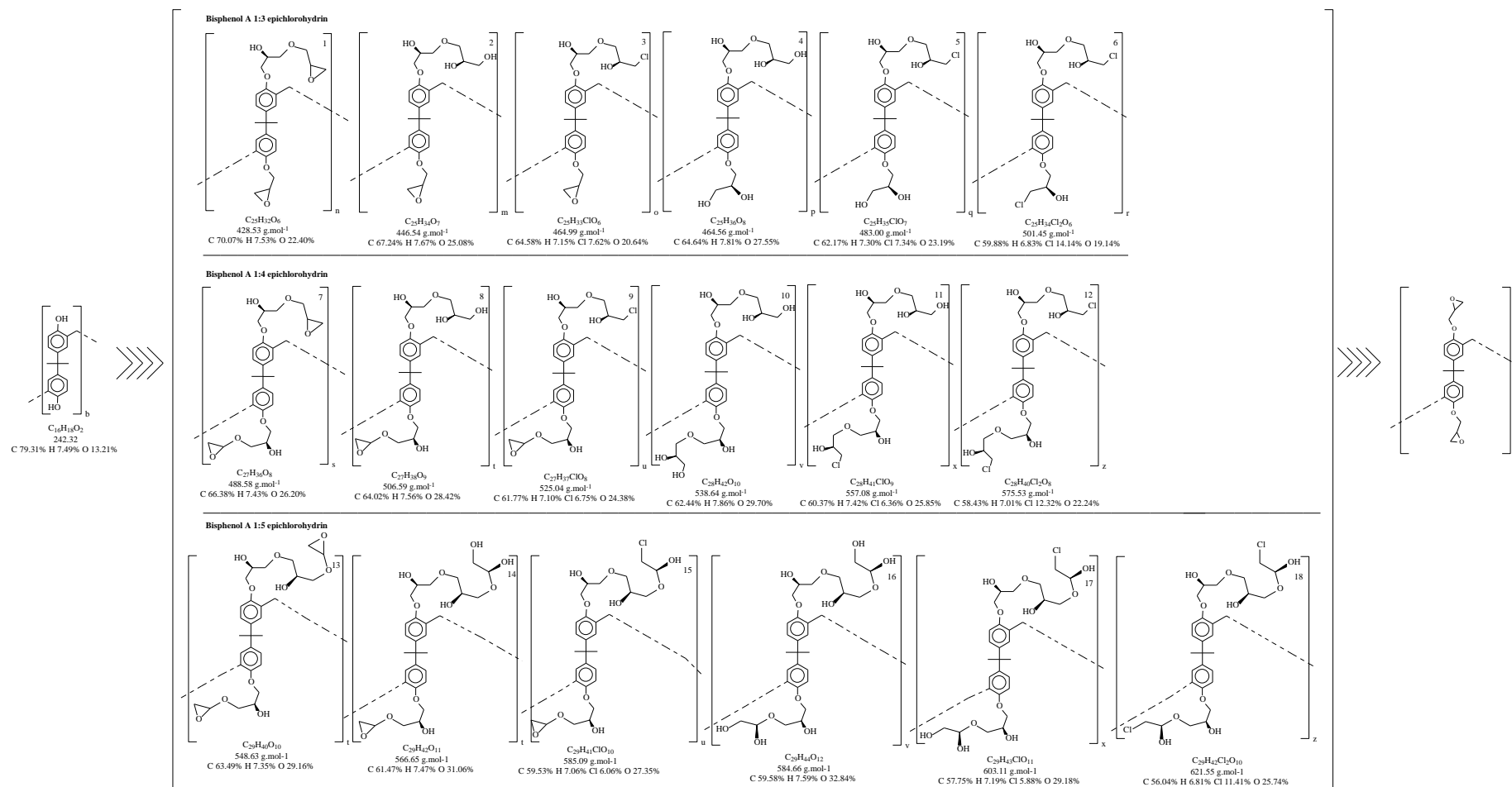


**Figure 61:** Possibilities of derivate during the alkylation reaction, considering the epoxidation degree until five units to one bisphenol-A. Reproduced from Vlnieska et al (2019) [75] (CC BY)

The epoxidized resins were also characterized with ESI- $\mu$ -TOF-MS mass spectroscopy. The characterization was performed in the mass region of the monomer. Once the oligomeric chains grow, the possibility of achieving derivate products progresses geometrically, which results being unfeasible a to characterize each single derivate product in the composition of the resins. Figure 62 presents the mass spectra in the region of the monomer for the epoxidized resins R1-ep, R2-ep, and R3-ep.”

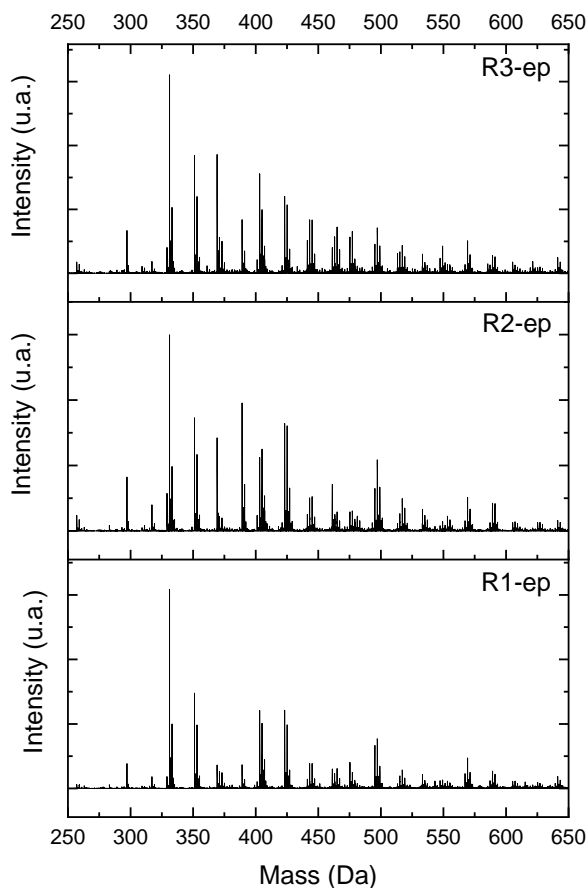


**Figure 62:** ESI- $\mu$ -TOF-MS spectra from epoxidized resins, amplified in the monomer region. Reproduced from Vlnieska et al (2019) [75] (CC BY)

The same characterization approach used for the oligomers was applied to identify the epoxidized products. In Figure 63 one can see that all molecule structures from Figure 58 and Figure 61 can be present in the epoxidized resin compositions. Nevertheless, for masses from 340 to 505  $\text{g}\cdot\text{mol}^{-1}$  there was higher relative intensity. The range of mass is related to the molecules 1:2 to 1:3 (bisphenol-A:epichlorohydrin) derivate, which are depicted in Figure 58 (c) and Figure 61 3, 5, 9 and 11.

Characterization with NMR spectroscopy also indicated a range ratio of 1:2 to 1:3 (bisphenol-A:epichlorohydrin) for the epoxidized resins. In order to elucidate the ratio between bisphenol-A and epichlorohydrin the assigned integral values of the epoxy groups were compared with the assigned integral values of methyl groups present in bisphenol-A. Ten experiments were prepared, changing the ratio between bisphenol-A and epichlorohydrin, from 1:1 to 1:10 (bisphenol-A:epichlorohydrin). Table 14 presents the integral values of the epoxy groups.

**Table 14:** Molar ratio for epoxy groups versus integral values

Ratio <sup>a</sup>	Integral <sup>b</sup>
1:1	0.78
1:2	1.51
1:3	2.24
1:4	2.80
1:5	3.77
1:6	4.42
1:7	5.07
1:8	5.89
1:9	6.60
1:10	7.26

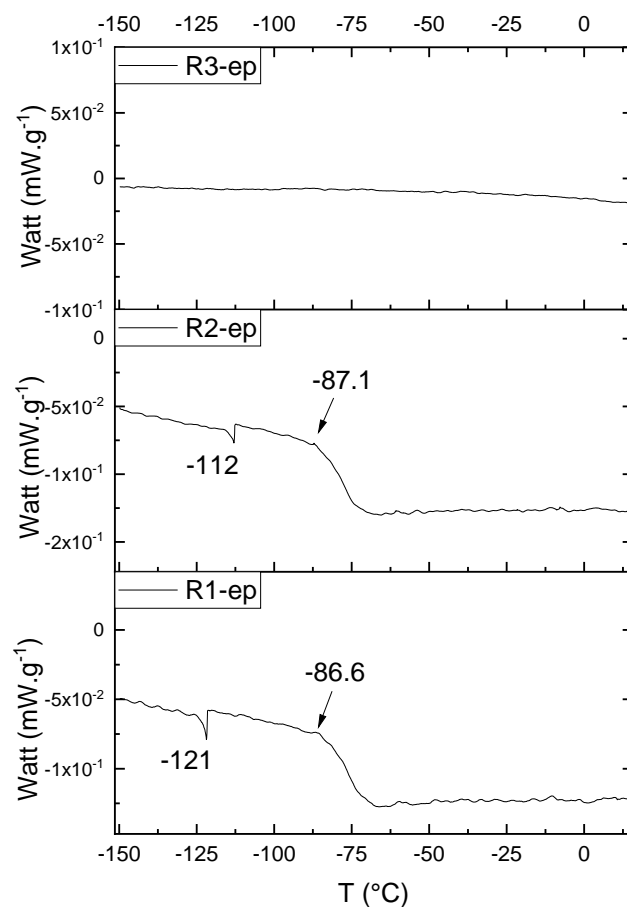
<sup>a</sup> ratio bisphenol-A:epichlorohydrin

<sup>b</sup> Integral values assigned for epoxy groups

Reproduced from Vlnieska et al (2019) [75] (CC BY)

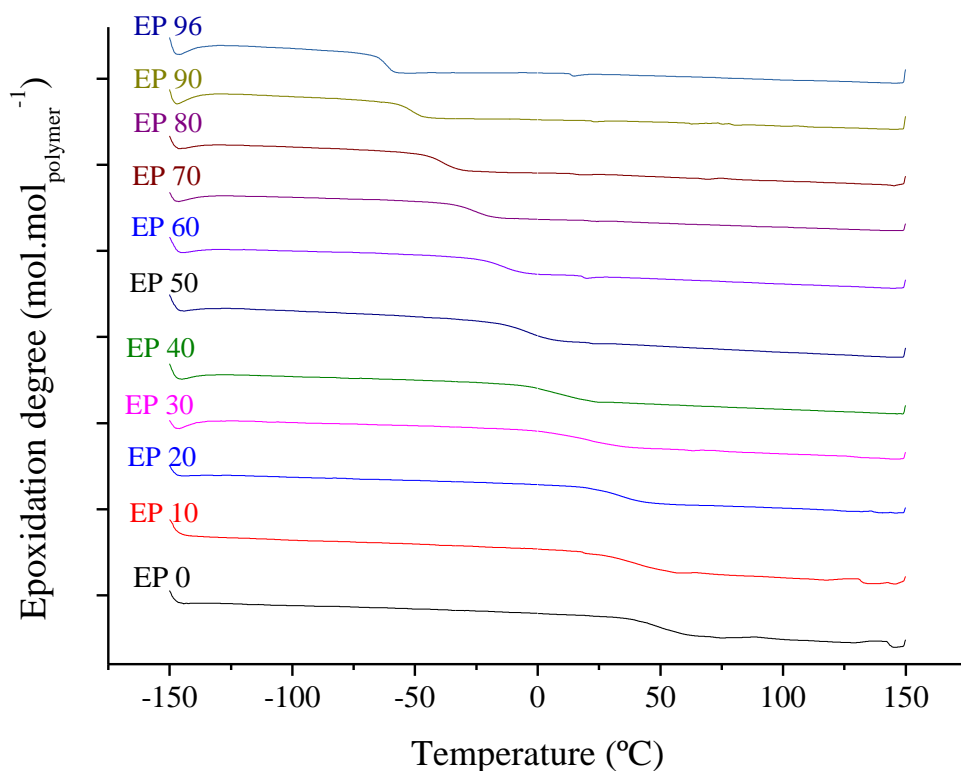
The substitution ratio for the epoxidized resins seems to be in accordance with the results for the elemental analysis and the ESI- $\mu$ -TOF-MS. R1-ep, R2-ep, and R3-ep presented epoxy groups integral values of 1.76, 1.80, and 1.86 respectively. These results confirm probably a mixture of oligomers composed by 1:2 and 1:3 ratio of epoxidized products.

Figure 63 presents the thermal behavior of the epoxidized resins.



**Figure 63:** DSC curves of the epoxidized resins R1-ep, R2-ep and R3-ep. Reproduced from Vlnieska et al (2019) [75] (CC BY)

Comparing samples before and after epoxidation reaction (Figure 56 and Figure 63), the overall profile of the products is the same. However, the epoxidized samples presented  $T_g$  at the low temperatures (reduced approximately  $110\text{ }^\circ\text{C}$ , comparing the resins R1; R1-ep and R2; R2-ep). The samples R1-ep and R2-ep also presented a  $T_g'$ , assigned to small free movements at the end of the polymeric chains [97, 98]. The sample R1-ep presented  $T_g$  starting at  $-86.6\text{ }^\circ\text{C}$ , with  $0.77\text{ J}\cdot(\text{g}\cdot^\circ\text{C})^{-1}$ . The sample R2-ep presented  $T_g$  starting at  $-87.1\text{ }^\circ\text{C}$ , with  $0.70\text{ J}\cdot(\text{g}\cdot^\circ\text{C})^{-1}$ . The sample R3-ep still shows a profile without  $T_g$  or  $T_g'$ . After the epoxidation reaction, the R1 and R2 samples seem to present a similar crystalline phase once the enthalpy values are close, and the slopes of the derivative curve are similar [96]. R1-ep  $T_g'$  is  $9\text{ }^\circ\text{C}$  lower, indicating that the polymer chains have little more freedom to move. These achievements still show the following behavior: once the concentrations of derivate products increase, the crystalline phase decreases. The epoxy resins were studied regarding glass transition temperatures and the different concentrations of epoxidation degree in its compositions. For this study, it was used the resin R2-b as the based material. Figure 64 presents the samples DSC curves.



**Figure 64:** Glass transition temperatures ( $T_g$ ) versus epoxidation degree for resin R2-b. Reproduced from Vlnieska et al (2019) [75] (CC BY)

Figure 64 presents ten curves of the heating behavior for the resin R2-b, varying from 0 to 96%  $\text{mol.mol}_{\text{polymer}}^{-1}$  of epoxy groups in composition, with steps of  $10\text{ } \text{mol.mol}_{\text{polymer}}^{-1}$ . Table 15 presents the glass transition temperatures for each epoxidation degree.

**Table 15:** Glass transition temperatures and slopes of the R2-b epoxy resins.

Epoxidation degree (% mol.mol <sub>polymer</sub> <sup>-1</sup> )	Glass transition temperatures (°C)			
	Initial	Middle	Final	Cp (DIN) (J.g <sup>-1</sup> K <sup>-1</sup> )
EP0	36.7	50.4	63.1	0.580
EP10	25.8	40.7	53.6	0.543
EP20	22.3	33.8	44.1	0.405
EP30	6.35	22.1	35.2	0.500
EP40	-5.0	8.5	20.6	0.553
EP50	-13.3	-3.1	5.43	0.464
EP60	-20.7	-12.1	-4.9	0.445
EP70	-32.9	-25.1	-18.5	0.476
EP80	-45.2	-38.4	-32.7	0.432
EP90	-55.7	-50.7	-46.5	0.464
EP96	-65.4	-61.9	-59.1	0.543

In Table 15, observing the final temperature of the glass transitions, one can see that in the concentration between 30 to 40 % mol.mol<sub>polymer</sub><sup>-1</sup>, the  $T_g$  reaches room temperature. With epoxidation degrees above 40 % mol.mol<sub>polymer</sub><sup>-1</sup>, the resins will remain more flexible in room temperature, resulting certainly in poor performance in lithographic techniques. This information is crucial to synthesize the composition of the resin that will be applied in the formulation of the photoresists [105].

### 5.3 Conclusions

The main raw chemical compound to formulate negative tone photoresists was studied. They were synthesized, characterized, and a proposal to tune the oligomerization reaction can be performed varying the mass polymerization reaction parameters. The resins were mostly compound by a mixture of monomers, dimers, trimers, and traces of tetramers. The oligomers presented a wide range of derivate products, which were identified mainly by mass spectroscopy (ESI- $\mu$ -TOF-MS). DSC evaluation shows similar behavior for samples R1 and R2, with a  $T_g$  relatively more intense for R2, where the crystalline phase is more pronounced, and R3 presented no  $T_g$ .

Three different profiles of oligomers were chosen to proceed with the further step, the alkylation of the hydroxyl groups, described here as well as epoxidation reaction. The products achieved by the epoxidation reaction presented a wide range of structures, which were characterized and quantified using spectroscopy techniques such as ESI- $\mu$ -TOF-MS and NMR, as well as DSC and elemental analysis (SEM-EDX) characterization methods.

The epoxidized resins presented an epoxidation ratio near to 96 % in the phenolic positions. The alkylation reaction also presented derivative products. A proper estimation of the structures and composition was done. It indicates an epoxidation ratio between 1:2 and 1:3 (Bisphenol-A:Epichlorohydrin), considering the chloride derivative structure being part of epoxidation content. The DSC measurements confirmed the unique profile of thermal behavior for each batch of oligomerization reaction, where the enthalpies of the glass transition temperatures ( $T_g$ ) were significantly distinct.

In chapter 4, during the characterization of commercially photoresists, were found significant concentrations of non-epoxidized polymers in its composition. It is now interesting to note that epoxy resins with epoxidation degrees from 50 to 96 % mol·mol<sub>polymer</sub><sup>-1</sup>, presented Tg lower than room temperature, a characteristic that restricts its usage for photoresist formulations. Since the physical state remains always viscous, this result now elucidates the open question from chapter 4. For photoresists based in epoxy resins, the epoxidation degree plays a role in two properties: sensitivity of the photoresist and the physical state of the resins. This result is new and no publications related with this property were found in the literature.

The studies regarding the synthesis and characterization of the epoxidized oligomers to produce negative tone photo-resins (or photoresists) seem to lead to:

- It is crucial to define the profile of an epoxy oligomer to be produced.
- It is fundamental to strictly control the parameters of the reaction to achieve the desired profile of the resin.
- The epoxidation degree is definitely a significant parameter to be controlled.

## 6 LITHOGRAPHIC PERFORMANCE OF THE SYNTHESIZED EPOXY RESINS <sup>1</sup>

Optical components such as gratings are one of the examples for high-end applications fabricated through lithography. When it presents feature sizes in the range of few micrometers to sub micrometer scale combined with HAR structures, the best alternative to produce it is to use X-ray lithography together with negative-tone photoresists based on epoxy resins.

In chapter five, epoxy resins were studied regarding tuning of the deep-level of properties, and two parameters were defined and optimized, first the polydispersion profile of the oligomers, and second, but no less relevant, the epoxidation degree of the oligomers. Three different profiles of resins were obtained (regarding polydispersity). Afterwards the alkylation reaction was optimized (epoxidation). From the DSC analysis results, it was seen that the epoxidation degree is a significant parameter to be tuned and controlled. The epoxidation degree shall be tuned in the maximum of 40 % mol·mol<sub>polymer</sub><sup>-1</sup>. Regarding these parameters, in this chapter, photo-resins were formulated aiming to compare their lithographic properties with the polydispersity and different concentrations of epoxidation degree and photoinitiator. The strategy to tune the deep and macro levels of properties was applied for this chapter (see section 1.3).

It is important to mention that, since the formulations presented here are made in the simplest version possible, their properties and performance are expected to be inferior when they are compared with commercially available photoresists. Nevertheless, this study is crucial to understand the relationship between the chemical and the lithographic properties of the photoresists.

### 6.1 Photo-resins formulation

The formulation or macro-level properties of a photo-resin involve several steps and compounds to achieve its final formulation. Nevertheless, for chemically amplified formulations, the most straightforward possible composition must have at least three compounds: a polymer or oligomer; a photoinitiator and a solvent. As well, to improve its mechanical properties and lithographic performance several additives are usually added to the formulations (section 1.3).

Regarding epoxy resins, two characteristics were considered to be evaluated in the formulations, the polydispersity, and the epoxidation degree. From chapter 5 (Figure 48), three profiles of polydispersity were achieved and alkylated using epichlorohydrin. They were used in this section (R1-ep, R2-ep and R3-ep) to formulate photo-resins (or named as well as photoresists)

1. This chapter is based on the publication: Vnieska, V., Zakharova, M., Mikhaylov, A., Kunka, D., *Lithographic performance of aryl epoxy thermoset resins as negative tone photoresist for microlithography – Polymers* **2020**, *12*(10), 2359

Regarding tuning on the macro-level of properties, the amount of photoinitiator was studied from 0 to 100 % mol·mol<sub>polymer</sub><sup>-1</sup>. The photoinitiator applied in the formulations is a mix of triarylsulfonium hexafluoroantimonate salts (TAS) (50 wt. % in propylene carbonate). For some formulations, due to the high concentration, the photoinitiator is considered as a reagent of the system and not a catalyst (see section method 3.11). The solvent applied for the formulations was cyclopentanone, which the main function is to obtain a specific viscosity value for the formulation. All formulations were prepared with viscosity of 850±20 mPa·s<sup>-1</sup> (25 °C, 1·10<sup>3</sup> s) [76].

The resins were studied applying the tuning of deep-level properties. Three different profiles of polydispersity from the resins (R1-ep, R2-ep, R3-ep), and epoxidation degrees, with concentration range from 0 to 40 % mol·mol<sub>polymer</sub><sup>-1</sup> were evaluated in several formulations. For the first set of experiments, altogether 35 photo-resins were formulated (all concentration levels of epoxidation degree multiplied by all concentration levels of the photoinitiator, using R2 resin, resulting in the following formulations (see section method 3.11):

$$P_2ED_{0 \text{ to } 40}C_{0 \text{ to } 100}$$

In section 6.2, the results of this preliminary evaluation are discussed.

## 6.2 UV Lithography (qualitative evaluation)

Several formulations of photo-resins were processed through UV lithography, where a qualitative experiment was performed to evaluate the lithographic performance. The experiments were made in triplicates for each of the formulations. Figure 65 presents the formulations, in triplicates, where the substrates (SiTiOx – 500 µm thickness, 4 inches (app. 10cm) in diameter) were prepared with the framework, laminated and soft baked with the formulations (see section method 3.12).



(a) Triplicate 1 of the quality evaluation. (b) Triplicate 2 of the quality evaluation. (c) Triplicate 3 of the quality evaluation.

**Figure 65:** Triplicates of the laminated formulations. Reproduced from Vnieska et al (2020) [76] (CC BY)

In Figure 65 is depicted each substrate applied in the triplicates for quality evaluation. The marked lines (five of them) are the lines in which the cavities were used to laminate the formulations.

Table 16 presents the formulated photo-resins after soft baking. Table 17 shows the formulated photo-resins after development.

**Table 16:** Images of the photo-resin formulations after lamination, UV-exposure, and hard bake

	ED <sub>0</sub>			ED <sub>10</sub>			ED <sub>20</sub>			ED <sub>30</sub>			ED <sub>40</sub>		
	T <sub>1</sub>	T <sub>2</sub>	T <sub>3</sub>	T <sub>1</sub>	T <sub>2</sub>	T <sub>3</sub>	T <sub>1</sub>	T <sub>2</sub>	T <sub>3</sub>	T <sub>1</sub>	T <sub>2</sub>	T <sub>3</sub>	T <sub>1</sub>	T <sub>2</sub>	T <sub>3</sub>
C <sub>0</sub>															
C <sub>3</sub>															
C <sub>5</sub>															
C <sub>10</sub>															
C <sub>30</sub>															
C <sub>50</sub>															
C <sub>100</sub>															

ED = Epoxidation degree (% mol·(mol<sub>polymer</sub>)<sup>-1</sup>)  
 C = Amount of photoinitiator (% mol·(mol<sub>polymer</sub>)<sup>-1</sup>)  
 T = triplicate experiment 1, 2 and 3  
 Reproduced from Vlnieska et al (2020) [76] (CC BY)

**Table 17:** Images of the photo-resin formulations after development

	ED <sub>0</sub>			ED <sub>10</sub>			ED <sub>20</sub>			ED <sub>30</sub>			ED <sub>40</sub>		
	T <sub>1</sub>	T <sub>2</sub>	T <sub>3</sub>	T <sub>1</sub>	T <sub>2</sub>	T <sub>3</sub>	T <sub>1</sub>	T <sub>2</sub>	T <sub>3</sub>	T <sub>1</sub>	T <sub>2</sub>	T <sub>3</sub>	T <sub>1</sub>	T <sub>2</sub>	T <sub>3</sub>
C <sub>0</sub>															
C <sub>3</sub>															
C <sub>5</sub>															
C <sub>10</sub>															
C <sub>30</sub>															
C <sub>50</sub>															
C <sub>100</sub>															

ED = Epoxidation degree (% mol·(mol<sub>polymer</sub>)<sup>-1</sup>)C = Amount of photoinitiator (% mol·(mol<sub>polymer</sub>)<sup>-1</sup>)

T = triplicate experiment 1, 2 and 3

Reproduced from Vlnieska et al (2020) [76] (CC BY)

**Table 18:** Quality control for the evaluation of the photo-resin formulations

Samples	ED0 (t1)	ED0 (t2)	ED0(t3)	ED10(t1)	ED10(t2)	ED10(t3)	ED20(t1)	ED20(t2)	ED20(t3)	ED30(t1)	ED30(t2)	ED30(t3)	ED40(t1)	ED40(t2)	ED40(t3)	C average
C0	0	0	0	0	0	0	0	0	0	0	0	0	0	0	0	-
<b>C0 t-average</b>	<b>0.000</b>			<b>0.000</b>			<b>0.000</b>			<b>0.000</b>			<b>0.000</b>			<b>0.000</b>
C3	1	1	1	0	0.5	0.5	0	0.5	0.5	0.5	0.5	1	0.5	0.5	0.5	-
<b>C3 t-average</b>	<b>1.000</b>			<b>0.333</b>			<b>0.333</b>			<b>0.667</b>			<b>0.500</b>			<b>0.567</b>
C5	0	0	0	0.5	1	0.5	0.5	0.5	0.5	0.5	1	0.5	0.5	1	1	-
<b>C5 t-average</b>	<b>0.000</b>			<b>0.667</b>			<b>0.500</b>			<b>0.667</b>			<b>0.833</b>			<b>0.533</b>
C10	0.5	0	0	0.5	0.5	0.5	0.5	1	0.5	0.5	1	1	0.5	1	1	-
<b>C10 t-average</b>	<b>0.167</b>			<b>0.500</b>			<b>0.667</b>			<b>0.833</b>			<b>0.833</b>			<b>0.600</b>
C30	0	0	0	0.5	1	1	1	0.5	1	1	1	1	1	1	1	-
<b>C30 t-average</b>	<b>0.000</b>			<b>0.833</b>			<b>0.833</b>			<b>1.000</b>			<b>1.000</b>			<b>0.733</b>
C50	0	0	0	1	0.5	0.5	1	0.5	1	0.5	1	1	1	1	1	-
<b>C50 t-average</b>	<b>0.000</b>			<b>0.667</b>			<b>0.833</b>			<b>0.833</b>			<b>1.000</b>			<b>0.667</b>
C100	0	0	0	0	0	0	0.5	0.5	0.5	0.5	1	1	1	1	1	-
<b>C100 t-average</b>	<b>0.000</b>			<b>0.000</b>			<b>0.500</b>			<b>0.833</b>			<b>1.000</b>			<b>0.467</b>
<b>ED average</b>	<b>ED0 average</b>	<b>0.167</b>		<b>ED10 average</b>	<b>0.429</b>		<b>ED20 average</b>	<b>0.524</b>		<b>ED30 average</b>	<b>0.690</b>		<b>ED40 average</b>	<b>0.738</b>		-

\*t-average: the average values for the triplicate measurements

Reproduced from Vlnieska et al (2020) [76] (CC BY)

In Table 16, It is interesting to note the pattern of the structures straightforward after the hard baking step. Starting with 3 % mol·mol<sub>polymer</sub><sup>-1</sup>, all samples presented a darker tone color in the exposed region (when it is compared with the unexposed region). Figure 66 exemplifies this characteristic.



**Figure 66:** Image from optical microscope from the formulation P<sub>2</sub>ED<sub>0</sub>C<sub>3</sub> (t3). Reproduced from Vlnieska et al (2020) [76] (CC BY)

Although in Figure 66 is not possible to see the depth of the structure, the difference in the tones between exposed and no exposed areas allow the observation of the pattern contours. It can help to decide if the lithography process should proceed or not. In table 15, observing the formulations without epoxy groups (P<sub>2</sub>ED<sub>x</sub>C<sub>0</sub>), it seems to result in poor adhesion with the substrates. Formulations with high concentrations of photoinitiator (C50 and C100) combined with low epoxidation degree (ED0 and ED10) also resulted in poor results for most of these formulations (imperfections in the structures or low adhesion to the substrate).

In Table 17 are presented formulations after development. To evaluate the performance of the photo-resins, a qualitative scale was chosen, using three values. It follows the criteria:

- 0 for the not remained structure after the development step (poor adhesion)
- 0.5 for remained structures with defects after the development step
- 1.0 for entirely remained structures after the development step

Figure 67 presents the results of the photo-resins after the development step.

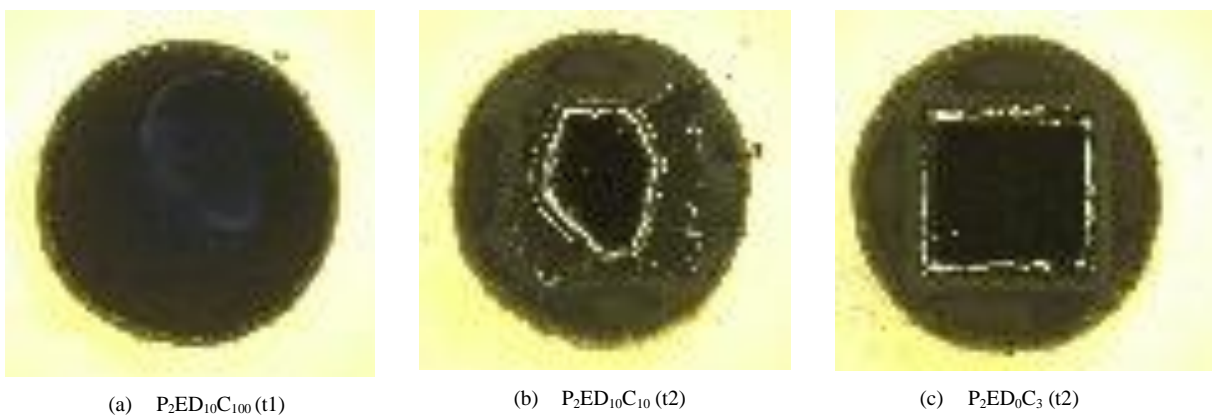


**Figure 67:** Examples of the evaluation criteria used in the quality evaluation of the photo-resins; in (a) an example of 0.0 value; in (b) an example of 0.5 value; in (c) an example of 1.0 value. Reproduced from Vlnieska et al (2020) [76] (CC BY)

In Figure 67 (a), value 0.0 was given to the lithographic performance of  $P_2ED_{10}C_{100}$  (t1), where the formulation was completely removed after development. In (b), it is an example of a partially remained structure, which had the value 0.5 given. In (c), the structure is entirely remained, receiving the value 1.0.

In Table 18 are available the calculations of the quality evaluation. The quality criteria were assigned observing the structures at an optical microscope (see section method 3.19). Figures 68 to 71 present the results calculated in Table 18, which shows the influence of the epoxidation degree and the photoinitiator concentrations in the quality of the obtained structures. Figures were Reproduced from Vlnieska et al (2020) [76] (CC BY).

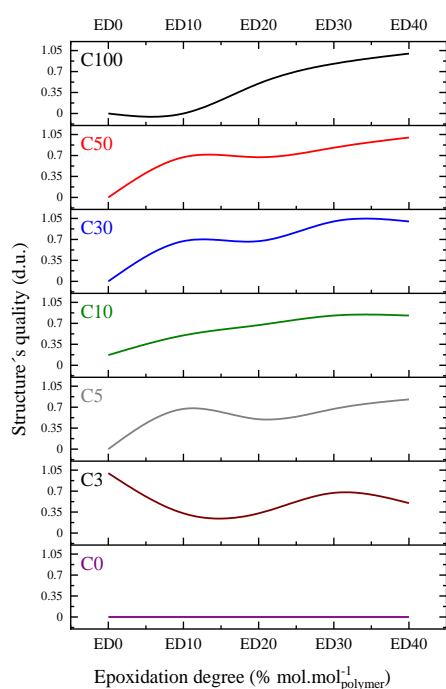


**Figure 68:** Amount of photoinitiator correlated with the epoxidation degree and the quality of the patterned structures

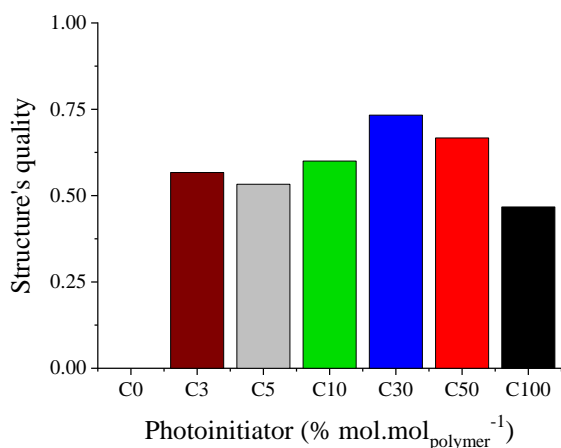


**Figure 70:** Averaged performance correlated with the amount of photoinitiator

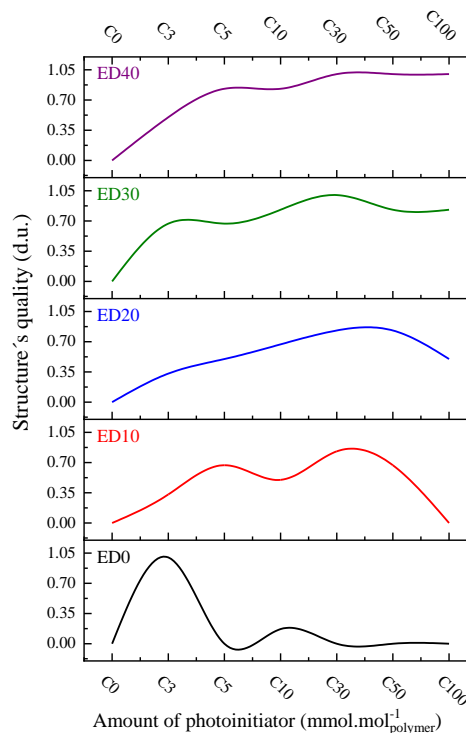


**Figure 69:** Epoxidation degree correlated with the amount of photoinitiator and the quality of the patterned structures

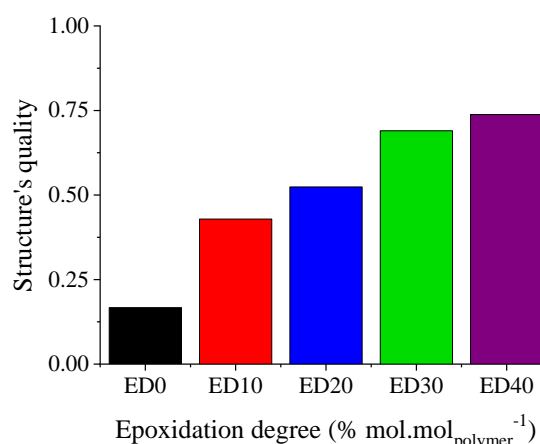


**Figure 71:** Averaged performance correlated with the epoxidation degree

Figures 68 and 70 results emphasizing the amount of photoinitiator in the formulations, whereas Figures 69 and 71 show the results correlating it with the epoxidation degree in the formulations. In general, the formulations start to

present reliable results with concentrations beginning with 30 % mol·mol<sub>polymer</sub><sup>-1</sup> for epoxidation degree and amount of photoinitiator. In Figure 68 it is possible to observe better results (values 1.0 and close to it) in formulations with photoinitiator above 5 % mol·mol<sub>polymer</sub><sup>-1</sup> and epoxidation degree of 30 and 40 % mol·mol<sub>polymer</sub><sup>-1</sup>. Still in Figure 68, it is interesting to note the performance with 3 % mol·mol<sub>polymer</sub><sup>-1</sup> of photoinitiator, where without epoxidation degree was possible to have good quality structures (value 1.0). Nevertheless, the results with 10 and 20 % mol·mol<sub>polymer</sub><sup>-1</sup> presented low quality (0.33), followed by averaged results (0.66 and 0.5 respectively) with 50 and 100 % mol·mol<sub>polymer</sub><sup>-1</sup>.

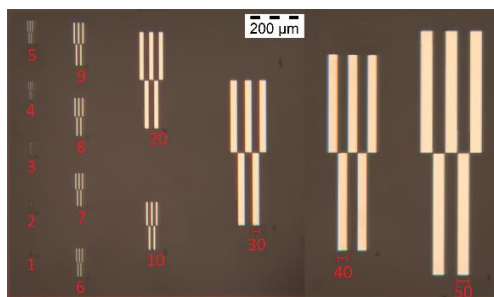
Regarding Figure 69, one can see improvement of the structure's quality once the epoxidation degree is increased, with the exception of 0 % mol·mol<sub>polymer</sub><sup>-1</sup>. With 3 % mol·mol<sub>polymer</sub><sup>-1</sup> of photoinitiator good structures were achieved (value 1.0), which is a surprising result. Figures 70 and 71 present the averaged value considering all experiments performed at certain concentration. In Figure 70, one can see the influence of the photoinitiator concentration in the quality of the structures. In Figure 71 the results show the influence of the epoxidation degree in the quality of the structures. To exemplify, in Figure 70, C30 (30 % mol·mol<sub>polymer</sub><sup>-1</sup> of photoinitiator) has a value of 0.73. This value can be interpreted as the following statement: for any formulation studied with photoinitiator content of 30 % mol·mol<sub>polymer</sub><sup>-1</sup>, 2 of 3 structures would present a free-defect shape (result of 1.0). The same approach is valid for Figure 71, however, the results are correlated with the epoxidation degree.

Figure 70 illustrates that the best results were achieved with 30 and 50 % mol·mol<sub>polymer</sub><sup>-1</sup>, regarding the amount of photoinitiator. In Figure 71, for the epoxidation degree one can see that the best performance is achieved with concentrations of 30 and 40 % mol·mol<sub>polymer</sub><sup>-1</sup>. In this case, the epoxidation degree of 40 % mol·mol<sub>polymer</sub><sup>-1</sup> presented slightly better performance.

After the evaluation of the qualitative experiments, one can see that the best lithographic performance was achieved with P<sub>x</sub>ED<sub>40</sub>C<sub>30</sub> or P<sub>x</sub>ED<sub>40</sub>C<sub>50</sub> formulations. Since the results between C30 and C50 are very similar (Figure 70), the formulation with less photoinitiator was chosen to perform the next step of investigation regarding lithographic properties. In the next section, the P<sub>x</sub>ED<sub>40</sub>C<sub>30</sub> formulations using the polydispersity profiles of R1, R2 and R3 were prepared and evaluated using a pattern from 50 down to 1 μm feature sizes.

### 6.3 UV and Deep-UV lithography (50 down to 1 μm)

The results from section 6.2 indicate the P<sub>x</sub>ED<sub>40</sub>C<sub>30</sub> as the best formulation to proceed with further studies. This formulation was prepared using three profiles of resins, R1, R2 and R3, resulting in P<sub>1</sub>ED<sub>40</sub>C<sub>30</sub>, P<sub>2</sub>ED<sub>40</sub>C<sub>30</sub>, and P<sub>3</sub>ED<sub>40</sub>C<sub>30</sub>, which were processed through UV and Deep-UV lithography techniques (see section method 3.14), using a pattern test mask with feature sizes from 50 to 1 μm. Figure 72 presents the design of the chromium mask (the picture was made with an optical microscope, see section method 3.19).



**Figure 72:** Design and periodicity of the chromium mask used in UV and deep-UV lithographies. Reproduced from Vlnieska et al (2020) [76] (CC BY)

After lithographic processing, the samples were observed through an optical microscope (section method 3.18) and scanning electron microscopy (section method 3.17). Table 19 correlates the polydispersity of the photo-resins with the obtained structures. SEM images from Table 19 are available in full format in the Appendix, Figures A15 to A17.

**Table 19:** Comparison between formulations and structures performed through UV and DUV lithography techniques

	P <sub>1</sub> ED <sub>40</sub> C <sub>30</sub>	P <sub>2</sub> ED <sub>40</sub> C <sub>30</sub>	P <sub>3</sub> ED <sub>40</sub> C <sub>30</sub>
Polydispersity			
Microscope (UV Lithography)			
Microscope (DUV lithography)			
SEM* (UV lithography)			

Reproduced from Vlnieska et al (2020) [76] (CC BY)

As shown in Table 19, in general, good quality structures were obtained from 50 down to 10  $\mu\text{m}$  period. Since the thickness of the photo-resins was in the range of 30  $\mu\text{m}$ , structures smaller than 10  $\mu\text{m}$  period will not present enough sharpness due to the diffraction effects [106]. Comparing the formulations, one can see a better sharpness of the structures when the formulation P<sub>1</sub>ED<sub>40</sub>C<sub>30</sub> is utilized. It is interesting to note that through Deep-UV lithography, the formulations P<sub>x</sub>ED<sub>40</sub>C<sub>30</sub> presented overexposed structures, easily recognized by the fringes and disruptions in the structures. This result was expected since the dose intensity used is considered too high for DUVL. However, the intention of this evaluation was initially to use the same irradiation doses for UV and deep-UV wavelengths, which was in both cases  $1 \times 10^4 \text{ mJ}\cdot\text{cm}^2$ . Regarding UV lithography, the best result was achieved with the R1 resin, where the polydispersity is the intermediate one. In this case, one can see a better photosensitivity and resolution of the structures. It was possible to reach the limit of the resolution for this technique since structures smaller than 10  $\mu\text{m}$  period are not expected to be successful due to the diffraction effects. Still, in Table 19, it is worth to observe the SEM pictures from UV lithography, where the sharpest structures were obtained using P<sub>1</sub>ED<sub>40</sub>C<sub>30</sub>. The SEM evaluation for all samples were made in the same measurement with exactly the same optical parameters (section method 3.17).

For this kind of epoxy resin, the crosslinking reaction that occurs during the exposure step is open to discussion in the literature and not completely elucidated. Figure 30 (section 1.3) describes the crosslinking mechanism considering the simplest reaction path. Consequently, a few constraints were assumed to understand the reaction mechanism, which are:

- The photoinitiator is a Lewis acid, releasing a proton to the reaction medium
- Poly(2,2-Bis(4-hydroxyphenyl)propane) (the oligomers) has no derivate products and termination groups
- All the epoxy rings are intact, and there is no epoxy derivate
- Poly(2,2-Bis(4-hydroxyphenyl)propane) is 100% epoxidized

Nevertheless, comparing the polydispersity and SEM pictures (rows 1 and 4 - Table 19), it is plausible to suggest: 1 - the polydispersity of the photo-resins shall be considered in crosslinking mechanism; 2 - the crosslinking efficiency (irradiation step) tend to be improved if the oligomer chains present less derivate products.

Regarding the epoxidation degree, Figure 73 presents the composition of the photo-resins studied in the second trial of experiments. For the oligomer composition, it is crucial to mention that this representation is the simplest one, not considering the ending and derivate groups from the oligomer's chains as well as the derivate products from the epoxidation reaction.

Compound	a. Oligomer chain		b. Photoinitiator	c. Solvent
Chemical structure				
Composition (% mol · mol <sub>polymer</sub> <sup>-1</sup> )	60	40	30	0 - 22
Name	*	**	Hexafluoroantimonate Triarylsulfonium salts	Cyclopentanone

\* (poly(2,2-bis-(4-hydroxyphenyl)-propan))  
 \*\* (poly(2,2-bis-(4-oxy-(2-(methyloxirane)-phenyl)-propan))

**Figure 73:** Best formulation composition and its chemical structures. Reproduced from Vlnieska et al (2020) [76] (CC BY)

## 6.4 Conclusions

In this chapter, photo-resins were formulated using based on the deep and macro levels of properties. For this purpose, the resins previously synthesized and characterized in chapter five were applied. Two series of experiments were conducted, both in a qualitative manner. The photo-resins were prepared in the simplest version possible regarding the macro-level of properties, employing the epoxy resins, a photoinitiator (TAS) and cyclopentanone as a solvent.

The first trial of experiments through UV lithography showed that good quality structures (values from 0.67 to 1.0) can be achieved using a broad range of concentrations for the epoxidation degree and photoinitiator. In this case, the photo-resins can be formulated with epoxidation degrees from 10 % mol · mol<sub>polymer</sub><sup>-1</sup> to 40 % mol · mol<sub>polymer</sub><sup>-1</sup>. Regarding photoinitiator the concentration can vary from 3 % mol · mol<sub>polymer</sub><sup>-1</sup> to 100 % mol · mol<sub>polymer</sub><sup>-1</sup>. It seems that the tuning of deep and macro levels of properties is not significant to improve the quality of large structures (in this experiment the formulations were evaluated with a squared pattern of 1.3 mm<sup>2</sup>, and 120 μm of thickness). A few assumptions can be suggested to explain the results: for a large volume of the structure, the adhesion between the photo-resin and the substrate is less critical compared with sub micrometer structures; the oligomer chains most probably do not need to be totally crosslinked, consequently less amount of photoinitiator is necessary in the formulation.

In the second trial of experiments regarding UV lithography, structures from 50 to 10 μm pitch were successfully produced using the photo-resins. In this case, a few characteristics for the formulations were observed:

Concentrations of epoxy degree and photoinitiator presented better results in a narrow range of composition, with respectively 40 % mol·mol<sub>polymer</sub><sup>-1</sup> and 30 % mol·mol<sub>polymer</sub><sup>-1</sup>. The polydispersity of the epoxy resins starts to play a significant role with structures smaller than 50 µm. In this case, formulations with epoxy resin R1 presented better quality in the structures when it was compared with the other two resins (R2 and R3). For DUV lithography, were observed over exposed behavior. This effect was expected since the initial approach was to compare the same irradiation dose for both techniques. The best result was achieved with P<sub>1</sub>ED<sub>40</sub>C<sub>30</sub> formulation.

Observing the results, two main statements can be proposed:

- 1 - For large structures (above 1 mm<sup>2</sup>), the tuning of the deep and macro levels of properties can be relaxed;
- 2 - For structures under 50 µm it is necessary to consider specific polydispersion profile of the photo-resin to achieve better reproducibility (deep-level of properties). It is also suggested to restrict the concentrations for the epoxidation degree (deep-level of properties), and photoinitiator (macro-level of properties).

## 7 CONCLUSIONS AND FUTURE PERSPECTIVES

From the beginnings of twenty first century grating-based interferometric techniques were demanding optical components with size dimensions beyond the capabilities of deep-UV and UV lithography technologies, which only could be fulfilled with X-ray irradiation at synchrotron sources. Since then, imaging techniques based on gratings are one of the high-end applications pushing lithography techniques to their technological limits.

The best alternative to produce gratings with high aspect ratio (HAR) structures is applying X-ray lithography. This complex process fabrication involves several intermediate steps and relies on the quality of its primary material, the photoresists. Regarding the photoresists, during the history of it, several polymer matrixes and formulations were proposed (with considerable success) mainly to the development and to the advance of the semiconductor industry, which is currently the biggest application for lithography.

For X-ray lithography, the literature suggests that the best suitable raw material is the negative-tone photoresists, especially a photoresist based on bisphenol-A and chemically modified with epoxy groups. Commercially, this type of photoresist is known as SU-8 (developed and patented by IBM in 1989). Nevertheless, even with the best material, the reproducibility of the process fabrication is low, and it is very challenging to fabricate gratings classified as a "defect-free component". The literature provides information about its basic formulation and chemicals; however, this information was not enough to elucidate the difficulties that lead to the low reproducibility of the gratings.

In this direction, a characterization methodology was proposed and developed to classify and to comprehend the chemical composition of the photoresists. A series of commercially available photoresists were evaluated. The functional organic groups, solvent content, polydispersion of the polymer matrixes, and epoxidation degree were characterized. The evaluated photoresists, among different fabrication lots, presented variations in the mentioned properties. The different compositions of the photoresists originate distinct lithographic performance. These results indicate the necessity to control and adjust the chemical composition of the photoresists.

To elucidate the correlation of low reproducibility of the gratings fabrication and the photoresists chemical composition, the synthesis, characterization, and optimization of the polymer matrixes for photoresists were studied. In this study, essential characteristics not reported in the literature were found, such as the broad polydispersity profile of the oligomer chains, their derivative, secondary, and termination groups. They were characterized in an extensive study. Afterwards the alkylation reaction of the polymers was studied (epoxidation). It was found that the epoxidation degree plays an essential role in two properties of the photoresist: the photosensitivity and the viscous state of the polymer matrix. These correlations provided novel insight not yet known in the pertinent open literature.

A methodology named as deep and macro levels of properties was proposed to control the photoresists chemical production. In the deep-level, the chemical properties of the photoresists were optimized, where it was possible to achieve three distinct profiles of polydispersities and epoxidation degree varying from 0 to 96 % mol·mol<sub>polymer</sub><sup>-1</sup>. In

the macro-level of properties (which is the control and optimization of the chemical components in the photoresist formulation), the simplest formulation possible was studied using the synthesized resins, a photoinitiator and a solvent.

In order to evaluate whether the chemical composition of the photoresists could affect their lithographic performance, a qualitative experiment was carried out. The results indicated a low relevance of the chemical properties of the photoresist if structures above 1  $\mu\text{m}^2$ . However, if structures smaller than 50  $\mu\text{m}$  are produced, the polydispersity, epoxidation degree and amount of photoinitiator are crucial properties to be observed during the formulation of the photoresists. Once again the results were novel, to our knowledge no publications in the literature have been reported until recently. A quantitative correlation regarding the chemical composition and lithographic performance of the photoresists shall be developed. It is clear after this thesis that the chemical composition can determine the success of the lithography process.

The deep and macro levels of properties is a methodology that structures and correlates chemical properties of the photoresists and their lithographic performance. It is a valuable tool to improve the connection between three completely different fields of research, the lithography technologies, grating-based imaging systems and polymer chemistry. This methodology integrates the whole process chain for gratings production, from the raw material to its final application. This integration can potentially provide better quality control to the lithography process and increase the reproducibility of the gratings production. Consequently, gratings with smaller periods and large areas could be developed, opening new possibilities for X-ray imaging.

An example of these new possibilities is a multidisciplinary achievement may be for broadening the X-ray imaging techniques to tailor each optical element for in situ investigations of functional composite materials, heterogeneous catalysts, etc. In one of the possible experiments, hard X-rays and customized two-dimensional gratings, the absorption-based imaging will be complemented with phase contrast and small-angle scattering information, delivering insight about (sub) micrometer-sized particles and clusters of the catalyst during the reaction. If at synchrotron facilities, it will be possible to track micrometer to nano-sized features by exploring the small-angle scattering channel in a dynamic system. If laboratory sources with a microfocus beam are available, it is possible to investigate large samples with millimeters to centimeters sizes. Furthermore, as part of the research activities in our group, the next step is to discuss the feasibility of exploring time-resolved differential phase-contrast and small-angle scattering measurements of fast dynamic processes to be performed at the CAT-ACT beamline at the Karlsruhe Research Accelerator (KARA).

To reach such point of advance, gratings with smaller periods and fully defect-free area sizes shall be developed. It is necessary to change how the photoresists for X-ray lithography are produced. They shall be designed considering the features of the gratings. In this case, for X-ray lithography the design of the photoresist must involve the tuning of the deep and the macro levels of properties as started in this thesis.

## 8 REFERENCES

1. Pfeiffer, F., et al., *Hard-X-ray dark-field imaging using a grating interferometer*. Nature Materials, 2008. **7**(2): p. 134-137.
2. Momose, A., *Phase-sensitive imaging and phase tomography using X-ray interferometers*. Optics Express, 2003. **11**(19): p. 2303-2314.
3. Pfeiffer, F., et al., *Grating-based X-ray phase contrast for biomedical imaging applications*. Zeitschrift für Medizinische Physik, 2013. **23**(3): p. 176-185.
4. Vlnieska, V., et al., *Chemical and Molecular Variations in Commercial Epoxide Photoresists for X-ray Lithography*. Applied Sciences, 2018. **8**(4).
5. Pfeiffer, F., et al., *Phase retrieval and differential phase-contrast imaging with low-brilliance X-ray sources*. Nature Physics, 2006. **2**(4): p. 258-261.
6. Ruilin, Z., S. Wei, and C. Xuyuan, *Characterizing and smoothing of striated sidewall morphology on UV-exposed thick SU-8 structures for micromachining millimeter wave circuits*. Journal of Micromechanics and Microengineering, 2010. **20**(3): p. 035007.
7. Seidemann, V., S. Bütelfisch, and S. Büttgenbach, *Fabrication and investigation of in-plane compliant SU8 structures for MEMS and their application to micro valves and micro grippers*. Sensors and Actuators A: Physical, 2002. **97-98**(0): p. 457-461.
8. Toshihiko, T., et al., *Freeze-Drying Process to Avoid Resist Pattern Collapse*. Japanese Journal of Applied Physics, 1993. **32**(12R): p. 5813.
9. Toshiyuki, M., et al., *Influences of pretreatment and hard baking on the mechanical reliability of SU-8 microstructures*. Journal of Micromechanics and Microengineering, 2013. **23**(10): p. 105016.
10. Hamlett, C.A.E., G. McHale, and M.I. Newton, *Lithographically fabricated SU8 composite structures for wettability control*. Surface and Coatings Technology, 2014. **240**(0): p. 179-183.
11. Tanaka, T., M. Morigami, and N. Atoda, *Mechanism of Resist Pattern Collapse during Development Process*. Japanese Journal of Applied Physics, 1993. **32**(12S): p. 6059.
12. Khan Malek, C.G., *SU8 resist for low-cost X-ray patterning of high-resolution, high-aspect-ratio MEMS*. Microelectronics Journal, 2002. **33**(1-2): p. 101-105.
13. Namatsu, H., *Supercritical Drying for Nanostructure Fabrication*. Journal of Photopolymer Science and Technology, 2002. **15**(3): p. 381-388.
14. Namatsu, H., K. Yamazaki, and K. Kurihara, *Supercritical resist dryer*. Journal of Vacuum Science & Technology B, 2000. **18**(2): p. 780-784.
15. Kunka, D., et al., *Characterization method for new resist formulations for HAR patterns made by X-ray lithography*. Microsystem Technologies, 2014. **20**(10): p. 2023-2029.
16. Pfeiffer, F., et al., *Hard-X-ray dark-field imaging using a grating interferometer*. Nat Mater, 2008. **7**(2): p. 134-137.
17. Talbot, H.F., *LXXVI. Facts relating to optical science. No. IV*. The London, Edinburgh, and Dublin Philosophical Magazine and Journal of Science, 1836. **9**(56): p. 401-407.
18. Gkoumas, S., et al., *Grating-based interferometry and hybrid photon counting detectors: Towards a new era in X-ray medical imaging*. Nuclear Instruments and Methods in Physics Research Section A: Accelerators, Spectrometers, Detectors and Associated Equipment, 2016. **809**: p. 23-30.
19. Schröter, T.J., et al., *Large-area full field x-ray differential phase-contrast imaging using 2D tiled*

- gratings*. Journal of Physics D: Applied Physics, 2017. **50**(22): p. 225401.
20. Trimborn, B., et al., *Imaging properties of high aspect ratio absorption gratings for use in preclinical x-ray grating interferometry*. (1361-6560 (Electronic)).
  21. Koch, F.J., et al., *Note: Gratings on low absorbing substrates for x-ray phase contrast imaging*. Review of Scientific Instruments, 2015. **86**(12): p. 126114.
  22. Birnbacher, L., et al., *Experimental Realisation of High-sensitivity Laboratory X-ray Grating-based Phase-contrast Computed Tomography*. Scientific Reports, 2016. **6**(1): p. 24022.
  23. Danays Kunka, J.M., Vladimir, et al., *Characterization method for new resist formulations for HAR patterns made by X-ray lithography*. Microsyst Technologies, 2014. **20**: p. 2023–2029
  24. Broers, A.N., M.E. Welland, and J.K. Gimzewski, *Fabrication limits of electron beam lithography and of UV, X-ray and ion-beam lithographies*. Philosophical Transactions of the Royal Society of London. Series A: Physical and Engineering Sciences, 1995. **353**(1703): p. 291-311.
  25. Yang, R. and W. Wang, *A numerical and experimental study on gap compensation and wavelength selection in UV-lithography of ultra-high aspect ratio SU-8 microstructures*. Sensors and Actuators B: Chemical, 2005. **110**(2): p. 279-288.
  26. Chan-Park, M.B., et al., *Fabrication of large SU-8 mold with high aspect ratio microchannels by UV exposure dose reduction*. Sensors and Actuators B: Chemical, 2004. **101**(1–2): p. 175-182.
  27. Turner, S.R. and R.C. Daly, *7 - Photochemical and Radiation Sensitive Resists*, in *Comprehensive Polymer Science and Supplements*, G. Allen and J.C. Bevington, Editors. 1989, Pergamon: Amsterdam. p. 193-225.
  28. Henderson, C.L., *Thick Resist Lithography*, in *Encyclopedia of Microfluidics and Nanofluidics*, D. Li, Editor. 2008, Springer US: Boston, MA. p. 2073-2079.
  29. Jiguet, S., et al., *SU-8 nanocomposite coatings with improved tribological performance for MEMS*. Surface and Coatings Technology, 2006. **201**(6): p. 2289-2295.
  30. Gut, K., *Bimodal Layers of the Polymer SU8 as Refractometer*. Procedia Engineering, 2012. **47**(0): p. 326-329.
  31. Hill, G.C., et al., *SU-8 MEMS Fabry-Perot pressure sensor*. Sensors and Actuators A: Physical, 2007. **138**(1): p. 52-62.
  32. Mehdizadeh, S., et al., *The Influence of Lithographic Patterning on Current Distribution: A Model for Microfabrication by Electrodeposition*. Journal of The Electrochemical Society, 1992. **139**(1): p. 78-91.
  33. Mehdizadeh, S., et al., *The Influence of Lithographic Patterning on Current Distribution in Electrodeposition: Experimental Study and Mass - Transfer Effects*. Journal of The Electrochemical Society, 1993. **140**(12): p. 3497-3505.
  34. Hydes, P.C. and H. Middleton, *The sulphito complexes of gold*. Gold Bulletin, 1979. **12**(3): p. 90-95.
  35. Charles, B., D. Yohannes, and K. Kevin, *Ultra-deep x-ray lithography of densely packed SU-8 features: II. Process performance as a function of dose, feature height and post exposure bake temperature*. Journal of Micromechanics and Microengineering, 2005. **15**(6): p. 1249.
  36. Cheng, C.-M. and R.-H. Chen, *Key issues in fabricating microstructures with high aspect ratios by using deep X-ray lithography*. Microelectronic Engineering, 2004. **71**(3–4): p. 335-342.
  37. Kang, W.-J., et al., *Novel exposure methods based on reflection and refraction effects in the field of SU-8 lithography*. Journal of Micromechanics and Microengineering, 2006. **16**(4): p. 821.
  38. Kondo, T., S. Juodkazis, and H. Misawa, *Reduction of capillary force for high-aspect ratio nanofabrication*. Applied Physics A, 2005. **81**(8): p. 1583-1586.

39. Koukharenko, E., et al., *A comparative study of different thick photoresists for MEMS applications*. Journal of Materials Science: Materials in Electronics, 2005. **16**(11-12): p. 741-747.
40. Peele, A.G., et al., *Overcoming SU-8 stiction in high aspect ratio structures*. Microsystem Technologies, 2005. **11**(2-3): p. 221-224.
41. Williams, J.D. and W. Wang, *Using megasonic development of SU-8 to yield ultra-high aspect ratio microstructures with UV lithography*. Microsystem Technologies, 2004. **10**(10): p. 694-698.
42. Yeh, W.-M., *PATTERN COLLAPSE IN LITHOGRAPHIC NANOSTRUCTURES: QUANTIFYING PHOTORESIST NANOSTRUCTURE BEHAVIOR AND NOVEL METHODS FOR COLLAPSE MITIGATION*. 2013.
43. Yoshio, Y., *S u b -0.1 μ m Patterning with High Aspect Ratio of 5 Achieved by Preventing Pattern Collapse*. Japanese Journal of Applied Physics, 1996. **35**(4R): p. 2385.
44. Ruano-López, J.M., et al., *A new SU-8 process to integrate buried waveguides and sealed microchannels for a Lab-on-a-Chip*. Sensors and Actuators B: Chemical, 2006. **114**(1): p. 542-551.
45. M.Bednorz, M.U., T.Pustelny, A.Piotrowska, E.Papis, Z.Sidor, E.Kamińska, *Application od SU8 polymer in waveguide interferometer ammonia sensor*. Molecular and Quantum Acoustics, 2006. **27**: p. 10.
46. Bogunovic, L., D. Anselmetti, and J. Regtmeier, *Photolithographic fabrication of arbitrarily shaped SU-8 microparticles without sacrificial release layers*. Journal of Micromechanics and Microengineering, 2011. **21**(2): p. 027003.
47. Jiguet, S., et al., *SU-8 nanocomposite photoresist with low stress properties for microfabrication applications*. Microelectronic Engineering, 2006. **83**(10): p. 1966-1970.
48. Zhang, J., K.L. Tan, and H.Q. Gong, *Characterization of the polymerization of SU-8 photoresist and its applications in micro-electro-mechanical systems (MEMS)*. Polymer Testing, 2001. **20**(6): p. 693-701.
49. MacDonald, S.A., H. Ito, and C.G. Willson, *Advances in the design of organic resist materials*. Microelectronic Engineering, 1983. **1**(4): p. 269-293.
50. Willson, C., R. Dammel, and A. Reiser, *Photoresist materials: A historical perspective*. Proceedings of SPIE - The International Society for Optical Engineering, 1997. **3050**.
51. Wikimedia Commons. *First successful permanent photograph from nature*. Available from: [https://upload.wikimedia.org/wikipedia/commons/e/e8/Point\\_de\\_vue\\_du\\_Gras\\_by\\_Ni%C3%A9pce%2C\\_1826.jpg](https://upload.wikimedia.org/wikipedia/commons/e/e8/Point_de_vue_du_Gras_by_Ni%C3%A9pce%2C_1826.jpg). Accessed on 12.03.2021
52. Wikimedia Commons. *Point de vue du Gras*. Available from: [https://commons.wikimedia.org/wiki/File:View\\_from\\_the\\_Window\\_at\\_Le\\_Gras,\\_Joseph\\_Nic%C3%A9pore\\_Ni%C3%A9pce.jpg](https://commons.wikimedia.org/wiki/File:View_from_the_Window_at_Le_Gras,_Joseph_Nic%C3%A9pore_Ni%C3%A9pce.jpg). accessed on 12.03.2021
53. Wikimedia Commons. *Heliography of Joseph Nicephore Niepce*. Available from: [https://upload.wikimedia.org/wikipedia/commons/2/2f/Cardinal\\_Georges\\_D%27Amboise\\_Heliograph\\_Engraving\\_Joseph\\_Niepce.jpg](https://upload.wikimedia.org/wikipedia/commons/2/2f/Cardinal_Georges_D%27Amboise_Heliograph_Engraving_Joseph_Niepce.jpg). Accessed on 14.03.2021
54. Willson, C.G., *Organic Resist Materials — Theory and Chemistry*, in *Introduction to Microlithography*. 1983, AMERICAN CHEMICAL SOCIETY. p. 87-159.
55. Wang, X., et al., *Gelatin-Based Hydrogels for Organ 3D Bioprinting*. Polymers, 2017. **9**(9).
56. Blyth, J., C. Lowe, and J. Pecora, *Improving the remarkable photosensitivity of dichromated gelatin for hologram recording in green laser light*. 2006.
57. Wu, L.E., et al., *Carcinogenic Chromium(VI) Compounds Formed by Intracellular Oxidation of Chromium(III) Dietary Supplements by Adipocytes*. Angewandte Chemie International Edition, 2016. **55**(5): p. 1742-1745.
58. George H. Smith, J.A.B., *Photosolubilizable Compositions and Elements*. 1973. p. 12.

59. Crivello, J.V. and J.H.W. Lam, *Photosensitive polymers containing diaryliodonium salt groups in the main chain*. Journal of Polymer Science: Polymer Chemistry Edition, 1979. **17**(12): p. 3845-3858.
60. Ito, H., *Chemical amplification resists for microlithography*, in *Advances in Polymer Science*. 2005. p. 37-245.
61. Tarascon, R.G., et al., *Poly(t-BOC-styrene sulfone)-based chemically amplified resists for deep-UV lithography*. Polymer Engineering & Science, 1989. **29**(13): p. 850-855.
62. Chris, A.S., A.M. Scott, and S. Hubert. *Silylation of poly (t-BOC) styrene resists: performance and mechanisms*. in *Proc.SPIE*. 1990.
63. Yoshiyuki T., N.-s.Y., *EP0440376A2 - Process for forming pattern*. 1991.
64. Taylor, G.N., *Gas-Phase-Functionalized Plasma-Developed Resists:Initial Concepts and Results for Electron-Beam Exposure*. Journal of The Electrochemical Society, 1984. **131**(7): p. 1658.
65. Brien, J.O., et al., *Advanced photoresist technologies for microsystems*. Journal of Micromechanics and Microengineering, 2001. **11**(4): p. 353.
66. Gelorme; Jeffrey D., C.R.J., Gutierrez; Sergio A. R., *Photoresist composition and printed circuit boards and packages made therewith* 1989, International Business Machines Corporation (IBM). p. 16.
67. Dargent, T., et al., *Micromachining of an SU-8 flapping-wing flying micro-electro-mechanical system*. Journal of Micromechanics and Microengineering, 2009. **19**(8): p. 085028.
68. Chuang, Y.J., F.G. Tseng, and W.K. Lin, *Reduction of diffraction effect of UV exposure on SU-8 negative thick photoresist by air gap elimination*. Microsystem Technologies, 2002. **8**(4-5): p. 308-313.
69. Arana, N., et al., *SU8 protective layers in liquid operating SAWs*. Sensors and Actuators B: Chemical, 2006. **118**(1-2): p. 374-379.
70. Campo, A.d. and C. Greiner, *SU-8: a photoresist for high-aspect-ratio and 3D submicron lithography*. Journal of Micromechanics and Microengineering, 2007. **17**(6): p. R81.
71. De Vittorio, M., et al., *Two-dimensional photonic crystal waveguide obtained by e-beam direct writing of SU8-2000 photoresist*. Microelectronic Engineering, 2004. **73-74**(0): p. 388-391.
72. Becnel, C., Y. Desta, and K. Kelly, *Ultra-deep x-ray lithography of densely packed SU-8 features: I. An SU-8 casting procedure to obtain uniform solvent content with accompanying experimental results*. Journal of Micromechanics and Microengineering, 2005. **15**(6): p. 1242.
73. Kalaiselvi, S.M.P., et al., *X-ray lithography of SU8 photoresist using fast miniature plasma focus device and its characterization using FTIR spectroscopy*. Physics Letters A, 2015. **379**(6): p. 560-569.
74. Mark, J.E., *Polymer Data Handbook*. 2009: Oxford University Press.
75. Vlnieska, V., et al., *Epoxy Resins for Negative Tone Photoresists*. Polymers, 2019. **11**(9).
76. Vlnieska, V., et al., *Lithographic Performance of Aryl Epoxy Thermoset Resins as Negative Tone Photoresist for Microlithography*. Polymers, 2020. **12**(10).
77. Semenov, A.N. and I.A. Nyrkova, *1.02 - Statistical Description of Chain Molecules*, in *Polymer Science: A Comprehensive Reference*, K. Matyjaszewski and M. Möller, Editors. 2012, Elsevier: Amsterdam. p. 3-29.
78. Field, L.D., S. Sternhell, and J.R. Kalman, *Organic Structures from Spectra*. 2002: Wiley.
79. Silverstein, R.M., F.X. Webster, and D.J. Kiemle, *Spectrometric identification of organic compounds*. 2005: John Wiley & Sons.
80. Rath, S.K., F.Y.C. Boey, and M.J.M. Abadie, *Cationic electron - beam curing of a high - functionality epoxy: effect of post - curing on glass transition and conversion*. Polymer International, 2004. **53**(7): p. 857-862.

81. Mustata, F., N. Tudorachi, and I. Bicu, *The kinetic study and thermal characterization of epoxy resins crosslinked with amino carboxylic acids*. Journal of Analytical and Applied Pyrolysis, 2015. **112**: p. 180-191.
82. Tirta, A., et al., *Fabrication of porous material for micro component application by direct X-ray lithography and sintering*. Microelectronic Engineering, 2012. **98**: p. 297-300.
83. Mautjana, N.A. and H. Pasch, *Matrix-Assisted Laser Desorption Ionization Mass Spectrometry of Synthetic Polymers*. Macromolecular Symposia, 2012. **313-314**(1): p. 157-161.
84. Puglisi, C., et al., *MALDI-TOF Investigation of Polymer Degradation. Pyrolysis of Poly(bisphenol A carbonate)*. Macromolecules, 1999. **32**(26): p. 8821-8828.
85. Bahr, U., et al., *Mass spectrometry of synthetic polymers by UV-matrix-assisted laser desorption/ionization*. Analytical Chemistry, 1992. **64**(22): p. 2866-2869.
86. Esser, E., et al., *Matrix-assisted laser desorption/ionization mass spectrometry of synthetic polymers. 4. Coupling of size exclusion chromatography and MALDI-TOF using a spray-deposition interface*. Polymer, 2000. **41**(11): p. 4039-4046.
87. Du, G., et al., *Synthesis-structure-performance relationship of cocondensed phenol-urea-formaldehyde resins by MALDI-ToF and <sup>13</sup>C NMR*. Journal of Applied Polymer Science, 2008. **110**(2): p. 1182-1194.
88. Murgasova, R. and D.M. Hercules, *MALDI of synthetic polymers—an update*. International Journal of Mass Spectrometry, 2003. **226**(1): p. 151-162.
89. Schrod, M., et al., *Matrix-assisted laser desorption/ionization mass spectrometry of synthetic polymers. VI. Analysis of phenol-urea-formaldehyde cocondensates*. Journal of Applied Polymer Science, 2003. **90**(9): p. 2540-2548.
90. Belu, A.M., et al., *Evaluation of matrix-assisted laser desorption ionization mass spectrometry for polymer characterization*. Journal of the American Society for Mass Spectrometry, 1996. **7**(1): p. 11-24.
91. Jahanshahi, S., et al., *MALDI-TOF, <sup>13</sup>C NMR and FT-MIR analysis and strength characterization of glycidyl ether tannin epoxy resins*. Industrial Crops and Products, 2016. **83**: p. 177-185.
92. Hoong, Y.B., et al., *Phenol-urea-formaldehyde resin co-polymer synthesis and its influence on Elaeis palm trunk plywood mechanical performance evaluated by <sup>13</sup>C NMR and MALDI-TOF mass spectrometry*. International Journal of Adhesion and Adhesives, 2015. **63**: p. 117-123.
93. Clayden, J., N. Greeves, and S. Warren, *Organic Chemistry*. 2012: OUP Oxford.
94. Komorowska-Durka, M., et al., *A concise review on microwave-assisted polycondensation reactions and curing of polycondensation polymers with focus on the effect of process conditions*. Chemical Engineering Journal, 2015. **264**: p. 633-644.
95. Lewicki, J.P., C.A. Fox, and M.A. Worsley, *On the synthesis and structure of resorcinol-formaldehyde polymeric networks – Precursors to 3D-carbon macroassemblies*. Polymer, 2015. **69**: p. 45-51.
96. Jenkins, A.D., *Polymer Science: A Materials Science Handbook*. 2013: Elsevier Science.
97. Canevarolo, S.V., *Polymer characterization techniques*. 2004: Artliber.
98. Meyer, T. and J. Keurentjes, *Handbook of polymer reaction engineering*. 2005: Wiley-VCH.
99. Nordt, S., *Analytik von Novolak-Epoxidharzen für die Resistentwicklung in der Mikrosystemtechnik, in Fachbereich Chemie*. 2010, Technischen Universität Darmstadt: Darmstadt.
100. Dorsey, J.G., et al., *Determination of the epoxide equivalent weight of glycidyl ethers by proton magnetic resonance spectrometry*. Analytical Chemistry, 1977. **49**(8): p. 1144-1145.
101. Fleming, W.W., *Carbon-13 NMR characterization of DGEBA epoxy resins*. Journal of Applied

Polymer Science, 1985. **30**(7): p. 2853-2862.

102. Garcia, F.G. and B.G. Soares, *Determination of the epoxide equivalent weight of epoxy resins based on diglycidyl ether of bisphenol A (DGEBA) by proton nuclear magnetic resonance*. Polymer Testing, 2003. **22**(1): p. 51-56.
103. March, J.S., Michael B., *March's Advanced Organic Chemistry: Reactions, Mechanisms, and Structure, Sixth Edition*. 2007: John Wiley & Sons, Inc. .
104. Bodfors, S., *Über die Einwirkung des Lichts auf Ketoxidverbindungen*. Berichte der deutschen chemischen Gesellschaft, 1918. **51**(1): p. 214-219.
105. *Introduction to Plastics and Elastomers*, in *Chemical Resistance of Thermoplastics*, W.A. Woishnis and S. Ebnesajjad, Editors. 2012, William Andrew Publishing: Oxford. p. xxi-xxxiv.
106. Zakharova, M., et al., *Development and Characterization of Two-Dimensional Gratings for Single-Shot X-ray Phase-Contrast Imaging*. Applied Sciences, 2018. **8**(3).

# 9 Appendix A

## 9.1 Scientific supporting information

### List of Figures

<b>Figure 1:</b> Conventional X-ray imaging setup .....	2
<b>Figure 2:</b> Three contrast modalities in a grating-based interferometer: (a) attenuation (transmission) of the X-ray beam, (b) phase shift, and (c) scattering produced by the sample. Additionally, the reference and sample signals are shown on the right side, adapted from Pfeiffer et al., 2013 [3] (Elsevier and Copyright Clearance Center, license number 5060261297355).....	3
<b>Figure 3:</b> General X-ray interferometric imaging system with a laboratory source.....	4
<b>Figure 4:</b> Comparison of a Teflon (PTFE) and natural rubber plastic tubes: (a) conventional X-ray transmission image, (b) dark-field contrast image, (c) differential-phase contrast image, (d) intensity oscillations extracted from a series of eight measurements in an interferometric setup. Images from Pfeiffer et al. (2008) [16] (Springer Nature and Copyright Clearance Center, license number 5060290933842) ....	5
<b>Figure 5:</b> Comparison between conventional X-ray image and images generated based on the Talbot effect. (a) Conventional X-ray radiography. (b) Dark-field contrast. In the upper part, between (a) and (b), Phase contrast imaging. Reproduced from Gkoumas et al. (2016) [18] (Elsevier and Copyright Clearance Center, license number 5060300022673) .....	6
<b>Figure 6:</b> Grating design and concepts of aspect ratio and period .....	7
<b>Figure 7:</b> Images of a gold HAR grating. (a) 5 x5 cm <sup>2</sup> grating. (b) SEM picture showing the lamella height of the grating. (c) SEM picture showing the periodicity of the grating. The grating was produced trough X-ray lithography technology (IMT and Kara – KIT, Karlsruhe - Germany).....	9
<b>Figure 8:</b> Defects during the microfabrication process using lithography technology: (a) unwanted cross-links, (b) lamellae deformation, (c) HAR structure collapse, (d) cracks (e) bubbles, (f) poor adhesion (non-homogeneity in the focusing imaging at microscope). Reproduced from Vlnieska et al (2018) [4] (CC BY).....	10
<b>Figure 9:</b> Main processing steps used in the lithography process (details see text) .....	11
<b>Figure 10:</b> Example of commercially available substrates.....	11
<b>Figure 11:</b> Schematic drawing representing the spin coating and soft bake steps.....	12
<b>Figure 12:</b> Exposure step at LITHO 2 beamline at KARA - KIT (Karlsruhe - Germany).....	13
<b>Figure 13:</b> Positive and negative-tone photoresists adapted from Henderson (1978) [28] (Springer Nature and Copyright Clearance Center, license number 5060300885010).....	13
<b>Figure 14:</b> Electrodepositing bath located in the cleanroom facilities at IMT- KIT (Karlsruhe-Germany)	14
<b>Figure 15:</b> electrochemical reactions for Gold sulfite salt. (a) Standard reduction potential. (b) Chemical reduction of Gold in neutral pH. (c) Chemical reduction with a pH above 8.0. Adapted from Hydes et al.(1979) [34] (Copyright under open access license).....	15
<b>Figure 16:</b> Parameters to control correlated with the lithographic steps .....	15

<b>Figure 17:</b> The famous “ <i>Point de vue du Gras</i> ”, first Niépce’s permanent photograph: a) pewter plate after development, b) reproduction of the pewter plate. Both images are under public domain, via Wikimedia Commons [51, 52] .....	17
<b>Figure 18:</b> Comparison between the original engraving and the heliography of Joseph Nicéphore Niepce: a) engraving of "Portrait of Georges d'Amboise" (1650), b) heliography of the engraving (1826). Both images are under public domain, via Wikimedia Commons [53].....	18
<b>Figure 19:</b> Dichromate gelatin formulation. (a) Gelatin and ammonium dichromate. (b) reduction of chromium 7+ to chromium 5+ . (c) reduction of chromium 5+ to chromium 3+,schematics adapted from Wang et al. (2017) (CC BY) and Blyth et al. (2006) (CC BY) [55, 56] .....	18
<b>Figure 20:</b> Photoresist of Louis Minsk. In (a), preparation of the poly(vinylcinnamate) through the esterification of poly(vinylalcohol) with cinnamic acid. In (b), exposure of poly(vinylcinnamate), resulting in the dimerization between two polymeric chains (crosslinking).....	20
<b>Figure 21:</b> 2,6-bis(4-azidobenzal)-4-methylcyclohexanone, bis-azide proposed by Hans Wagner .....	21
<b>Figure 22:</b> Chemical reactions of the Blueprint resist from Kalle Company .....	22
<b>Figure 24:</b> THP-Novolac system. Positive-tone photoresist developed by Smith and Bonham .....	23
<b>Figure 25:</b> First amplified photoresist produced at IBM. (a) Anionic polymerization of phthalaldehyde. (b) cleavage of poly(phthalaldehyde), catalyzed by iodonium salts, a photoacid generator .....	24
<b>Figure 26:</b> Poly( <i>t</i> -bocstyrene) and its deprotection reaction. Poly(vinylphenol) is the main product.....	24
<b>Figure 27:</b> Typical contrast curves for positive and negative photoresists. Reproduced from Turner et al (1989) [27] (Elsevier and Copyright Clearance Center, license number 5060361388160) .....	25
<b>Figure 28:</b> Ideal Contrast curves for positive and negative photoresists. The contrast curve is a logarithmic sensitivity plot showing the normalized resist thickness vs. exposure dose .....	26
<b>Figure 29:</b> Contrast curves from the same photoresist (same brand and different fabrication lots).....	26
<b>Figure 30:</b> Main chemical compounds in the SU-8 photoresist. a. Triarylsulfonium hexafluoroantimonate salts; b. Aryl-epoxy polymer; c. Butyrolactone .....	27
<b>Figure 31:</b> Crosslinking reaction for SU-8 photoresist. Reproduced from Vlnieska et al (2020) [76] (CC BY).....	28
<b>Figure 32:</b> Deep and macro levels of formulation for epoxy based photo-resins. Reproduced from Vlnieska et al (2020) [76] (CC BY).....	29
<b>Figure 33:</b> Qualitative evaluation of the photo-resins. Reproduced from Vlnieska et al (2020) [76] (CC BY).....	39
<b>Figure 34:</b> FTIR of the sample EPR-S1-b. Reproduced from Vlnieska et al (2018) [4] (CC BY) .....	45
<b>Figure 35:</b> Organic groups identified in FTIR analysis. Reproduced from Vlnieska et al (2018) [4] (CC BY).....	45
<b>Figure 36:</b> FTIR spectra for EPR-S1 and EPR-S2 photoresists. Reproduced from Vlnieska et al (2018) [4] (CC BY).....	46
<b>Figure 37:</b> TGA and derivative curve from sample EPR-S1-a. Reproduced from Vlnieska et al (2018) [4] (CC BY).....	47
<b>Figure 38:</b> TGA of the photoresists. Adapted from Vlnieska et al (2018) [4] (CC BY).....	48
<b>Figure 39:</b> Oligomer structures, their molecular masses and chemical formulas. In (a) non epoxidized oligomer; in (b) partially epoxidized oligomer, and in (c) completely epoxidized oligomer.....	49
<b>Figure 40:</b> MALDI-TOF of EPR-S1 and EPR-S2 photoresists. Reproduced from Vlnieska et al (2018) [4] (CC BY).....	50

<b>Figure 41:</b> Region of 450–1200 Da in the MALDI-TOF of EPR-S1 and EPR-S2 photoresists. Reproduced from Vlnieska et al (2018) [4] (CC BY) .....	51
<b>Figure 42:</b> Mass variation in function of the substitution epoxidation rate for the dimer molecular structure. Reproduced from Vlnieska et al (2018) [4] (CC BY) .....	51
<b>Figure 43:</b> Aryl-epoxy resin monomer and its adducts. (a) Dihydroxybenzoic acid (DHB) adduct, (b) Sodium adduct. Reproduced from Vlnieska et al (2018) [4] (CC BY) .....	53
<b>Figure 44:</b> Oligomer structures related to the mass peaks in the MALDI-TOF spectra. Reproduced from Vlnieska et al (2018) [4] (CC BY) .....	54
<b>Figure 45:</b> EPR-S1 and EPR-S2 series and its epoxidized oligomer compositions. Reproduced from Vlnieska et al (2018) [4] (CC BY) .....	55
<b>Figure 46:</b> EPR-S1 and EPR-S2 series and their non-totally epoxidized oligomer compositions. Reproduced from Vlnieska et al (2018) [4] (CC BY) .....	55
<b>Figure 47:</b> Mass polymerization of bisphenol-A and formaldehyde .....	57
<b>Figure 48:</b> Proposed mechanism for the bisphenol-A polymerization in basic medium .....	58
<b>Figure 49:</b> ESI- $\mu$ -TOF-MS spectra of the polymerization reactions R1, R2 and R3. Reproduced from Vlnieska et al (2019) [75] (CC BY) .....	59
<b>Figure 50:</b> Mass polymerization derivate products, considering the monomer as chain size example. Reproduced from Vlnieska et al (2019) [75] (CC BY) .....	60
<b>Figure 51:</b> Proposed chemical structure for the termination groups. Reproduced from Vlnieska et al (2019) [75] (CC BY) .....	60
<b>Figure 52:</b> ESI- $\mu$ -TOF-MS spectra of the mass polymerization reaction R3-c. In (a), full spectra, where the neutral <i>mers</i> and sodium adducts were identified. In (b), derivate products in the dimer region. Reproduced from Vlnieska et al (2019) [75] (CC BY) .....	61
<b>Figure 53:</b> Sodium adducts from derivate products in the dimer region spectra (mass peak measures from sample R3-c). Reproduced from Vlnieska et al (2019) [75] (CC BY) .....	62
<b>Figure 54:</b> Multiple structure assignment in the ESI- $\mu$ TOF-MS characterization technique. (a) two different structures for the same range of mass. (b) ionization of the phenol groups in one of the tetramers structure. Reproduced from Vlnieska et al (2019) [75] (CC BY) .....	64
<b>Figure 55:</b> Amplification of the dimer derivate spectra (1Na/1rad.) in the region of 515 to 530 Da. Reproduced from Vlnieska et al (2019) [75] (CC BY) .....	65
<b>Figure 56:</b> Monomer chemical structure and its derivate with labeled hydrogens. Reproduced from Vlnieska et al (2019) [75] (CC BY) .....	65
<b>Figure 57:</b> R1, R2, and R3 DSC curves. Reproduced from Vlnieska et al (2019) [75] (CC BY) .....	67
<b>Figure 58:</b> Epoxidation reaction (alkylation of the phenolic groups). Reproduced from Vlnieska et al (2019) [75] (CC BY) .....	68
<b>Figure 59:</b> Derivate from epoxidation reaction. In (a): epoxidation derivate; in (b): bisphenol-A mono-epoxy derivate; in (c): bisphenol-A di-epoxy derivate. Reproduced from Vlnieska et al (2019) [75] (CC BY) .....	69
<b>Figure 60:</b> Oligomer “p”, epoxidized oligomers “r” and “s” and its chemical structures with labeled hydrogens. Reproduced from Vlnieska et al (2019) [75] (CC BY) .....	71
<b>Figure 61:</b> Chemical structures with numbered carbons of the bisphenol-A, oligomer, and epoxidized oligomer. Reproduced from Vlnieska et al (2019) [75] (CC BY) .....	72
<b>Figure 62:</b> Possibilities of derivate during the alkylation reaction, considering the epoxidation degree until five units to one bisphenol-A. Reproduced from Vlnieska et al (2019) [75] (CC BY) .....	74

<b>Figure 63:</b> ESI- $\mu$ -TOF-MS spectra from epoxidized resins, amplified in the monomer region. Reproduced from Vlnieska et al (2019) [75] (CC BY).....	75
<b>Figure 64:</b> DSC curves of the epoxidized resins R1-ep, R2-ep and R3-ep. Reproduced from Vlnieska et al (2019) [75] (CC BY).....	76
<b>Figure 65:</b> Glass transition temperatures ( $T_g$ ) versus epoxidation degree for resin R2-b. Reproduced from Vlnieska et al (2019) [75] (CC BY).....	77
<b>Figure 66:</b> Triplicates of the laminated formulations. Reproduced from Vlnieska et al (2020) [76] (CC BY).....	81
<b>Figure 67:</b> Image from optical microscope from the formulation P <sub>2</sub> ED <sub>0</sub> C <sub>3</sub> (t3). Reproduced from Vlnieska et al (2020) [76] (CC BY).....	85
<b>Figure 68:</b> Examples of the evaluation criteria used in the quality evaluation of the photo-resins; in (a) an example of 0.0 value; in (b) an example of 0.5 value; in (c) an example of 1.0 value. Reproduced from Vlnieska et al (2020) [76] (CC BY).....	85
<b>Figure 69:</b> Amount of photoinitiator correlated with the epoxidation degree and the quality of the patterned structures	86
<b>Figure 70:</b> Epoxidation degree correlated with the amount of photoinitiator and the quality of the patterned structures	86
<b>Figure 71:</b> Averaged performance correlated with the amount of photoinitiator.....	86
<b>Figure 72:</b> Averaged performance correlated with the epoxidation degree.....	86
<b>Figure 73:</b> Design and periodicity of the chromium mask used in UV and deep-UV lithographies. Reproduced from Vlnieska et al (2020) [76] (CC BY).....	88
<b>Figure 74:</b> Best formulation composition and its chemical structures. Reproduced from Vlnieska et al (2020) [76] (CC BY).....	90

## List of Tables

<b>Table 1:</b> Equations associated with the transmission, phase contrast, and dark-field contrast [1, 5].	4
<b>Table 2:</b> Parameters and its values for the polymerization reaction	32
<b>Table 3:</b> Oligomer characteristics, quantities for the photo-resin formulations and, chemical compounds	37
<b>Table 4:</b> Evaluated negative-tone photoresists.	44
<b>Table 5:</b> Oligomer size mass peaks compared with the substitution epoxidation rate.	52
<b>Table 6:</b> Mass peaks related to oligomer sizes, epoxidation rate and type of adduct.	53
<b>Table 7:</b> Characterization of the <i>mers</i> and derivate products for R1, R2, and R3, based on the spectra presented in Figure 43 I (b), II (b), and III (b).	62
<b>Table 8 :</b> Amplified <sup>1</sup> HNMR spectra of the samples bisphenol-A, R1, R2, and R3.	66
<b>Table 9:</b> R1, R2 and R3 substitution ratios.	67
<b>Table 10:</b> <sup>1</sup> H NMR spectra (zoom in) for the samples P1, P1-ep; P2, P2-ep, and P3; P3-ep	70
<b>Table 11:</b> Epoxidation ratio for the samples R1-ep, R2-ep, and R3-ep.”	71
<b>Table 12:</b> <sup>13</sup> C NMR shift values (ppm) for the samples bisphenol-A, R1, R2, R3, R1-ep, R2-ep and R3-ep	72
<b>Table 13:</b> Relative percentage ratio of the atoms for non-epoxidized and epoxidized resins	73
<b>Table 14:</b> Molar ratio for epoxy groups versus integral values	76
<b>Table 15:</b> Glass transition temperatures and slopes of the R2-b epoxy resins.	78
<b>Table 16:</b> Images of the photo-resin formulations after lamination, UV-exposure, and hard bake.	82
<b>Table 17:</b> Images of the photo-resin formulations after development.	83
<b>Table 18:</b> Quality control for the evaluation of the photo-resin formulations	84
<b>Table 19:</b> Comparison between formulations and structures performed through UV and DUV lithography techniques	88

## Full spectra and extra images

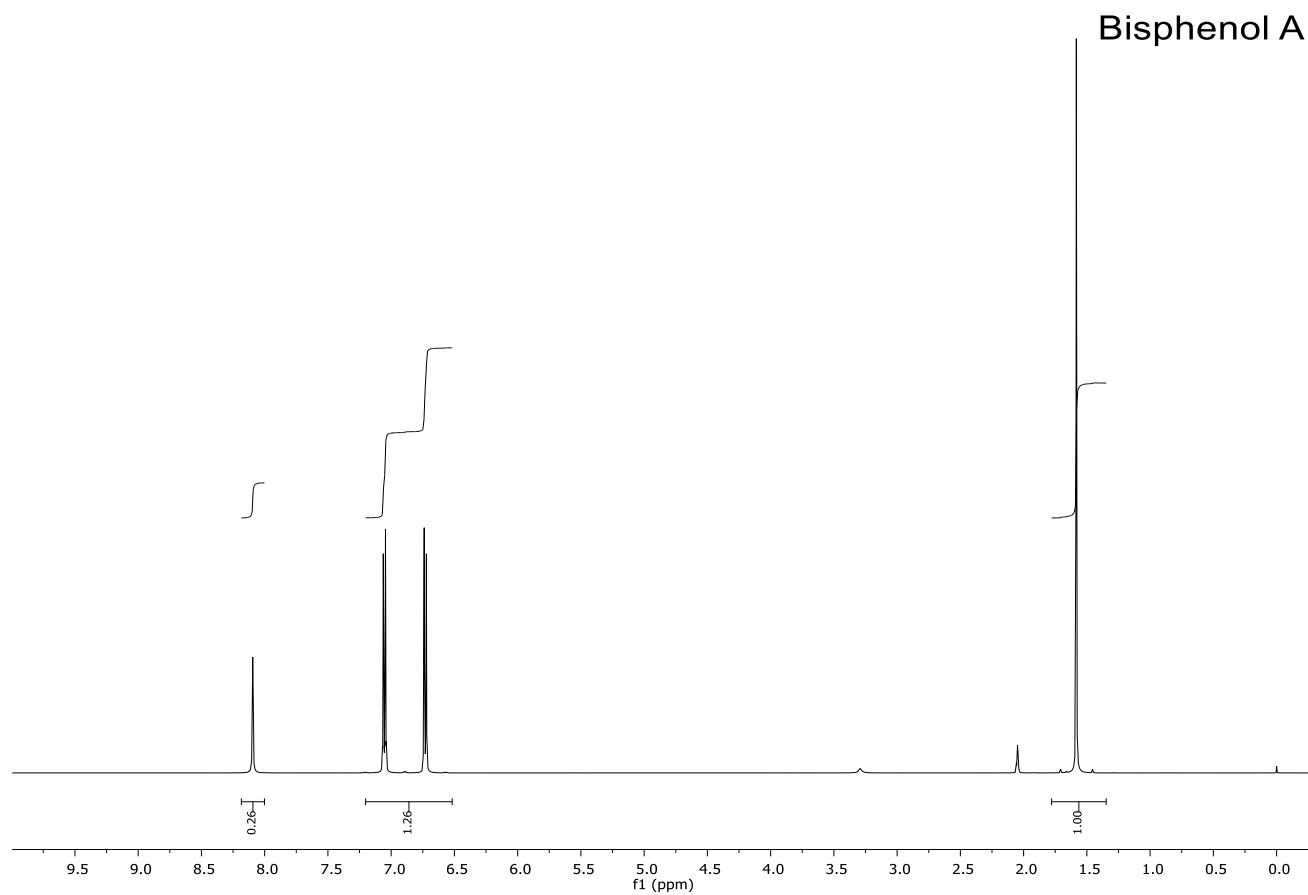


**Figure A1:** Bisphenol-A spectra ( $^1\text{H}$  NMR)

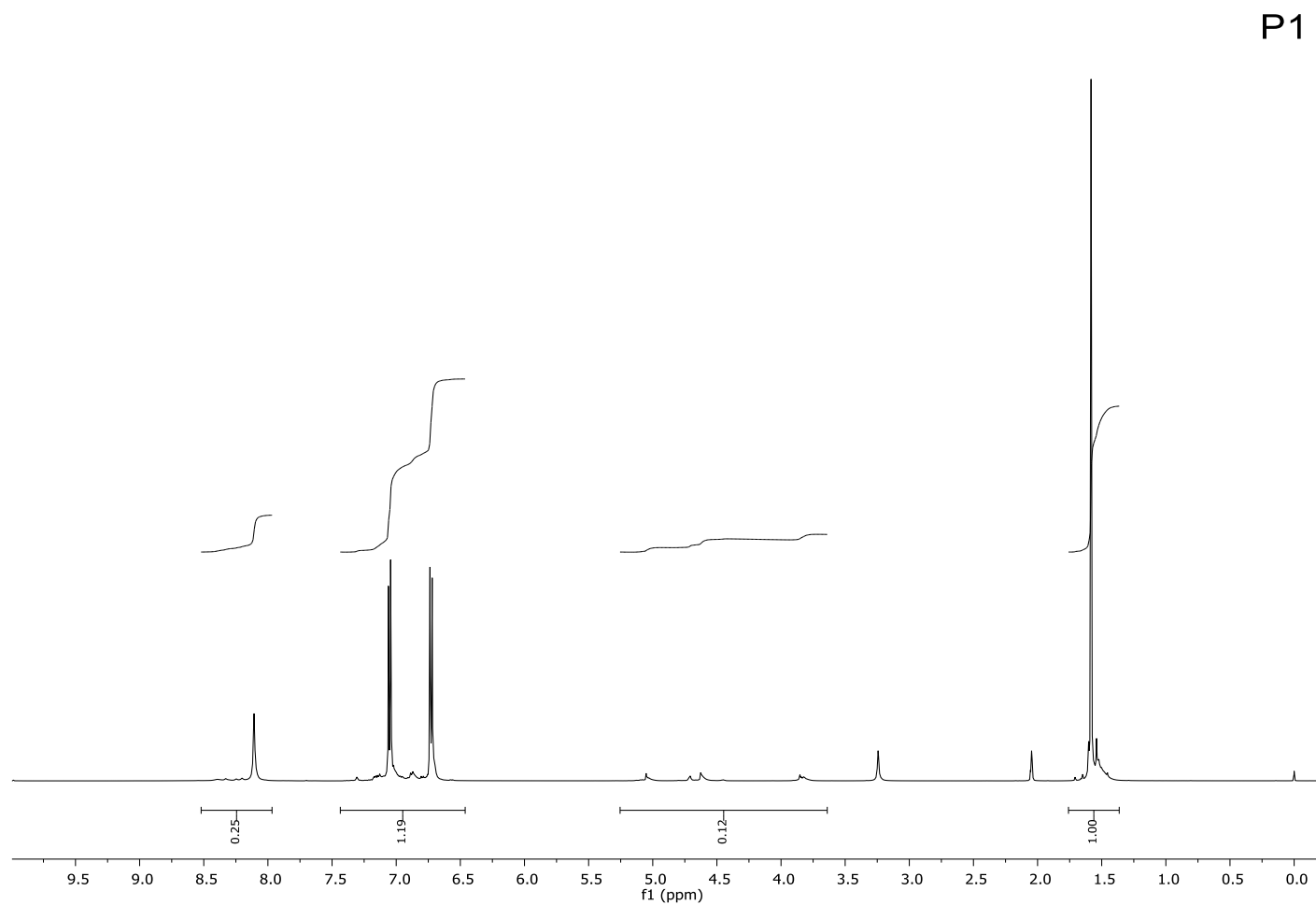


**Figure A2:** Resin 1 spectra (<sup>1</sup>H NMR)

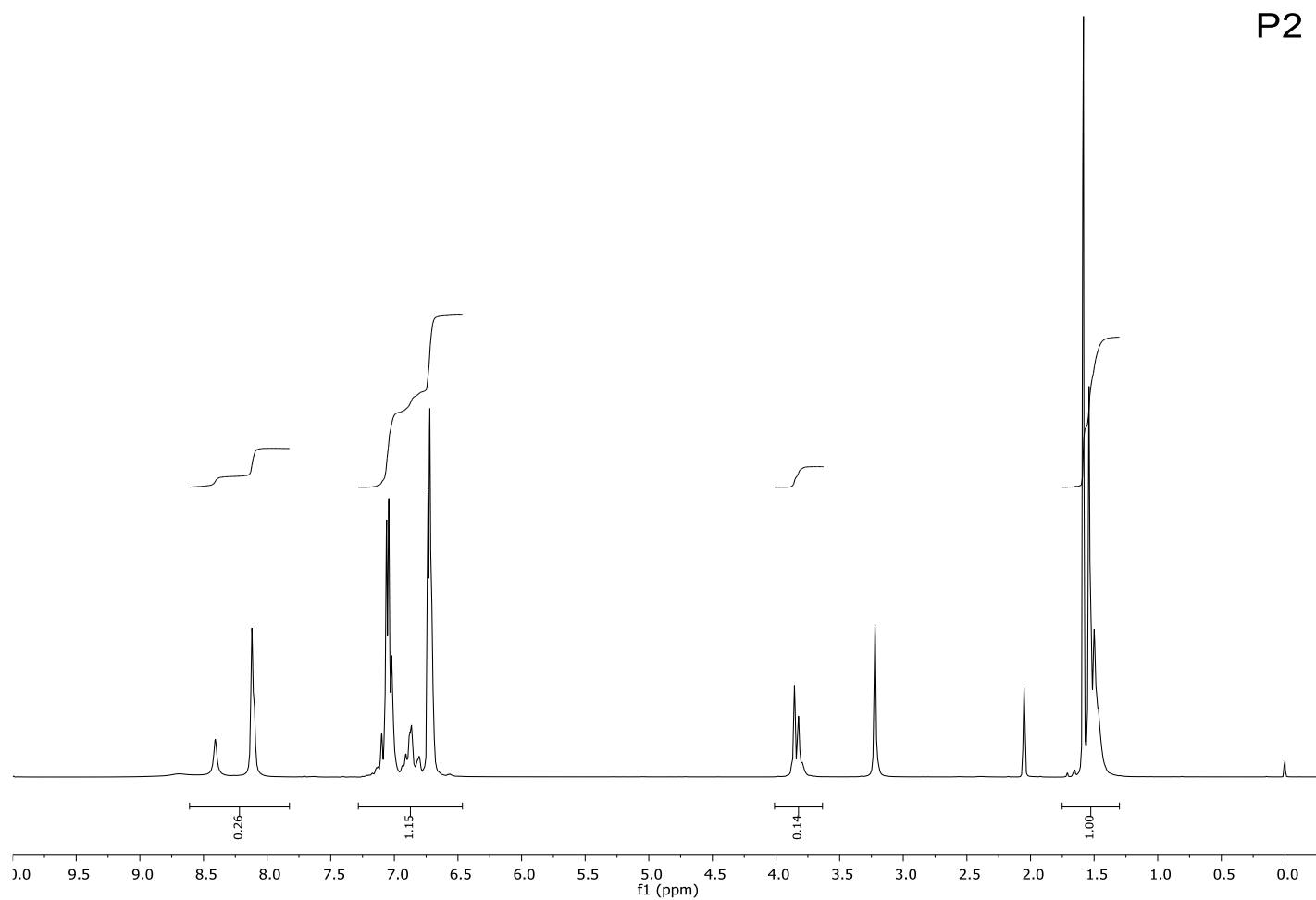


Figure A3: Resin 2 spectra ( $^1\text{H}$  NMR)

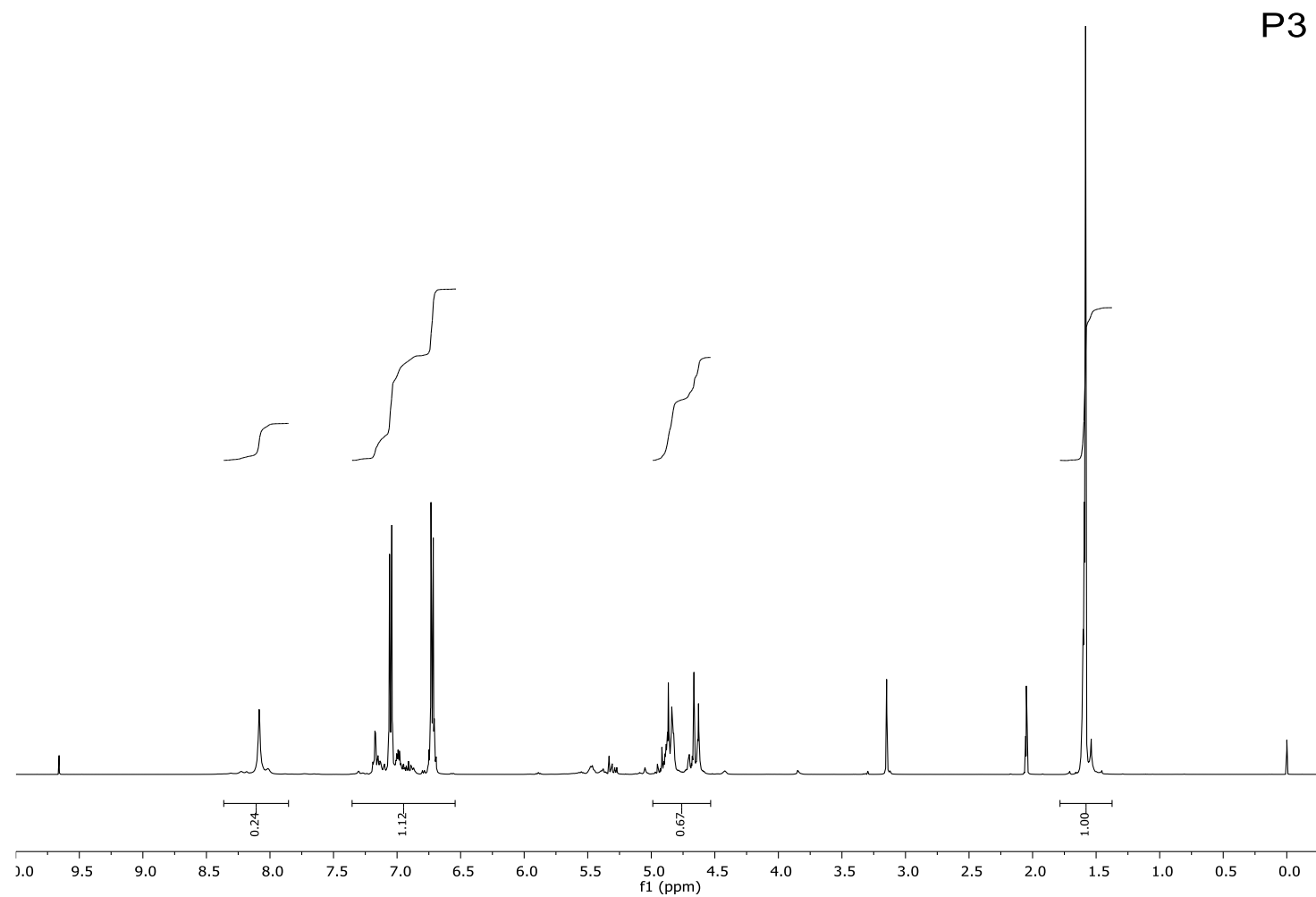


Figure A4: Resin 3 spectra ( $^1\text{H}$  NMR)

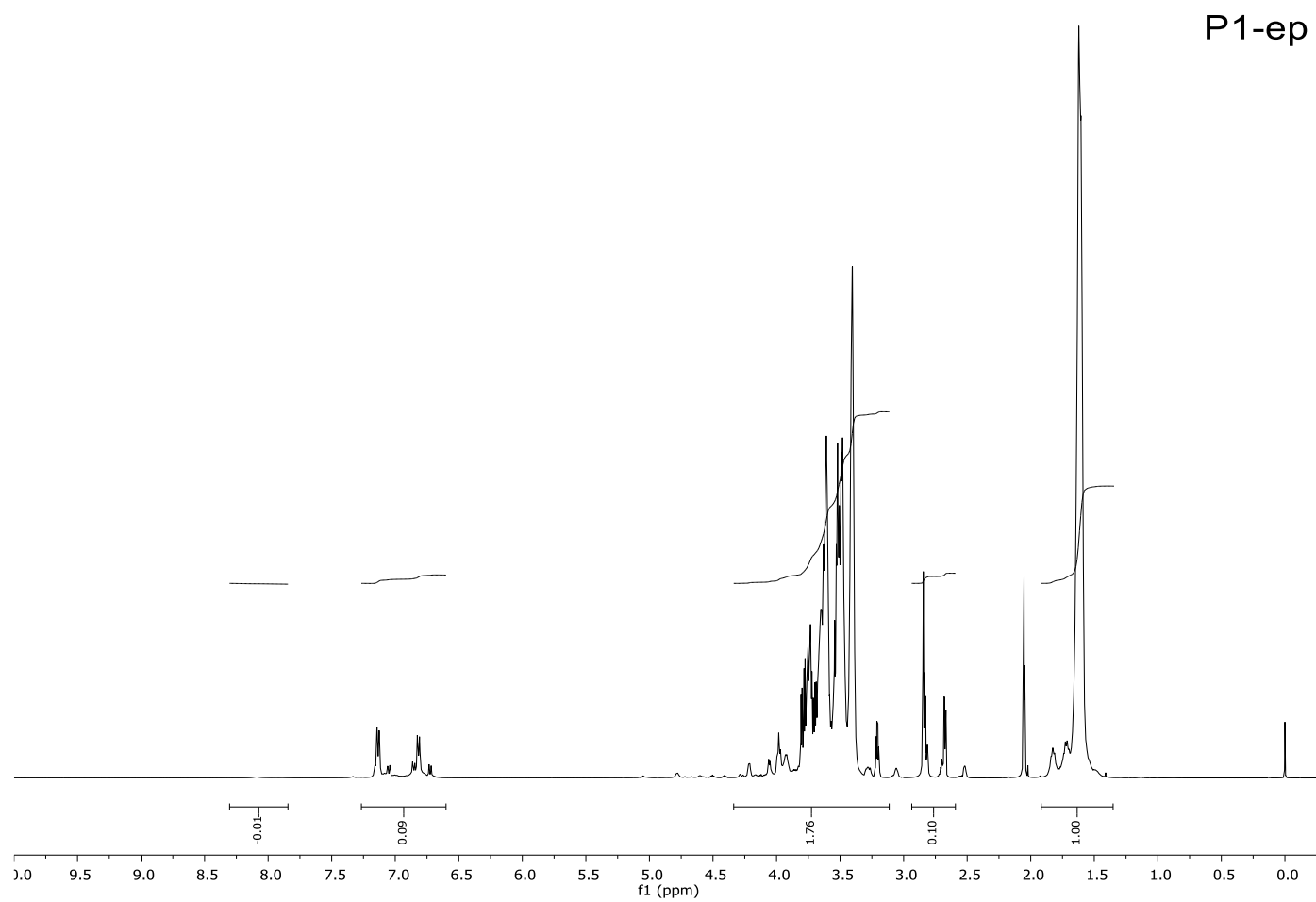
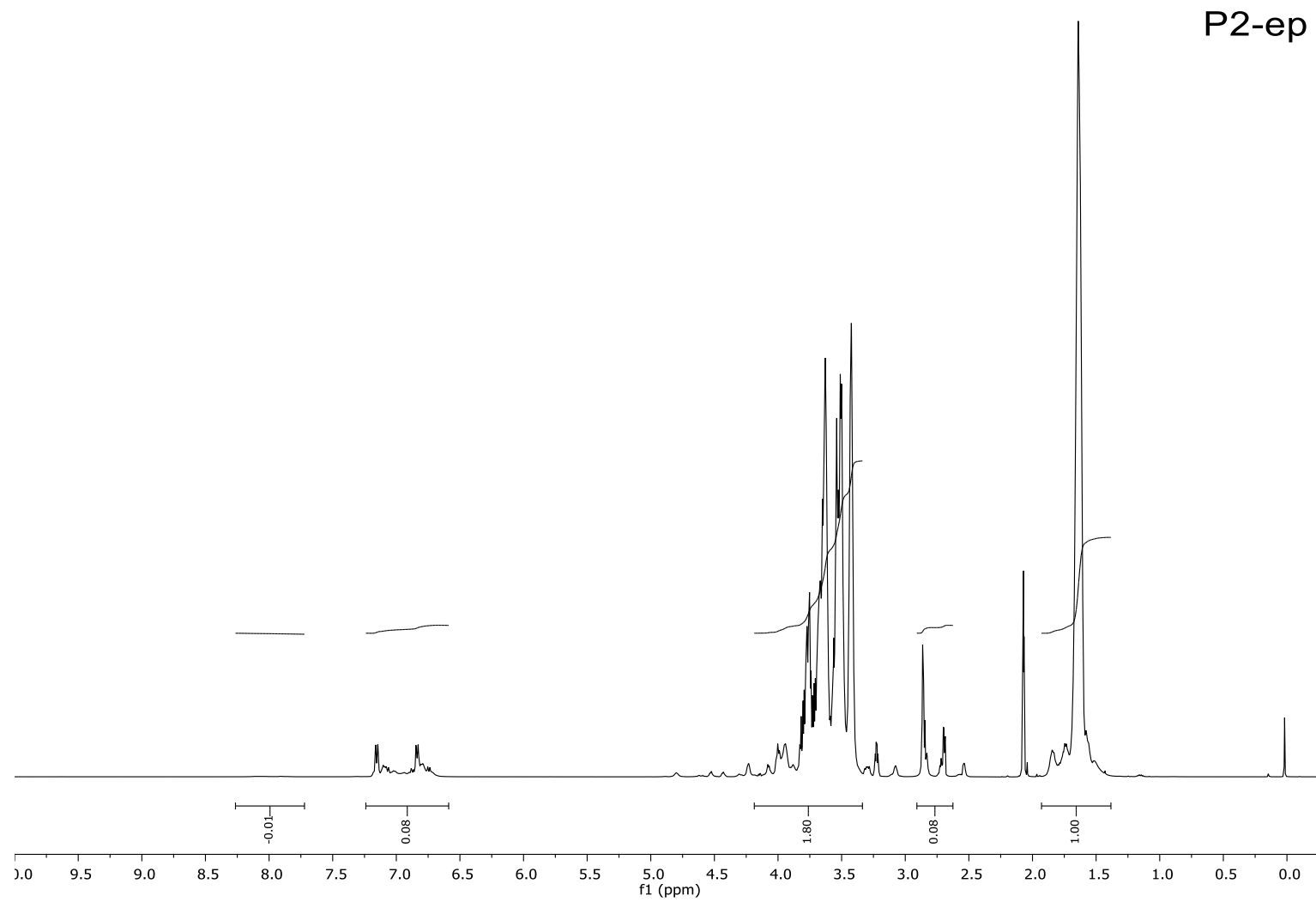


Figure A5: Epoxidized resin 1 spectra ( $^1\text{H}$  NMR)



**Figure A6:** Epoxidized resin 2 spectra ( $^1\text{H}$  NMR)

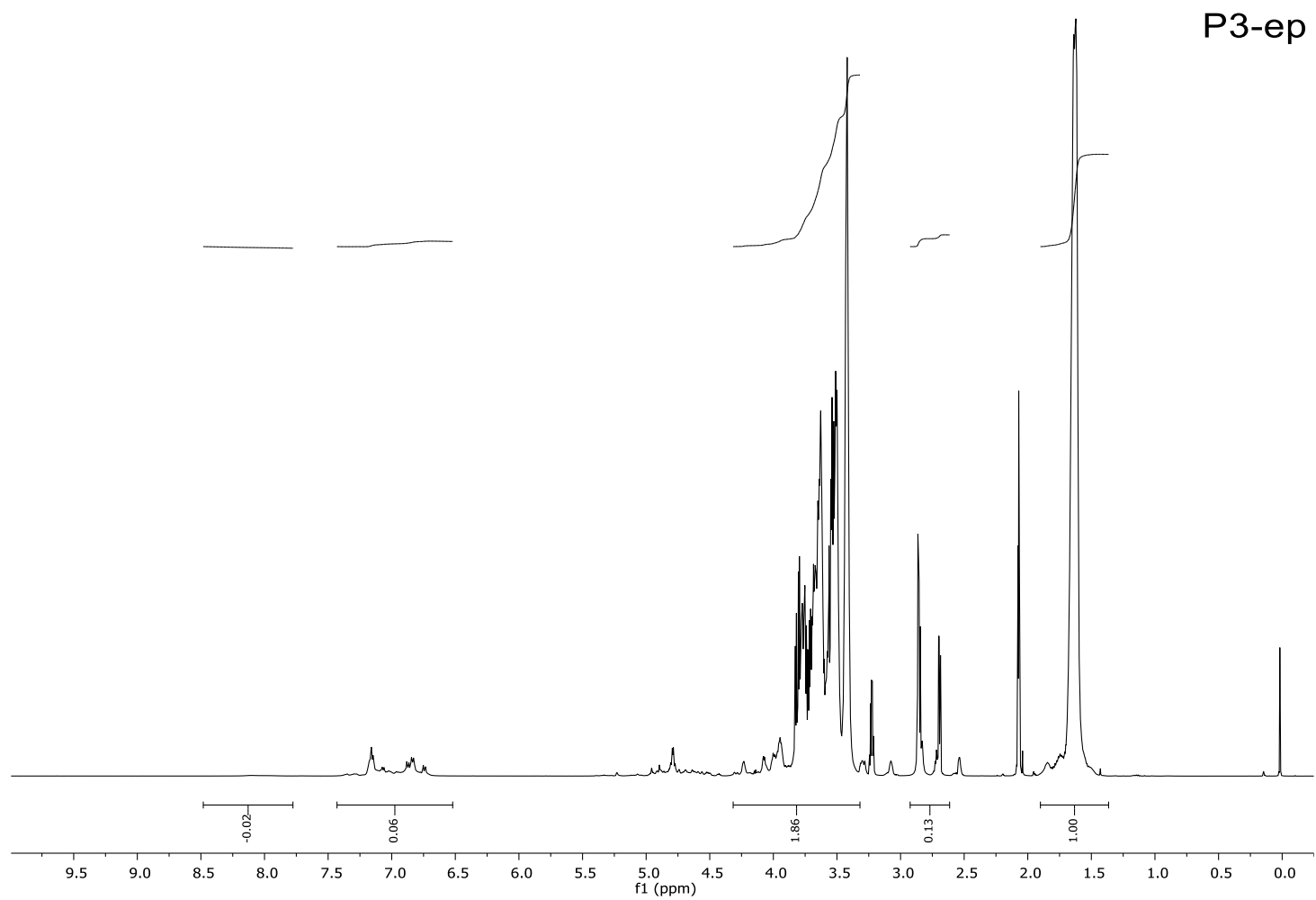
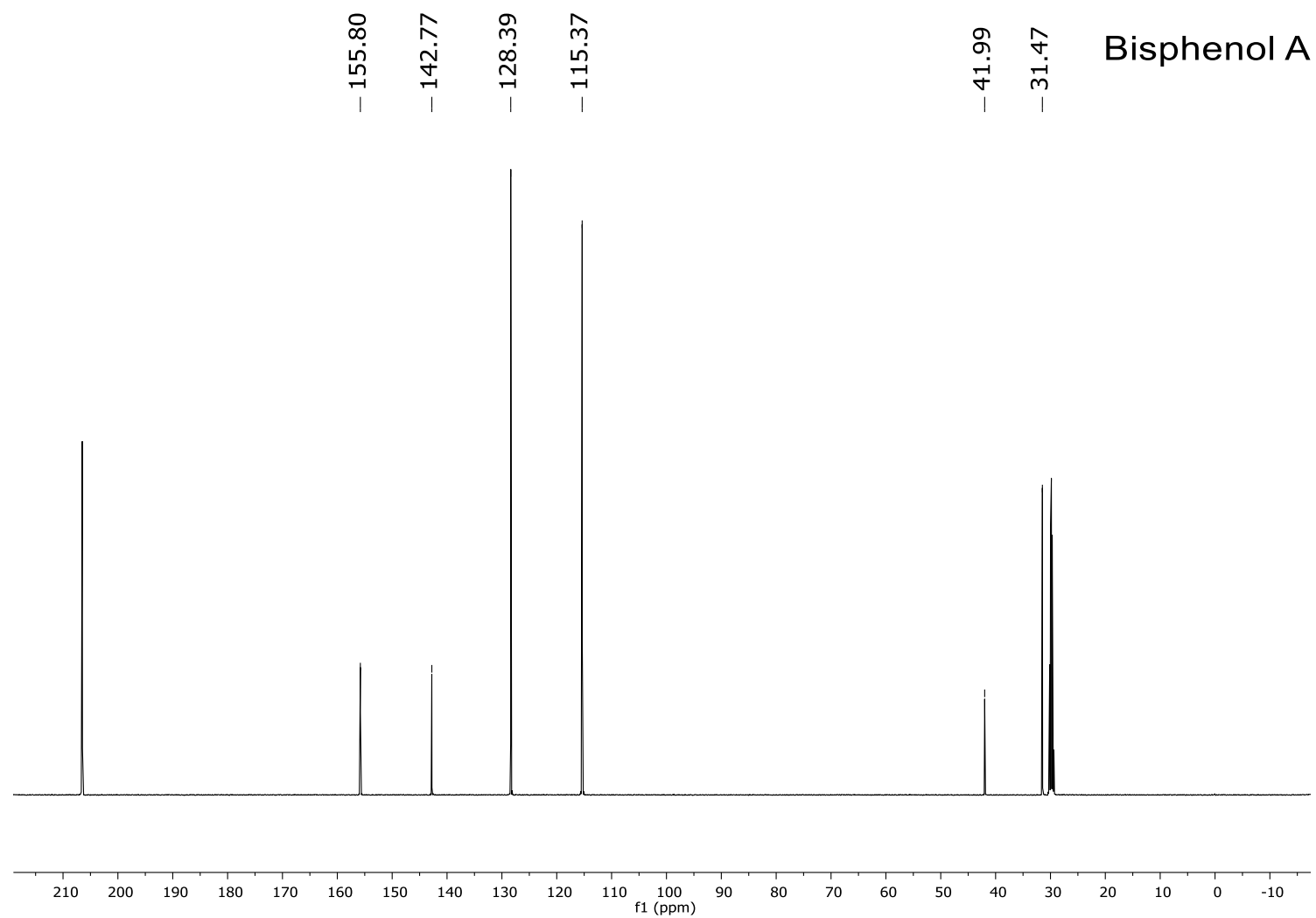
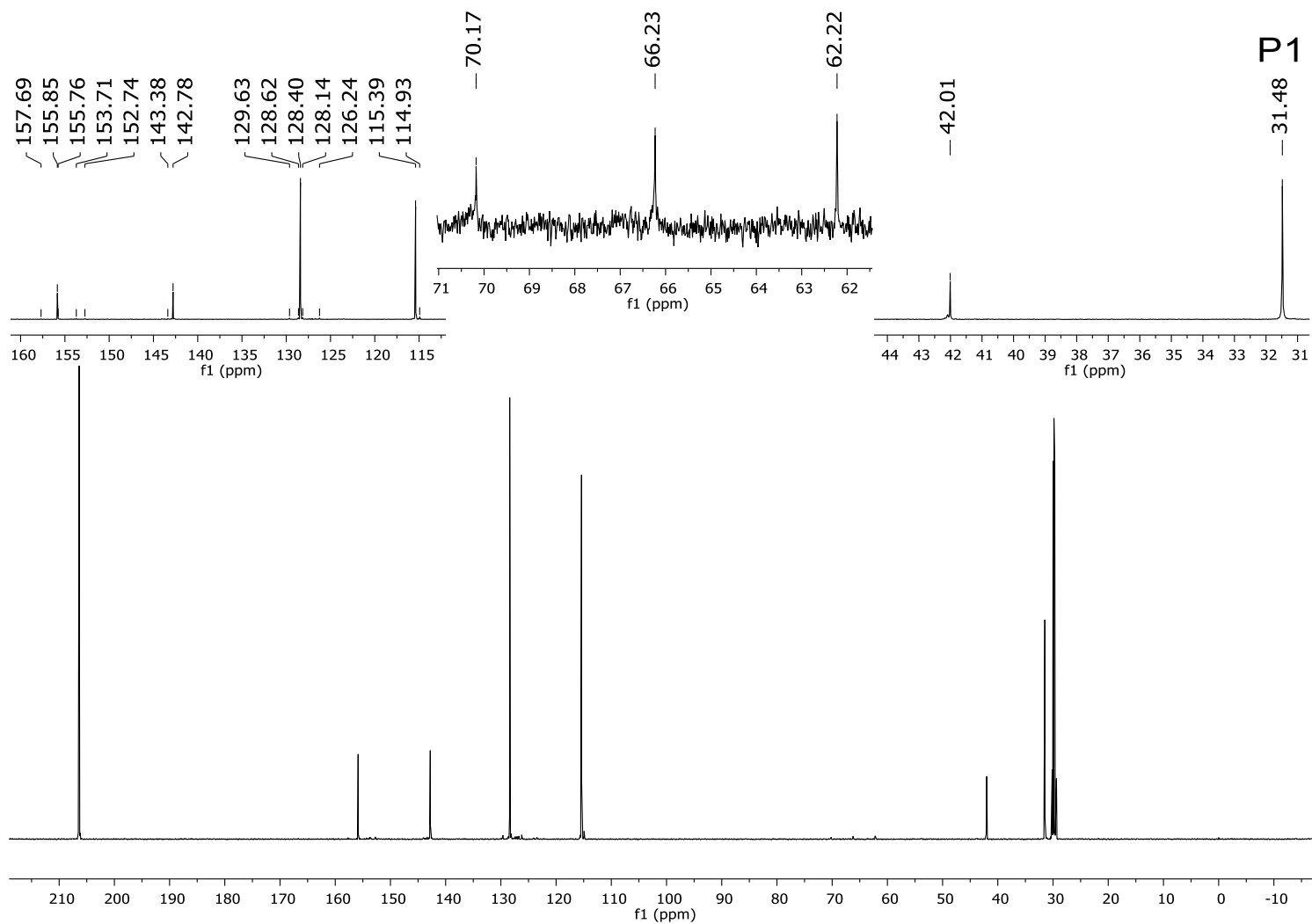


Figure A7: Epoxidized resin 1 spectra ( $^1\text{H}$  NMR)



**Figure A8:** Bisphenol-A spectra ( $^{13}\text{C}$  NMR)

Figure A9: Resin 1 spectra ( $^{13}\text{C}$  NMR)

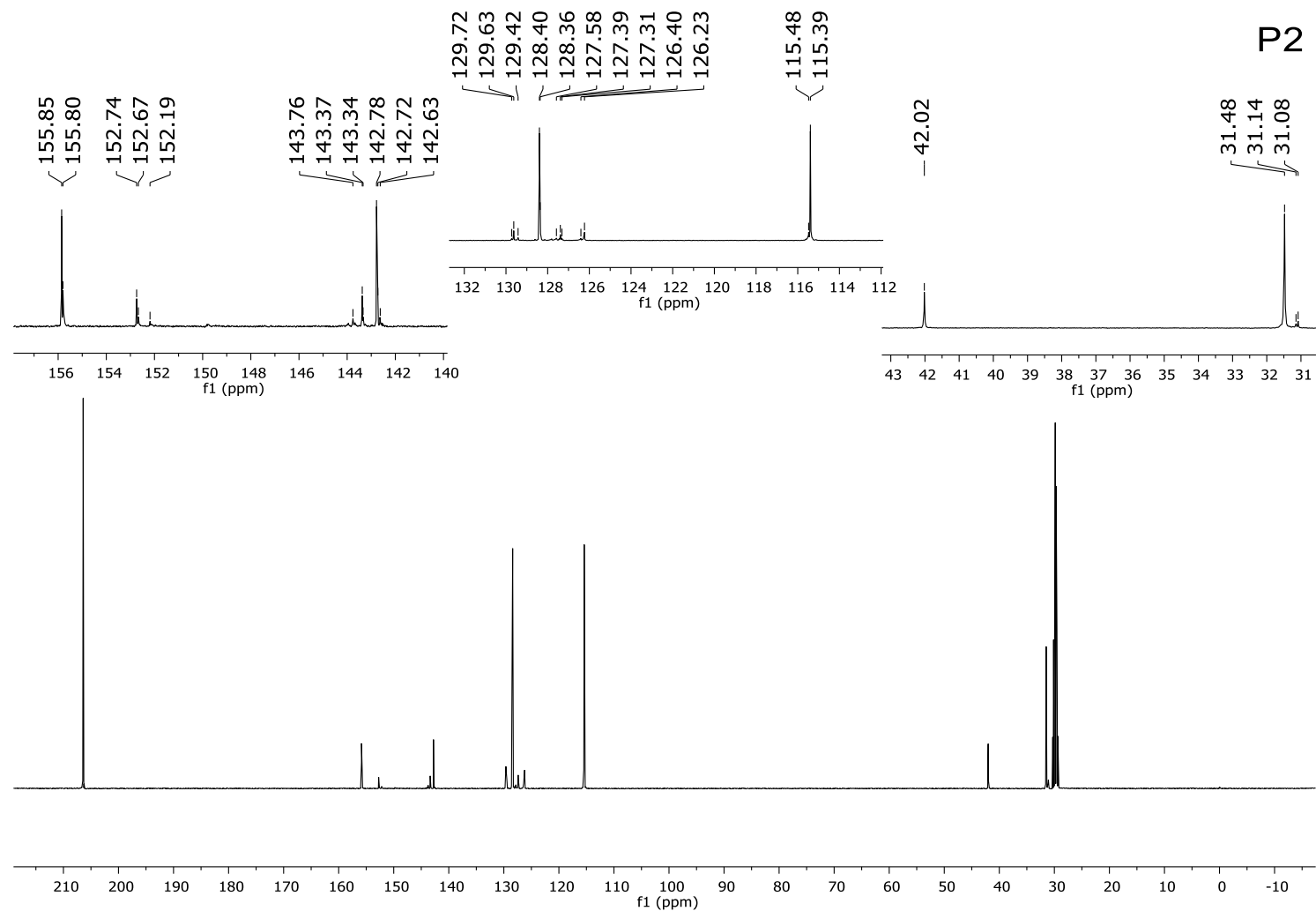
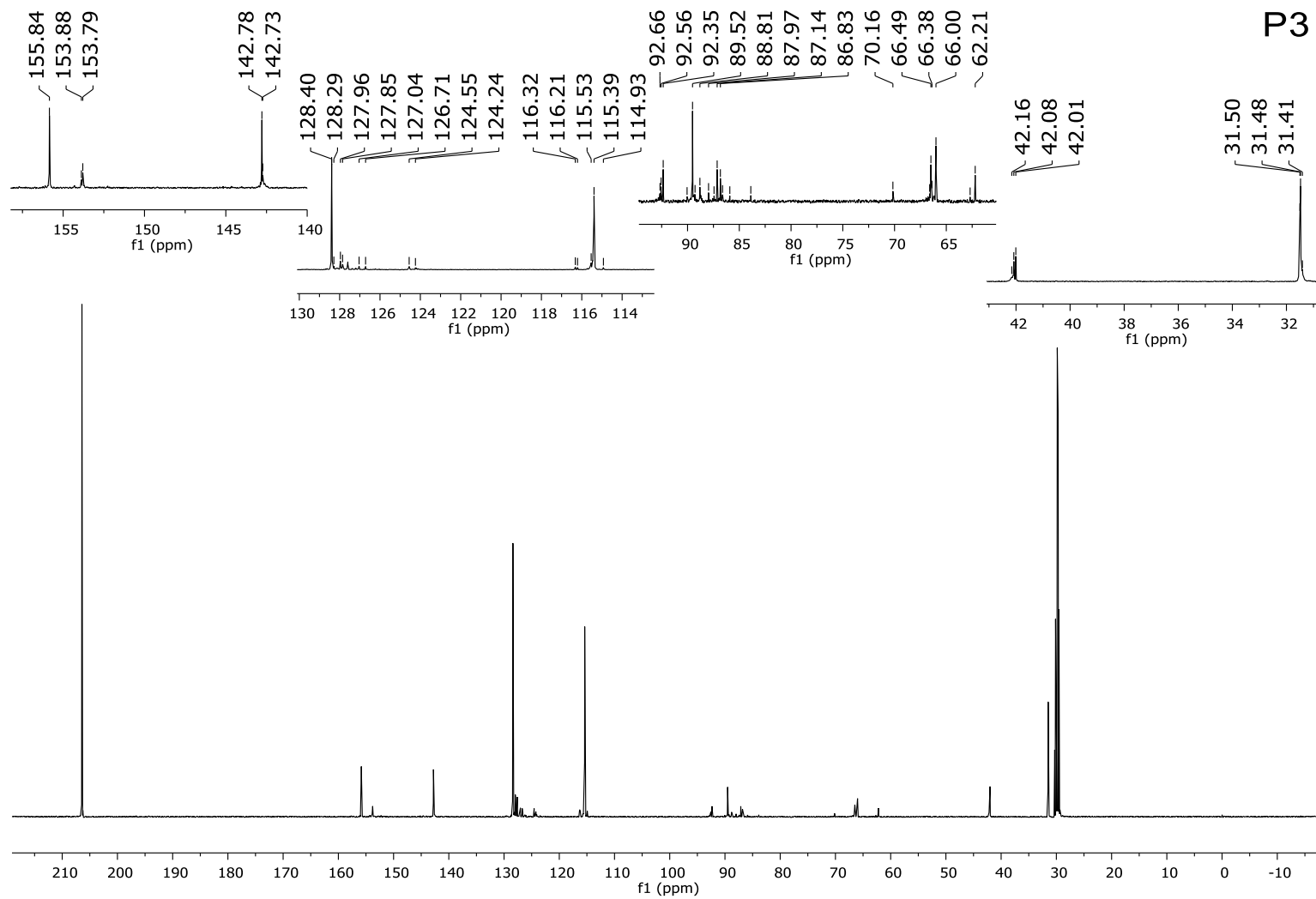


Figure A10: Resin 2 spectra ( $^{13}\text{C}$  NMR)

Figure A11: Resin 3 spectra ( $^{13}\text{C}$  NMR)

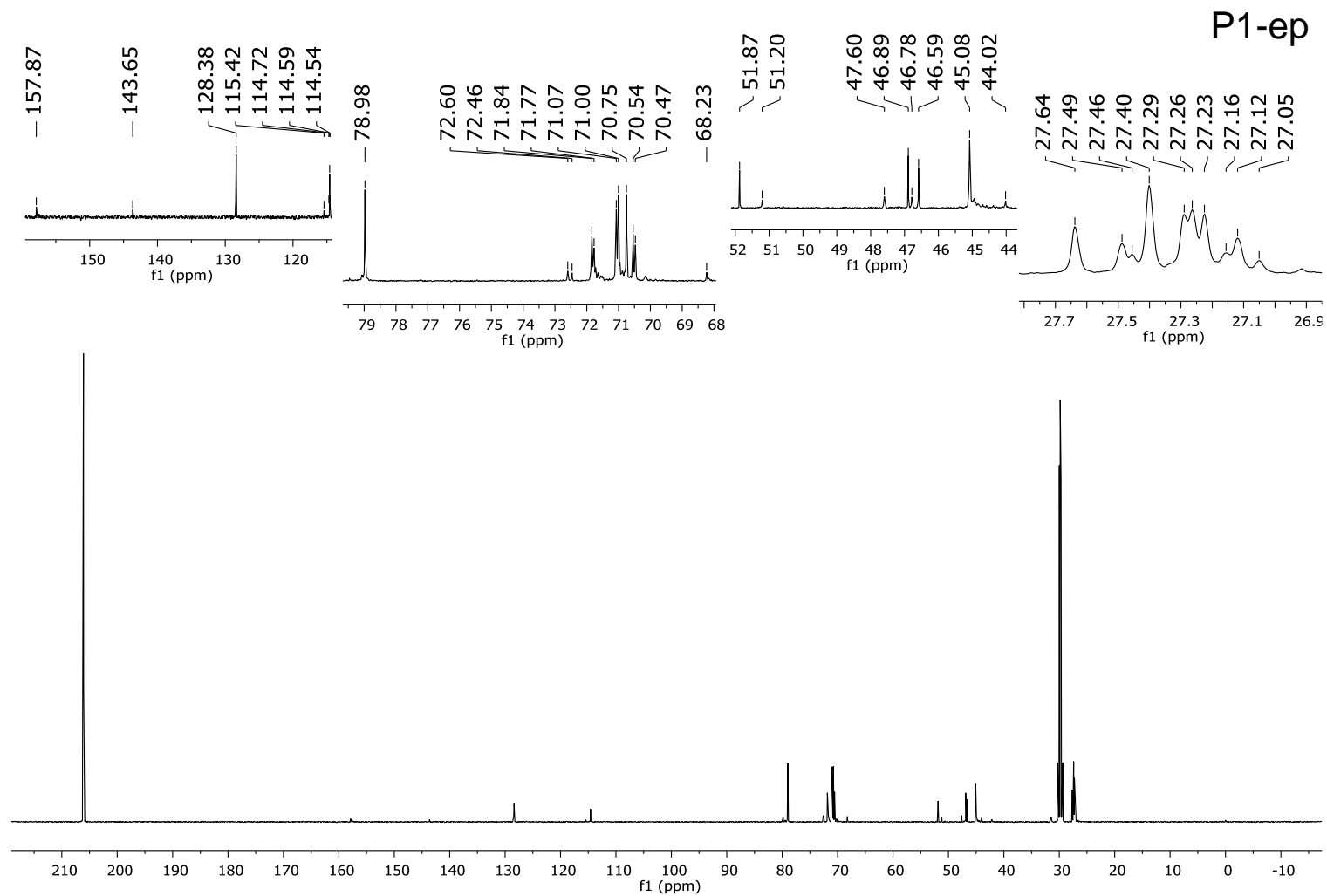
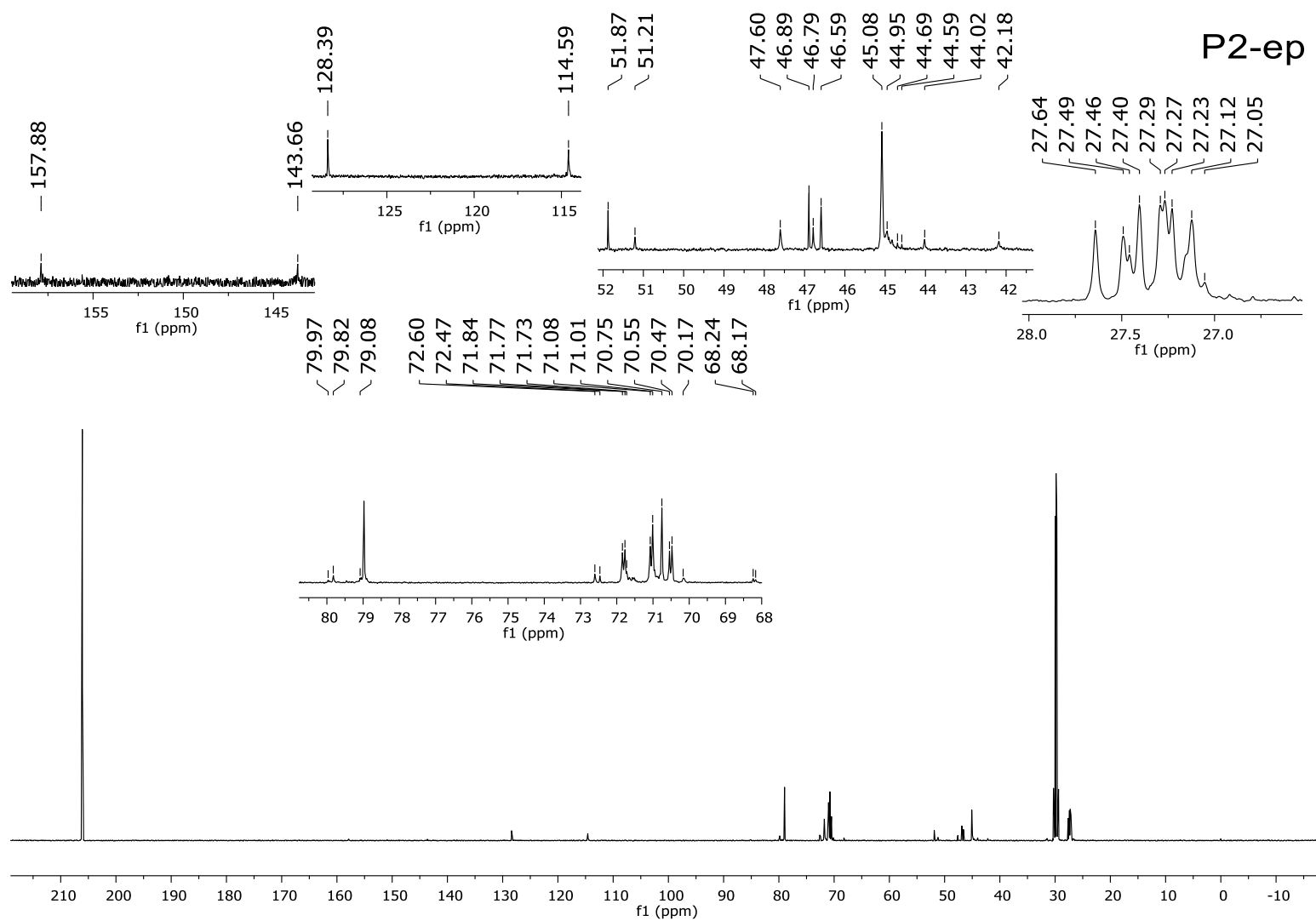


Figure A12: Epoxidized resin 1 spectra ( $^{13}\text{C}$  NMR)

Figure A13: Epoxidized resin 2 spectra ( $^{13}\text{C}$  NMR)

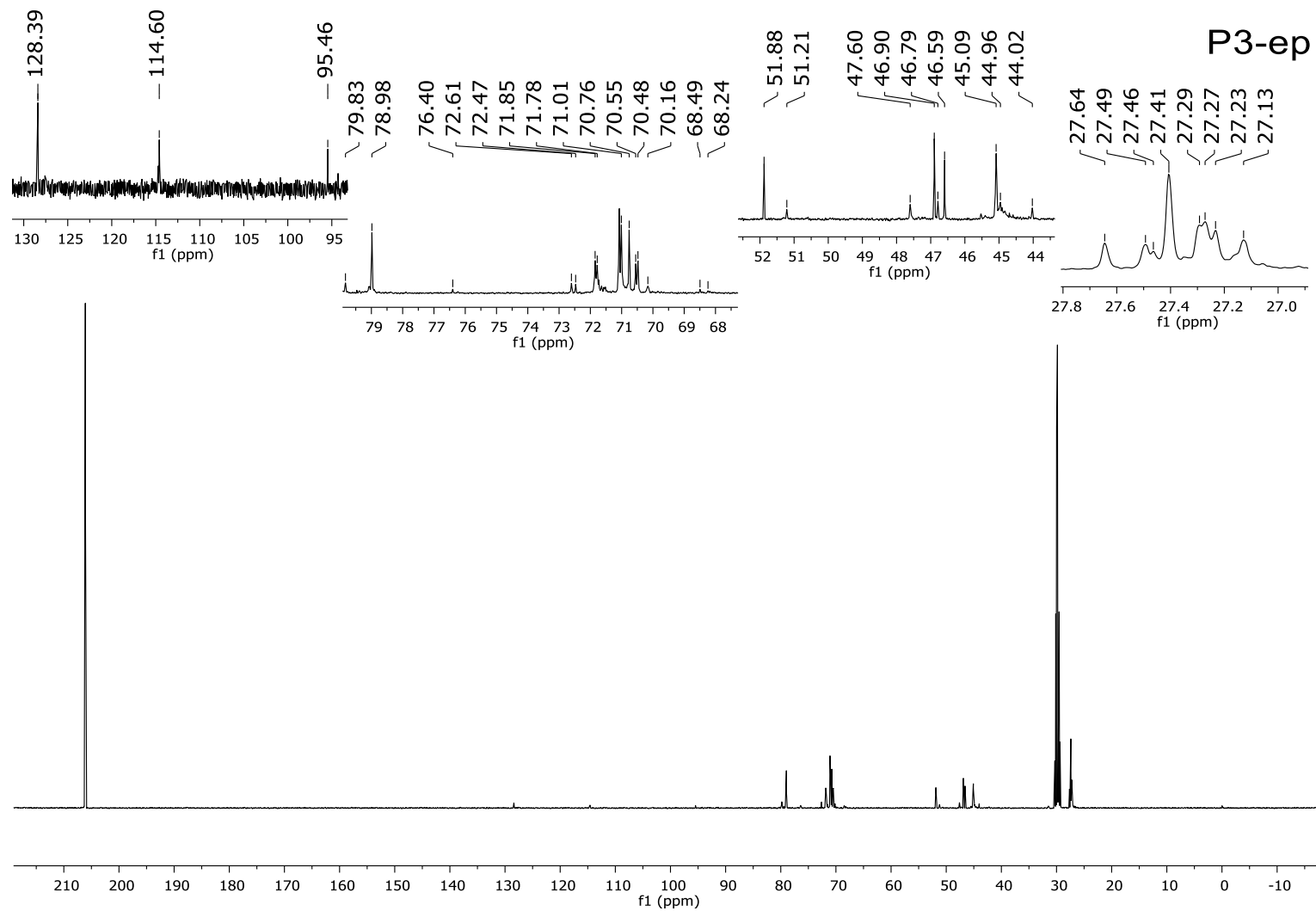
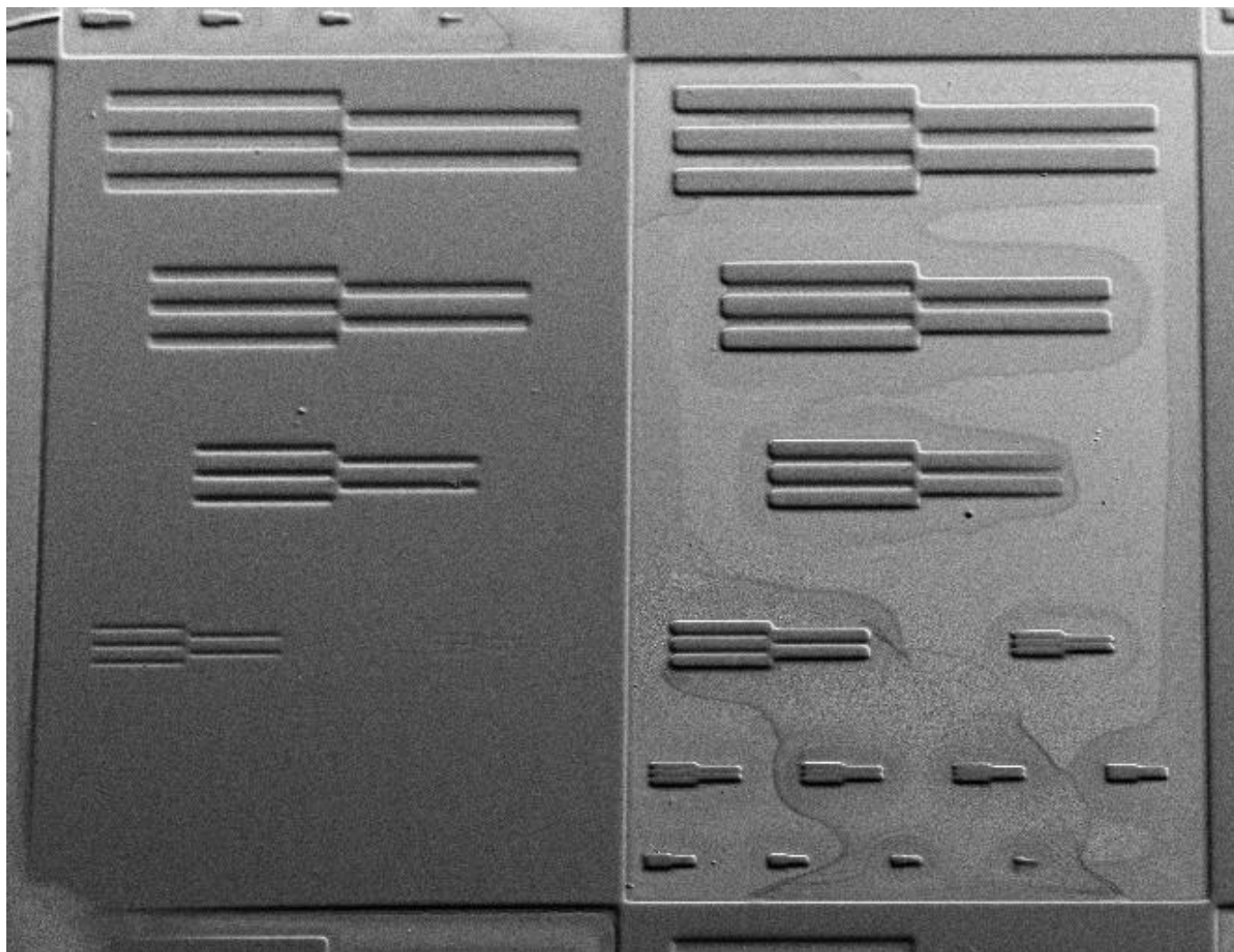
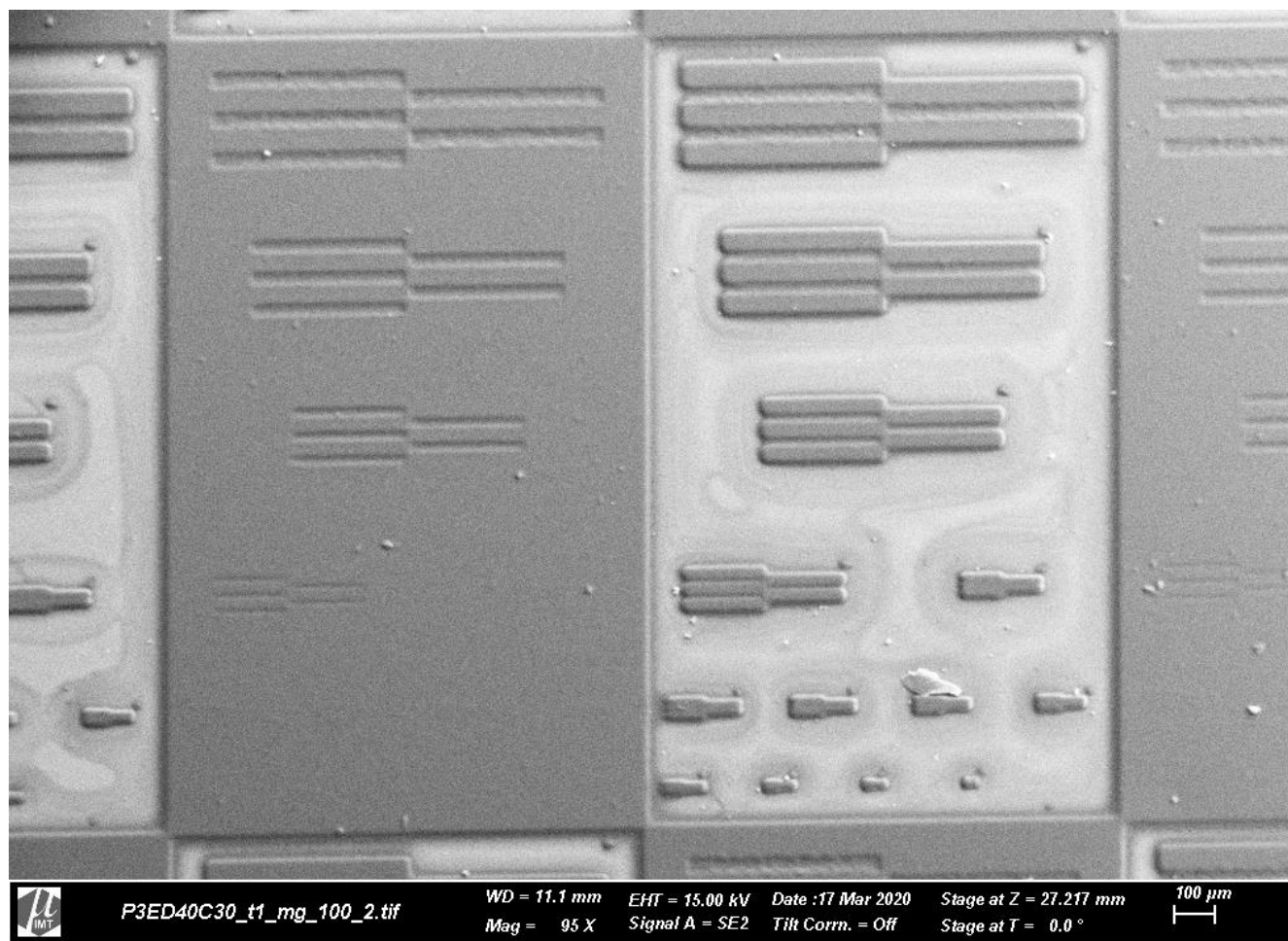


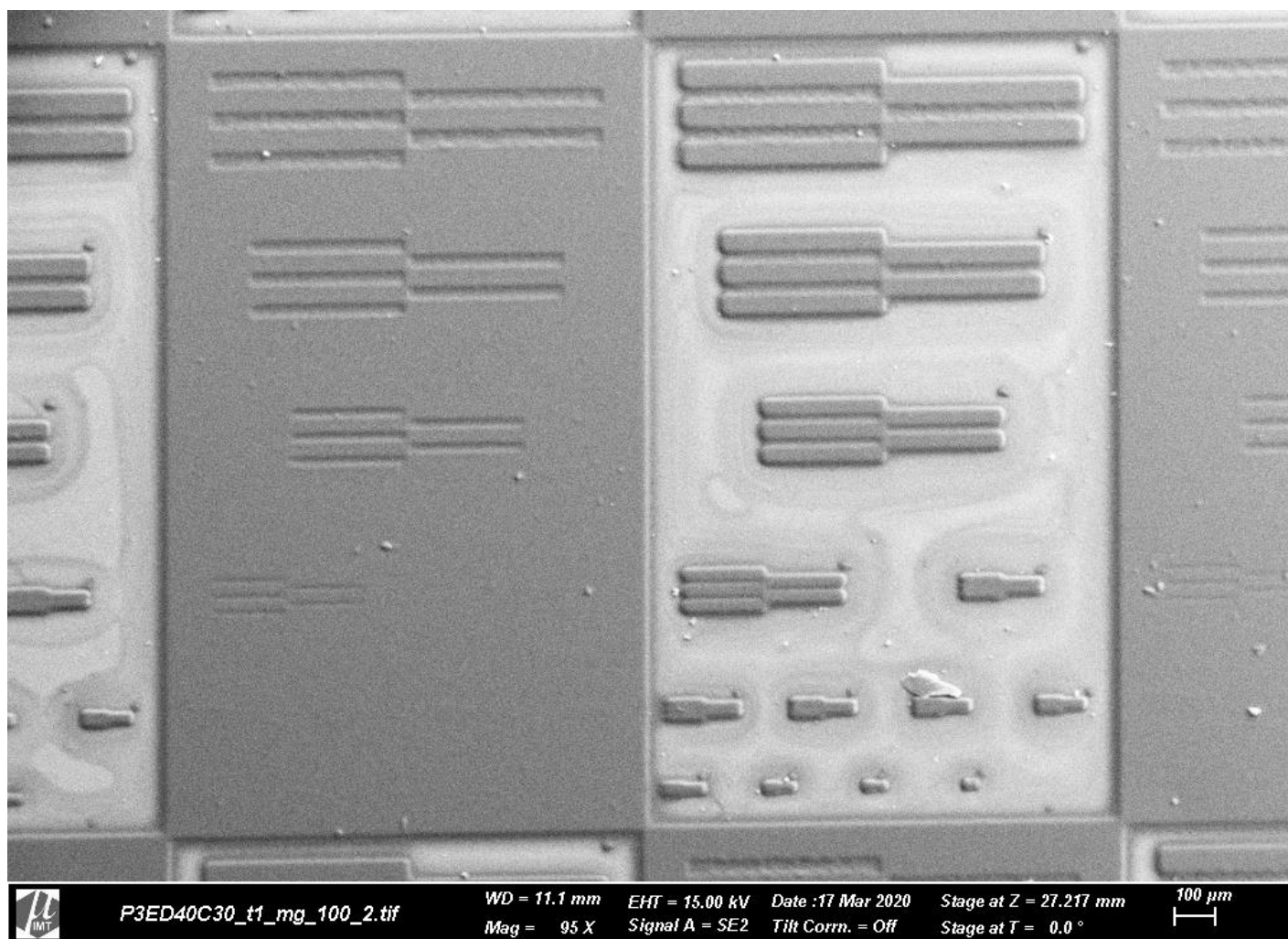
Figure A14: Epoxidized resin 2 spectra ( $^{13}\text{C}$  NMR)



**Figure A15:** SEM Images of P<sub>1</sub>ED<sub>40</sub>C<sub>30</sub> formulation. Patterned structures generated thorough UV Lithography after development. Reproduced from Vnieska et al (2020) [76] (CC BY)

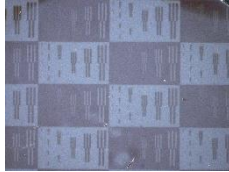
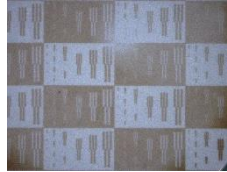
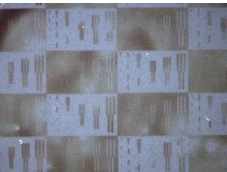
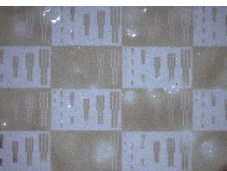
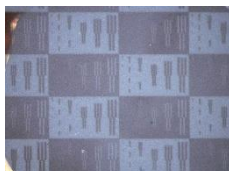
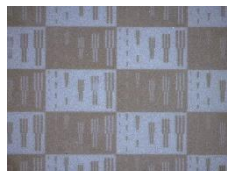
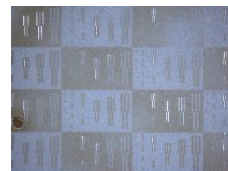


**Figure A16:** SEM Images of P<sub>2</sub>ED<sub>40</sub>C<sub>30</sub> formulation. Patterned structures generated through UV Lithography after development. Reproduced from Vlnieska et al (2020) [76] (CC BY)



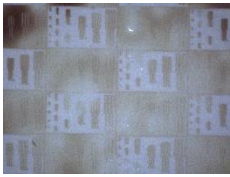
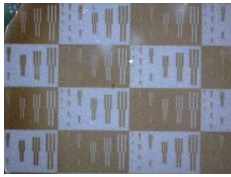
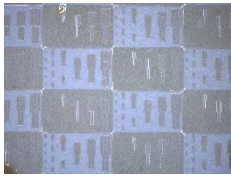
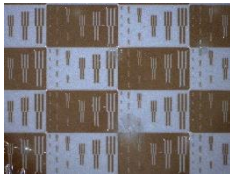
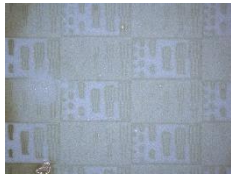
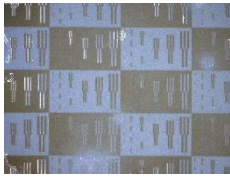
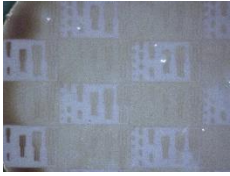
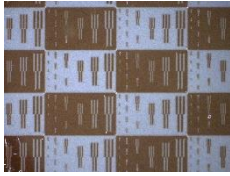
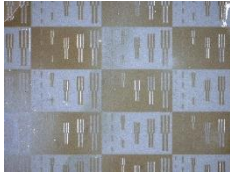
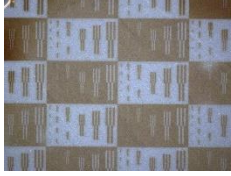
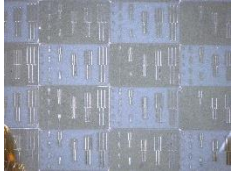
**Figure A17:** SEM Images of P<sub>3</sub>ED<sub>40</sub>C<sub>30</sub> formulation. Patterned structures generated through UV Lithography after development. Reproduced from Vlnieska et al (2020) [76] (CC BY)

**Table A1:** Patterned structures generated thorough UV Lithography after hard bake.

Triplicate	$P_1ED_0C_3$	$P_1ED_{40}C_{30}$	$P_2ED_0C_3$	$P_2ED_{40}C_{30}$	$P_3ED_0C_3$	$P_3ED_{40}C_{30}$
t1						
t2						
t3						

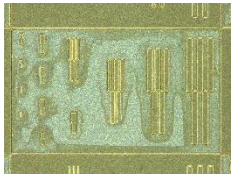
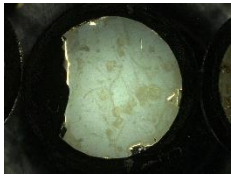
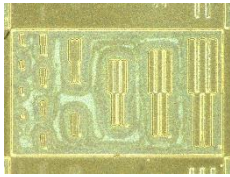
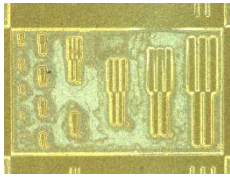
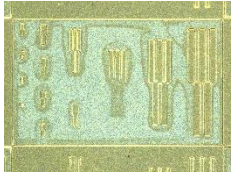
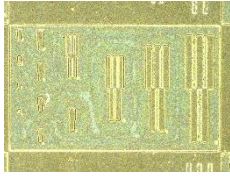
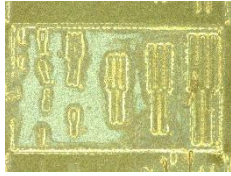
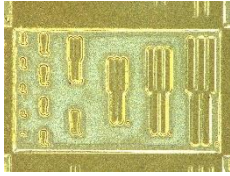
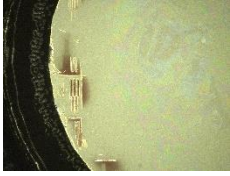
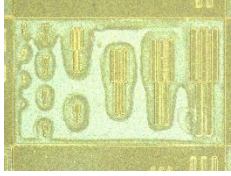
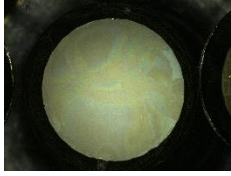
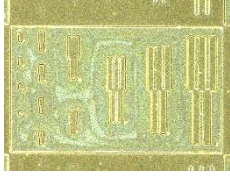
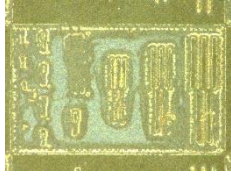
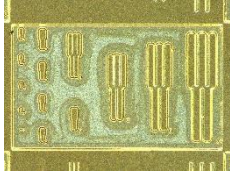
Reproduced from Vlnieska et al (2020) [76] (CC BY)

**Table A2:** Patterned structures generated thorough Deep-UV Lithography after hard bake.

Triplicate	$P_1ED_0C_3$	$P_1ED_{40}C_{30}$	$P_2ED_0C_3$	$P_2ED_{40}C_{30}$	$P_3ED_0C_3$	$P_3ED_{40}C_{30}$
t1						
t2						
t3						

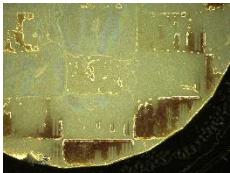
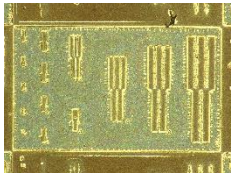
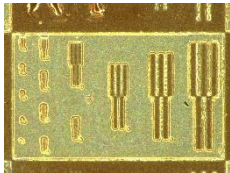
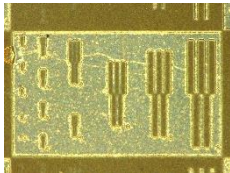
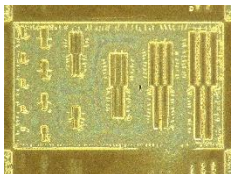
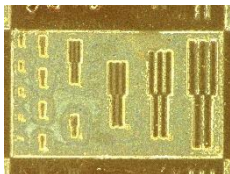
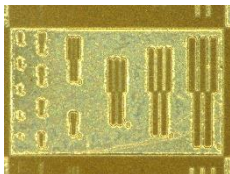
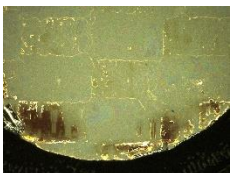
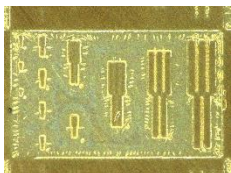
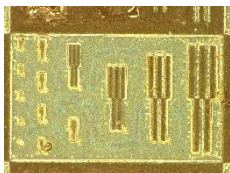
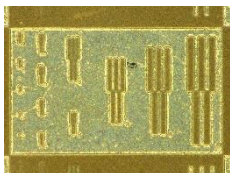
Reproduced from Vlnieska et al (2020) [76] (CC BY)

**Table A3:** Patterned structures generated thorough UV Lithography after development.

Triplicate	$P_1ED_0C_3$	$P_1ED_{40}C_{30}$	$P_2ED_0C_3$	$P_2ED_{40}C_{30}$	$P_3ED_0C_3$	$P_3ED_{40}C_{30}$
t1						
t2						
t3						

Reproduced from Vlnieska et al (2020) [76] (CC BY)

**Table A4:** Patterned structures generated thorough deep-UV Lithography after development.

Triplicate	$P_1ED_0C_3$	$P_1ED_{40}C_{30}$	$P_2ED_0C_3$	$P_2ED_{40}C_{30}$	$P_3ED_0C_3$	$P_3ED_{40}C_{30}$
t1						
t2						
t3						

Reproduced from Vlnieska et al (2020) [76] (CC BY)

## 9.2 List of publications during Ph.D. period

04.2020 – Vlnieska V., Zakharova M., Mikhaylov A., Kunka D.; Lithographic Performance of Aryl Epoxy Thermoset Resins as Negative Tone Photoresist for Microlithography. *Polymers*, 2020. 12(10).

03.2020 - Mikhaylov A., Reich S., Zakharova M., Vlnieska V., Laptev R., Plech A. and Kunka D.; Shack-Hartmann wavefront sensors based on 2D refractive lens arrays and super-resolution multi-contrast X-ray imaging. *Journal of Synchrotron Radiation*, 2020. 27(3): p. 788-795.

10.2019 - Vlnieska V., Mikhaylov A., Zakharova M., Blasco, E., Kunka D.; Epoxy Resins for Negative Tone Photoresists. *Polymers*, 2019. 11(9).

04.2019 - Zakharova, M., Reich, S., Mikhaylov A., Vlnieska V., Rolo T. d. S., Plech A., Kunka D.; Inverted Hartmann mask for single-shot phase-contrast x-ray imaging of dynamic processes. *Optics Letters*, 2019, 44(9): 2306-2309.

03.2019 - Mikhaylov, A., Reich, S., Plech, A., Zakharova, M., Vlnieska, V., Kunka, D.; 2D lens array for multi-contrast X-ray imaging. *EUV and X-ray Optics: Synergy between Laboratory and Space VI*. Ed.: R. Hudec, 2019. Article no: 1103208, SPIE, Bellingham, WA.

03.2019 - Zakharova, M., Reich, S., Mikhaylov, A., Vlnieska, V., Zuber, M., Engelhardt, S., Baumbach, T., Kunka, D.; A comparison of customized Hartmann and newly introduced inverted Hartmann masks for single-shot phase-contrast X-ray imaging. *EUV and X-ray Optics: Synergy between Laboratory and Space VI*. Ed.: R. Hudec, 2019. Article no: 110320U, SPIE, Bellingham, WA.

02.2019 - Muniz, A. S., Vlnieska, V., Ferraz, F. A., dos Santos Oliveira, A. R., Ramos, L. P. and César-Oliveira, M. A.; Polymer Additives as Cold Flow Improvers for Palm Oil Methyl Esters. *Macromol. Symp.*, 2019. 383: 1800026.

03.2018 - Vlnieska, V., Zakharova, M., Börner, M., Bade, K., Mohr, J., Kunka, D.; Chemical and Molecular Variations in Commercial Epoxide Photoresists for X-ray Lithography. *Applied Sciences*, 2018. 8(4)

02.2018 - Zakharova, M., V. Vlnieska, Fronasier, H., Börner M., Rolo T. d. S., Mohr, J., Kunka, D.; Development and Characterization of Two-Dimensional Gratings for Single-Shot X-ray Phase-Contrast Imaging. 2018. *Applied Sciences* 8(3).